

Air-cooled condenser steam flow distribution and related dephlegmator design considerations

Michael Owen



Dissertation presented for the degree of Doctor of Philosophy
in the Faculty of Engineering at
Stellenbosch University

Promoter: Prof. Detlev G. Kröger

December 2013

DECLARATION

By submitting this dissertation electronically, I declare that the entirety of the work contained therein is my own, original work, that I am the sole author thereof (save to the extent explicitly otherwise stated), that reproduction and publication thereof by Stellenbosch University will not infringe any third party rights and that I have not previously in its entirety or in part submitted it for obtaining any qualification.

Date:

ABSTRACT

The steam-side side operation of a practical air-cooled steam condenser is investigated using a combination of CFD, numerical, analytical and experimental methods. Particular attention is directed towards the vapor flow distribution in the primary condensers and dephlegmator performance.

Analysis of the vapor flow in the distributing manifold, connecting the steam turbine exhaust to the air-cooled heat exchangers, highlights the importance of careful design of the guide vanes in the manifold bends and junctions. Improved guide vane design and configuration can reduce the steam-side pressure drop over the manifold and improve the vapor flow distribution, which may be beneficial to condenser operation.

The vapor flow in the primary condensers is shown to exhibit a non-uniform distribution amongst the heat exchanger tubes. The vapor flow distribution is strongly linked to the distribution of tube inlet loss coefficients through the heat exchanger bundles. The non-uniform flow distribution places an additional demand on dephlegmator performance, over and above the demands of row effects in the case of multi-row primary condenser bundles. Row effects are shown to account for as much as 70 % of available dephlegmator capacity in this case. Simultaneously, inlet loss coefficient distributions can account for up to 30 % of dephlegmator capacity. In some situations then, the dephlegmator is fully utilized under ideal operating conditions and there is no margin of safety to cope with non-ideal operation of the primary condensers. The upstream regions of the primary condensers are therefore exposed to a high risk of undesirable non-condensable gas accumulation. Reduced dephlegmator capacity due to insufficient ejector performance may further compound this problem. Single-row primary condenser bundles eliminate row effects and thereby significantly reduce the demands on dephlegmator performance. The use of such bundles in the dephlegmator would also measurably reduce ejector loading. In light of the findings of this study, it is recommended that single-row bundles be considered as the primary option for future air-cooled condenser applications.

A hybrid (dry/wet) dephlegmator concept is analysed and shown to be able to provide measurably enhanced dephlegmator performance when operating in wet mode, while consuming only a small amount of water. The enhanced dephlegmator cooling translates to an increase in total air-cooled condenser capacity of up to 30 % at high ambient temperatures in this case. The benefit of this enhanced cooling capacity to steam turbine output may be significant. The hybrid dephlegmator concept therefore offers a simple, cost-effective and sustainable solution to the issue of reduced air-cooled condenser performance during hot periods. Careful design of the first and second stage bundle configurations in the hybrid dephlegmator is necessary to avoid flooding in the first stage during wet operation of the second. Furthermore, the slightly poorer dry-operation performance of the hybrid dephlegmator results in increased risk of non-condensable gas accumulation in multi-row primary condensers. Again, single-row primary condenser bundles would lay rest to such concerns.

OPSOMMING

Die bedryf aan die stoom-kant van 'n praktiese lugverkoelde-stoomkondensor word ondersoek met behulp van 'n kombinasie van berekeningsvloeiemechanika, numeriese, analitiese en eksperimentele metodes. 'n Spesifieke fokus word geplaas op die dampvloeiverspreiding in die primêre kondensors asook die deflegmator-werksverrigting.

Ontleding van die damp vloeï in die verdeelspruitstuk, wat die uitlaat van die stoomturbine aan die lugverkoelde-stoomkondensor koppel, beklemtoon die belangrikheid van noukeurige ontwerp van die leilemme in die spruitstukdraaie en aansluitings. Verbeterde leilemontwerp en opstelling kan die drukval aan die stoom-kant van die draaie en aansluitings verminder en die dampvloeiverspreiding verbeter. Dit kan gevolglik lei tot verbeterde werksverrigting van die kondensor.

Die studie toon dat 'n nie-eenvormige dampvloeiverspreiding in die warmteruilerbuis van die primêre kondensors bestaan. Die verspreiding van buisinlaat-verlieskoëffisiënte deur die bundels van die warmteruiler is sterk afhanklik van die voorgenome dampvloeiverspreiding. Die nie-eenvormige vloeiverspreiding veroorsaak 'n groter aanvraag na deflegmator-werksverrigting, bo-en-behalwe nog vereistes van ry-effekte in die geval waar multi-ry-bundels vir primêre kondensors gebruik word. Ry-effekte is verantwoordelik vir so veel as 70 % van die beskikbare deflegmator kapasiteit. Terselfdertyd kan die verspreiding van inlaat-verlieskoëffisiënte verantwoordelik wees vir tot 30 % van die deflegmator kapasiteit. In sommige gevalle is die deflegmator dus ten volle aangewend onder ideale bedryfstoeestande, en bestaan daar geen band van veiligheid om nie-ideale werksverrigting van die primêre kondensor te hanteer nie. Sekere dele van die stroom-op primêre kondensors word dus blootgestel aan 'n hoë risiko vir die opbou van ongewenste nie-kondenseerbare gasse. Verder kan 'n vermindering in deflegmator kapasiteit, weens onvoldoende werksverrigting van die vakuumpompe, dié probleem vererger. Enkel-ry-bundels vir primêre kondensors vermy ry-effekte en lei sodoende tot 'n aansienlike vermindering in die

aanvraag na deflegmator-werksverrigting. Die gebruik van sulke bundels in die deflegmator sou die vakuumpomplas ook meetbaar verminder. Uit die bevindinge van hierdie studie word dit aanbeveel dat enkel-ry bundels beskou word as die primêre opsie vir toekomstige lugverkoelde-kondensor aansoeke.

'n Konsep vir 'n hibriede-deflegmator (droog/nat) word ontleed. Die studie toon dat, deur hierdie konsep in die nat-modus te gebruik, 'n meetbare verbetering in deflegmator-werksverrigting gesien kan word, ten koste van net 'n klein hoeveelheid waterverbruik. Die verbetering in verkoelingsvermoë van die deflegmator beteken 'n toename van tot 30 % in die totale verkoelingsvermoë van die lugverkoelde-kondensor gedurende periodes wanneer hoë omgewingstemperature heersend is. Die voordeel van hierdie verbeterde verkoelingsvermoë op die werksuitset van die stoomturbine kan beduidend wees. Die konsep vir 'n hibriede-deflegmator bied dus 'n eenvoudige, koste-effektiewe en volhoubare oplossing vir warm atmosferiese periodes, wanneer die lugverkoelde-kondensor se verkoelingsvermoë afneem. Noukeurige ontwerp van die eerste en tweede fase bundelkonfigurasies in die hibriede-deflegmator is nodig om oorstroming in die eerste fase, tydens nat werking van die tweede fase, te verhoed. Verder veroorsaak die effens swakker werksverrigting, gedurende die bedryf van die hibriede-deflegmator in die droog-modus, 'n verhoogde risiko vir die opbou van nie-kondenseerbare gasse in multi-ry primêre kondensors. Weereens sal enkel-ry-bundels in primêre kondensors hierdie probleem oplos.

ACKNOWLEDGEMENTS

I would like to express my sincerest gratitude to everyone who supported and assisted me along this journey. Special thanks to Robyn Kime, my parents Chris and Julie Owen and my sister Candice; who were always there when I needed them most. My greatest thanks must be extended to Prof. Detlev Kröger, my supervisor and mentor for so long. Your patience and belief in me made all the difference.

The financial assistance of the National Research Foundation (NRF) towards this research is hereby acknowledged. Opinions expressed and conclusions arrived at, are those of the author and are not necessarily to be attributed to the NRF.

TABLE OF CONTENTS

	Page
Declaration	i
Abstract	ii
Opsomming	iv
Acknowledgments	vi
List of figures	xi
List of tables	xvi
Nomenclature	xvii
1. Introduction	1.1
1.1 Background and motivation	1.1
1.2 Existing research regarding ACC performance	1.2
1.3 Objectives	1.4
1.4 Outline	1.5
2. Operating principles	2.1
2.1 The operation of an ACC in a direct air-cooled power plant ...	2.1
2.2 The operation of an air-cooled condenser cell	2.2
2.3 The role of the dephlegmator	2.3
2.4 The relationship between ACC and steam turbine performance	2.5
3. Vapor flow in a distributing manifold	3.1
3.1 Introduction	3.1
3.2 CFD model	3.2
3.3 Assumptions and simplifications	3.4
3.4 Meshing	3.6
3.5 Verification	3.8
3.5.1 Fully developed turbulent flow in a circular duct	3.9
3.5.2 Miter bend	3.10
3.5.3 Conical reducer	3.11
3.5.4 T-junction	3.13
3.6 Results	3.15
3.6.1 Flow patterns in the distributing manifold	3.15
3.6.2 Vapor pressure change over the distributing manifold ...	3.19

3.6.3	Boundary conditions for the heat exchanger models	...	3.20
4.	Vapor flow distribution in the primary condensers of an ACC	4.1
4.1	Modelling procedure	4.1
4.2	CFD model	4.2
4.2.1	Description	4.2
4.2.2	Meshing	4.3
4.2.3	Verification	4.5
4.3	Numerical flow distribution calculation code	4.8
4.3.1	Description of the numerical code	4.8
4.3.2	SNIP calculation procedure	4.12
4.3.3	Verification	4.14
4.4	Steam-side primary condenser tube inlet loss coefficient distribution	4.16
4.4.1	Determining inlet loss coefficients from CFD data	4.16
4.4.2	Results	4.18
4.5	Steam-side tube outlet loss considerations	4.23
4.6	Vapor flow distribution in the primary condensers	4.26
5.	Dephlegmator considerations	5.1
5.1	Vapor backflow in the primary condensers	5.1
5.2	Dephlegmator sizing requirements	5.3
5.2.1	Inlet loss coefficient distribution requirements	5.3
5.2.2	Row effect requirements	5.6
5.2.3	Total dephlegmator requirement under ideal operating conditions	5.7
5.3	Vapor backflow in a conventional dephlegmator	5.10
5.3.1	Required ejector capacity	5.12
5.3.2	Backflow trends in a multi-row dephlegmator due to inadequate ejector performance	5.15
5.3.3	The effect of inlet rounding on backflow in a multi-row dephlegmator	5.17
6.	Hybrid (dry/wet) dephlegmator	6.1
6.1	Introduction	6.1
6.2	Description of the HDWD concept	6.3

6.3	Performance evaluation	6.5
6.3.1	Heat transfer rate	6.6
6.3.2	Flooding concerns	6.21
6.3.3	Steam-side pressure drop	6.24
6.3.4	Ejector loading	6.34
6.3.5	Water consumption	6.35
6.3.6	Recommended HDWD configuration	6.36
6.4	The effect of an HDWD on steam turbine output	6.37
7.	Concluding remarks and recommendations	7.1
	References	R.1
	Appendix A. Air-cooled steam condenser specifications	A.1
A.1	Finned-tube heat exchanger	A.1
A.2	Axial flow fan	A.2
A.3	Plant design specifications	A.3
	Appendix B. Fluid properties	B.1
B.1	Dry air ($220\text{ K} \leq T \leq 330\text{ K}$, $p = 101325\text{ N/m}^2$)	B.1
B.2	Saturated water vapor ($273.15\text{ K} \leq T \leq 380\text{ K}$)	B.1
B.3	Saturated water liquid ($273.15\text{ K} \leq T \leq 380\text{ K}$)	B.2
B.4	Mixtures of air and water vapor	B.2
	Appendix C. The effect of guide vanes on miter bend loss coefficient	C.1
C.1	Internal flow in a bend	C.1
C.2	CFD model	C.3
C.3	Experimental setup	C.4
C.4	Calculating the bend loss coefficient	C.5
C.5	Results	C.6
C.6	Conclusion	C.7
	Appendix D. Verification of the vapor flow distribution model	D.1
D.1	Verification of the CFD model	D.1
D.2	Verification of the numerical flow distribution code	D.2
	Appendix E. Ejector capacity and vapor backflow in a conventional dephlegmator	E.1
E.1	Sample calculation: Required ejector capacity	E.1
E.2	Sample calculation: Backflow length in the dephlegmator	E.7

Appendix F. Induced draft HDWD performance evaluation	F.1
F.1 Solution parameters and performance evaluation results	F.2
F.2 Sample calculation: HDWD operating as an evaporative cooler	F.3
F.2.1 Draft equation	F.3
F.2.2 First stage energy equation	F.7
F.2.3 Second stage energy equation	F.10
F.2.4 The effect of pressure drop related vapor temperature changes	F.19
F.3 Sample calculation: HDWD operating as an air-cooled condenser	F.21
F.3.1 Draft equation	F.21
F.3.2 First stage energy equation	F.27
F.3.3 Second stage energy equation	F.29

LIST OF FIGURES

	Page
Figure 2.1 Schematic representation of a direct air-cooled power plant	2.1
Figure 2.2 ACC street with five primary condensers and one dephlegmator	2.2
Figure 2.3 ACC street steam flow diagram	2.2
Figure 2.4 A-frame air-cooled condenser cell	2.3
Figure 2.5 Steam turbine performance characteristic and required ACC heat rejection rate	2.6
Figure 3.1 Schematic of the distributing manifold	3.2
Figure 3.2 Comparison of tetrahedral and polyhedral meshing schemes	3.7
Figure 3.3 Fully developed flow in a circular duct	3.9
Figure 3.4 Single miter bend with a cascade of circular-arc guide vanes	3.10
Figure 3.5 Predicted miter bend loss coefficient	3.11
Figure 3.6 Schematic of the conical reducer CFD model	3.12
Figure 3.7 Comparison of the predicted pressure distribution in the conical reducer: CFD versus empirical	3.12
Figure 3.8 Schematic of the T-junction CFD model	3.13
Figure 3.9 Loss coefficient in a sharp cornered T-junction between the supply duct and the perpendicular branch	3.14
Figure 3.10 Loss coefficient in the supply duct of a sharp cornered T-junction	3.14
Figure 3.11 Comparison of the predicted pressure distribution through the T-junction: CFD versus empirical	3.15
Figure 3.12 Contours of velocity magnitude on the mid-plane through the lower duct model	3.16
Figure 3.13 Contours of velocity magnitude on the mid-plane through the middle duct model	3.17
Figure 3.14 Pathlines illustrating the flow through the miter bend upstream of the heat exchangers	3.18

Figure 3.15	Contours of velocity magnitude on the mid-plane through the miter bend upstream of the heat exchangers	3.18
Figure 3.16	Pressure distribution in the distributing manifold	3.19
Figure 3.17	Radial velocity profiles in the distributing duct upstream of the heat exchanger bundles in the first street	3.20
Figure 3.18	Radial velocity profiles in the distributing duct upstream of the heat exchanger bundles in the final street	3.21
Figure 4.1	ACC cell numbering scheme	4.2
Figure 4.2	Details of the dividing and combining headers	4.2
Figure 4.3	Schematic of the CFD model of the dividing header of Cell 1 with the first bundle under investigation	4.4
Figure 4.4	Mesh in the heat exchanger tubes	4.5
Figure 4.5	Mesh in the heat exchanger dividing header	4.5
Figure 4.6	Zipfel's (1997) experimental setup	4.6
Figure 4.7	Lateral box	4.6
Figure 4.8	Comparison of the CFD and experimental results for $v_{hi}/v_l = 0.89$	4.7
Figure 4.9	Comparison of header pressure distributions for a parallel flow manifold	4.15
Figure 4.10	Comparison of the header pressure distributions for a reverse flow manifold	4.16
Figure 4.11	Static pressure distribution in a duct with a sudden contraction	4.17
Figure 4.12	Inlet loss coefficients in the first and second bundles of Cell 1	4.18
Figure 4.13	Inlet loss coefficients in the third and fourth bundles of Cell 1	4.18
Figure 4.14	Inlet loss coefficients in Cell 2	4.19
Figure 4.15	Inlet loss coefficients in Cell 4	4.19
Figure 4.16	Inlet loss coefficients in Cell 5	4.19
Figure 4.17	Inlet loss coefficients in Cell 6	4.20

Figure 4.18	Vector plot on the tube-row mid-plane illustrating the influence of the step on the flow entering the upstream tubes of Cell 1	4.22
Figure 4.19	Outlet loss coefficients in the first tube row of Cell 1	4.23
Figure 4.20	Flow patterns in Bundle 1 at the outlet of the (a) upstream tubes, (b) centrally located tubes, (c) downstream tubes	4.24
Figure 4.21	Flow patterns in Bundle 4 at the outlet of the (a) upstream tubes, (b) centrally located tubes, (c) downstream tubes	4.24
Figure 4.22	Vapor flow distribution in the first row of the first bundle of the primary condenser cells	4.27
Figure 4.23	Pressure distribution in the dividing header of an ACC street	4.28
Figure 5.1	Primary condenser tubes with vapor backflow	5.1
Figure 5.2	Primary condenser regions at greatest risk of non-condensable gas accumulation	5.4
Figure 5.3	Additional vapor flow required in the primary condensers to overcome inlet loss coefficient distributions	5.4
Figure 5.4	Additional vapor flow required in the primary condensers to overcome row effects	5.6
Figure 5.5	Ratio of second row to first row condensation rate	5.7
Figure 5.6	Total additional vapor flow requirement to prevent backflow in the primary condensers	5.8
Figure 5.7	Fraction of the dephlegmator capacity required to provide sufficient additional primary condenser vapor flow	5.8
Figure 5.8	Dephlegmator tubes with backflow	5.11
Figure 5.9	Required ejector suction as a function of vapor temperature	5.12
Figure 5.10	Required ejector suction as a function of approach temperature difference	5.12
Figure 5.11	Comparison of required and available ejector capacity	5.14
Figure 5.12	Thermographic imagery of an operating ACC street with severe accumulation of non-condensable gases in the dephlegmator	5.14

Figure 5.13	The effect of inadequate ejector sizing on backflow in a conventional dephlegmator	5.15
Figure 5.14	Contraction loss coefficient for a rounded inlet	5.17
Figure 5.15	The effect of inlet rounding in the upstream tubes on vapor backflow	5.18
Figure 6.1	Schematic of the forced draft HDWD concept	6.3
Figure 6.2	Comparison of air-side pressure drop correlations for a deluged tube bundle	6.15
Figure 6.3	Bundle of plain tubes in cross-flow	6.16
Figure 6.4	Heat transfer rate comparison between a conventional dephlegmator and the HDWD operating as an air-cooled condenser	6.18
Figure 6.5	Heat transfer rate comparison between a conventional dephlegmator and the HDWD operating as an evaporative cooler	6.19
Figure 6.6	Flooding considerations in the first stage of the HDWD ...	6.23
Figure 6.7	Schematic of the induced draft HDWD concept	6.23
Figure 6.8	Comparison of the steam-side pressure drop over a conventional dephlegmator and the HDWD operating as an air-cooled condenser	6.31
Figure 6.9	Comparison of the steam-side pressure drop over a conventional dephlegmator and the HDWD operating as an evaporative condenser	6.32
Figure 6.10	Concentration of water vapor in the ejection mixture required to prevent vapor backflow in the dephlegmator ...	6.35
Figure 6.11	Water consumption in the HDWD	6.36
Figure 6.12	The effect of dephlegmator configuration on turbine backpressure	6.38
Figure 6.13	The effect of dephlegmator configuration on vapor temperature	6.39
Figure 6.14	The effect of dephlegmator configuration on steam turbine output	6.39

Figure C.1	Single miter bend with a cascade of circular-arc guide vanes	C.1
Figure C.2	Experimental setup	C.4
Figure C.3	Typical hydraulic gradient through a bend	C.5
Figure C.4	The effect of the number of guide vanes on miter bend loss coefficient	C.6
Figure D.1	Comparison of the CFD and experimental results for $v_{hi}/v_l = 0.68$	D.1
Figure D.2	Comparison of the CFD and experimental results for $v_{hi}/v_l = 0.89$	D.1
Figure D.3	Comparison of the CFD and experimental results for $v_{hi}/v_l = 1.46$	D.2
Figure D.4	Comparison of the CFD and experimental results for $v_{hi}/v_l = 1.90$	D.2
Figure D.5	Comparison of the header pressure distributions for a 10 lateral parallel flow manifold	D.3
Figure D.6	Comparison of the header pressure distributions for a 10 lateral reverse flow manifold	D.3
Figure D.7	Comparison of the header pressure distributions for a 20 lateral parallel flow manifold	D.4
Figure D.8	Comparison of the header pressure distributions for a 20 lateral reverse flow manifold	D.4
Figure E.1	Dephlegmator tubes with non-condensable gas accumulation	E.1

LIST OF TABLES

	Page
Table 5.1 The effect of inlet rounding on the contraction loss coefficient	5.17
Table 6.1 HDWD second stage tube bundle configurations	6.5
Table 6.2 Contributors to the steam-side pressure drop in the HDWD (Config. I, wet)	6.32
Table A.1 Finned-tube heat exchanger specifications	A.1
Table A.2 Axial flow fan specifications	A.2
Table A.3 Design point specifications	A.3
Table E.1 Condensation rates for 100 % effective operation	E.1
Table F.1 Second stage plane tube bundle Configuration I	F.1
Table F.2 Operating conditions	F.2
Table F.3 Solution parameters for wet operation of the HDWD	F.2
Table F.4 Solution parameters for dry operation of the HDWD	F.2
Table F.5 Converged performance evaluation results	F.3
Table F.6 Mean vapor temperatures through the HDWD second stage	F.21

NOMENCLATURE**Symbols**

a	-	constant or dimension, m
b	-	dimension, m
A	-	area, m ²
c	-	chord length, m
c_p	-	specific heat, J/kgK
C_d	-	lateral discharge coefficient
C_T	-	turning loss coefficient
C_μ	-	constant
d	-	diameter, m
DAE	-	dry air equivalent
e	-	heat transfer effectiveness
E	-	error
f	-	dimensionless friction factor
Fr_D	-	Froude number
G	-	mass flux, kg/m ² s
h	-	heat transfer coefficient, W/m ² K
H	-	height, m
i	-	enthalpy, J/kg
I	-	turbulent intensity, %
k	-	turbulent kinetic energy, m ² /s ² ; or thermal conductivity, W/mK
K	-	dimensionless loss coefficient
l	-	characteristic turbulent length, m
L	-	length, m
m	-	mass flow rate, kg/s
M	-	total mass flow rate, kg/s

n	-	number
NTU	-	number of heat transfer units
Nu	-	Nusselt number
Ny	-	characteristic heat transfer parameter, m^{-1}
Oh	-	Ohnesorge number
p	-	pressure, N/m^2
P	-	power, W; or pitch, m
Pr	-	Prandtl number
Q	-	heat transfer rate, W
r	-	radial distance or radius, m
R	-	entrainment ratio
Re	-	Reynolds number
RH	-	relative humidity, %
Ry	-	characteristic flow parameter, m^{-1}
S	-	circumference, m
T	-	temperature, °C or K
u	-	header velocity, m/s
UA	-	overall heat transfer coefficient, W/K
v	-	velocity, m/s
V	-	volumetric flow rate, m^3/s
W	-	width, m
x	-	two-phase mixture quality or axial distance, m
y^+	-	dimensionless wall distance
z	-	elevation, m

Greek symbols

α	-	kinetic energy correction factor or void fraction
Γ	-	deluge water flow rate over half a tube per unit length, kg/ms
Δ	-	difference or increment
ε	-	turbulent energy dissipation rate, m^2/s^3 ; or surface roughness, m
θ	-	angle, $^\circ$
μ	-	dynamic viscosity, kg/ms
ρ	-	density, kg/m^3
σ	-	area ratio or surface tension, N/m
ϕ	-	diameter, m; arrangement factor or two-phase friction multiplier
φ	-	parameter

Subscripts

a	-	air or ambient
app	-	approach
avg	-	average
b	-	bundles
bf	-	backflow
c	-	combining header, condensation or contraction
con	-	continuity
$conv$	-	conventional dephlegmator
ct	-	droplet collecting troughs
d	-	dividing header or mass transfer
de	-	drift eliminators
dep	-	dephlegmator
dj	-	downstream jetting
do	-	downstream obstacles

<i>D</i>	-	Darcy
<i>e</i>	-	effective
<i>ej</i>	-	ejection
<i>eq</i>	-	equivalent
<i>evap</i>	-	evaporated
<i>f</i>	-	film
<i>fg</i>	-	vaporization
<i>fr</i>	-	frontal
<i>F_s</i>	-	fan static
<i>g</i>	-	geodetic
<i>gen</i>	-	generated
<i>h</i>	-	header
<i>he</i>	-	normal isothermal flow through a finned-tube heat exchanger
<i>H</i>	-	steam supply header
<i>i</i>	-	inlet, internal or counter
<i>in</i>	-	total inlet
<i>l</i>	-	longitudinal, lateral or liquid
<i>L</i>	-	heat exchanger lateral
<i>lam</i>	-	laminar
<i>m</i>	-	momentum or mean
<i>M</i>	-	molar weight
<i>max</i>	-	maximum
<i>mb</i>	-	miter bend
<i>min</i>	-	minimum
<i>mom</i>	-	momentum
<i>nc</i>	-	non-condensables
<i>o</i>	-	outlet or free-stream

<i>pri</i>	-	primary condenser
<i>r</i>	-	roughness, riser or row
<i>red</i>	-	conical reducer
<i>ref</i>	-	reference
<i>req</i>	-	required
<i>s</i>	-	superficial
<i>t</i>	-	tube or transverse
<i>tot</i>	-	total
<i>tp</i>	-	tubes per pass or two-phase
<i>tr</i>	-	tubes per row
<i>ts</i>	-	tower supports or tube cross-sectional
<i>turb</i>	-	turbulent
<i>up</i>	-	upstream
<i>v</i>	-	vapor or guide vanes
<i>vp</i>	-	vapor passes
<i>vn</i>	-	normal to bulk vapor flow direction
<i>w</i>	-	water film
<i>θt</i>	-	overall for a finned-tube bundle

1. INTRODUCTION

1.1 Background and motivation

The production of electricity is traditionally a water intensive activity. With increasing pressure on fresh water supplies around the world (Barker, 2007) there is ever increasing pressure on the power producing industry to reduce water consumption. Approximately half of all existing thermoelectric power plants in the United States make use of evaporative (wet) cooling (Carney et al., 2008). This trend is similar in many other parts of the world. At evaporative cooled plants, the condenser typically accounts for more than 80 % of the total water consumed (DiFilippo, 2008). The use of alternative means of cooling therefore holds the greatest potential for reducing water consumption at thermoelectric power plants.

Air-cooled steam condensers (ACCs) are designed to service the cooling requirements of power plants using ambient air as the cooling medium. No water is directly consumed in the cooling process and the water consumption at an air-cooled plant is thus significantly less than at a wet cooled plant. Furthermore, because no water is required for cooling purposes, the location of an ACC equipped power plant is less dependent on the proximity of abundant fresh water resources. Plants can therefore be located nearer to load centres and/or fuel/energy sources resulting in reduced transmission losses, increased supply reliability and reduced transport costs (Gadhamshetty et al., 2006). Independence from water resources also renders air-cooled plants particularly suitable for use in arid regions, making ACCs an attractive option for use in solar thermal applications in South Africa and many other parts of the world.

ACCs are, however, currently more capital intensive than wet cooling systems and typically exact a penalty in terms of plant performance. The energy generation cost at air-cooled plants is therefore typically greater than at their wet-cooled counterparts (Barker, 2007). These cost disadvantages are a result of the relatively poor heat transfer characteristics and thermodynamic properties of air

relative to water, as well as the sensitivity of ACC performance to meteorological and ambient conditions.

Since air has a low density and specific heat, large volumes must be circulated to achieve adequate cooling (Hassani et al., 2003). Fan power consumption in mechanical draft ACCs is therefore significant and expensive finned-tube heat exchangers are required to maximize the potential for heat transfer. In addition, to achieve adequate circulation, the air-side pressure drop across the ACC should be as low as possible (Hassani et al., 2003) and air velocities through the system need to be minimized. Large cross-sectional air flow areas are therefore necessary, resulting in increased capital costs. According to Maulbestch (2008), the capital cost of an ACC can be as much as three times greater than the equivalent wet cooling system, while the running costs are typically double. Current rapidly increasing fresh water prices, however, are beginning to improve the competitiveness of ACC operating costs.

ACCs can experience a decrease in heat transfer rate in excess of 10 % (Gadhamshetty et al., 2006) during periods of unfavourable operating conditions (high ambient temperatures and/or strong winds for example). ACC performance is also sensitive to the proximity and orientation of other power plant structures (Goldschagg et al., 1997; Gao et al., 2009). A decrease in the ACC heat transfer rate results in a reduction in steam turbine output and ultimately a loss in operating income. In extreme cases reduced condenser performance can lead to emergency turbine shutdowns.

The undesirable aspects of ACC performance need to be addressed and mitigated if ACCs are to assume the position of the cooling strategy of choice for all thermoelectric power plants. In light of ever worsening global water security concerns, this they surely must.

1.2 Existing research regarding ACC performance

The vast majority of recent research relating specifically to ACC performance has focused on the air-side operation of these systems. A number of experimental and

numerical investigations using computational fluid dynamics (CFD) have been undertaken in an attempt to identify and quantify the negative effects of ambient and meteorological conditions, and wind in particular, on ACC effectiveness. Examples of relevant publications include Duvenhage and Kröger (1996), McGowan et al. (2008) and Liu et al. (2009), amongst a multitude of others. Furthermore, numerous studies have attempted to identify measures of mitigating the negative effects of wind on ACC performance. Meyer (2005), Gao et al. (2010) and Owen and Kröger (2010) are examples of pertinent publications.

Few studies have addressed steam-side performance considerations specific to ACCs. A wide range of literature is available regarding the important topics of in-tube condensation heat transfer and pressure drop. Examples for the former include Chato (1962) and Shah (1979). Lockhart and Martinelli (1949), Friedel (1979) and Groenewald and Kröger (1995), amongst several others, are examples of the latter. Heat transfer in the presence of non-condensable gases – see for example Minkowycz and Sparrow (1966), Al-Shammari et al. (2004) and Li et al. (2011) – and flooding in reflux condensers – see Zapke and Kröger (1996), Palen and Yang (2001) and Sacramento and Heggs (2009) – are also well researched. Unfortunately, very few of these studies are based on parameters and conditions similar to those characteristic of large scale ACCs for power plant applications.

Flow distributions in heat exchanger-type manifold systems have been addressed in several texts including Datta and Majumdar (1980), and more recently Ablanque et al. (2010). Berg and Berg (1980) investigated vapor backflow due to row effects in multi-row, single-vapor-pass, air-cooled condensers with isothermal vapor flow. Breber et al. (1982) used Berg and Berg's method to develop equations describing the effect of backflow on the cooling performance of air-cooled heat exchangers. Fabbri (2000) modified Berg and Berg's model to account for the influence of changing vapor temperature and non-uniformities in the air-flow distribution over the heat exchanger. Berg and Berg, and

subsequently Breber et al. and Fabbri, ignore inlet/outlet and acceleration effects caused by condensation inside the tubes in their models. Zipfel and Kröger (1997) experimentally investigated lateral inlet loss coefficients in a manifold system representative of a typical ACC primary heat exchanger bundle. They report a variation in the inlet loss coefficient along the header flow direction. Such variations in inlet loss coefficients cannot be ignored in the analysis of vapor flow distribution trends in ACCs. Zapke (1997) experimentally investigated the characteristics of gas-liquid counter-flow in inclined flattened tubes typical of modern ACCs. His results and subsequent publications (Zapke and Kröger, 1997) are an important contribution to this field.

Also of interest are studies by Shi et al. (2009) and Shi and Shi (2009), whose CFD results indicate room for improvement in the design of the steam distributing manifold upstream of the ACC heat exchangers. Improved manifold design may reduce steam-side pressure losses and improve the uniformity of the vapor flow distribution amongst the ACC streets.

Specific information regarding the vapor flow distribution through ACC heat exchanger bundles and subsequent dephlegmator performance and design considerations could not be found in the literature.

1.3 Objectives

As the use of ACCs becomes more widespread, the importance of ensuring adequate and predictable cooling performance becomes critical to the efficient operation of individual plants and ultimately the entire energy network (Maulbetsch and DiFilippo, 2007). The objectives of this study are therefore to investigate the steam-side operation of an ACC with particular emphasis on vapor flow distribution in the heat exchanger bundles and dephlegmator performance. A practical hypothetical condenser is considered as a case study. Details of this ACC are included in Appendix A.

A combination of CFD, numerical, analytical and experimental methods is used to analyse the vapor flow distribution upstream of and through the heat exchanger

bundles, and to quantify dephlegmator performance requirements. In addition, an alternative dephlegmator concept, expected to enhance overall condenser performance, and subsequently increase operating income, is to be evaluated.

1.4 Outline

Chapter 2 provides background knowledge necessary to support the remainder of the work presented in this study. The basic operating principles of an ACC in a direct dry-cooled thermoelectric power plant are briefly described, along with the operation of an individual ACC cell. The relationship between condenser performance and steam turbine output is then discussed before the chapter concludes with a discussion of the role of the dephlegmator in ensuring safe and reliable ACC performance.

Chapter 3 addresses the flow of vapor in the distributing manifold between the turbine exhaust and the air-cooled heat exchangers.

The vapor flow distribution in the primary condenser heat exchangers themselves is addressed in Chapter 4. A numerical calculation procedure is described. This procedure makes use of CFD predictions of steam-side inlet loss coefficient distributions to calculate the distribution of vapor amongst the tubes in the primary condenser bundles.

The demands on dephlegmator capacity to prevent the accumulation of non-condensable gases in the primary condensers are examined in Chapter 5 and vapor backflow in the dephlegmator itself is discussed.

A hybrid (dry/wet) dephlegmator concept is described, developed and analysed in Chapter 6. The performance of the concept is evaluated using a one-dimensional calculation procedure based on empirical correlations. Various plain-tube bundle configurations are analysed for the wet/dry component of this concept and recommendations are made regarding the most favourable tube configuration.

Chapter 7 offers concluding remarks and recommendations.

2. OPERATING PRINCIPLES

2.1 The operation of an ACC in a direct air-cooled power plant

In a direct air-cooled power plant, illustrated schematically in Figure 2.1, a heat source is used to generate high pressure steam. This steam is then expanded in a turbine to produce power. The low pressure steam leaving the turbine exhaust is condensed in an ACC to complete the cycle.

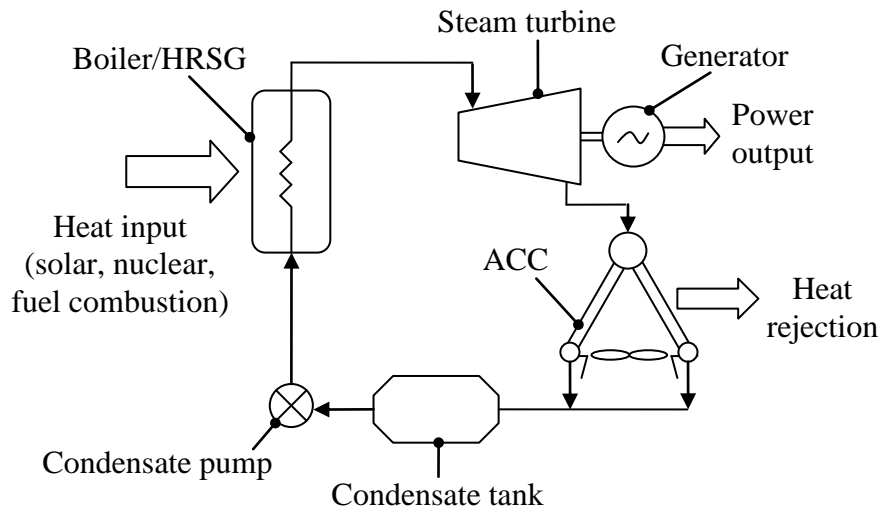


Figure 2.1: Schematic representation of a direct air-cooled power plant

The ACC of a direct air-cooled power plant is made up of several “streets” of A-frame condenser units or cells, as shown in Figure 2.2. Steam is fed via a distributing manifold to the dividing header of the primary condenser units which are connected in parallel in a street. Partial condensation takes place in a co-current vapor/condensate flow arrangement in the primary condenser cells. Excess vapor leaving these cells is condensed in the secondary reflux (counter-current vapor/condensate flow) condenser, or dephlegmator. The dephlegmator is connected in series with the primary condenser units, as illustrated in the steam flow diagram of Figure 2.3.

The following sections describe the operating principles of an ACC cell (Section 2.2) and discuss the role of the dephlegmator in ensuring safe and

reliable ACC performance (Section 2.3). The relationship between ACC effectiveness and steam turbine output is discussed in Section 2.4.

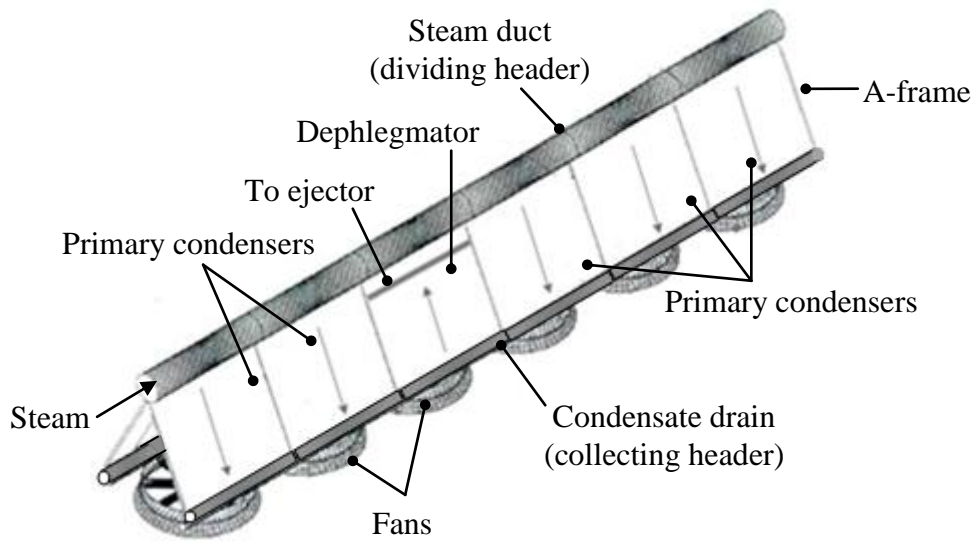


Figure 2.2: ACC street with five primary condensers and one dephlegmator

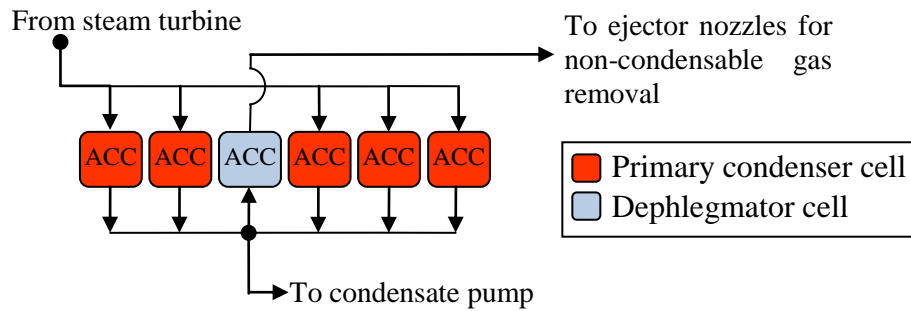


Figure 2.3: ACC street steam flow diagram

2.2 The operation of an air-cooled condenser cell

A schematic of a typical primary condenser cell is illustrated in Figure 2.4. During operation, ambient air at (1) is accelerated towards the fan platform supports (2) under the influence of the axial flow fan. The air flows through the fan inlet screen (3) into the inlet shroud, through the fan, and into the plenum chamber (4). Heat is transferred from the condensing steam to the air as it is forced through the finned-tube heat exchanger (5 to 6), which may consist of one or more tube rows,

after which it is exhausted into the atmosphere (7). Windwalls are installed along the periphery of the ACC to reduce plume recirculation.

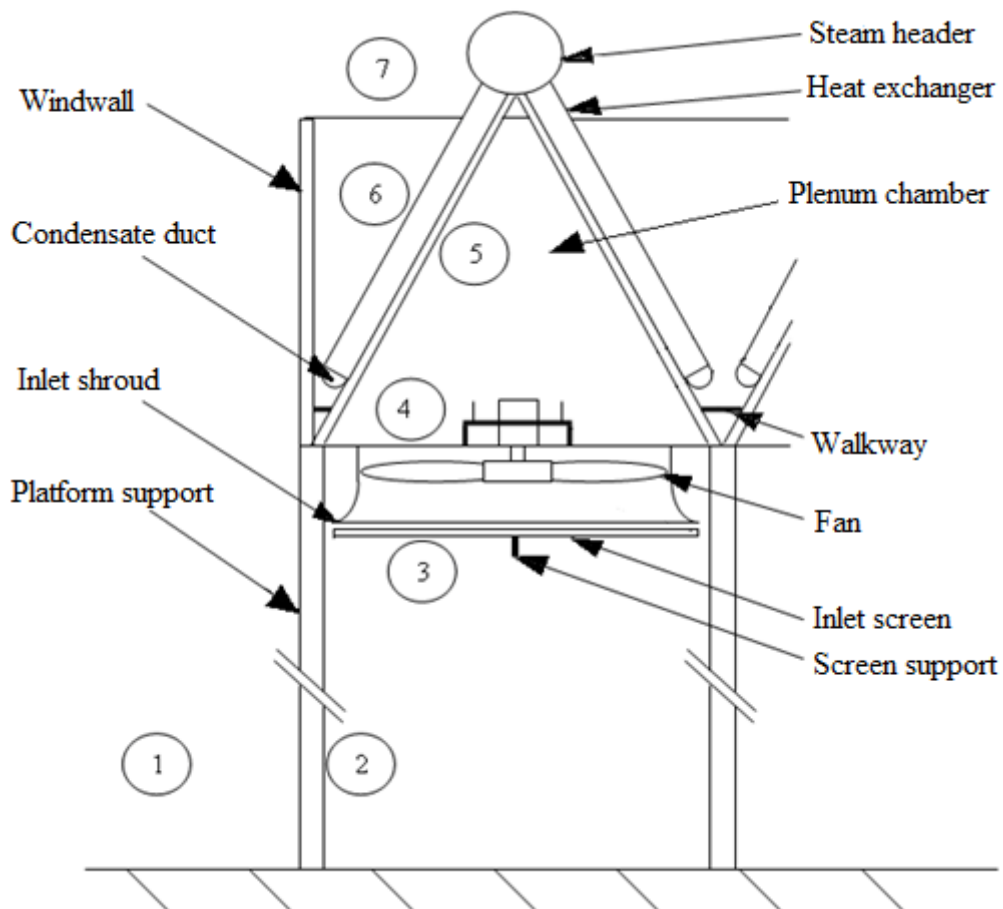


Figure 2.4: A-frame air-cooled condenser cell

2.3 The role of the dephlegmator

In an ACC with multi-row heat exchanger bundles, the vapor temperature is essentially constant in all the tubes in the primary condenser cells. However, the cooling air is progressively heated as it moves past successive tube rows. Different condensation rates therefore exist in each tube row. Non-ideal operating conditions - such as non-uniform air flow rate and fan inlet temperature distributions caused by winds, or localized decreases in heat transfer effectiveness due to tube fouling, for example - can also result in varying condensation rates between tubes in the same row. Differing rates of condensation, coupled with non-

uniform inlet loss coefficient distributions (discussed in Chapter 4), result in each heat exchanger tube tending towards a different steam-side pressure change. However, the tubes in the primary condenser bundles are connected in parallel between common headers. The steam-side pressure drop over the tubes is therefore dictated by the pressure distributions in the headers. These pressure distributions vary with axial position as flow is added to or removed from the respective headers.

If an ACC street consisted of primary condenser units only, all connected in parallel, then variations in individual tube steam-side pressure changes, due to different condensation rates, would be normalized by the manifestation of vapor backflow into some of the tubes. Vapor backflow is discussed in detail in Chapter 5. Backflow results in regions of stagnation forming within certain tubes. Non-condensable gases - which leak into the system from the atmosphere since the ACC operates at sub-atmospheric pressures - are transported to these stagnation regions where they accumulate. The accumulation of non-condensables forms so-called “dead zones” where no heat transfer takes place. The presence of dead zones is detrimental to ACC performance since they reduce the effective heat transfer surface area. Furthermore, condensate can be trapped in these dead zones resulting in enhanced risk of tube corrosion and the potential for catastrophic tube damage due to condensate freezing during cold periods (Berg and Berg, 1980).

One way of reducing the likelihood of vapor backflow in multi-row heat exchangers is to install tubes with different and increasing heat transfer characteristics in successive tube rows (Berg and Berg, 1980). This is typically achieved by reducing the fin pitch on the tubes in downstream rows. The varying heat transfer effectiveness strategy is employed in most modern multi-row ACCs but has the disadvantage of working well at only a single value of effectiveness (Berg and Berg, 1980). Since heat transfer effectiveness is also a function of the air-flow rate through the heat exchanger, this method does not guarantee protection against backflow.

Backflow due to different condensation rates in successive rows of a multi-row heat exchanger (termed row effects) can be avoided entirely by using single tube row heat exchanger bundles. Advances in tube technology have seen such bundles become increasingly popular in modern applications. Single-row heat exchangers remain susceptible to backflow due to transverse variations in condensation rates brought about by non-ideal operating conditions.

The most widely employed strategy to prevent non-condensable gas accumulation is the use of a secondary condenser connected in series with, and downstream of, the primary condensers (Berg and Berg, 1980). This secondary condenser, commonly referred to as a dephlegmator, facilitates additional vapor flow through the primary condensers, flushing them of non-condensables and preventing the formation of dead zones. The dephlegmator must be adequately sized to account for row effects, in the case of multi-row heat exchanger bundles, as well as the influence of transverse variations in tube inlet loss coefficients and non-ideal operating conditions.

2.4 The relationship between ACC and steam turbine performance

Consider a power plant cooled by an ACC (Figure 2.1). Energy is supplied to the steam cycle at a constant rate. Some of this energy is captured and removed in the steam turbine. To complete the cycle, the remaining energy must be rejected to the atmosphere by the ACC.

Steam turbine efficiency, and subsequently turbine power output, is a function of the turbine exhaust pressure, referred to as backpressure. The performance characteristic of a particular steam turbine is shown in Figure 2.5. Since the input from the boiler is constant, the required ACC heat rejection rate must exhibit an inverse trend to that of the turbine characteristic so that the sum of the turbine and ACC output is also constant. The required ACC heat rejection rate is also illustrated in Figure 2.5.

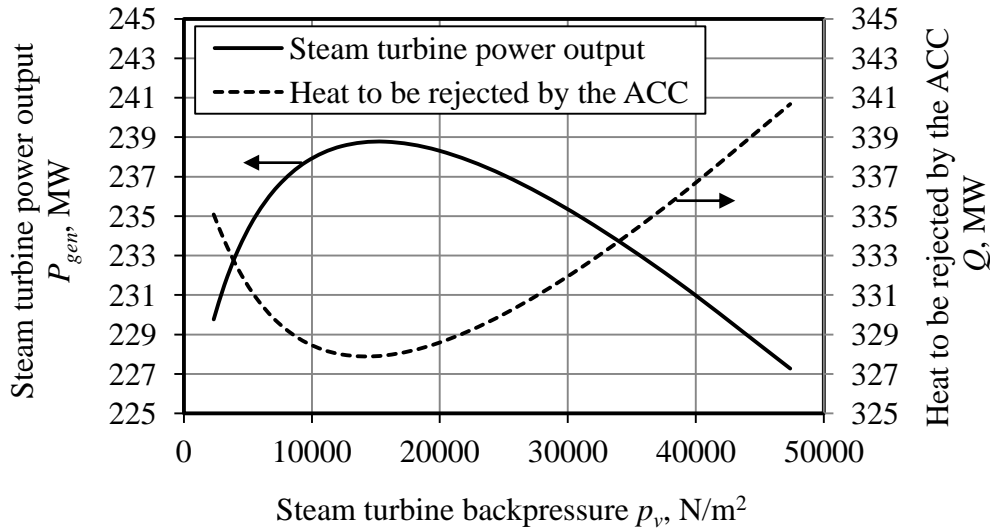


Figure 2.5: Steam turbine performance characteristic and required ACC heat rejection rate

For this particular turbine an optimum operating point exists at a certain turbine backpressure where the turbine extracts the most amount of energy from the cycle. Plant output can therefore be maximised by maintaining the backpressure as close as possible to this optimum. The turbine backpressure is, in turn, determined by the performance of the ACC. ACCs are therefore typically designed to maintain near optimum backpressure at a specific ambient condition.

The amount of heat that can be rejected by an ACC is a function of the ACC configuration (finned tube performance characteristics, fan performance etc.), and the approach temperature difference between the condensing steam and the ambient air ($\Delta T_{app} = T_v - T_a$). Neglecting steam-side pressure changes through the heat exchangers for the time being, the ACC is operating at an approximately constant vapor temperature corresponding to the saturation temperature of steam at the turbine backpressure. Consider the case where a power plant is operating at its optimum design point (certain ambient temperature and near-optimum backpressure). If the ambient temperature increases, the ACC can no longer reject the required amount of heat at the existing vapor temperature. Since the ACC can no longer condense enough steam, the pressure in the ACC (backpressure) begins to rise causing a corresponding increase in vapor temperature. As the

backpressure increases, the turbine output decreases and even more heat must be rejected by the ACC for a constant heat input in the boiler. The backpressure and corresponding vapor temperature therefore continue to rise until some new equilibrium is reached where the vapor temperature is high enough that the ACC is able to reject the required amount of heat at the higher ambient temperature. Since the new operating point is at a backpressure greater than the optimum, the turbine output is reduced.

As mentioned in Chapter 1, ACCs can experience measurable performance reductions when operating conditions are unfavourable. In addition, the accumulation of non-condensable gases and high steam-side losses (due to poorly designed systems) can further degrade cooling effectiveness. As explained here, reduced ACC performance is detrimental to turbine output and subsequently plant reliability and profitability. It is therefore critical that the steam-side performance of ACCs be examined to ensure reliable and predictable cooling performance.

3. VAPOR FLOW IN A DISTRIBUTING MANIFOLD

3.1 Introduction

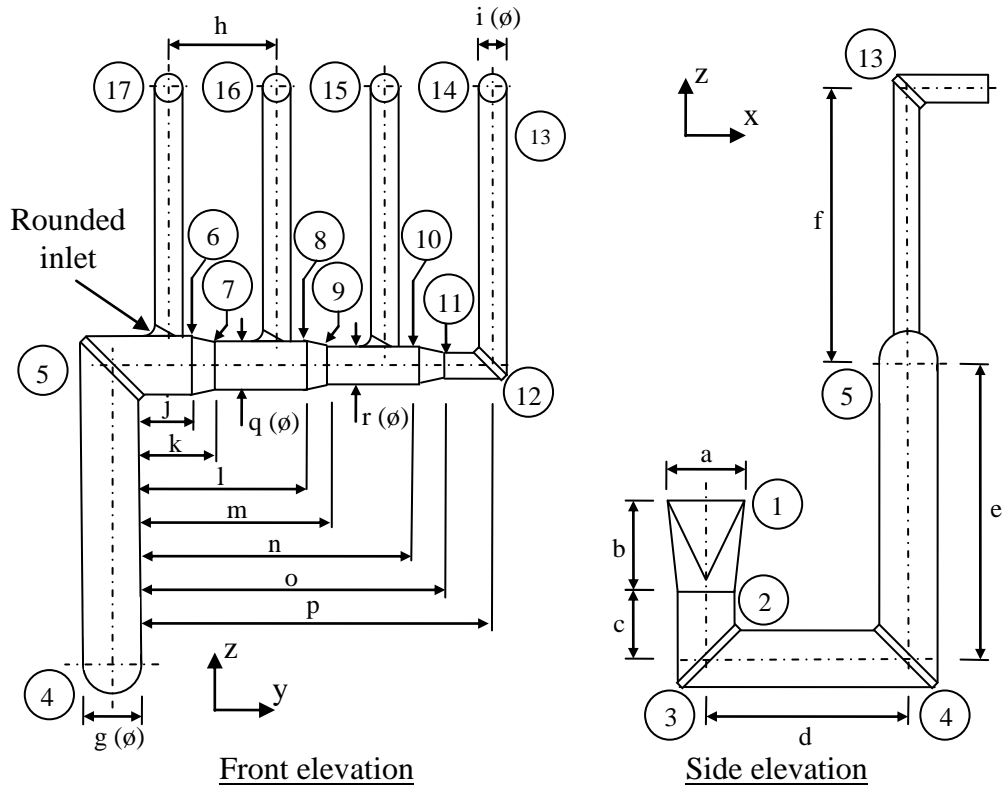
In an air-cooled power plant, the turbine exhaust is connected to the ACC by a distributing manifold. Manifold configuration differs from plant to plant and affects the cooling effectiveness of the ACC by influencing both the vapor temperature and flow distribution upstream of the heat exchangers.

Shi et al. (2009) investigated the flow of wet steam in a distributing manifold, similar in configuration to the one considered in this study, and found there to be an uneven vapor flow distribution amongst the ACC streets. Their model did not account for the suction effect of the heat exchangers but nonetheless identified the need for further investigation of the flow in such distributing manifolds. In a subsequent investigation, Shi and Shi (2009) investigated a “tree-branch” type manifold. This manifold offers reduced steam-side losses and more uniform flow distribution. Shi and Shi found that it is possible to further enhance the flow distribution benefits of the tree-branch manifold by improving the guide vane configuration at the branch points.

The flow in a typical distributing manifold is investigated here by means of a CFD analysis. Although interesting in itself, the primary purpose of the manifold simulation is to generate appropriate inlet boundary conditions for use in the subsequent simulation of the heat exchanger bundles. Figure 3.1 illustrates the manifold considered in this study. Steam from the turbine exhaust enters the manifold at (1) and is then transported to the inlet of each of the four ACC streets that make up the condenser considered here at (14), (15), (16) and (17) via horizontal and vertical sections of circular duct. The duct diameter is reduced after each branching point by a conical reducer in an attempt to maintain near constant vapor velocity through the system.

The CFD model used in this investigation is described in relative detail in Sections 3.2 – 3.4. Much of the modelling strategy applied here is also of

relevance to the detailed modelling of the heat exchanger bundles (Chapter 4). A verification of the accuracy of the model is discussed in Section 3.5 before the CFD results are presented in Section 3.6.



Dimensions, m											
a	5.84	d	19.62	g	4.99	j	1.21	m	14.34	p	30.66
b	4.70	e	24.00	h	10.56	k	3.81	n	21.90	q	4.29
c	4.35	f	25.11	i	2.50	l	11.34	o	24.90	r	3.49

Figure 3.1: Schematic of the distributing manifold (not to scale)

3.2 CFD model

The nature of the vapor flow in an ACC system renders a detailed three-dimensional numerical representation using CFD quite difficult. The scale of the system being considered requires large flow domains while the high vapor flow rates, and associated fully turbulent flow, suggest that the boundary layers being

dealt with are relatively thin. A high grid resolution is therefore required in order to accurately represent the flow using a numerical turbulence model with wall functions. The computational expense of simulating the vapor flow in an ACC is thus substantial.

In order to handle the numerical modelling with the available computational resources, the ACC distributing manifold was divided into the three sections described below (all position references, given in brackets, refer to Figure 3.1).

- Lower duct – extending from (1) to 1.5 duct diameters upstream of the miter bend at (5).
- Middle duct – extending from the outlet of the lower duct (5) to 1.5 diameters upstream of the miter bends that mark the beginning of the air-cooled heat exchanger dividing headers (13).
- Upper ducts – extending from the middle duct (13) to the inlet of the first finned-tube bundles in each ACC street (14, 15, 16 and 17).

A “march-through” solution procedure was followed whereby the flow distribution in the lower duct was solved first. Fully developed turbulent flow was assumed at the model inlet as a first approximation. Profiles of velocity, turbulent kinetic energy and turbulent energy dissipation rate were extracted at a cross-section corresponding to the inlet of the middle duct model. The middle duct flow distribution could then be computed using the aforementioned profiles as the inlet boundary conditions. Similar profiles were extracted from the middle duct model at locations corresponding to the inlet of the upper duct models. Finally, the upper duct flow distributions could be solved with the appropriate inlet conditions to predict the nature of the vapor flow immediately upstream of the heat exchangers in each of the four ACC streets.

ANSYS FLUENT, a commercially available CFD software package, was used in this study. Turbulence was accounted for using the realizable k - ε turbulence model (Shih et al., 1995) with standard wall functions. Non-equilibrium wall functions, sensitive to pressure gradient effects, were investigated and found to

have a negligible effect on the results while requiring measurably finer near-wall grid resolution, and thus significantly greater computational expense. The SIMPLE algorithm for pressure-velocity coupling (Patankar, 1980) was applied with second order upward differencing schemes for the discretization of the momentum and turbulence parameter conservation equations.

3.3 Assumptions and simplifications

The following assumptions and simplifications were made in the CFD model of the distributing manifold:

- a) The flow is incompressible, with constant fluid properties, through each section (lower, middle and upper) of the manifold system. The fluid properties differ from section to section and are calculated based on the absolute pressure predicted at the inlet of the relevant section model.
- b) The flow is steady. While it is highly likely that secondary flow patterns, which may be transient in nature, will develop as a result of transverse pressure gradients through the various bends (Ito, 1960), the significant additional computational expense of modelling transient flow is not justified here. A suitable representation of the flow pattern immediately upstream of the finned tubes should be achievable using a steady flow representation of the problem in question.
- c) The turbine exhaust steam is dry ($x = 1$) and is subsequently modelled as a single-phase fluid with physical properties determined according to the equations described in Appendix B.2. In reality, turbine exhaust steam is often slightly wet ($x < 1$). Considering a single-phase fluid significantly simplifies the solution procedure as modelling two-phase flow would require measurable additional computational expense. For a first approximation analysis this simplification is justified since the quality of the steam is typically high and so any inaccuracies should be relatively small. The presence of liquid in the turbine exhaust steam is known to have important consequences in some contexts including corrosion considerations and feedwater chemistry. Such

issues fall outside the scope of this analysis and the assumption of dry steam remains valid.

- d) The flow is adiabatic and therefore no condensation takes place in the distributing manifold. This again negates the need for multi-phase flow modelling.
- e) The flow in the manifold is mathematically parabolic in nature. The individual components of the system (bends, reducers etc.) therefore do not influence the flow upstream of their location. Ito (1960) shows that the influence of a bend extends a few diameters upstream, but a measurably larger distance (30 – 50 diameters) downstream of its location. Bearing this in mind the interfaces between the lower/middle and middle/upper duct models were chosen to be as far downstream of the last flow altering component as reasonably possible.
- f) The values of the turbulence parameters applied at the lower duct inlet boundary were derived based on the average velocity in the duct (v) according to Equations (3.1) – (3.4) (FLUENT, 2006).

$$I = 0.16 Re^{-1/8} \quad (3.1)$$

$$l = 0.07d \quad (3.2)$$

$$k = 1.5(vI)^2 \quad (3.3)$$

$$\varepsilon = C_\mu^{0.75} k^{1.5}/l \quad (3.4)$$

In the equations above I is the turbulent intensity, l is the characteristic turbulent length, k is the turbulent kinetic energy, and ε is the turbulent energy dissipation rate. According to FLUENT (2006), $C_\mu = 0.09$.

- g) Pressure outlet boundary conditions represent the outlets of each section. In each model, the flow domain was extended 1.5 duct diameters downstream of the location of the interface boundaries connecting successive section models. The pressure specified at the outlet boundaries was calculated using a one-dimensional theoretical approximation, with friction losses in the extended

sections accounted for by the correlation of Haaland (1983), shown in Equation (3.5).

$$f_D = 0.3086 \left[\log_{10} \left\{ \frac{6.9}{Re} + \left(\frac{\varepsilon_r/d}{3.75} \right)^{1.11} \right\} \right]^{-2} \quad (3.5)$$

In Equation (3.5) the roughness of the duct surface was assumed to be $\varepsilon_r = 0.001$ m.

- h) The rounded inlet sections at the T-junctions between the horizontal duct section and the vertical risers (see Figure 3.1) were not modelled. The risers therefore join the horizontal duct with a sharp edge. This simplification was necessary to allow for a good quality mesh to be generated in the vicinity of these junctions. The guide vanes in the rounded section of the T-junction were subsequently also not considered.

3.4 Meshing

The flow domain in each of the manifold section models was discretized using a polyhedral grid. In order to generate such a grid, an unstructured mesh consisting of tetrahedral elements was initially generated in the ANSYS meshing platform GAMBIT. The highest possible grid resolution was used considering the available computational resources. The tetrahedral mesh was able to capture the relatively complex geometry in the vicinity of the vaned miter bends and the horizontal/vertical duct junctions. Unfortunately, the resulting mesh consisted of a very large number of cells (approximately 6.1×10^6 for the lower duct model) with arbitrary alignment and a relatively high average skewness. The likelihood of the numerical results exhibiting measurable numerical diffusion and poor stability was therefore high.

The quality of the mesh was improved by converting it to a polyhedral structure using FLUENT's built-in tetrahedral-to-polyhedral mesh converter. The converter identifies clusters of tetrahedral cells that share a common vertex and combines

them into a single cell with an arbitrary number of faces. An example of a tetrahedral-to-polyhedral mesh conversion is illustrated in Figure 3.2.

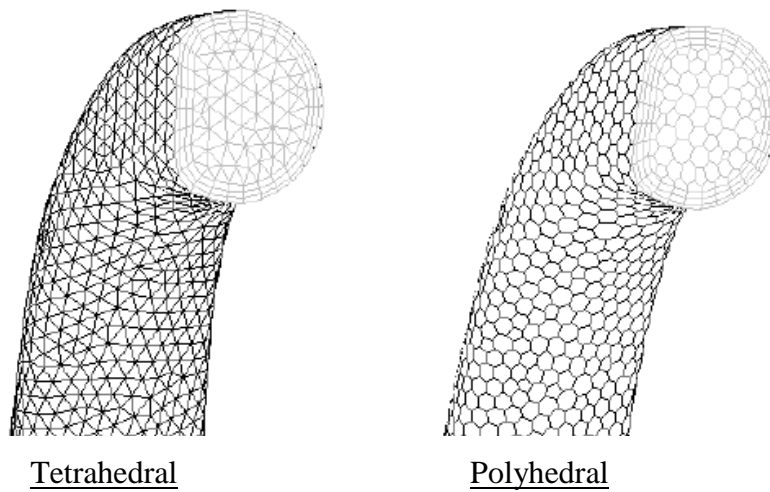


Figure 3.2: Comparison of tetrahedral and polyhedral meshing schemes

The advantages of a polyhedral grid include:

- a) Reduced cell count (approximately five times fewer cells in this case), and subsequently reduced computational expense, while still maintaining sufficiently high resolution in the near-wall region.
- b) Flexibility to adapt to complex geometry. The resulting mesh was therefore able to capture the same geometry as the unstructured tetrahedral mesh with significantly fewer cells.
- c) Orthogonality. In a polyhedral mesh the cell faces are always perpendicular to the connecting line between two cell centroids. The non-orthogonal terms in the discretization equations can therefore be neglected (Tritthart and Gutknecht, 2007).
- d) Reduced numerical diffusion. Polyhedral meshes have an increased number of cell faces which, combined with the orthogonality of the grid, means that the mesh is largely aligned with flow in any direction. Numerical diffusion is therefore reduced when using a polyhedral grid as opposed to its tetrahedral counterpart. In this case, where the flow undergoes several changes in

direction and secondary flow patterns will be present, the reduction in numerical diffusion associated with a polyhedral mesh is of particular significance.

- e) Reduced skewness. Skew cells (with a high aspect ratio) that share a common vertex with one or more cells are combined to form larger cells with lower aspect ratios.

Every effort was made to achieve sufficient grid resolution in the near-wall region while still remaining within the computational limits and maintaining acceptable aspect and expansion ratios in the axial and radial directions. Upon inspection of the grid, however, it was found that the wall adjacent cell heights fall slightly beyond the upper limit of $y^+ \leq 300$ ($y^+ \leq 2000$ everywhere with $y^+ \approx 500$ in the critical regions in this case) for the $k-\varepsilon$ turbulence model with standard wall functions (FLUENT, 2006). Additional grid refinement was unfortunately not possible due to computational limitations.

A grid sensitivity analysis was nonetheless executed considering less refined meshes (several cases down to approximately 33 % fewer cells than the reference case). Little grid dependence was found near the upper limit of grid resolution considered here. Additional refinement of the grid beyond the maximum achieved in this case is therefore expected to have a negligible effect on the results despite the somewhat inadequate existing near-wall resolution.

3.5 Verification

The accuracy of the distributing manifold CFD model was verified in a piece-wise fashion by comparing the predicted flow through each of the manifold components (straight circular duct, miter bends, conical reducers and T-junctions) to existing empirical data and correlations.

Dry vapor at $T_v = 60$ °C was considered and the simulations were based on a turbine exhaust mass flow rate of $m_v = 200$ kg/s ($Re_v \approx 4.6 \times 10^6$).

3.5.1 Fully developed turbulent flow in a circular duct

A circular duct with a diameter of $d_i = 4.99$ m and a length of $L = 50d_i$ was considered. A uniform velocity profile was specified at the inlet of the duct and the flow was allowed to develop along its length. According to Nikuradse (1933), flow becomes fully developed after a distance of 25 to 40 diameters downstream of a uniform velocity inlet. Velocity profiles were extracted 35 diameters downstream of the inlet boundary in this model.

The predicted velocity profile downstream of the inlet boundary compares well with the empirical correlation of Zucrow and Hoffman (1976) for fully developed turbulent flow in a circular duct, as shown in Figure 3.3.

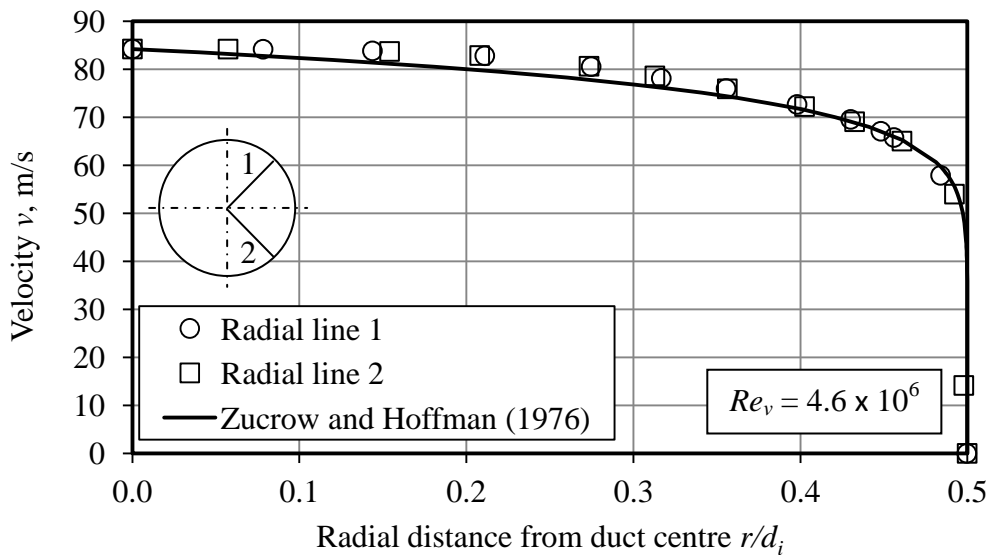


Figure 3.3: Fully developed flow in a circular duct

Profiles of the fully developed velocity, turbulent kinetic energy and turbulent energy dissipation rate were extracted from this model for use as inlet conditions in subsequent single component models.

3.5.2 Miter bend

Duct bends made by angle cutting (mitering) and joining the ends of ducts are referred to as miter bends. Such bends offer a convenient way, in terms of manufacturing and installation, to change the direction of flow.

Single 90° miter bends are often found in ACC distributing manifolds. These bends typically have cascades of guide vanes, as shown in Figure 3.4, to reduce their loss coefficient and improve the uniformity of the flow downstream of their location.

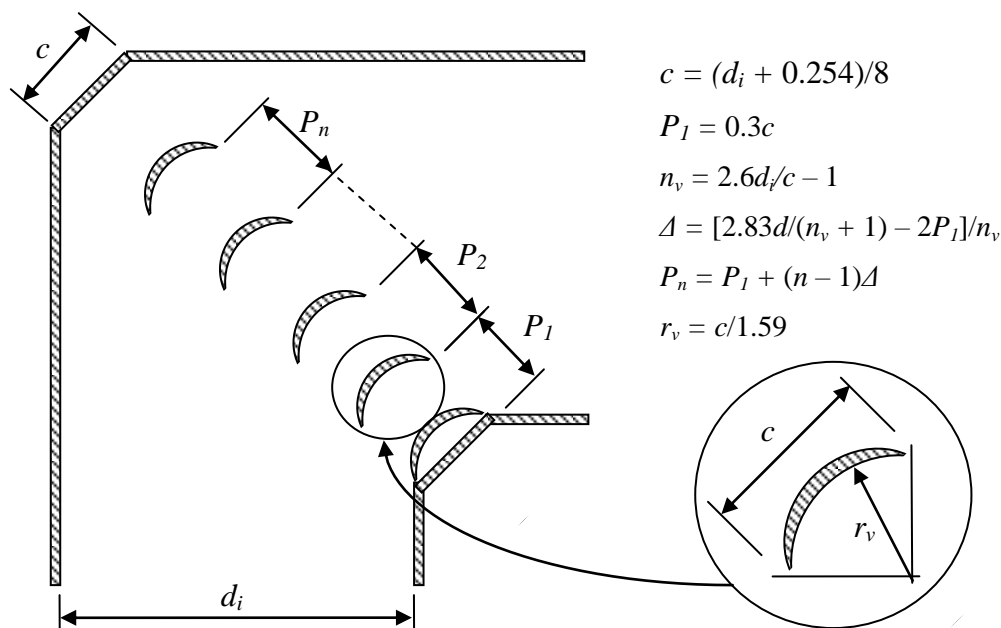


Figure 3.4: Single miter bend with a cascade of circular-arc guide vanes (Kröger, 2004)

According to Kröger (2004), insufficient systematic data exists to provide detailed information on pressure losses in miter bends with cascades of guide vanes, however, the probable range of loss coefficient is $0.15 \leq K_{mb} \leq 0.40$. Jorgensen (1961) suggests that the loss coefficient for a single 90° miter bend with guide vanes is $K_{mb} = 0.28$, while Lindgren et al. (1998) mentions $K_{mb} \approx 0.2$ for 90°

bends with simple quarter-circle profile guide vanes with a prolonged trailing edge.

A CFD model of the miter bend used in the distributing manifold considered in this study ($d_i = 4.99$ m) was created and the loss coefficient over the bend predicted using, as closely as possible, the method described by Ito (1960). The predicted loss coefficient is shown as a function of the number of guide vanes in the bend in Figure 3.5. Based on Figure 3.4, the miter bend in the manifold under consideration here should have 19 guide vanes. The corresponding bend loss coefficient is predicted to be $K_{mb} = 0.35$. This compares well with that suggested by Jorgensen (1961) and is within the probable range identified by Kröger (2004).

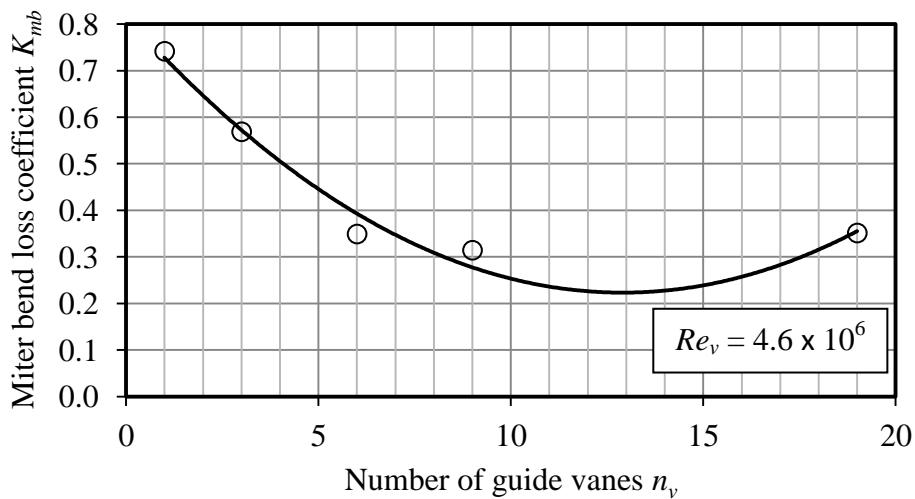


Figure 3.5: Predicted miter bend loss coefficient

An interesting trend in the relationship between miter bend loss coefficient and the number of guide vanes is evident in Figure 3.5 with the loss coefficient beginning to increase for a high number of vanes. This trend is discussed in greater detail in Appendix C.

3.5.3 Conical reducer

Fried and Idelchick (1989) suggest Equation (3.6) to determine the loss coefficient over a conical reducer based on the velocity in the smaller section of the duct (d_o).

$$K_{red} = (-0.0125\sigma^4 + 0.02244\sigma^3 - 0.00723\sigma^2 + 0.00444\sigma - 0.00745) \quad (3.6)$$

$$\times (8\theta^3 - 4\pi\theta^2 - 20\theta)$$

In Equation (3.6), σ is the ratio of the smaller to larger duct area and θ is the reduction angle, shown in the CFD model schematic of Figure 3.6.

For the reducer shown in Figure 3.6, the loss coefficient is calculated from Equation (3.6) to be $K_{red} = 0.0079$. The loss coefficient predicted by the CFD model is within 2 % of this value.

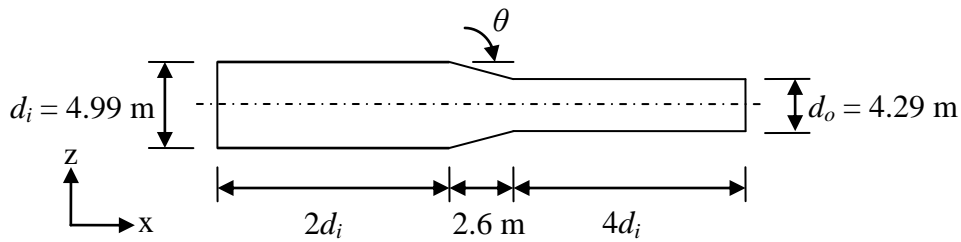


Figure 3.6: Schematic of the conical reducer CFD model

A comparison of the theoretically and numerically predicted pressure distribution through the conical reducer is illustrated in Figure 3.7. Friction effects in the theoretical model were accounted for using Equation (3.5). It is clear that the CFD model is able to accurately represent the flow through the conical reducer.

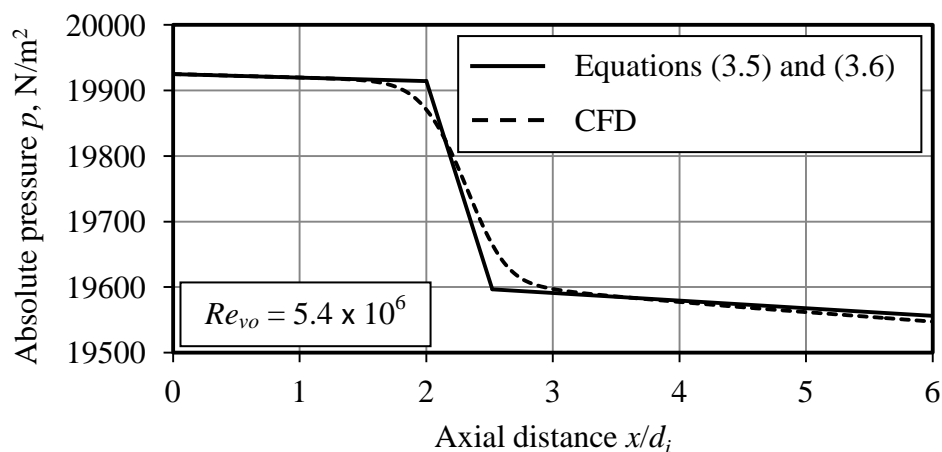


Figure 3.7: Comparison of the predicted pressure distribution in the conical reducer: CFD versus empirical

3.5.4 T-junction

The geometry of the T-junction model is shown in Figure 3.8. The outlet boundary conditions were set such that the flow splits in a 3:1 ratio with 25 % exiting through the vertical riser (r). This model is therefore representative of the upstream vertical riser in the distributing manifold.

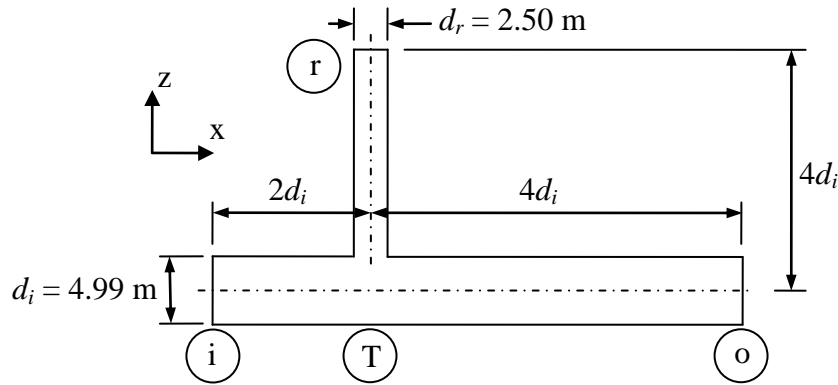


Figure 3.8: Schematic of the T-junction CFD model

According to Figure 3.9, with a volumetric flow ratio of $V_1/V_3 = m_r/m_i = 0.25$ and a riser/duct cross-sectional flow area ratio of $A_1/A_3 = (d_r/d_i)^2 = (2.50/4.99)^2 \approx 0.25$, the loss coefficient between the supply duct and the vertical riser is $K_{ir} = 1.16$. The corresponding loss coefficient over the bend in the supply duct is, from Figure 3.10, $K_{io} = -0.017$.

The theoretical prediction of the pressure distribution through the T-junction model, with friction losses accounted for using the Equation (3.5), is compared to the CFD result in Figure 3.11.

The CFD and theoretical predictions correspond well in the supply duct (i - T - o). In the vertical riser (T - r) there is a discrepancy between the numerical and theoretical results near the junction while the predictions converge further downstream. In the theoretical model, the loss coefficient between the supply duct and the vertical riser describes the change in pressure between the last point of attachment upstream of the junction and the first point of re-attachment in the riser.

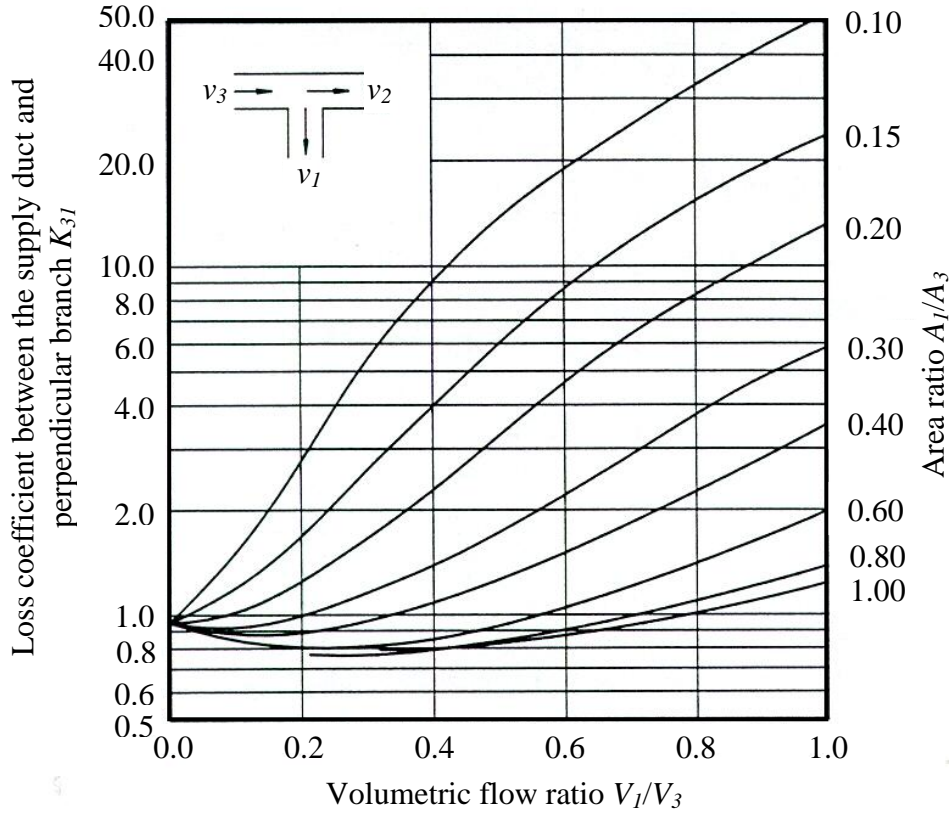


Figure 3.9: Loss coefficient in a sharp cornered T-junction between the supply duct and the perpendicular branch (Kröger, 2004)

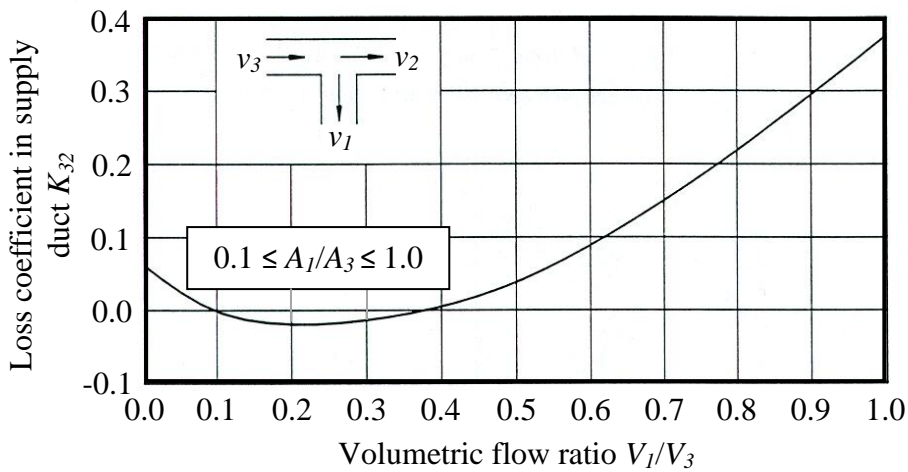


Figure 3.10: Loss coefficient in the supply duct of a sharp cornered T-junction (Kröger, 2004)

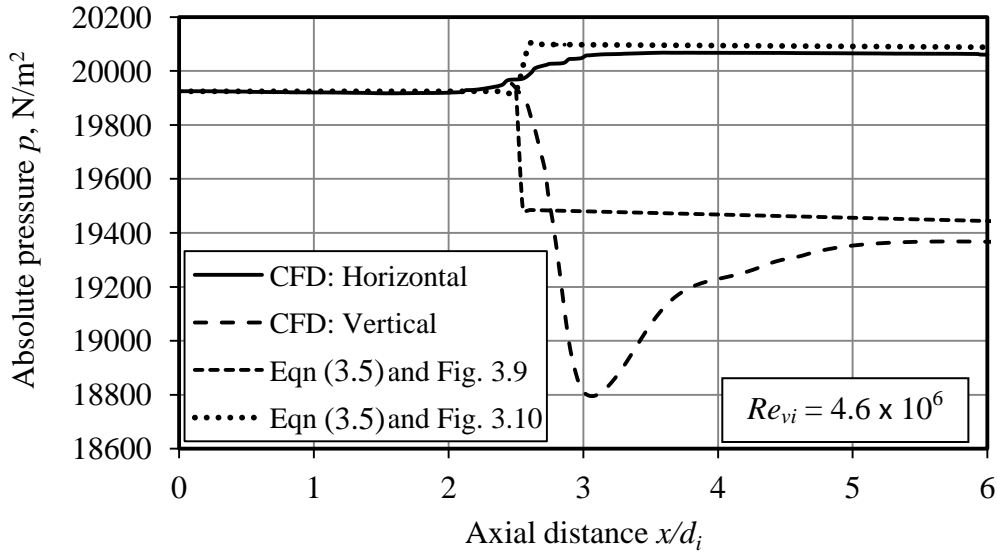


Figure 3.11: Comparison of the predicted pressure distribution through the T-junction: CFD versus empirical

Flow separation at the junction is not explicitly accounted for in the theoretical model. The agreement in the eventual pressure change over the junction is therefore an indicator of the accuracy of the CFD model.

3.6 Results

While the results of the CFD analysis of the distributing manifold were used primarily to generate inlet boundary conditions for the heat exchanger analysis, they nonetheless serve to illustrate some interesting flow considerations. All position indicators in the figures that follow refer to Figure 3.1.

3.6.1 Flow patterns in the distributing manifold

Figure 3.12 shows contours of velocity magnitude on the mid-plane of the lower duct model. A degree of separation is evident after the miter bends despite the presence of the guide vanes. Simple quarter-circle guide vanes with a constant thickness are considered in this investigation.

Shi et al. (2009) and Shi and Shi (2009) found that guide vane shape can have a measurable impact on the flow distribution downstream of a bend. The

importance of appropriate guide vane profile is well documented in the field of closed-circuit wind tunnel design - see for example Mehta and Bradshaw (1979), Lindgren et al. (1998) and Lindgren and Johansson (2002). Careful design of more sophisticated guide vanes for application in ACC distributing manifolds would result in improved flow distribution and reduced losses.

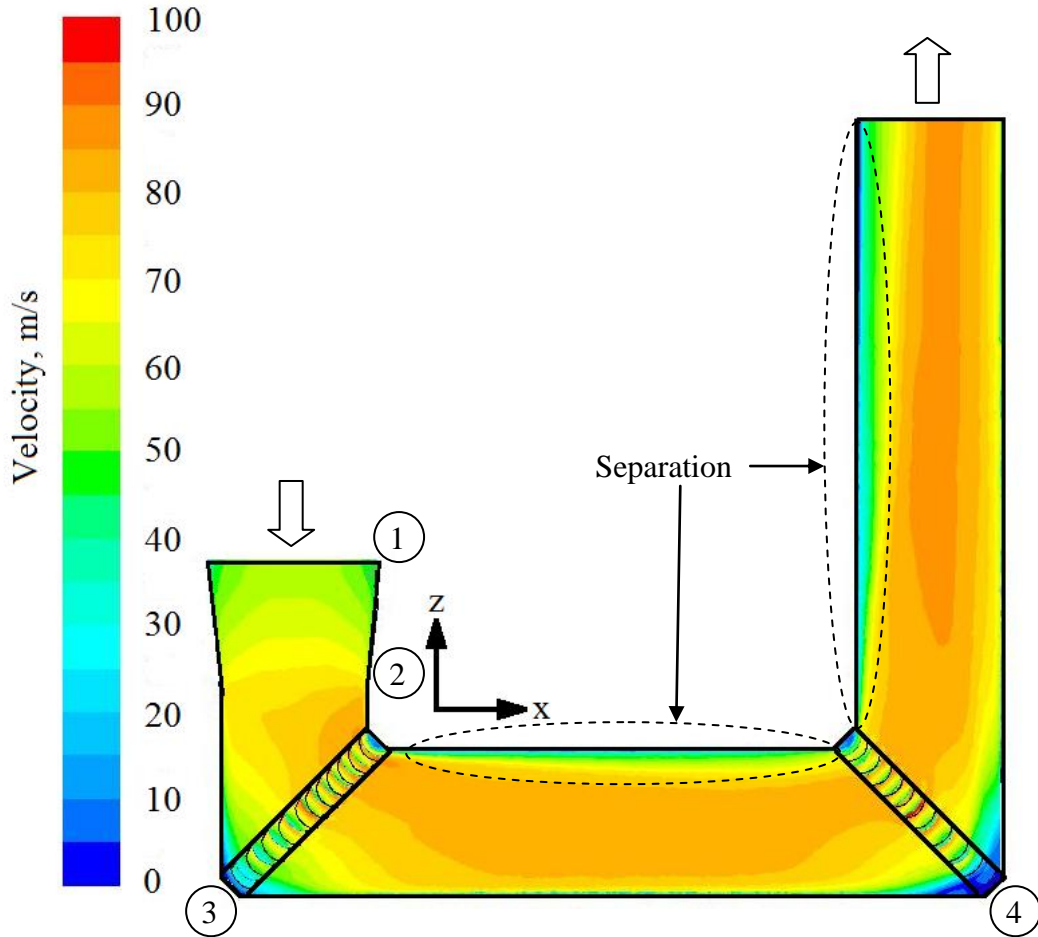


Figure 3.12: Contours of velocity magnitude on the mid-plane through the lower duct model

Figure 3.13 shows contours of velocity magnitude on the mid-plane of the middle duct model. Despite their simple profile, guide vanes still have a positive influence on the flow through the bends. This positive influence is clearly illustrated by the difference in the flow distribution in the final vertical riser (12 – 17 in Figure 3.1 and furthest right in Figure 3.13), connected to the horizontal manifold by a vaned bend; and the upstream risers, connected to the manifold at

vaneless T-junctions. Separation is evident downstream of the T-junctions resulting in highly distorted flow distributions in the vertical risers.

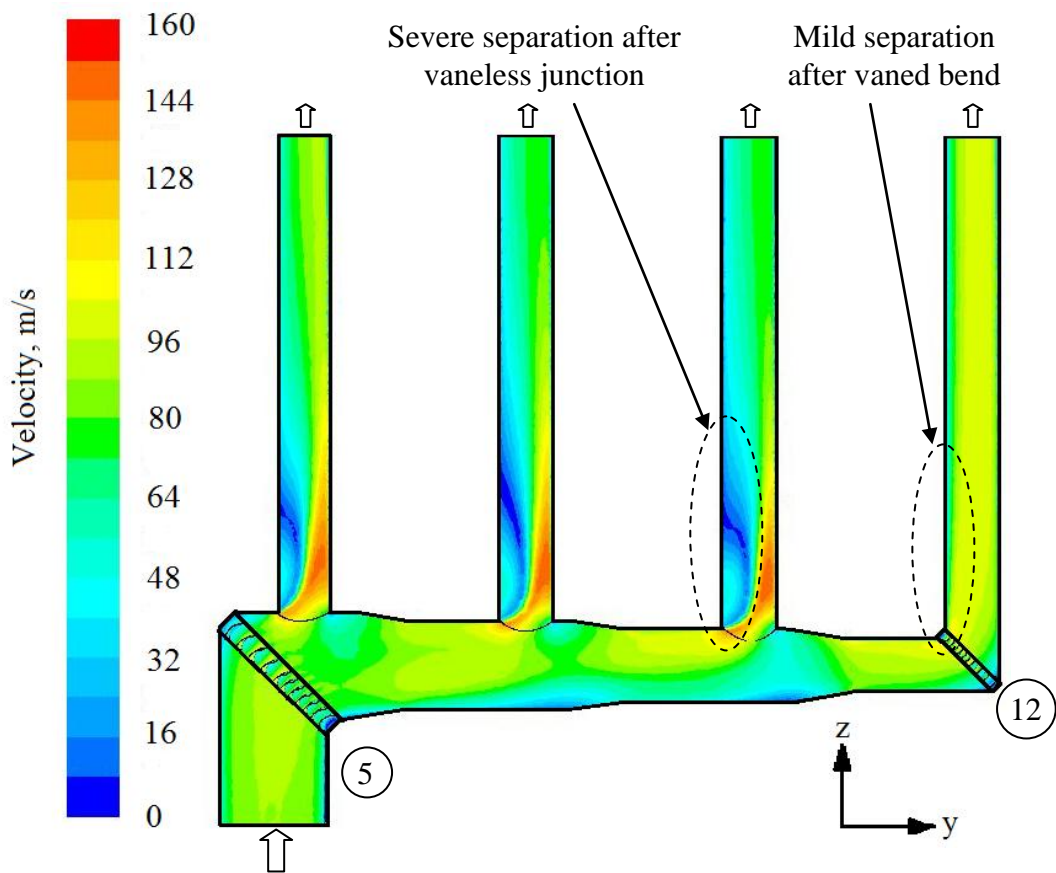


Figure 3.13 : Contours of velocity magnitude on the mid-plane through the middle duct model

In reality the separation in the vertical risers will be less severe than indicated in Figure 3.13 since the actual risers connect to the manifold with a rounded inlet and have some guide vanes installed. Nonetheless, the simulation results serve as an indicator of the potential severity of separation that may occur if careful thought is not applied to the design of these junctions.

The vaned miter bends connecting the vertical risers to the steam headers (section 13 in Figure 3.1) improve the uniformity of the flow upstream of the heat exchanger bundles. However, a degree of secondary flow remains evident between the bends and the heat exchanger bundles as illustrated in Figure 3.14.

Some separation also exists on the inside of the bend, as shown in the velocity magnitude contour plot of Figure 3.15. These undesirable flow patterns could be mitigated through the use of improved guide vane configuration and profile.

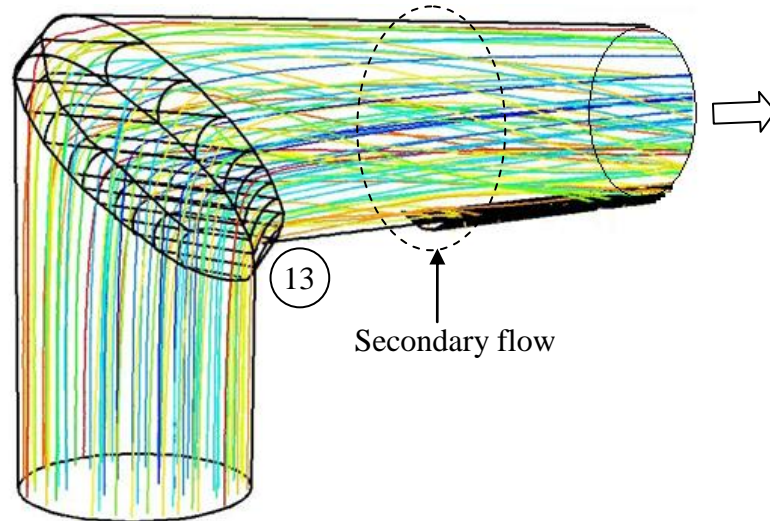


Figure 3.14: Pathlines illustrating the flow through the miter bend upstream of the heat exchangers

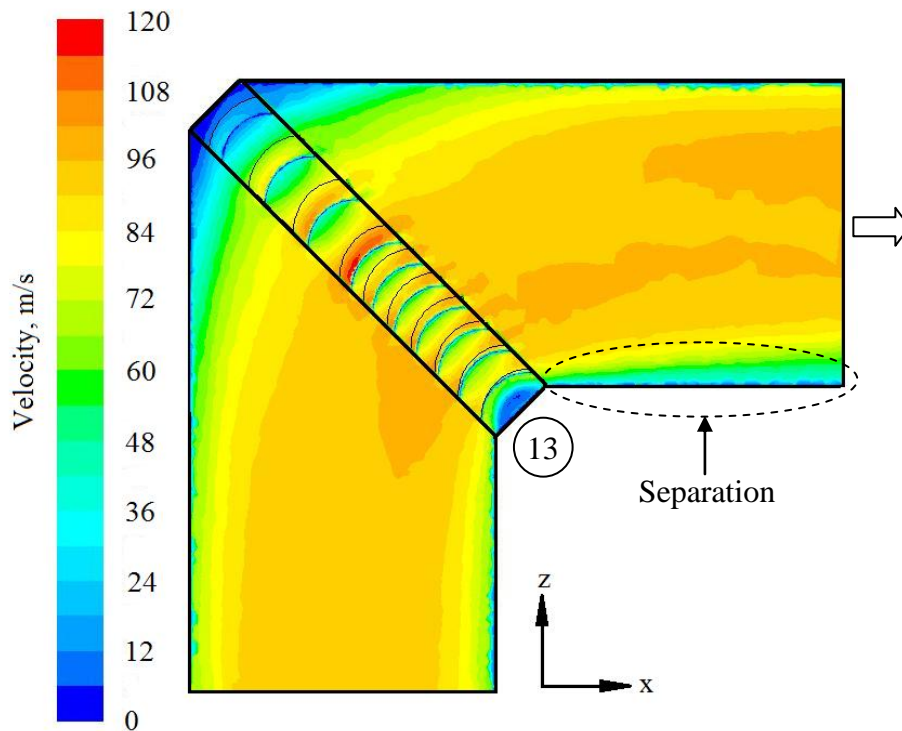


Figure 3.15: Contours of velocity magnitude on the mid-plane through the miter bend upstream of the heat exchangers

3.6.2 Vapor pressure change over the distributing manifold

The absolute pressure distribution through the distributing manifold, as predicted by the CFD simulations, is illustrated in Figure 3.16 for dry steam at a turbine backpressure of $p_v = 19925.12 \text{ N/m}^2$ ($T_v = 60 \text{ }^\circ\text{C}$). Cross-section numbers refer to Figure 3.1.

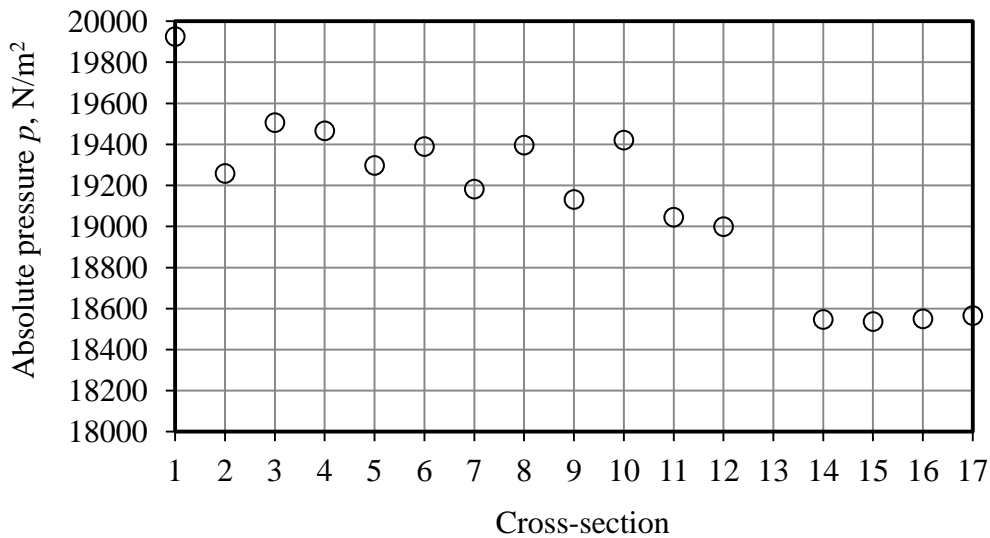


Figure 3.16: Pressure distribution in the distributing manifold

The pressure drop across the manifold, depending on which ACC street is considered, is approximately $\Delta p_v = 1400 \text{ N/m}^2$. The bends and branches account for 70 % – 80 % of this pressure change. The corresponding decrease in vapor temperature is $\Delta T_v \approx 1.4 \text{ }^\circ\text{C}$. Lindgren et al. (1998) reports that bend loss coefficients can be reduced by a factor of five through careful design of the guide vanes (relative to a bend with simple quarter-circle vanes). The losses over the distributing manifold could therefore be measurably reduced through the use of more sophisticated guide vanes. A cost analysis relating the turbine output benefits of lower manifold losses, and the subsequent increase in vapor temperature at the heat exchanger inlets, to the increased manufacturing cost of more sophisticated guide vanes would be valuable.

3.6.3 Boundary conditions for the heat exchanger models

Radial velocity profiles in the dividing header upstream of the first heat exchanger bundles are shown for the first and last ACC streets (respectively sections 17 and 14 in Figure 3.1) in Figures 3.17 and 3.18 respectively. The distorted nature of the velocity profile upstream of the heat exchangers is clearly visible in these figures and the result of separation at the inner bend corner can be seen in the profile for $\theta = 180^\circ$.

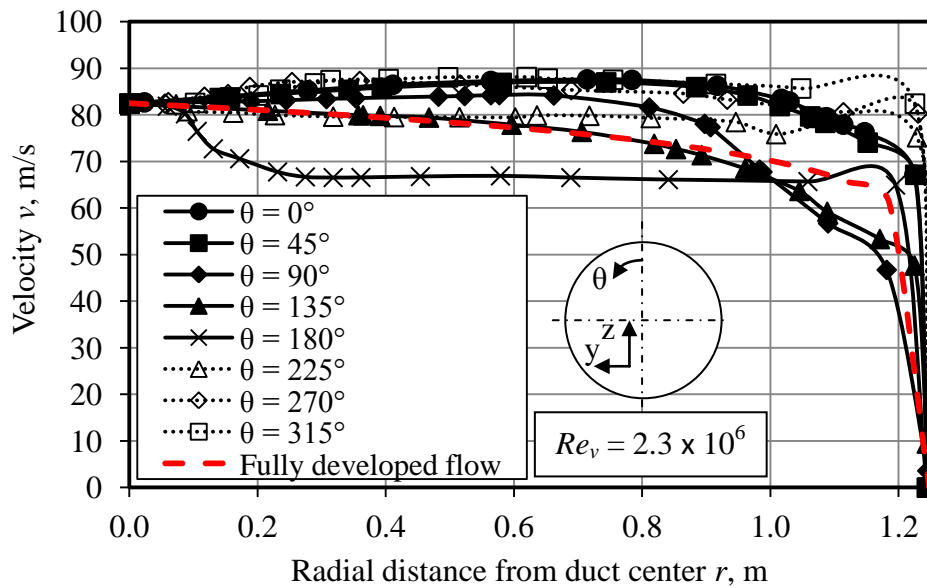


Figure 3.17: Radial velocity profiles in the distributing duct upstream of the heat exchanger bundles in the first street (17)

The velocity profiles in the last street (14 in Figure 3.1) resemble fully developed flow more strongly as a result of the more uniform flow in the vertical riser preceding this street (caused by the vaned miter bend as opposed to the T-junctions at the upstream risers). Inlet conditions for the heat exchanger models are subsequently extracted from this location. Again, the use of more sophisticated guide vanes would improve the uniformity of the flow distribution upstream of the heat exchangers by reducing separation at the inner bend surface. Such an improvement may be beneficial to ACC performance and warrants further investigation.

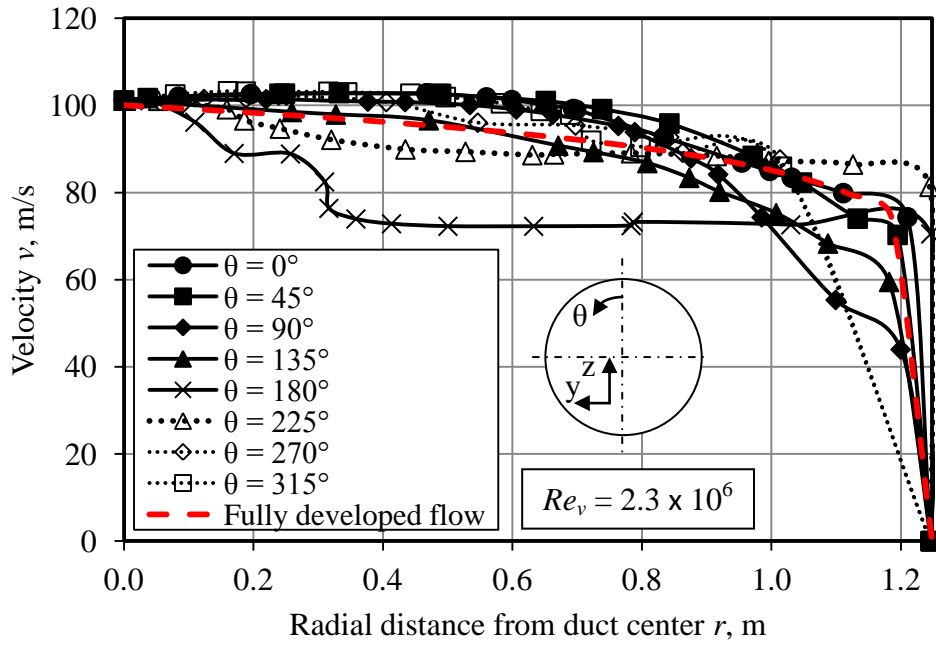


Figure 3.18: Radial velocity profiles in the distributing duct upstream of the heat exchanger bundles in the final street (14)

4. VAPOR FLOW DISTRIBUTION IN THE PRIMARY CONDENSERS OF AN ACC

A numerical modelling procedure has been developed to investigate the vapor flow distribution in the condensing section of an ACC. The procedure consists of CFD models of the heat exchanger bundles belonging to each primary condenser cell, as well as a numerical calculation code that predicts the flow distribution in parallel and reverse flow manifolds.

This chapter describes the modelling procedure (Section 4.1) and the details of the CFD model (Section 4.2) and numerical calculation code (Section 4.3). Steam-side heat exchanger tube inlet and outlet loss coefficient distributions are then presented (Sections 4.4 and 4.5) before the vapor flow distribution in the condensing section of an ACC is discussed (Section 4.6).

4.1 Modelling procedure

An iterative modelling procedure is implemented as follows:

- a) Tube inlet loss coefficients in the ACC primary heat exchanger bundles are determined from CFD data generated assuming a uniform vapor flow distribution amongst the tubes. The flow rate entering each tube is taken as being equal to the condensation rate for the relevant tube row.
- b) These inlet loss coefficients are implemented in the numerical flow distribution calculation code and an updated vapor flow distribution is determined.
- c) The updated flow distribution is applied in the CFD model and new inlet and outlet loss coefficients are predicted.
- d) Steps (b) and (c) are repeated until the inlet loss coefficient and vapor flow distributions predicted in subsequent iterations converge. Typically only a single iteration was required.

4.2 CFD model

4.2.1 Description

The CFD model considers the steam-side operation of a street of six A-frame air-cooled condenser cells, as shown in Figure 4.1 (see Appendix A for specifications). Each cell is modelled separately, starting with the upstream cell (Cell 1) and moving to the downstream cell (Cell 6) in a sequential manner. Cells 1, 2, 4, 5, and 6 are primary condenser units (co-current flow condensers) while Cell 3 is a dephlegmator unit (counter-current or reflux condenser). Cells 1 and 2 have parallel (Z-type) manifold configurations while Cells 4, 5 and 6 have reverse (U-type) manifold configurations. Details of the dividing and combining headers are given in Figure 4.2.

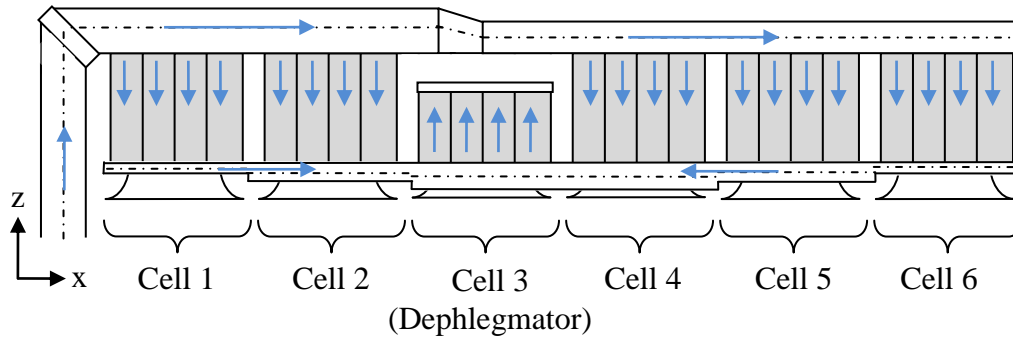


Figure 4.1: ACC cell numbering scheme

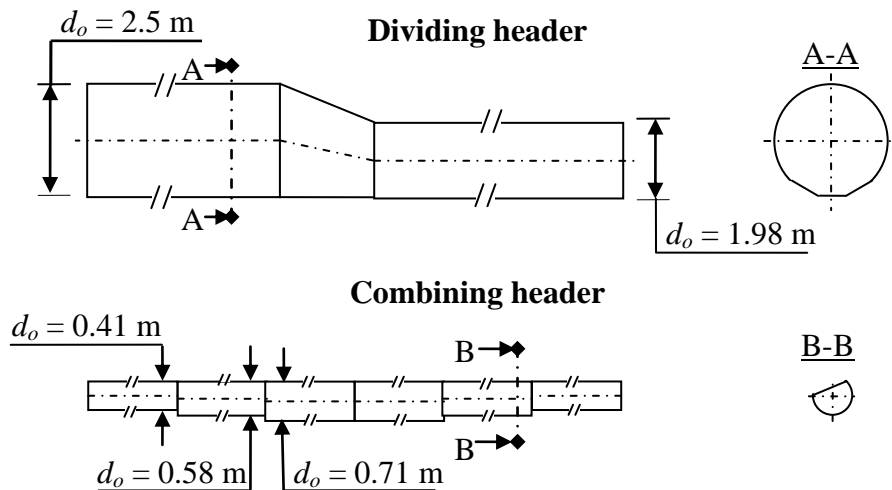


Figure 4.2: Details of the dividing and combining headers

Each cell consists of eight heat exchanger bundles arranged in pairs about the x-axis. Inlet loss coefficients are assumed to vary only with axial position (x-direction) in the heat exchanger, and as such, corresponding tubes in opposing bundle pairs will have equal mass flow rates. Tubes are therefore only modelled in detail on one side of the heat exchanger as shown schematically in Figure 4.3 for the dividing header model of Cell 1. The dividing and combining headers of each cell are modelled individually, and the header models connected by an analytical representation of the flattened tubes between them. Modelling the entire length of the tubes in each bundle is thus avoided, considerably reducing computational expense.

In the bundle under consideration in a particular simulation, tubes are modelled to 50 hydraulic diameters beyond the tube inlet to allow for full development of the flow after the inlet disturbances. In this manner, outlet boundary conditions are also prevented from affecting the flow in the vicinity of the region of interest. The remaining tubes in a cell are represented simply as velocity outlets with the appropriate velocity magnitudes applied according to their location.

In addition, each of the tube bundles in a given cell is modelled separately due to computational limitations. Eight simulations are thus carried out for each cell: one for each of the four bundle pairs in the dividing and combining header models respectively.

Pertinent CFD solution settings, models, assumptions and simplifications are discussed in Sections 3.2 and 3.3.

4.2.2 *Meshing*

A polyhedral meshing scheme, as discussed in Section 3.4, was employed. The mesh in this case differs from that described previously only in the vicinity of the heat exchangers.

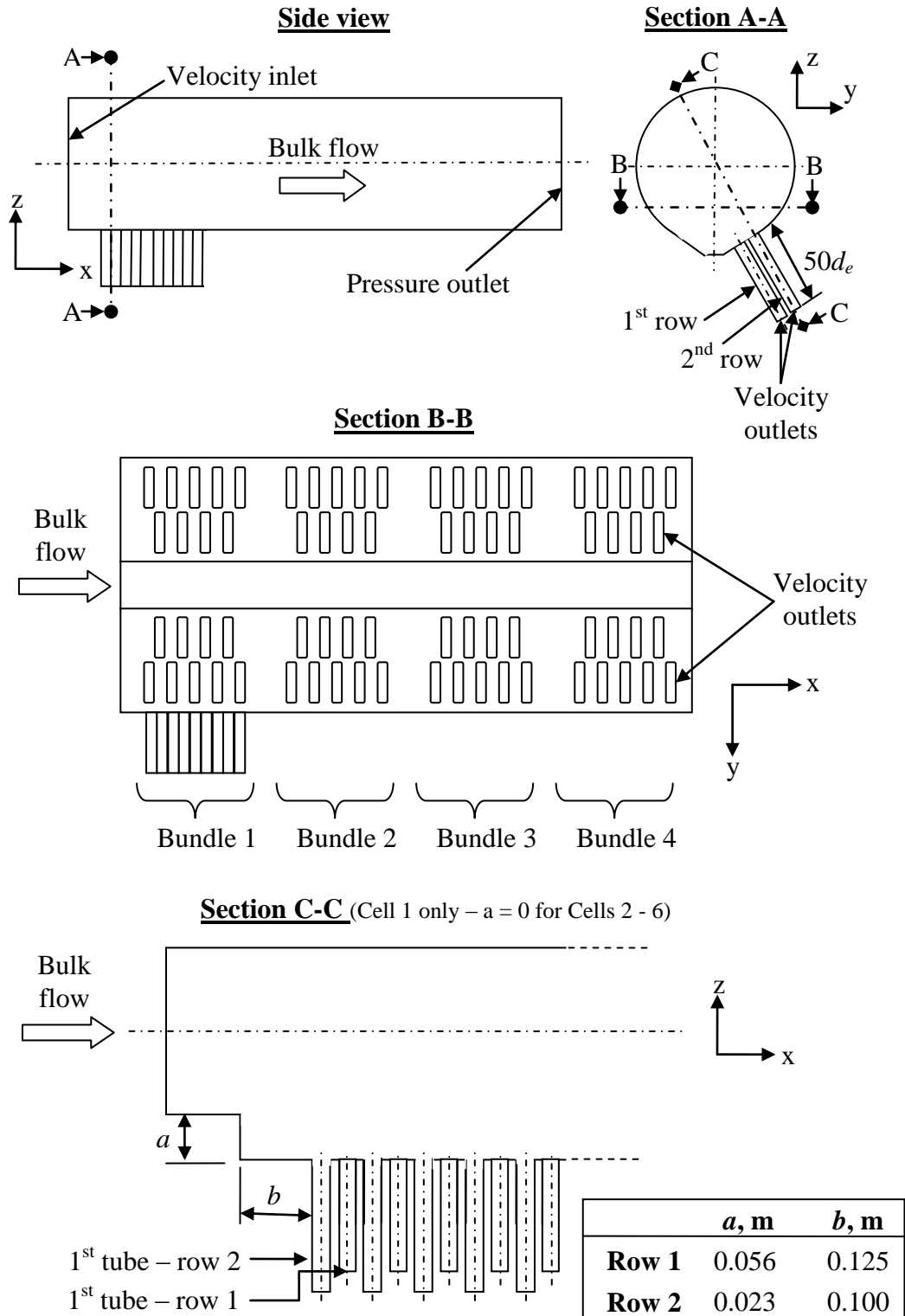


Figure 4.3: Schematic of the CFD model of the dividing header of Cell 1 with the first bundle under investigation

Figures 4.4 and 4.5 respectively show examples of the polyhedral mesh on the inlet of a flattened tube and across the dividing header cross-section. Each bundle model consists of approximately 4×10^6 cells with 215 cells spanning the cross-section of each tube.

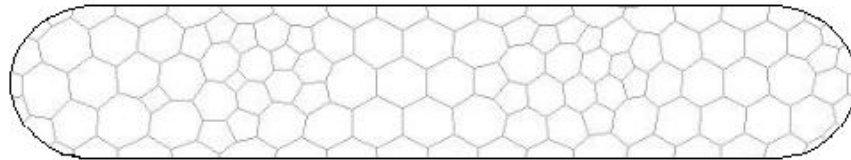


Figure 4.4: Mesh in the heat exchanger tubes

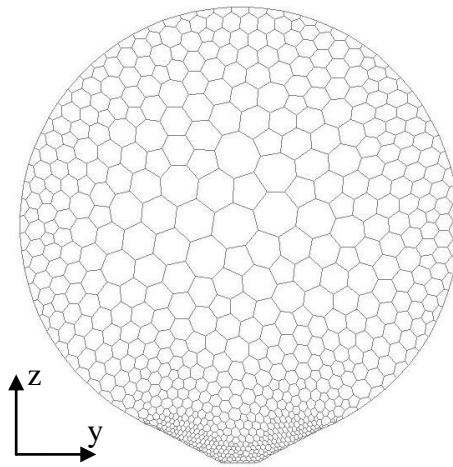


Figure 4.5: Mesh in the heat exchanger dividing header

4.2.3 Verification

The accuracy of the CFD model was verified through a comparison to the flow distribution experiments conducted by Zipfel (1997). Zipfel's experimental setup is shown in Figure 4.6.

The experimental setup consisted of a lateral box (see Figure 4.7 for more detail) installed perpendicular to the outlet section of a wind tunnel. Ambient air is forced past the lateral inlets under the action of a centrifugal fan. A second centrifugal fan sucks air through the laterals via calibrated pipes.

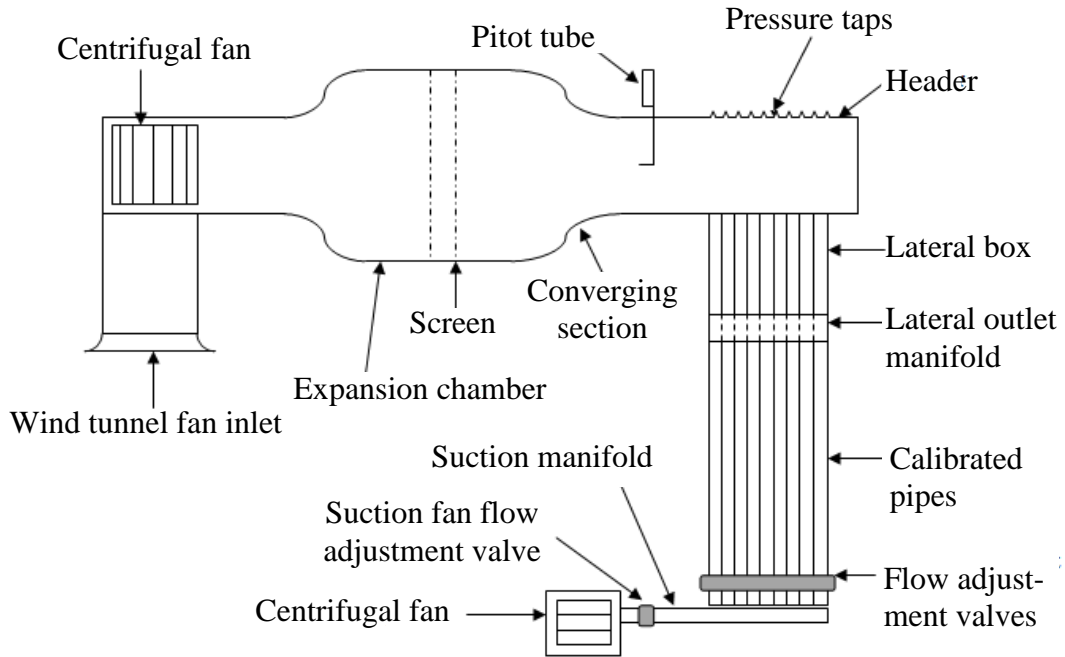


Figure 4.6: Zipfel's (1997) experimental setup

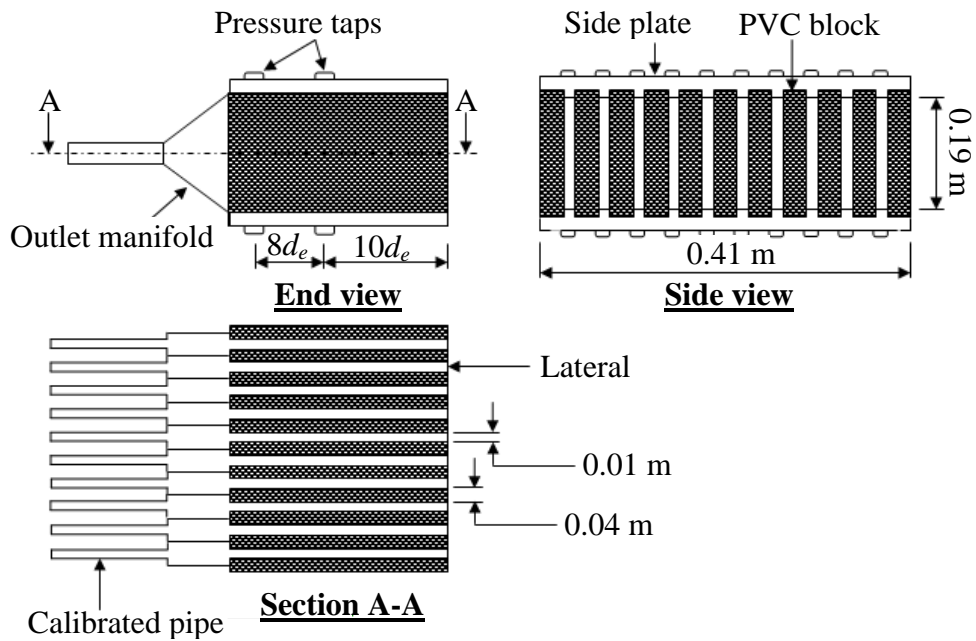


Figure 4.7: Lateral box

Zipfel used a pitot tube to measure the average velocity in the header (v_{hi}). The mean velocity through each lateral (v_l) was determined using the calibrated pipes. The flow through the laterals was controlled using the suction fan flow adjustment valve as well as flow adjustment valves on each of the calibrated pipes. A mean velocity of $10 \text{ m/s} \leq v_l \leq 11 \text{ m/s}$ was maintained in all laterals during each experiment.

Zipfel measured the pressure difference between points in the centre of the header top surface, directly opposite each lateral inlet (p_h) as illustrated in Figure 4.6, and the average of two pressure readings taken on opposite sides of the lateral walls at distances of roughly 10 and 18 (p_l) lateral hydraulic diameters downstream of the lateral inlets (see Figure 4.6)

The CFD modelling procedure described previously was used to simulate Zipfel's experiment. The predicted pressure difference ($p_h - p_l$) is compared to the experimental results in Figure 4.8 for a header-to-lateral velocity ratio of $v_{hi}/v_l = 0.89$. A comparison of the results for different velocity ratios is included in Appendix D.

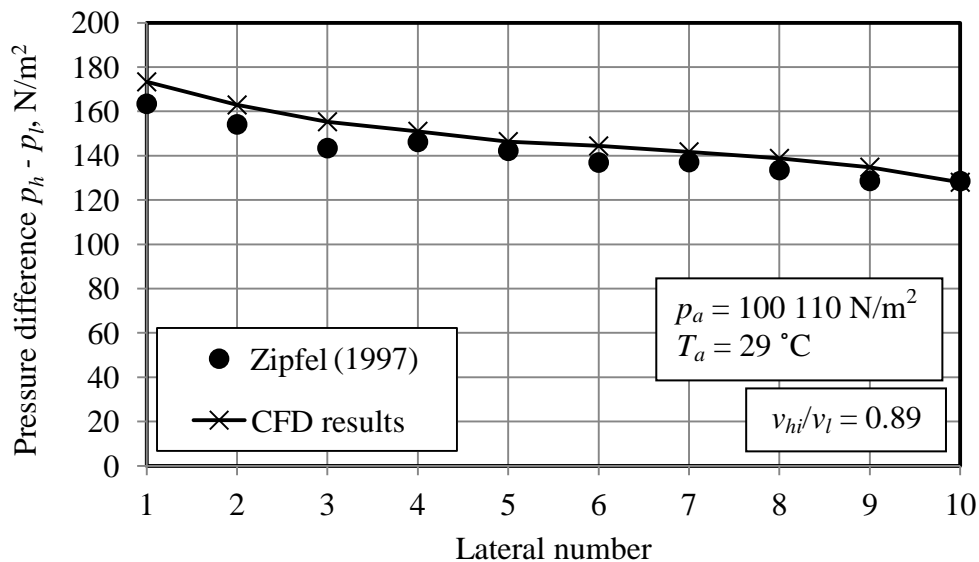


Figure 4.8: Comparison of the CFD and experimental results for $v_{hi}/v_l = 0.89$

The CFD results generally compare well with Zipfel's data. A strong correlation is evident for header-to-lateral velocity ratios in the region of unity while discrepancies increase somewhat for high velocity ratios (see Appendix D). At high velocity ratios the flow at the entrance to the laterals is highly distorted and separation will be severe. It is likely that in this case the experimental measurements may have been taken in a region of distorted flow, before the flow was able to develop fully, resulting in inaccurate readings.

In large ACCs, header-to-lateral velocity ratios in the region of unity are common. The model predicts the experimental data best in this region and is therefore considered to be able to accurately represent the flow in the ACC heat exchangers.

4.3 Numerical flow distribution calculation code

The finite difference procedure presented by Datta and Majumdar (1980) for predicting the flow in parallel and reverse flow manifolds is applied in a numerical calculation code implemented in SCILAB (an open source numerical computation software package similar to the commercially available MATLAB). Datta and Majumdar propose an elliptical formulation to represent the flow in the headers, allowing for downstream influences to propagate upstream in the solution. The elliptical formulation offers an improvement on earlier methods such as those by Enger and Levy (1929), Van der Hegge Zijen (1952), Markland (1959) and Acrivos et al. (1959); which use a parabolic formulation for the header flow and therefore cannot account for the influence of downstream conditions on the lateral flow distribution.

4.3.1 Description of the numerical code

An iterative numerical scheme solves the governing differential equations for momentum and continuity in the axial direction in the headers, Equations (4.1) and (4.2) respectively, while an integral equation for momentum, Equation (4.3), is solved in the lateral direction.

$$C_T \rho u \frac{du}{dx} = -\frac{dp}{dx} - \frac{f_D}{8} \frac{\rho u^2 S}{A_H} \quad (4.1)$$

$$P_l \frac{d}{dx} (\rho u A_H) = m \quad (4.2)$$

$$v = C_d \sqrt{\frac{p_d - p_c}{\rho}} \quad (4.3)$$

In Equation (4.1), u is the average local header velocity, p the local header pressure, S represents the header circumference and A_H is the header cross-sectional area. The turning loss coefficient, C_T , accounts for changes in pressure in the headers due to turning of the flow towards the laterals. Based on experimental data, Bajura (1971) recommends $C_T = 1.05$ for dividing headers and $C_T = 2.66$ for combining headers.

The second term on the right hand side of Equation (4.1) represents friction losses in the headers. Equation (4.4) is used to calculate the Darcy friction factor, f_D , for laminar flow, while the Blasius equation - shown in Equation (4.5) - is used to calculate f_D for turbulent flow (these equations were used instead of Equation (3.5) as they are easier to implement in the numerical code).

$$f_D = 64/Re_v; \quad Re_v \leq 2300 \quad (4.4)$$

$$f_D = 0.3164/Re_v^{0.25}; \quad Re_v > 2300 \quad (4.5)$$

In Equation (4.2), P_l is the tube pitch and m represents flow entering or leaving the header via the laterals and is defined by Equation (4.6). This lateral mass flow term behaves as a sink/source term in the header continuity equation with a negative value in the dividing header and a positive value in the combining header, due respectively to the removal or addition of vapor.

$$m = \rho v A_L \quad (4.6)$$

In Equation (4.3), v is the vapor velocity at the lateral inlets, while p_d and p_c represent the pressure in the dividing and combining headers at the lateral inlet and outlet respectively. C_d is the discharge coefficient of the laterals and is calculated according to Equation (4.7).

$$C_d = \left(K_{eq} - f_l L_t / d_e \right)^{-0.5} \quad (4.7)$$

The loss coefficient K_{eq} in Equation (4.7) takes into account inlet/outlet, acceleration and gravitational effects. The value of K_{eq} is determined from Equation (4.8).

$$K_{eq} = K_i + K_o \left(\frac{v_{vo}}{v_{vi}} \right)^2 + \frac{2(\Delta p_g + \Delta p_m)}{\rho v_{vi}^2} \quad (4.8)$$

Here, the inlet and outlet loss coefficients for the tubes, K_i and K_o , are determined from the CFD results. The pressure changes due to gravitational and momentum/acceleration effects, Δp_g and Δp_m respectively, are calculated from Equations (4.9) and (4.10).

$$\Delta p_g = \rho g \Delta z \quad (4.9)$$

$$\Delta p_m = \rho (v_{vi}^2 - v_{vo}^2) \quad (4.10)$$

In Equations (4.8) – (4.10), v_{vi} and v_{vo} are the vapor velocities at the inlet and outlet of the lateral tubes respectively, while Δz represents the change in elevation between the dividing and combining headers.

The second term on the right hand side of Equation (4.7) represents friction losses in the lateral tubes with L_t the lateral tube length and d_e the tube hydraulic diameter. The lateral friction factor f_l must account for multi-phase flow and condensation in the laterals. Equations (4.4) and (4.5) are not suitable in this case and the correlations of Groenewald and Kröger (1995) are used instead. These

correlations, described hereafter, were determined specifically for condensing steam in inclined flattened tubes with similar geometries to those considered in this study.

Groenewald and Kröger (1995) use the separated flow approach (discussed in more detail in Section 6.3.3) to express the single-phase friction factor with wall suction in terms of an effective interfacial friction factor (f_{De}). The effective friction factor is based on the Darcy friction factor (f_D) – Equations (4.4) and (4.5) – as shown in Equations (4.11) and (4.12) for laminar and turbulent flow respectively.

$$f_{De} = f_D \left(1 + 6.56 \times 10^{-4} Re_{vn}^2 \right); \quad Re_v \leq 2300 \quad (4.11)$$

$$f_{De} = f_D (a_1 + a_2 / Re_v); \quad Re_v > 2300 \quad (4.12)$$

Here, Re_{vn} is the condensation Reynolds number and is expressed in terms of the vapor Reynolds number at the tube inlet (Re_{vi}) as shown in Equation (4.13) where W_t is the tube width.

$$Re_{vn} = Re_{vi} W_t / 2L_t \quad (4.13)$$

For high aspect ratio flattened tubes, as used in the primary condenser bundles, the parameters a_1 and a_2 in Equation (4.12) are given respectively by Equations (4.14) and (4.15).

$$a_1 = 1.0649 + 1.041 \times 10^{-3} Re_{vn} - 2.011 \times 10^{-7} Re_{vn}^3 \quad (4.14)$$

$$a_2 = 290.1479 + 59.3153 Re_{vn} + 1.5995 \times 10^{-2} Re_{vn}^3 \quad (4.15)$$

Using upwind differencing, Equation (4.1) can be expressed in finite difference form as shown in Equation (4.16).

$$D_i^u u_i = A_{i+1}^u u_{i+1} + B_{i-1}^u u_{i-1} + A_H (p_i - p_{i+1}) + C_i^u \quad (4.16)$$

Here,

$$A_i^u = C_T [-(\rho u A_H)_{i+1}] \quad (4.17)$$

$$B_i^u = C_T (\rho u A_H)_i \quad (4.18)$$

$$C_u^i = -\frac{f_D}{8} \rho u_i^2 S_i \Delta x_i \quad (4.19)$$

$$D_i^u = A_i^u + B_i^u \quad (4.20)$$

and Δx represents an incremental distance along the header.

The finite difference representation of the continuity equation in the headers, Equation (4.2), is shown in Equation (4.21).

$$\rho A_H u_i + m_i - \rho A_H u_{i-1} = 0 \quad (4.21)$$

Datta and Majumdar (1980) apply the SNIP (Start New Integration of Pressure) algorithm (Spalding, 1976), a modification of the widely used SIMPLE (Semi-Implicit Pressure Linked Equation) algorithm (Patankar and Spalding, 1972), in which Equation (4.21) is not solved directly but is instead used in the derivation of a pressure correction equation. The SNIP algorithm is described in the following section.

4.3.2 SNIP calculation procedure

The iterative SNIP calculation procedure is implemented as follows:

- a) The total mass flow (M) entering the dividing header is initially assumed to be uniformly distributed amongst the n lateral tubes (i.e. $m_i = M/n$).
- b) The guessed lateral flow distribution is used to solve for the velocity and pressure distribution in the dividing header. To do this:

- i) Equation (4.16) is solved using the Tri-diagonal Matrix Algorithm (TDMA) to generate an approximate header velocity distribution u^* based initially on a uniform header pressure distribution. The pressure distribution from the previous step is used in the calculation of u^* in each subsequent iteration.
- ii) The approximate velocity distribution is used to calculate a pressure correction term p' described by Equation (4.22).

$$D_i^p p_i' = A_i^p p_{i+1}' + B_i^p p_{i-1}' + C_i^p \quad (4.22)$$

With,

$$A_i^p = (\rho A_H^2 / D^u)_i \quad (4.23)$$

$$B_i^p = (\rho A_H^2 / D^u)_{i-1} \quad (4.24)$$

$$C_i^p = (\rho A_H u^*)_{i-1} - (\rho A_H u^*)_i - m_i \quad (4.25)$$

$$D_i^p = A_i^p + B_i^p \quad (4.26)$$

- iii) Equation (4.22) is solved using the TDMA and the results used to correct the velocity distribution as shown in Equations (4.27) and (4.28).

$$u_i' = (A_H / D^u)_i (p_i' - p_{i+1}') \quad (4.27)$$

$$u_i = u_i^* + u_i' \quad (4.28)$$

- iv) The pressure distribution is now recalculated from Equation (4.16).
- v) Steps (i) to (iv) are repeated until the momentum and continuity errors, calculated according to Equations (4.29) and (4.30), fall below a predefined limit.

$$E_{mom} = \frac{\sum_{i=1}^n [D_i^u u_i - A_i^u u_{i+1} - B_i^u u_{i-1} - A_H (p_i - p_{i+1}) - C_i^u]}{\rho u_{in}^2 A_H} \quad (4.29)$$

$$E_{con} = \frac{\sum_{i=1}^n |\rho A_H u_{i-1} - \rho A_H u_i - m_i|}{\rho u_{in} A_H} \quad (4.30)$$

- c) Step (b) is repeated for the combining header, starting with the same lateral flow and pressure distribution as calculated for the dividing header and accounting for the vapor condensed in each tube.
- d) Based on these results a new lateral flow distribution, m_i^* , is calculated using Equations (4.6) and (4.3).
- e) A flow rate error term, relating the predicted flow distribution to the total inlet flow rate, is calculated according to Equation (4.31).

$$E_M = M - \sum_{i=1}^n m_i^* \quad (4.31)$$

- f) The lateral flow distribution is now corrected as shown in Equation (4.32) and the pressure distribution in the dividing header is recalculated from Equation (4.3).

$$m_i = m_i^* + E_M / n \quad (4.32)$$

- g) Steps (b) – (f) are repeated until E_M becomes sufficiently small.

The total mass flow rate entering the dividing header (M) is chosen such that the minimum flow entering any tube is equal to the condensation rate in that tube (i.e. $m_{vi} = m_c$).

4.3.3 Verification

The experimental data of Bajura and Jones (1976) was used to verify the accuracy of the numerical flow distribution calculation code. Bajura and Jones experimentally investigated the air flow distribution in parallel and reverse flow

manifolds in which the lateral resistances were controlled using orifice plate inserts. Tests were conducted for manifolds with 10 and 20 lateral branches. The pressure distribution in the headers was measured by means of pressure taps installed mid-way between branch points in the header walls opposite the lateral inlets. The static pressures in the headers were referenced to a pressure at one end of the headers, depending on the manifold configuration. Reynolds numbers in the headers and laterals were in the range of $60\,000 \leq Re_H \leq 80\,000$ and $8\,000 \leq Re_l \leq 10\,000$ respectively.

A comparison of the predicted pressure distributions in the headers, and the pressure difference between the dividing and combining headers, of a 10 branch parallel manifold with a lateral discharge coefficient of $C_d = 0.4155$ is illustrated in Figure 4.9.

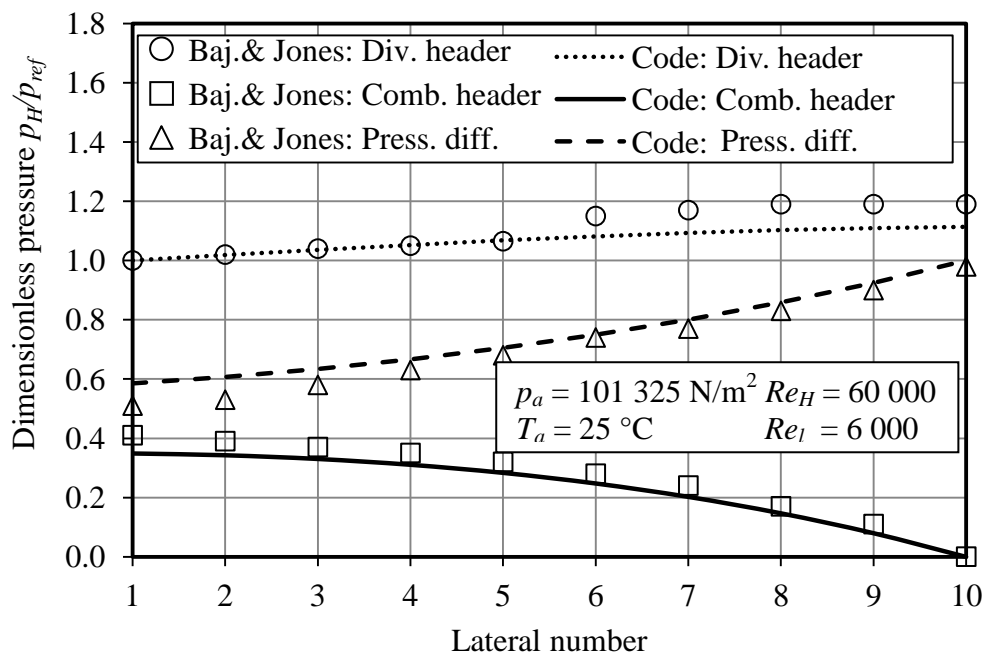


Figure 4.9: Comparison of header pressure distributions for a parallel flow manifold

Figure 4.10 shows a similar comparison for a reverse flow manifold. Comparisons for other lateral configurations are included in Appendix D.

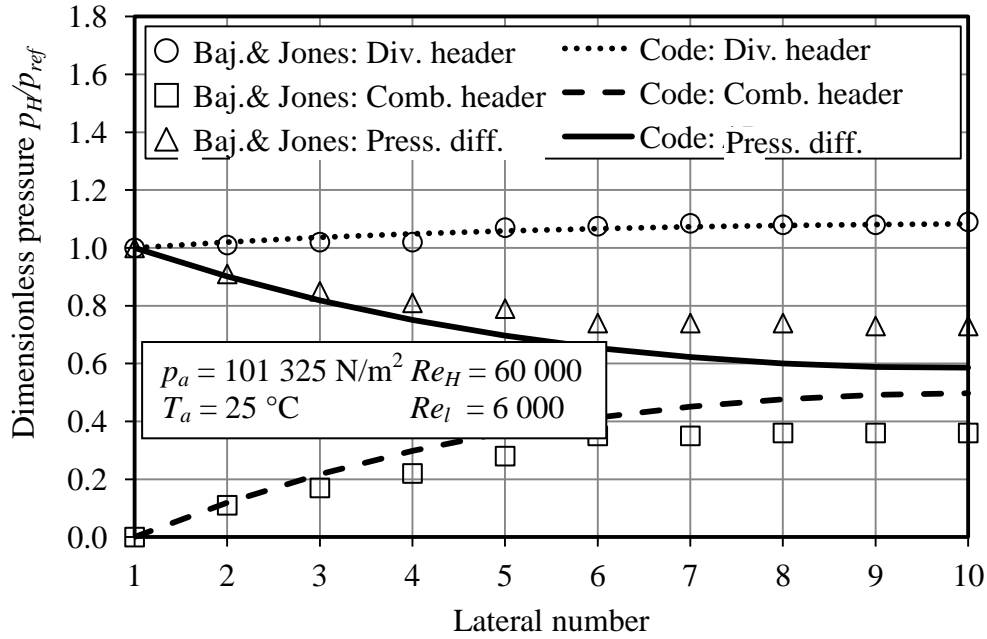


Figure 4.10: Comparison of header pressure distributions for a reverse flow manifold

The header pressure distributions determine the flow distribution through the laterals. The ability to accurately predict these distributions is therefore indicative of the code's ability to accurately represent the flow distribution in manifold systems. As can be seen in Figures 4.9 and 4.10, a good correlation exists between the CFD predictions and the experimental data.

4.4 Steam-side primary condenser tube inlet loss coefficient distribution

4.4.1 Determining inlet loss coefficients from CFD data

The total pressure drop at a sudden contraction in the flow is caused by a combination of acceleration of the flow and separation of the boundary layer, as illustrated in Figure 4.11.

The inlet pressure loss is described as the change in total pressure between the last point of attachment upstream of the tube inlet (point 1 in Figure 4.11) and the first point of re-attachment downstream of the inlet (2). This loss can be described as shown in Equation (4.33), where K_i is the inlet loss coefficient.

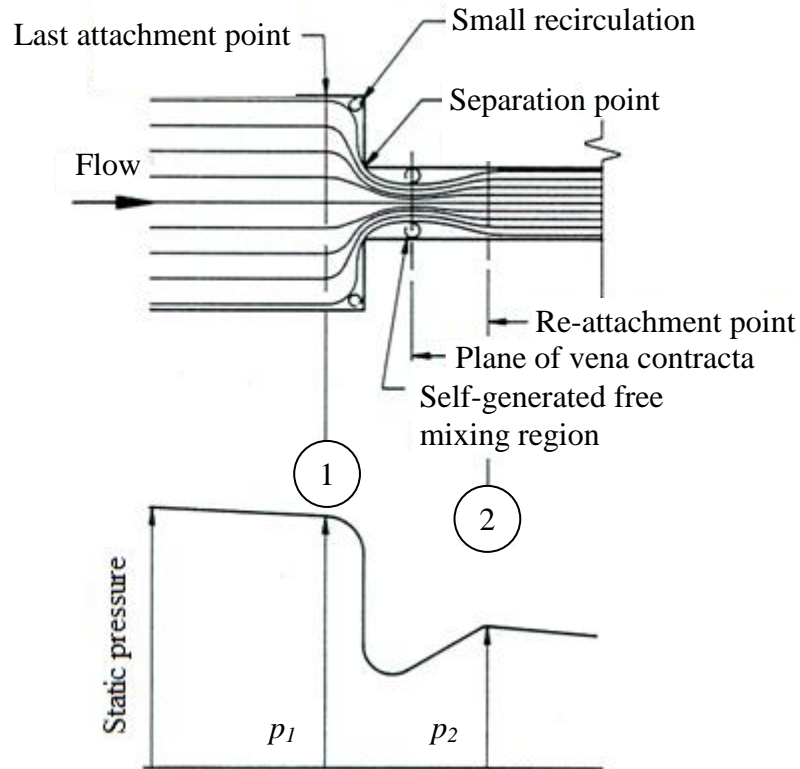


Figure 4.11: Static pressure distribution in a duct with a sudden contraction (Kröger, 2004)

$$(p_1 + \rho v_1^2 / 2) - (p_2 + \rho v_2^2 / 2) = K_i \rho v_2^2 / 2 \quad (4.33)$$

In order to determine the inlet loss coefficient distribution from the CFD results, total pressure distributions are extracted from the results along a line surface through the centre of each tube and extending through the header to the opposite header wall. A post-processing code identifies the last point of attachment upstream of each tube inlet, and the first point of re-attachment in each tube, by comparatively examining the gradient in the pressure distribution between consecutive data points along the line. The pressures at the relevant points are recorded and K_i is subsequently calculated from Equation (4.33).

4.4.2 Results

The predicted steam-side tube inlet loss coefficients in the primary condenser bundles are illustrated here. Figures 4.12 and 4.13 show the inlet loss coefficient distributions in Cell 1 while Figures 4.14 – 4.17 show the corresponding distributions for Cells 2, 4, 5 and 6 in succession. The dephlegmator (Cell 3) was not considered in the analysis. The results shown below are based on a steam turbine backpressure of $p_v = 19\,925.12\text{ N/m}^2$ ($T_v = 60\text{ }^\circ\text{C}$). Simulations conducted at several vapor temperatures ($40\text{ }^\circ\text{C} \leq T_v \leq 60\text{ }^\circ\text{C}$) proved the inlet loss coefficients to be largely independent of vapor properties.

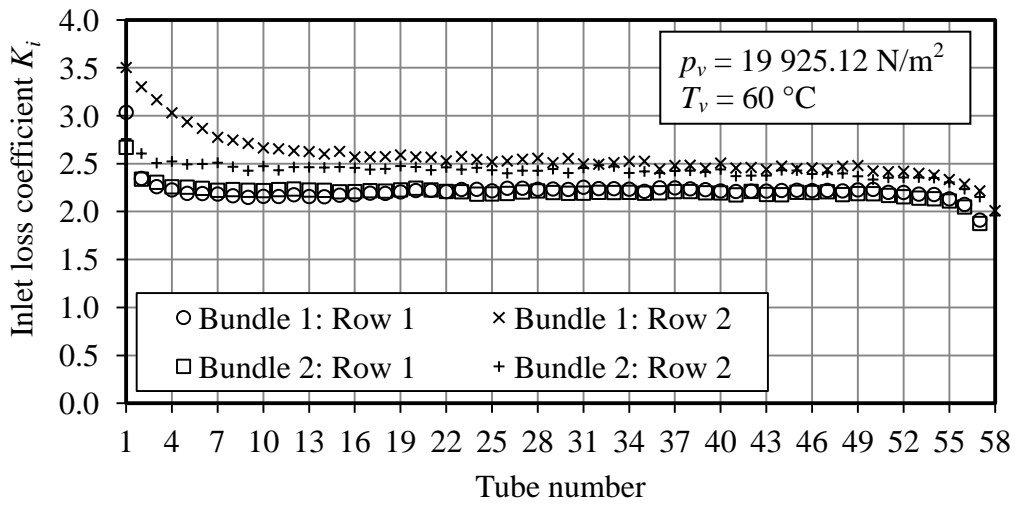


Figure 4.12: Inlet loss coefficients in the first and second bundles of Cell 1

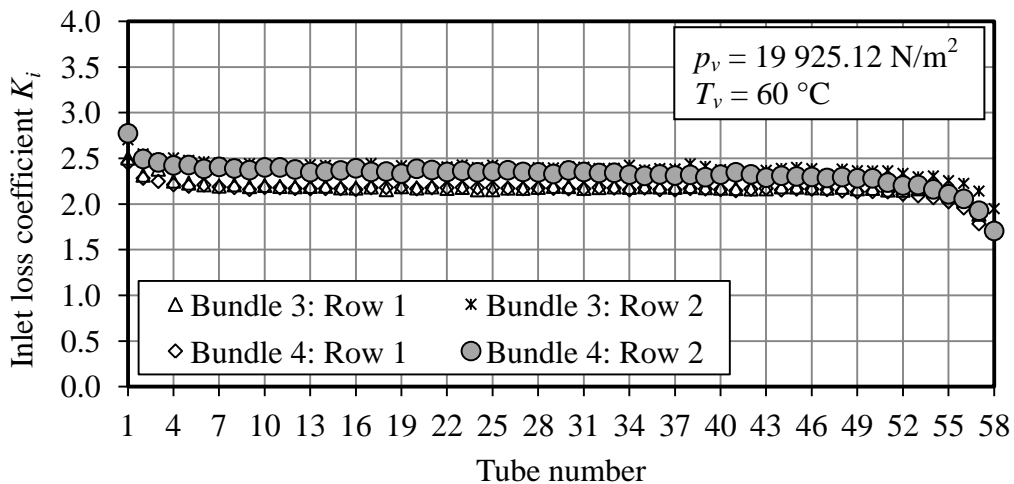


Figure 4.13: Inlet loss coefficients in the third and fourth bundles of Cell 1

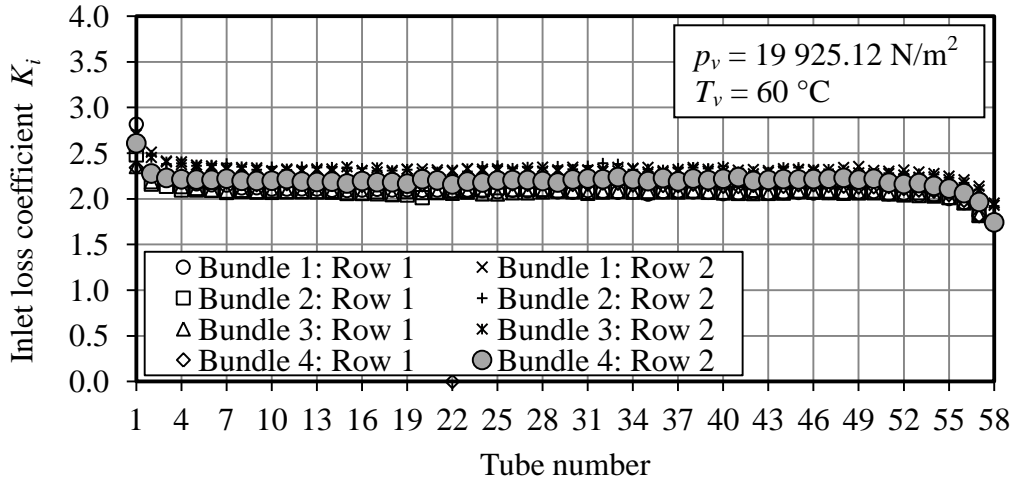


Figure 4.14: Inlet loss coefficients in Cell 2

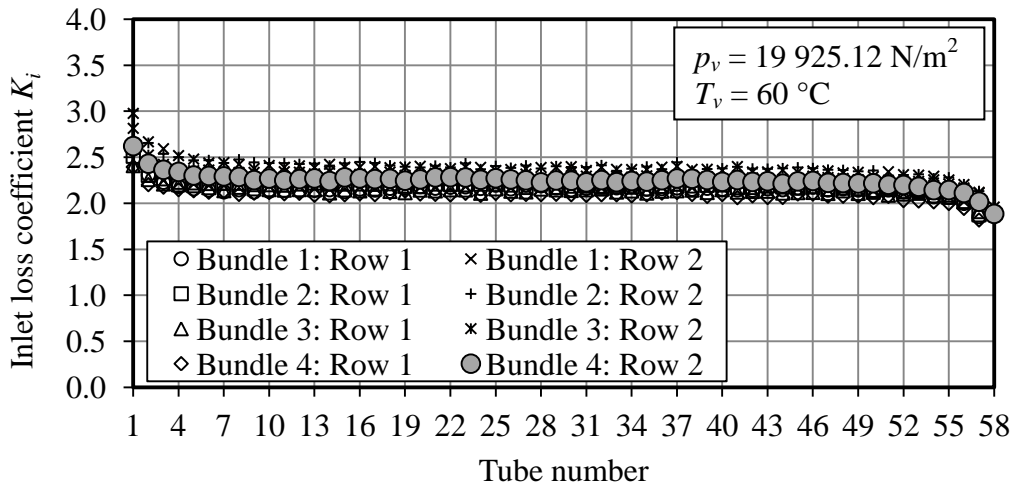


Figure 4.15: Inlet loss coefficients in Cell 4

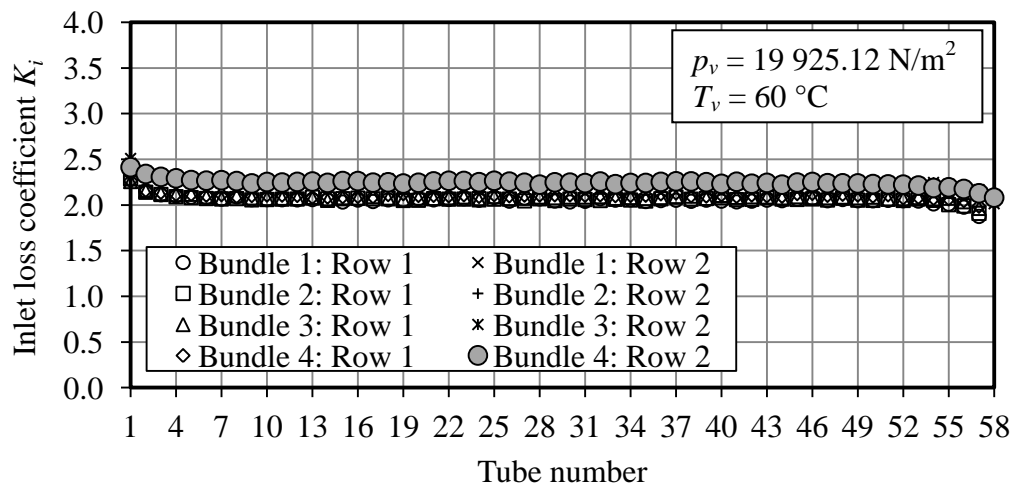


Figure 4.16: Inlet loss coefficients in Cell 5

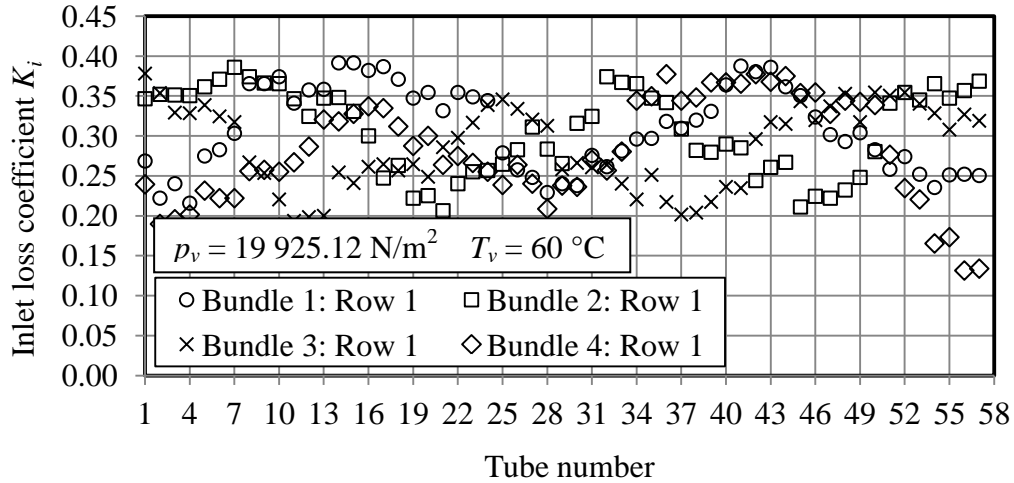


Figure 4.17: Inlet loss coefficients in Cell 6

The inlet loss coefficient distributions in Cells 1, 2, 4 and 5 (Figures 4.12 – 4.16) follow a similar trend although the magnitudes of the individual loss coefficients differ somewhat. The loss coefficients at the upstream tubes in a bundle are higher than at the downstream tubes due to the greater obliqueness of the flow approaching the upstream tubes. Evidence of such a distribution can be seen in Zipfel’s (1997) experimental results (see Figure 4.7 and Appendix D). This effect is slightly more pronounced in the first bundle of each cell where the gap between the last tube in the preceding cell and the first tube in a particular cell is larger than the tube pitch. The bulk flow in the header therefore becomes more aligned with the steam header axis in the region between cells, and hence more oblique to the tube inlets.

The difference between the upstream and downstream tube inlet loss coefficient diminishes in the header flow direction as a result of an ever decreasing axial flow component (compare, for example the results for Cell 2 shown in Figure 4.14 to those of Cell 5 in Figure 4.16).

At the upstream tubes in the first bundle of Cell 1 (Figure 4.12), the inlet loss coefficients are observed to be measurably greater than for the downstream bundles in that cell (Figure 4.13) or for any of the bundles in Cells 2, 4, 5 and 6 (Figures 4.14 – 4.17). These high inlet losses can be attributed to the fact that the

upstream tubes in Cell 1 are exposed to the most adverse inlet flow conditions due to a combination of the magnitude and strong axial alignment of the header flow upstream of their location. Slightly increased inlet losses are also evident in the upstream tubes of the first bundle in Cell 4 (Figure 4.15) where strong axial header flow alignment is found after the long section of header with no suction above Cell 3. The effect is less pronounced in Cell 4 however, since the magnitude of the axial component of the flow is smaller here after approximately 40 % of the vapor entering the header is removed in Cells 1 and 2.

In Cell 1, the inlet loss coefficients for the upstream tubes in the second row are larger than those in the first tube row (Figure 4.12). This occurrence is isolated to the first bundle in Cell 1 and is caused by the presence of a vertical step upstream of this bundle, as illustrated in Section C-C of Figure 4.3. The distance between the step and the upstream row of tubes (dimension b in Figure 4.3), as well as the height of the step (dimension a), is larger for the first row than for the second. Zipfel (1997) investigated the influence of a step upstream of a bundle of tubes in an essentially two dimensional flow situation. One of his experiments was conducted with $b = 0.1$ m which is very similar to this case (see Figure 4.3 for values of a and b). In his experiment, Zipfel considered step heights of $a = 0.01$ m and $a = 0.02$ m, comparable to the step heights in the heat exchanger considered here, and found that the tube inlet loss coefficient was smaller for the higher step. In general, Zipfel found a decrease in inlet loss coefficient with increasing distance between the step and the upstream tube (i.e. increasing b). The numerical results in Figure 4.12 correspond with Zipfel's observations. Figure 4.18 shows a vector plot on planes through the middle of the first and second tube rows, and clearly illustrates the better alignment of the flow at the inlet of the upstream tubes in the first tube row caused by the greater step height.

The CFD prediction of the inlet loss coefficients in Cell 6 (Figure 4.17) shows a measurable degree of scatter. No discernible pattern is evident in the results and the trend present in the upstream cells is not repeated here.

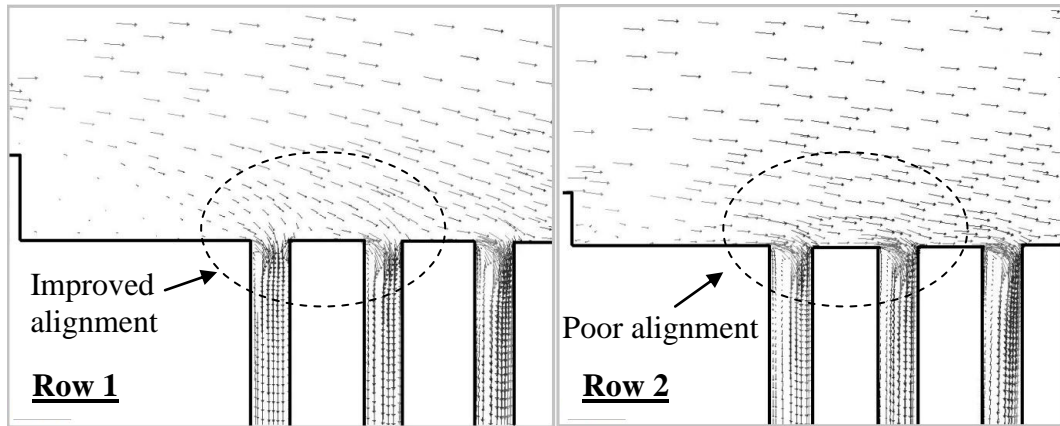


Figure 4.18: Vector plot on the tube row mid-plane illustrating the influence of the step on the flow entering the upstream tubes of Cell 1

The simulation of Cell 6 proved problematic due to the lack of passing flow in the dividing header which resulted in solution instability. Despite this fact, the results seem to indicate lower loss coefficients than in the upstream cells. This is expected since the axial component of the bulk flow in the dividing header is much reduced here and the flow is subsequently more aligned with the tubes.

The magnitude of the loss coefficients predicted in Cell 6 approach that of a sudden contraction with a cross-sectional area ratio of $\sigma = 0.5$, as defined by Equation (4.34) (Kays, 1950).

$$K_i = (1 - 1/\sigma_c)^2 \quad (4.34)$$

In Equation (4.34), σ_c is the contraction ratio defined by Equation (4.35) for parallel plates (Rouse, 1946), which are representative of the flattened heat exchanger tubes.

$$\begin{aligned} \sigma_c = & 0.6144517 + 0.04566493\sigma - 0.336651\sigma^2 + 0.4082743\sigma^3 \\ & + 2.672041\sigma^4 - 5.963169\sigma^5 + 3.558944\sigma^6 \end{aligned} \quad (4.35)$$

Based on Equations (4.34) and (4.35), a constant value of $K_i = 0.29$ was prescribed for all the tubes in Cell 6.

4.5 Steam-side tube outlet loss considerations

The predicted tube outlet loss coefficients (K_o) for the first tube row in Cell 1 are shown in Figure 4.19. These losses are calculated in a similar manner to that described for the inlet losses in Section 4.4.1, with the outlet loss defined as the pressure change between the last point of flow attachment inside the tubes and the first point of “re-attachment” in the combining header.

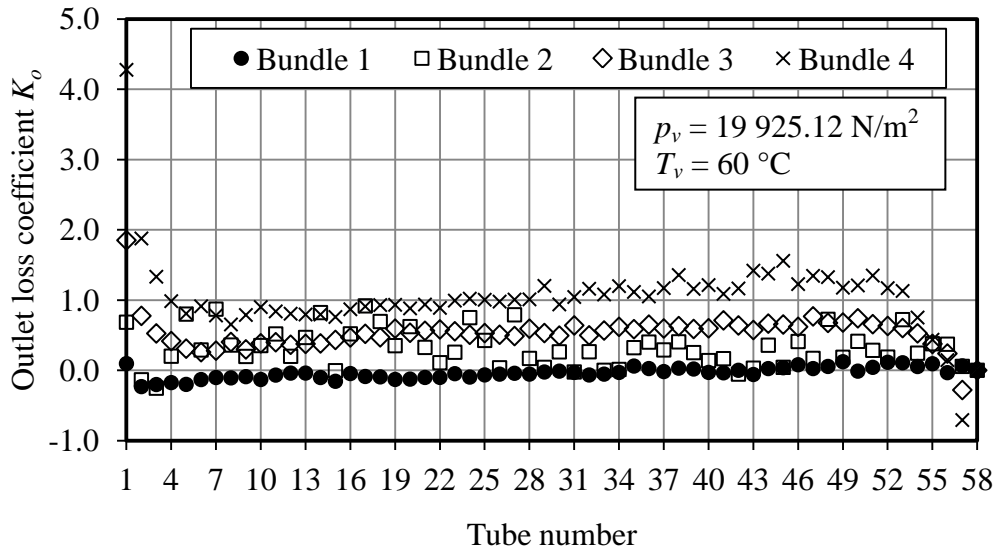


Figure 4.19: Outlet loss coefficients in the first tube row of Cell 1

In the first bundle the outlet loss coefficients are very small and are predicted to be negative for the upstream tubes ($K_o \rightarrow 0^-$), indicating a slight pressure recovery at the outlet of these tubes. Further downstream the outlet loss coefficients increase (i.e. the loss coefficients in Bundle 3 are slightly larger than in Bundle 2) and are mostly positive for Bundles 2 – 4, indicating a loss at the tube outlets. Figures 4.20 and 4.21 illustrate the flow patterns at the outlet to the tubes in Bundle 1 and Bundle 4 respectively through the use of velocity vectors superimposed on a contour plot of velocity magnitude. Examination of these figures offers some insight into the reasons for the outlet loss coefficient trends.

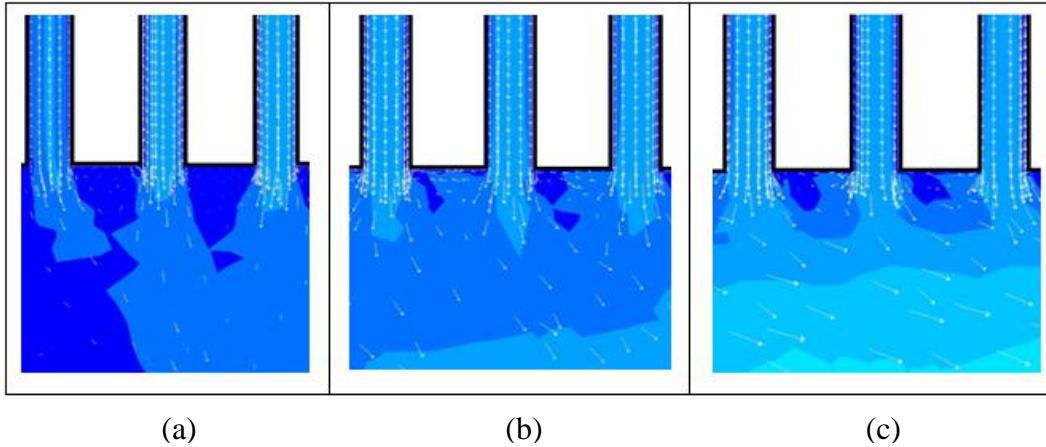


Figure 4.20: Flow patterns in Bundle 1 at the outlet of the (a) upstream tubes, (b) centrally located tubes, (c) downstream tubes

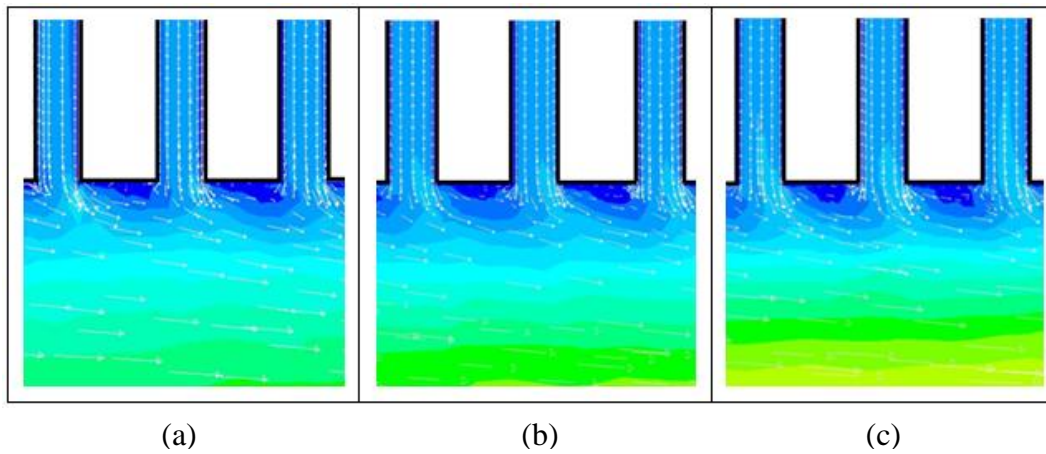


Figure 4.21: Flow patterns in Bundle 4 at the outlet of the (a) upstream tubes, (b) centrally located tubes, (c) downstream tubes

In the combining header upstream of Bundle 1 there is initially no axial flow since this header is closed at its upstream end. The axial component of the flow in the combining header is therefore weak in the upstream regions of this bundle, and has little effect on the flow leaving the upstream tubes, as can be seen in Figure 4.20 (a). The flow is therefore able to expand as it leaves the tubes in the upstream region of Bundle 1 resulting in a static pressure recovery. At the same time, separation occurs at the tube outlet edges and the resultant eddies cause a pressure loss which acts in opposition to the expansion-related recovery. In the

first bundle, the aforementioned opposing effects seem to be of similar magnitude resulting in very small net tube outlet pressure changes.

Further downstream, the axial component of the flow in the combining header increases steadily as more flow enters the header. The higher axial flow in the header restricts the expansion of the flow leaving the tubes and the amount of recovery experienced by the flow as it leaves the tubes is therefore reduced. Simultaneously, the higher axial header flow causes enhanced separation at the tube outlets and hence increased losses.

Figure 4.19 also reveals a similar trend in the outlet loss coefficients as is present in the inlet loss coefficient, where the upstream tubes have higher loss coefficients than the downstream tubes in each bundle. A similar argument as for the inlet loss coefficients holds in this case with the greater axial alignment of the flow at the upstream tubes causing greater separation and suppressed expansion, resulting in increased losses.

The outlet loss coefficients in Cells 2, 4 and 5 are similar to those in the downstream bundles in Cell 1. Cell 6 exhibits a similar trend to Cell 1 with a slight recovery at the outlet of the tubes near the closed end of the header.

In general, the outlet loss coefficients are measurably smaller than the corresponding inlet loss coefficients in each tube. This, combined with the much smaller vapor velocity at the tube outlets, results in the pressure changes at the tube outlets being an order of magnitude or more smaller than the corresponding inlet pressure losses. Outlet effects therefore have little influence on the flow distribution in the condenser bundles.

4.6 Vapor flow distribution in the primary condensers

The vapor flow distribution in the primary condensers is a function of the pressure changes over the heat exchanger tubes. As mentioned previously, the pressure change over a tube comprises of inlet/outlet, frictional, geodetic and acceleration effects and is constrained by the pressure distributions in the dividing and

combining headers. The header pressure distributions are in turn influenced by momentum effects as flow enters or leaves via the branching tubes.

The geodetic effect is small compared to the other losses and is equal for all tubes. Geodetic effects therefore do not influence the flow distribution amongst the tubes. Losses due to friction and pressure recovery due to deceleration of the flow with condensation are significant, but in most cases have largely similar magnitudes and therefore balance one another. Also, the magnitude of the aforementioned effects is similar in all tubes in a given row and they therefore do not play a major role in determining the axial flow distribution. Outlet effects were found to be significantly smaller than inlet effects and are of little consequence. Inlet effects and the header pressure distributions therefore remain as the primary factors that may influence the vapor flow distribution.

The predicted flow distribution in the first tube row of the upstream bundle in each of the primary condenser cells is shown in Figure 4.22. The ratio of the inlet vapor mass flow rate (m_{vi}) to the condensation rate (m_c) for ideal ACC operation is plotted for each tube. Again, note that the total flow rate entering the dividing header of the primary condenser was scaled such that the minimum inlet flow rate to any tube is equal to the condensation rate in that tube.

The flow distribution pattern is the same in the parallel flow manifolds of Cells 1 and 2 as in the reverse flow manifolds of Cells 4, 5 and 6. It was expected that the parallel and reverse flow manifolds would have different flow distribution patterns due to the differing nature of the pressure distributions in the dividing and combining headers for these different manifold configurations.

In the experimental results of Bajura and Jones (1976), discussed in Section 4.3.3, the flow distributions were strongly related to the pressure distribution in the headers and followed the trends of increasing flow rate in the axial direction in the parallel manifold, but decreasing flow rate in this direction in the reverse flow manifold.

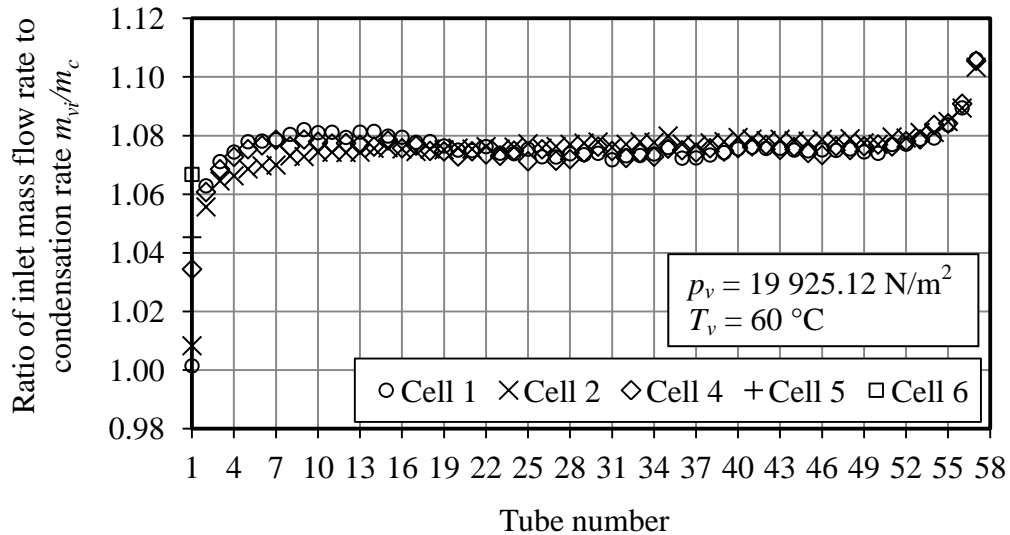


Figure 4.22: Vapor flow distribution in the first row of the first bundle of the primary condenser cells

In their experiment, Bajura and Jones controlled the loss coefficient for each lateral tube by means of orifice plate inserts which dominated the other losses across the tubes. Their experimental results are therefore representative of an approximately uniform lateral loss coefficient distribution. While the pressure distributions in the header of the ACC primary condensers follow the expected trends, as illustrated in Figure 4.23, the lateral tube loss coefficient is dominated by the inlet loss coefficient distribution. It is obvious from the results that the flow distribution in this case is strongly linked to the inlet loss coefficient distributions shown in Figures 4.12 – 4.16. It can therefore be concluded that the inlet loss coefficient distribution is the dominant factor determining the flow distribution through the primary condensers of an ACC.

From Figure 4.22 it can be seen that in order for the worst affected tube, in this case the upstream tube in the second tube row of Cell 1, to have complete condensation, additional flow must be drawn through the remaining tubes. This additional flow must be provided by the dephlegmator. The implication of inlet loss coefficient distributions on dephlegmator requirements is discussed in the next chapter.

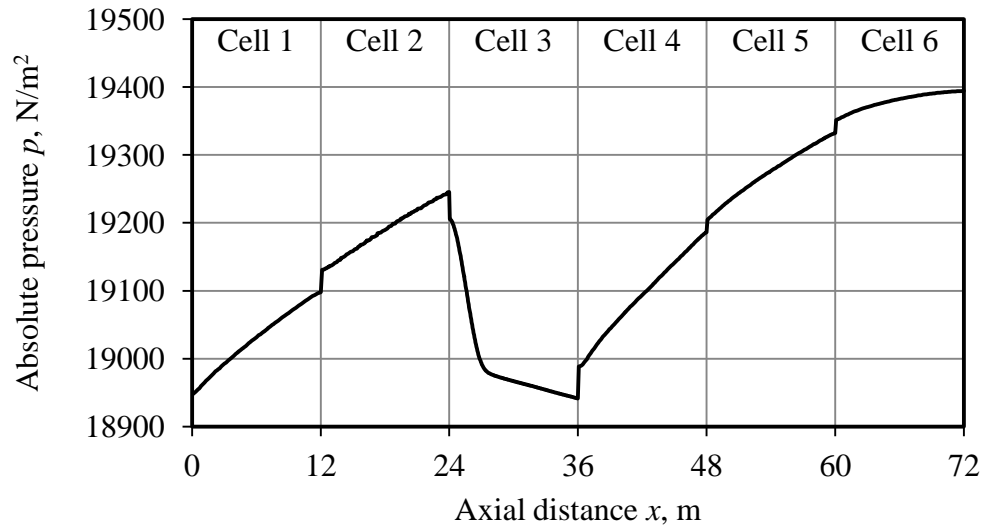


Figure 4.23: Pressure distribution in the dividing header of an ACC street

5. DEPHLEGMATOR CONSIDERATIONS

The dephlegmator must provide additional flow through the primary condensers to prevent vapor backflow, and the subsequent accumulation of non-condensable gases, in the primary condenser tubes.

This chapter begins by describing the mechanism of vapor backflow in the primary condensers (Section 5.1) before examining the implications of the results presented in Chapter 4 on dephlegmator sizing (Section 5.2). The final section of this chapter addresses vapor backflow in the dephlegmator itself.

5.1 Vapor backflow in the primary condensers

As an illustrative example, consider a pair of tubes in different rows of a two-row primary condenser heat exchanger bundle, as shown in Figure 5.1.

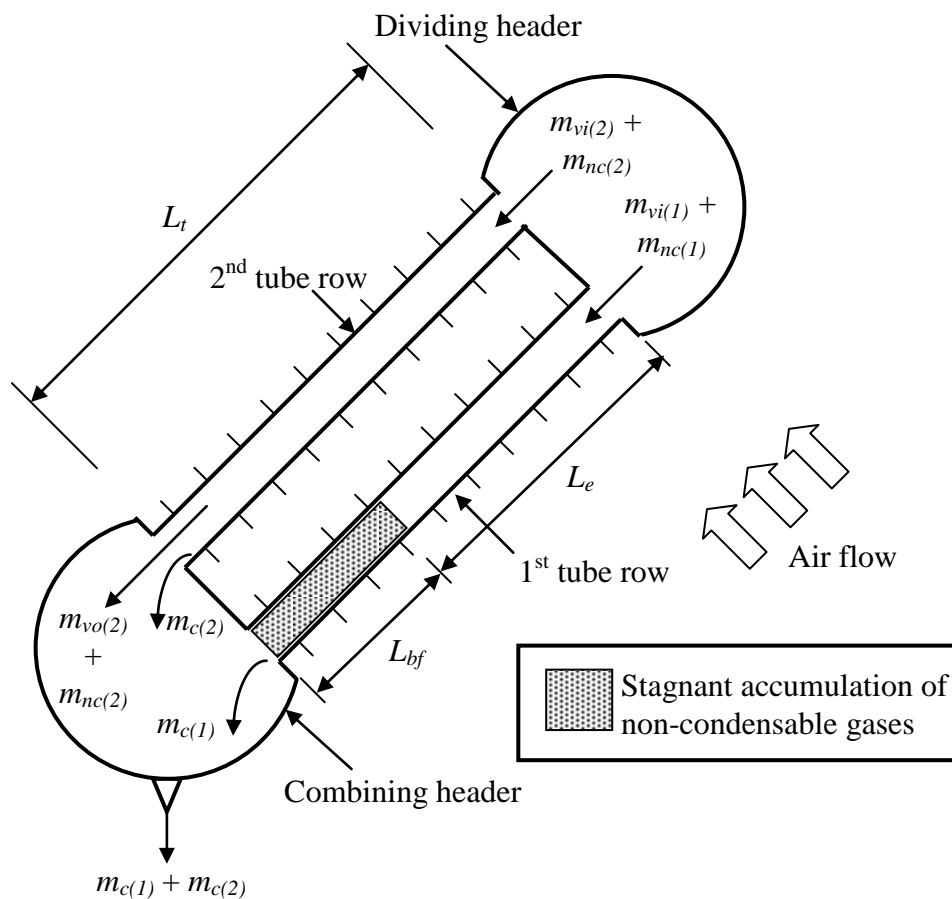


Figure 5.1: Primary condenser tubes with vapor backflow

The tube in the upstream row (first tube row in Figure 5.1) is exposed to cool ambient air. This air is heated as it moves past the upstream row and the downstream row (second row) is subsequently exposed to warmer air. The vapor temperature is the same in both rows and the condensation rate per unit length of tube is therefore greater in the upstream row. If condensation occurs along the entire length of both tubes (100 % effective operation) then the vapor flow rate entering the upstream tube will be greater than in the downstream tube.

In most multi-row heat exchangers, the heat transfer effectiveness of the tubes in the downstream row is enhanced (typically by reducing the fin pitch and thus creating greater heat transfer surface area) in an attempt to match the condensation rate in the first row despite the higher cooling air temperature. As mentioned in Section 2.2, however, such strategies are only effective over a limited range of operating conditions.

As a result of the generally higher vapor flow rates in the upstream row, the steam-side pressure drop over the upstream tube will tend to be greater than the corresponding loss over the downstream tube. This cannot be, however, since the tubes share common headers. Consequently, vapor must enter the upstream tube from both ends and a stagnation point is formed at some distance before this tube's outlet (L_{bf} in Figure 5.1). The effective length (L_e) of the upstream tube is thus reduced such that the steam-side pressure change over the effective lengths of both tubes is the same. A similar argument to that above applies to tubes in the same row but with different inlet loss coefficients (see Chapter 4).

The undesirable phenomenon of vapor entering a tube from both ends is known as vapor backflow and is detrimental to heat transfer effectiveness. Non-condensable gases that leak into the system are transported to the stagnation regions where they accumulate and form "dead zones" which reduce the effective heat transfer surface area of the ACC. During hot periods, when ACCs typically experience poor performance, dead zones cause further reductions in heat transfer rate. During cold periods, condensate trapped in the stagnation region may freeze. The

significant expansion of the condensate during freezing can rupture the heat exchanger tubes with obvious catastrophic consequences.

Continuing with the example from above, if additional vapor can be drawn through the downstream tube so that its steam-side pressure drop increases to match that over the upstream tube when operating at full effectiveness (i.e. $L_{bf} = 0$ m), then backflow can be avoided. The role of the dephlegmator is to provide this additional suction.

5.2 Dephlegmator sizing requirements

The dephlegmator must account for the combined demands of row effects and inlet loss coefficient distributions under ideal operating conditions (i.e. uniform flow through all fans and all finned tubes operating at full effectiveness). Non-ideal primary condenser operation due to, for example, non-uniform air flow through the fans, recirculation of hot plume air, and localized reduced tube effectiveness due to fouling; places additional demand on the dephlegmator.

The dephlegmator sizing requirements to overcome row effects and inlet loss coefficient distributions are predictable and are discussed in the sections that follow. The effects of non-ideal primary condenser operation are less predictable and require a safety margin to be included in the dephlegmator design.

5.2.1 Inlet loss coefficient distribution requirements

Section 4.5 discussed the distribution of vapor amongst the heat exchanger tubes in the primary condenser. The vapor flow distribution was shown to be strongly linked to the distribution of inlet loss coefficients, with the upstream tubes of Cell 1 experiencing the highest inlet losses and correspondingly the lowest vapor flow. These tubes therefore experience the greatest risk of vapor backflow. High inlet losses are also experienced at the upstream tubes in each of Cells 2, 4 and 5. These locations are also at risk of experiencing vapor backflow, although less so than in Cell 1. Figure 5.2 illustrates the areas most at risk of non-condensable accumulation in the primary condenser units.

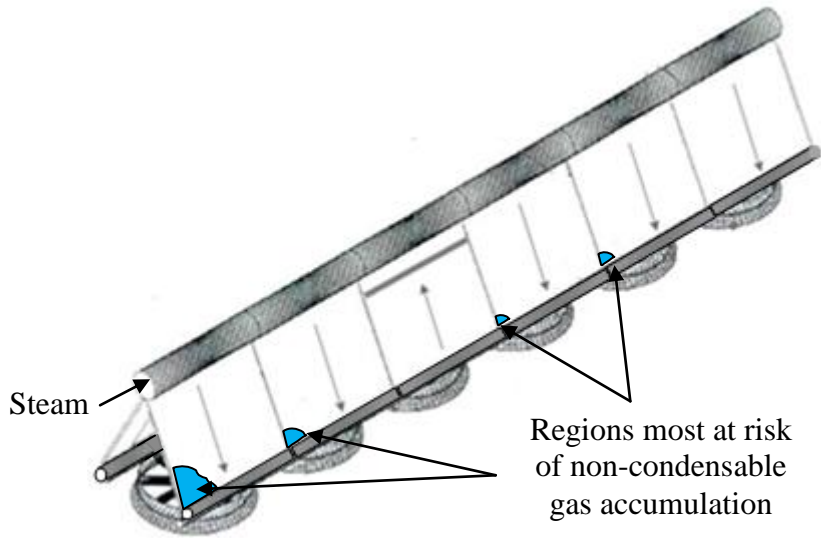


Figure 5.2: Primary condenser regions at greatest risk of non-condensable gas accumulation

The ratio of total inlet vapor flow to total condensation rate in the primary condensers, required to prevent backflow in the upstream tubes, is shown in Figure 5.3.

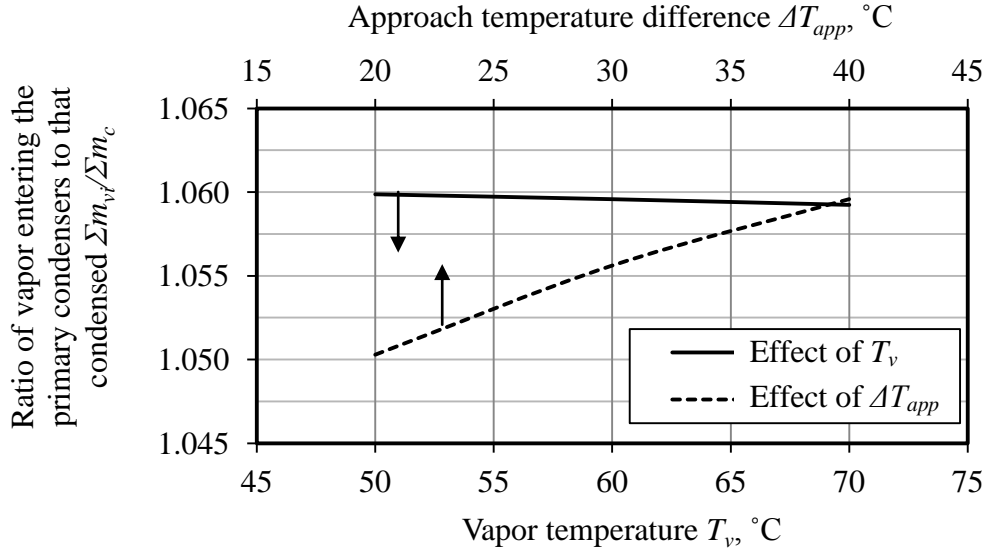


Figure 5.3: Additional vapor flow required in the primary condensers to overcome inlet loss coefficient distributions

The results in Figure 5.3 take into account all eight bundles in each of the five primary condenser cells. The effects of both vapor temperature and approach temperature difference ($\Delta T_{app} = T_v - T_a$), on the dephlegmator requirement are illustrated.

Over the range of vapor temperatures and approach temperature differences likely to be experienced in a practical ACC, between 5 % and 6 % additional vapor flow (i.e. flow over and above that condensed) is required through the primary condenser cells to prevent backflow due to inlet loss coefficient distributions.

The effect of vapor temperature is illustrated by the solid line in Figure 5.3. Vapor temperatures of $50\text{ }^\circ\text{C} \leq T_v \leq 70\text{ }^\circ\text{C}$ were considered with a constant approach temperature difference of $\Delta T_{app} = 40\text{ }^\circ\text{C}$. The required additional vapor flow can be considered almost independent of vapor temperature with a decrease of only 0.06 % between $T_v = 50\text{ }^\circ\text{C}$ and $T_v = 70\text{ }^\circ\text{C}$. The reason for this independence can be explained by noting that the heat transfer rate in the tubes is proportional to the approach temperature difference. For a fixed ΔT_{app} , the heat transfer rate (and hence the condensation rate in the heat exchanger tubes) changes very little over the range of vapor temperatures considered. However, vapor density increases with increasing vapor temperature and the velocities in the tubes therefore decrease. The steam-side tube inlet losses are proportional to the square of the tube inlet velocity. As inlet velocities decrease so does the magnitude of the difference in inlet pressure drop between tubes with different inlet loss coefficients. This effect is counteracted by the slight changes in vapor densities that serve to increase the inlet losses somewhat. As a result, the difference in tube inlet losses for complete condensation remains almost constant as the vapor temperature changes at a fixed ΔT_{app} .

Now consider the effect of the approach temperature difference (dashed line in Figure 5.3). For this purpose the vapor temperature was fixed at $T_v = 60\text{ }^\circ\text{C}$ while the ambient temperature was altered to achieve $20\text{ }^\circ\text{C} \leq \Delta T_{app} \leq 40\text{ }^\circ\text{C}$. The condensation rate in the tubes increases with increasing ΔT_{app} , resulting in greater

vapor velocities and steam-side losses. Since the losses are proportional to the square of the velocity, the difference between the inlet losses in tubes with different loss coefficients diverges with increasing ΔT_{app} . The required additional vapor flow therefore increases along with the approach temperature difference.

5.2.2 Row effect requirements

As discussed previously, different condensation rates in subsequent tube rows in the multi-row primary condenser heat exchanger bundles lead to additional vapor flow requirements in the downstream rows. Slight variations in the inlet loss coefficients of corresponding tubes in different rows also play a role in exacerbating the row effect.

Figure 5.4 shows the additional vapor flow required in the primary condenser units to prevent backflow due to row effects only.

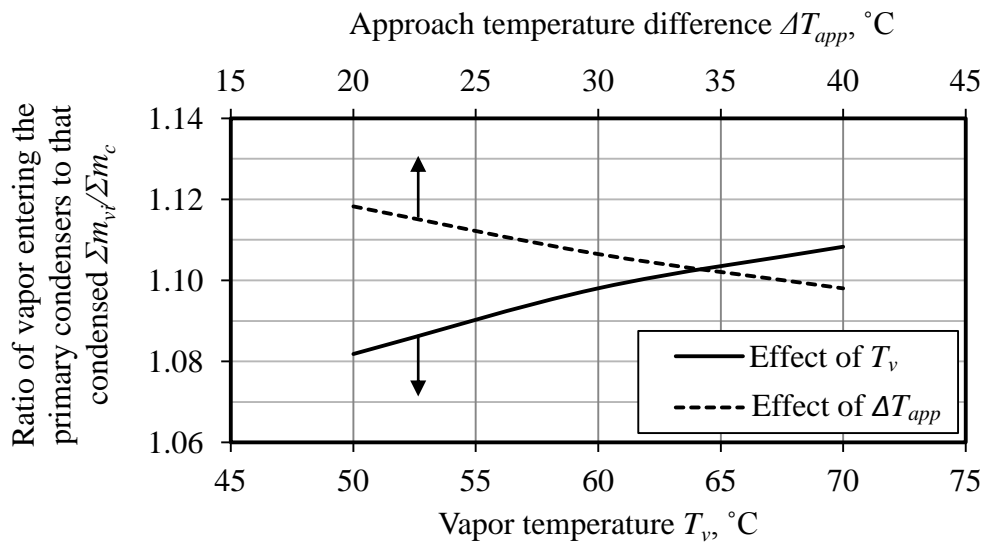


Figure 5.4: Additional vapor flow required in the primary condensers to overcome row effects

The additional flow requirement of between 8 % and 12 % of the condensation rate in the primary condensers is roughly double the requirement to overcome inlet loss coefficient distributions. This requirement increases with increasing vapor temperature but decreases with increasing approach temperature difference

in this case. The reason for these trends is illustrated in Figure 5.5 where it can be seen that the condensation rates in the first and second tube rows diverge with increasing vapor temperature and converge with increasing approach temperature difference. Diverging condensation rates lead to diverging losses and subsequently additional vapor flow requirements, and vice versa.

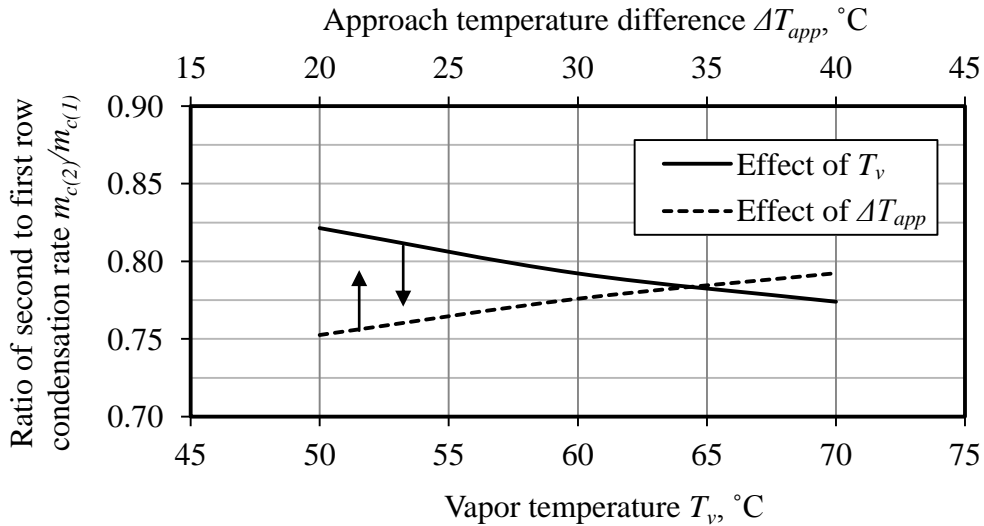


Figure 5.5: Ratio of second row to first row condensation rate

5.2.3 Total dephlegmator requirement under ideal operating conditions

The total additional vapor flow required in the primary condensers can be determined by superimposing the requirements to overcome inlet loss coefficient distributions and row effects as shown in Figure 5.6. The dephlegmator must provide between 14 % and 17 % of the total condensation rate in all five primary condensers to prevent vapor backflow.

The corresponding fraction of the dephlegmator capacity required to provide the total necessary additional vapor flow in the primary condensers is shown in Figure 5.7. With its shorter finned tubes, the dephlegmator has roughly 85 % of the heat transfer potential of a primary condenser cell. The 17 % additional vapor flow requirement therefore accounts for approximately $(17 \times 5)/0.85 = 100$ % of the dephlegmator capacity in the worst case. Depending on the operating condition, the dephlegmator capacity may be thus be fully utilized under ideal

operating conditions and there is no safety margin to account for non-ideal primary condenser operation.

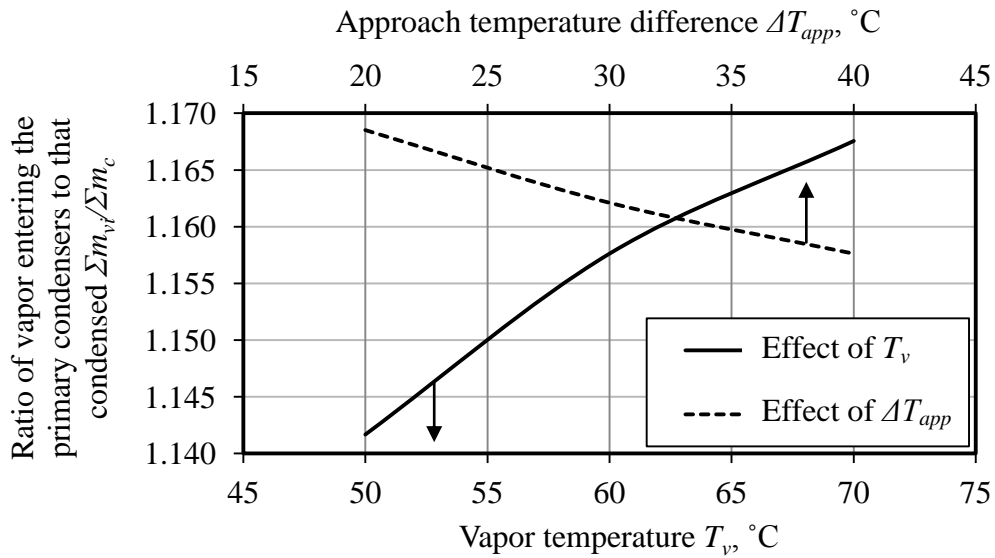


Figure 5.6: Total additional vapor flow requirement to prevent backflow in the primary condensers

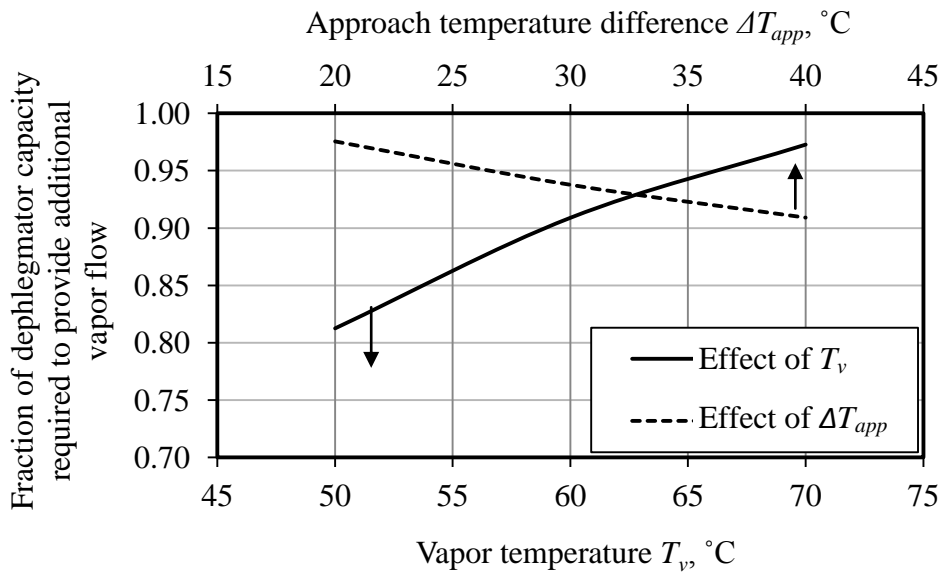


Figure 5.7: Fraction of the dephlegmator capacity required to provide sufficient additional primary condenser vapor flow

The design condition for the particular ACC considered here is $T_v = 60$ °C at $T_a = 20$ °C ($\Delta T_{app} = 40$ °C). At this condition, 91 % of the dephlegmator capacity

is required to prevent backflow in the primary condensers under ideal operating conditions. At off-design operating points (high T_v and/or low ΔT_{app}) the demand on the dephlegmator may approach 100 %. This is undesirable since any non-ideal operating conditions in the primary condensers, which are highly likely at off-design operating points, may then cause the additional vapor flow requirements to exceed the dephlegmator capacity; resulting in backflow in the primary condensers.

As mentioned in Section 5.2.2, the additional vapor flow required to overcome row effects is roughly double that required to account for inlet loss coefficient distributions in this particular case. The 8 % to 12 % additional primary condenser flow requirement identified in Section 5.2.2 translates to between 45 % and 70 % of total dephlegmator capacity. It therefore stands to reason that the greatest potential strategy for reducing dephlegmator loading would be to minimize row effects.

The demand on the dephlegmator to cope with row effects in the primary condensers can be mitigated in one of three ways:

- a) Eliminating the row effect altogether by using a single tube row heat exchanger. As mentioned in Section 2.3, advances in tube technology have resulted in this strategy becoming increasingly popular in modern applications.
- b) Further decreasing the difference in condensation rate between tubes in subsequent rows of the multi-row heat exchanger. As mentioned previously, this is most often accomplished by increasing the heat transfer effectiveness of the downstream tube row. In some cases, however, further attempts to enhance the second row heat transfer effectiveness by decreasing fin pitch is not practical and may lead to excessive air-side pressure losses that act in opposition to the enhanced heat transfer characteristics.
- c) Affecting different steam-side loss characteristics such that the steam-side pressure change over tubes in subsequent rows converges despite different condensation rates. Decreasing the losses in the upstream row is the most

attractive option of achieving such a change in steam-side losses. One method of achieving this is to round the inlets of the tubes in the upstream rows more than those in the downstream rows so that the inlet losses in the former are decreased. Such a modification is examined for the dephlegmator in Section 5.3.3.

The use of single-row primary condenser bundles holds the greatest potential for reducing the demands on the dephlegmator. By eliminating the row effect in the primary condensers, dephlegmator loading can be reduced by up to 70 %. The resultant large margin of safety to cope with non-ideal operation is highly desirable in light of the well documented negative effects of wind on fan performance and recirculation at large ACCs (see for example: Goldschagg et al., 1997; Meyer, 2005; Maulbetsch and DiFilippo, 2007; and Gao et al., 2009).

5.3 Vapor backflow in a conventional dephlegmator

In the case of a multi-row heat exchanger bundle, the dephlegmator itself is subject to row effects. The ejector, connected to the dephlegmator collecting header to remove the non-condensable gases, must therefore also eject sufficient vapor to prevent backflow in the upstream dephlegmator tube row.

Consider a pair of dephlegmator tubes as shown in Figure 5.8. An amount of vapor and entrained non-condensable gas enters each tube ($m_{vi(1)} + m_{nc(1)}$ and $m_{vi(2)} + m_{nc(2)}$ respectively). The vapor is condensed in the tubes and the non-condensables collect in the combining header where they are removed in the ejector stream (m_{ej}). As for the example described in Section 5.1, if complete condensation were to take place (i.e. $m_{vo(2)} = 0$ kg/s) with both tube rows operating at full effectiveness ($L_{bf} = 0$ m), then the steam-side pressure drop over the respective tubes would be different, which cannot be. Subsequently, sufficient additional vapor must be drawn through the downstream tube ($m_{vo} > 0$ kg/s) or vapor backflow will occur in the upstream tube. The ejector is the final component downstream of the dephlegmator tubes and must therefore facilitate the necessary additional vapor flow.

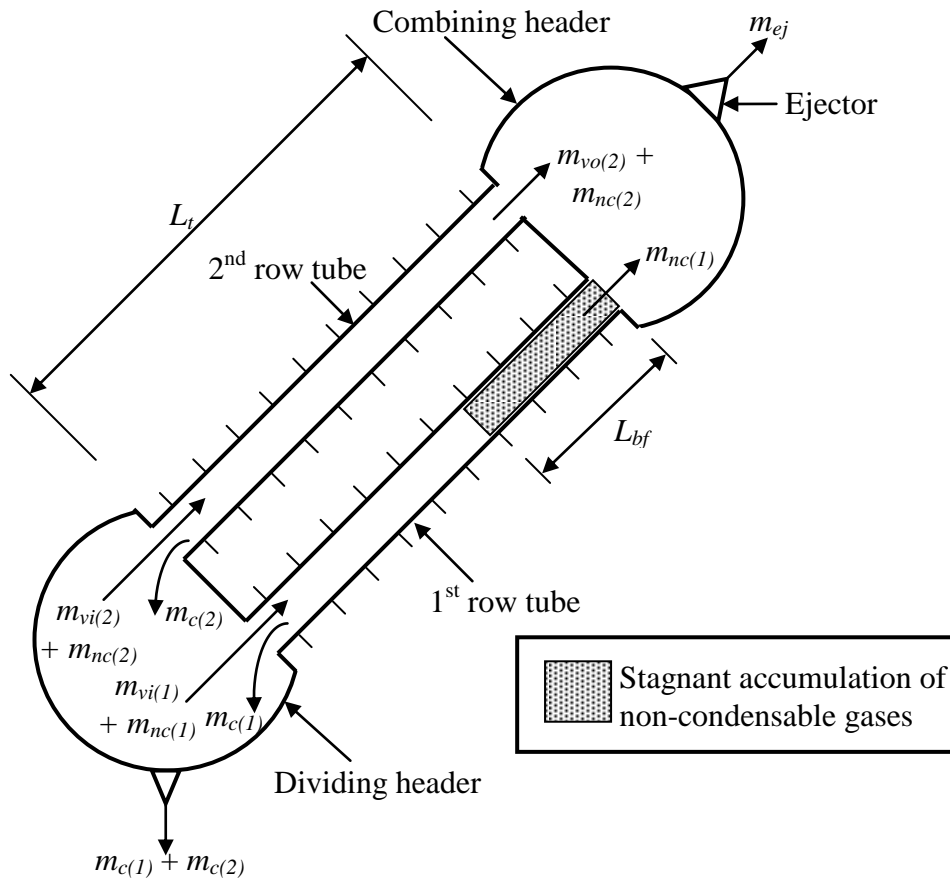


Figure 5.8: Dephlegmator tubes with backflow

Vapor backflow in the dephlegmator is highly undesirable as the subsequent reduction in dephlegmator suction, due to the reduced heat transfer surface area, may become severe enough to cause backflow in the primary condensers as well.

The following sections address the adequate sizing of the ejector to prevent backflow in a two-row dephlegmator unit (Section 5.3.1). The implications of insufficient ejector suction are examined in Section 5.3.2. Finally, the use of different tube inlet roundings is discussed as a potential method of reducing ejector loading in a multi-row dephlegmator (Section 5.3.3).

5.3.1 Required ejector capacity

The ejector capacity required to prevent backflow in the dephlegmator of the ACC under consideration is shown in Figures 5.9 and 5.10 as a function of vapor temperature and approach temperature difference respectively.

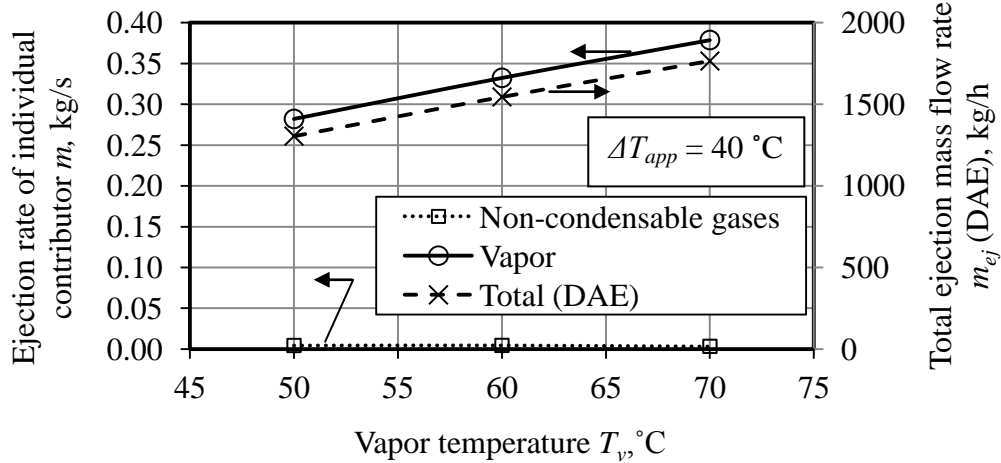


Figure 5.9: Required ejector suction as a function of vapor temperature

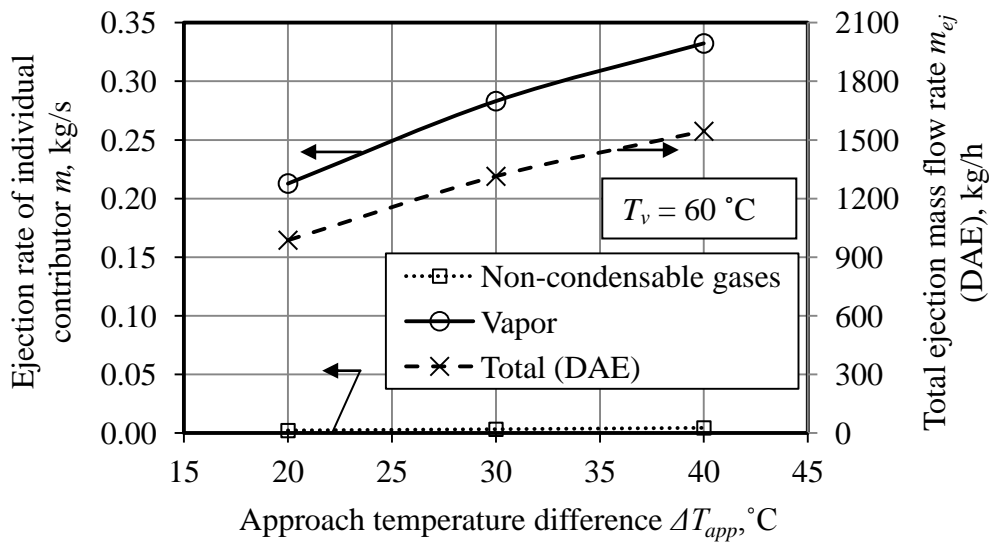


Figure 5.10: Required ejector suction as a function of approach temperature difference

In these figures, the mass flow rate of vapor and air to be ejected are represented separately along with the total dry air equivalent (DAE) ejection mass flow rate. A

sample calculation showing the derivation of these results is included in Appendix E. The calculation assumes a uniform inlet loss coefficient distribution amongst the dephlegmator tubes (see Section 4.4.2) and a non-condensable gas concentration of $1:10^4$ (i.e. 1 kg of non-condensables per 10^4 kg of vapor) based on the steam turbine outlet condition.

It is evident in Figures 5.9 and 5.10 that the vapor that must be ejected accounts for the vast majority of the required ejector capacity. Changing the assumption of a non-condensable gas concentration of $1:10^4$ based on the turbine condition, even by several orders of magnitude, will have little effect on the results. The demand on the ejector increases with increasing vapor temperature as well as with increasing approach temperature difference.

The ejector requirement increases with vapor temperature as a result of the increasing difference in condensation rate between subsequent tube rows, as described in Section 5.2.2. The influence of approach temperature difference on the ejector requirement is simply due to the greater amount of steam entering the tubes as this temperature difference increases. Even though the row effect diminishes somewhat with increasing ΔT_{app} (see Section 5.2.2 and Figure 5.4), the total amount of vapor to be ejected still rises by virtue of the growing condensation rate.

The predicted ejector capacity requirements shown in Figure 5.9 and 5.10 are compared to the performance characteristic of a practical holding ejector (the ejector designed to remove non-condensables during normal operation) in Figure 5.11. The characteristic of a typical ACC holding ejector is used here as an illustrative example. Two holding ejectors are specified per ACC street such that the demand per ejector is half of the values shown in Figures 5.9 and 5.10. Figure 5.11 shows the ejector in question to be incapable of meeting the suction requirements to prevent vapor backflow from occurring in the dephlegmator. Although only an illustrative example, practical experience has shown this to indeed be the case at several operating ACCs.

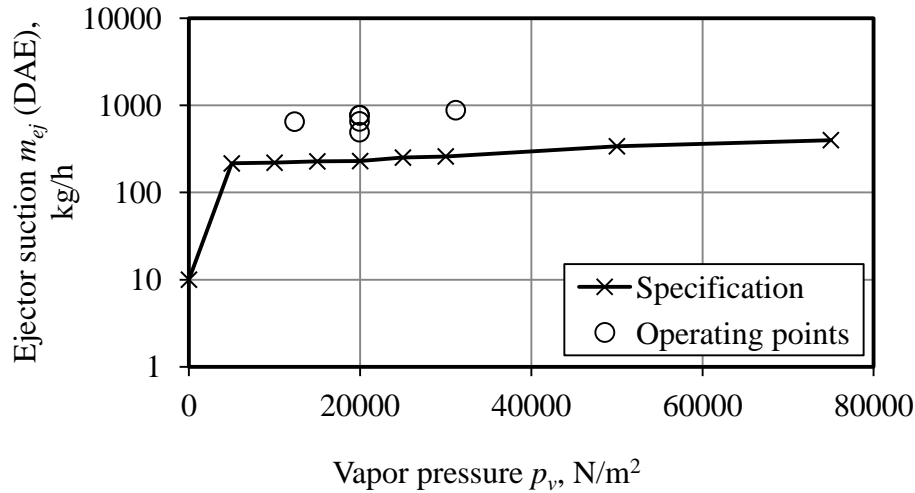


Figure 5.11: Comparison of required and available ejector capacity

Consider for example Figure 5.12, which shows a thermographic image of operating condenser units in an existing ACC.

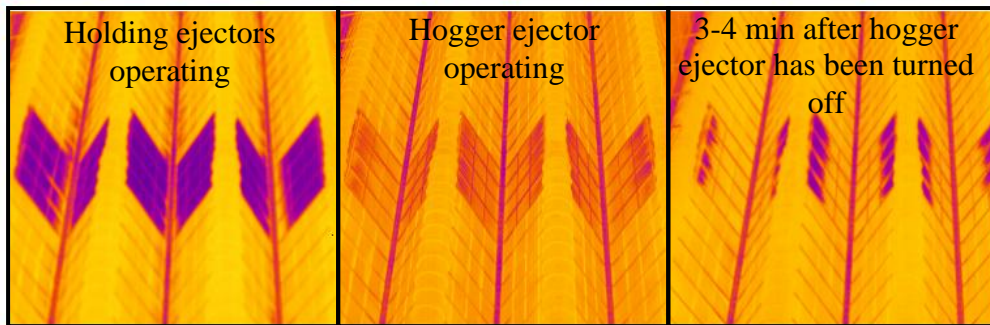


Figure 5.12: Thermographic imagery of an operating ACC street with severe accumulation of non-condensable gases in the dephlegmator

The purple regions, found only in the dephlegmator unit, indicate regions of low tube surface temperature. These regions are caused by the formation of dead zones due to the accumulation of non-condensable gases in the dephlegmator tubes. The case shown in Figure 5.12 is an extreme example where excessive air leakage into the ACC was experienced due to tube damage in the primary condensers. The holding ejectors are not sized to handle excessive leakage and are thus incapable of preventing the formation of dead zones in this case (left-most image in Figure 5.12). While out of the ordinary, this scenario nonetheless

illustrates the potential for ACC heat transfer effectiveness reduction due to inadequate ejector performance. When the larger hogger ejector - designed to flush the system of non-condensable gases and create sufficient vacuum during plant start-up - is in operation, the ejection rate is significantly enhanced and the non-condensable gases are removed resulting in the dephlegmator operating effectively (middle image). As soon as the hogger ejector is turned off, backflow is re-established in the dephlegmator due to the inadequate holding ejector capacity.

The effect of an undersized ejector on the severity of non-condensable gas accumulation in a dephlegmator during normal operation is discussed in the following section.

5.3.2 Backflow trends in a multi-row dephlegmator due to inadequate ejector performance

For the dephlegmator/ejector combination considered in this study, the ejector was shown to be undersized (see Figure 5.11) and backflow will occur in the dephlegmator tubes. The severity of vapor backflow due to the inadequate ejector suction is shown in Figure 5.13. Appendix E illustrates the method used to determine the extent of the vapor backflow by means of a sample calculation.

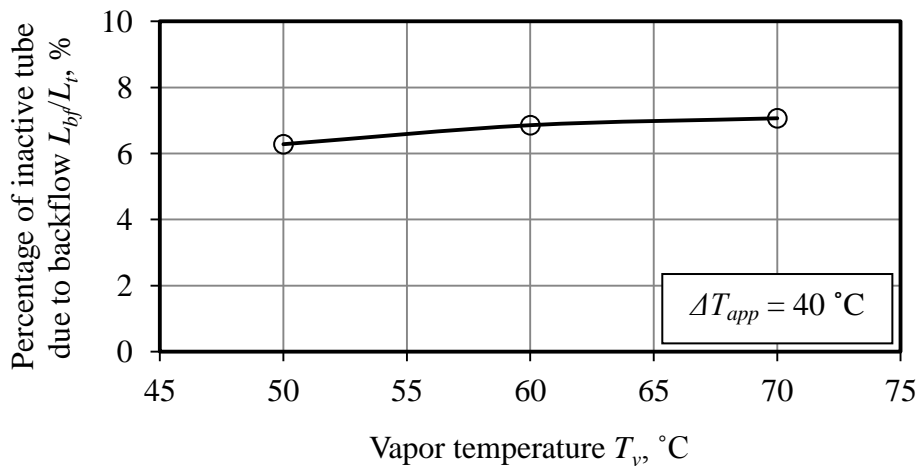


Figure 5.13: The effect of inadequate ejector sizing on backflow in a conventional dephlegmator

According to Figure 5.13, in the worst case, backflow in the first row of the dephlegmator may extend to a distance equivalent to 7 % of the tube length. This corresponds to a loss in heat transfer rate of approximately 2 % for the entire dephlegmator unit (taking into account that a portion of the second row tubes, with greater heat transfer surface area per unit length, is now exposed to cooler air).

In light of the results shown in Figures 5.7 and 5.13 it seems that, despite loss in efficiency due to backflow, the dephlegmator is still capable of providing sufficient suction to protect the primary condenser tubes from experiencing backflow under ideal operating conditions. Under non-ideal operating conditions, however, the inadequacies of an under-sized ejector will be further exposed and the operation of the primary condensers may be jeopardized. Careful examination of the left-most image in Figure 5.12 provides an example of such a situation. Here, regions of lower temperature are visible at the outlets of some of the primary condenser tubes. This is evidence of non-condensable gas accumulation in these tubes due to insufficient ejector capacity.

As mentioned in Section 5.2.3, it is possible to reduce row effects by one of three methods. Applied in the dephlegmator, any one of these three methods would result in reduced ejector loading. The benefits of single-row heat exchanger bundles with regards to dephlegmator loading concerns are relevant to ejector loading as well. By eliminating row effects in the dephlegmator itself, the vapor component of the ejection mixture is theoretically eliminated entirely. In practice, a small amount of excess vapor will always be ejected (regardless of the bundle configuration) to account for non-ideal dephlegmator operation (non-uniform air flow and temperature distributions for example), and to prevent high concentrations of non-condensable gases in the final portion of the heat exchanger tubes since high non-condensable concentrations have an adverse impact on heat transfer rates (Kröger, 2004).

Increasing the rounding of the tube inlets in the upstream tube row is discussed in the following section.

5.3.3 *The effect of inlet rounding on backflow in a multi-row dephlegmator*

According to Fried and Idelchick (1989) contraction loss coefficients at the inlet of round tubes can be reduced by rounding the edges of tubes as shown in Figure 5.14. Fried and Idelchick’s data was adapted to scale the inlet loss coefficients for the flattened tubes in the dephlegmator bundles as shown in Table 5.1.

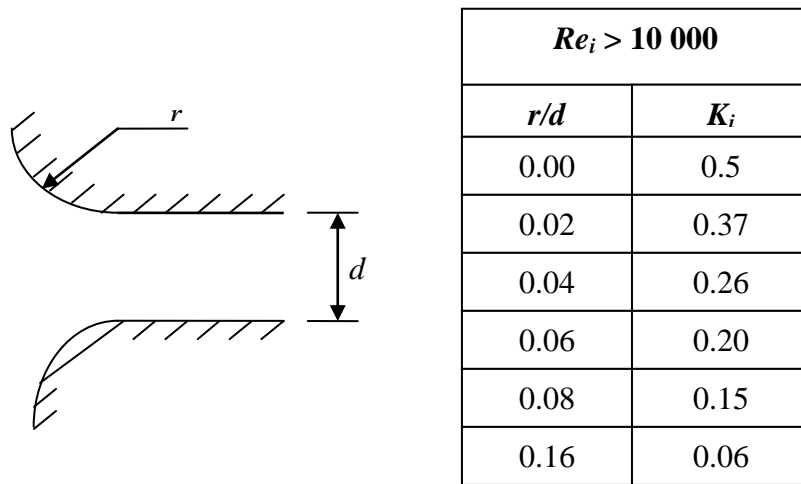


Figure 5.14: Contraction loss coefficient for a rounded inlet (Fried and Idelchick, 1989)

Table 5.1: The effect of inlet rounding on the contraction loss coefficient

r/d_i	0	0.02	0.04	0.06	0.08	0.16
$K_c/K_{c(90)}$	1.0	0.74	0.52	0.40	0.30	0.12

The effect of rounding the inlets of the upstream tubes on the severity of non-condensable gas accumulation in the dephlegmator is illustrated in Figure 5.15. The extent of vapor backflow can be reduced by more than 60 % relative to the theoretical case of $r/d_i = 0$ (in practise the tube-to-header welding seam creates a small rounding effect) for large inlet roundings. In the dephlegmator considered here, the hydraulic diameter of the tube is $d_e = 0.02975$ m and the tube width is

$W_i = 0.017$ m. An inlet rounding of $r/d = 0.08$ would require $r = 0.002$ mm which can be readily achieved in this case.

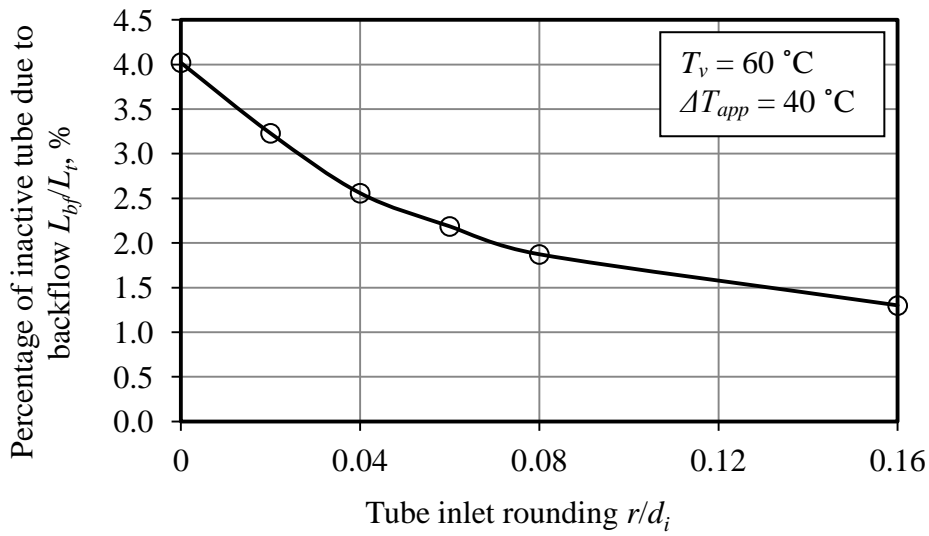


Figure 5.15: The effect of inlet rounding in the upstream tubes on vapor backflow

Considering the data presented in Figure 5.15, the severity of backflow can be decreased by roughly 50 %. While this in itself is not sufficient to overcome the accumulation of non-condensable gases in the dephlegmator, it does present a simple method of reducing ejector requirements in multi-row dephlegmators.

6. HYBRID (DRY/WET) DEPHLEGMATOR

6.1 Introduction

ACCs are known to experience reduced cooling effectiveness at high ambient temperatures and dry-cooled plants often experience performance penalties on hot days. In some cases dry/wet or wet/dry condensers are used in an attempt to provide improved cooling performance while still using less water than an all-wet evaporative cooling tower. Such condensers utilize characteristics of both dry- and wet-cooling systems arranged in a variety of configurations that differ markedly in terms of capital cost and operating capabilities. Dry/wet or wet/dry systems offer a performance advantage over all-dry systems in that they are not subject to the dramatic performance reduction experienced during hot periods. Furthermore, they typically have an overall water consumption rate of between 20 % and 80 % of an all-wet system of equivalent capacity (Maulbetsch, 2002). However, the initial capital costs, as well as the operating and maintenance costs of these systems are relatively high since they consist of both dry- and wet-cooling towers. Utilization of the wet-cooling tower only during short periods of high ambient temperatures tends to reduce the lifecycle economic viability of these cooling systems (Maulbetsch, 2002).

In addition to dry/wet or wet/dry condensers, strategies that attempt to enhance the performance of ACCs during periods of high ambient temperatures are sometimes employed. Two of the most common strategies are deluging of the finned-tube heat exchanger bundles and adiabatic spray cooling of the inlet air. In deluge systems, the air-side of the heat exchanger is flooded with cooling water causing a significant increase in the air-side heat transfer coefficient (Kröger, 2004). Unfortunately, wetting the finned tubes carries a high risk of unacceptable fouling and corrosion. Adiabatic spray cooling involves spraying a fine water mist into the air upstream of the heat exchanger. The air is subsequently cooled to near its wet-bulb temperature as a result of evaporation. Maulbetsch and DiFilippo (2003) investigated various spray nozzles for use in this method and

found that a small amount of water is always deposited on the finned tubes, resulting in an increased risk of corrosion. Undesirable rain-back, which causes surface and ground water contamination, was also found to be unavoidable.

Deliberate over-sizing of the ACC has also been employed in some cases as a strategy to address the issue of reduced cooling capacity at high ambient temperatures. The rationale behind this approach is that the additional performance, and subsequent profit gains associated with over-sizing the ACC, will eventually outweigh the substantial additional capital and operating costs. A case study investigating the economical feasibility of this approach at two sites in the United States found over-sizing to be impractical (Boulay et al., 2005).

Heyns and Kröger (2012) propose a novel hybrid (dry/wet) dephlegmator (HDWD) concept for use in ACCs. This concept involves replacing only the conventional all-dry dephlegmator unit in an ACC with a hybrid component, capable of operating in wet or dry mode. In their paper, Heyns and Kröger compared the performance of a steam turbine cooled by a conventional all-dry ACC to the performance of a turbine with the same ACC but using the HDWD. The effect of spray cooling enhancement and over-sizing the ACC by 33 % on turbine performance was also investigated. The decrease in turbine output at high ambient temperatures experienced by the air-cooled plant could be mitigated somewhat by over-sizing the ACC, employing spray cooling enhancement, or replacing the conventional dephlegmator with a HDWD. The turbine output benefits were similar for all cases. The HDWD, however, will be considerably less expensive than over-sizing the ACC to such an extent, and was shown to consume roughly 20 % less water than spray cooling enhancement.

The HDWD concept therefore has the potential to measurably enhance the thermal performance of an ACC during hot periods while consuming only a relatively small amount of water. In addition, it is estimated that the capital cost of the proposed HDWD will not be significantly more than that of a conventional air-cooled dephlegmator cell. The cost of an ACC equipped with a HDWD will

therefore be similar to that of its all-dry counterpart and the HDWD offers a measurable economic advantage over existing dry/wet systems.

This chapter begins by describing the HDWD concept (Section 6.2). Various configurations of the hybrid dephlegmator concept are evaluated in Section 6.3 and recommendations are made regarding specific design parameters and configurations for best performance. The effect of the HDWD on turbine output is examined in Section 6.4.

6.2 Description of the HDWD concept

Heyns and Kröger (2012) proposed that the conventional air-cooled dephlegmator unit be replaced by a forced draft hybrid (dry/wet) dephlegmator. The HDWD consists of a dry first stage and a second dry/wet stage connected in series in the same condenser unit. The concept is illustrated schematically in Figure 6.1.

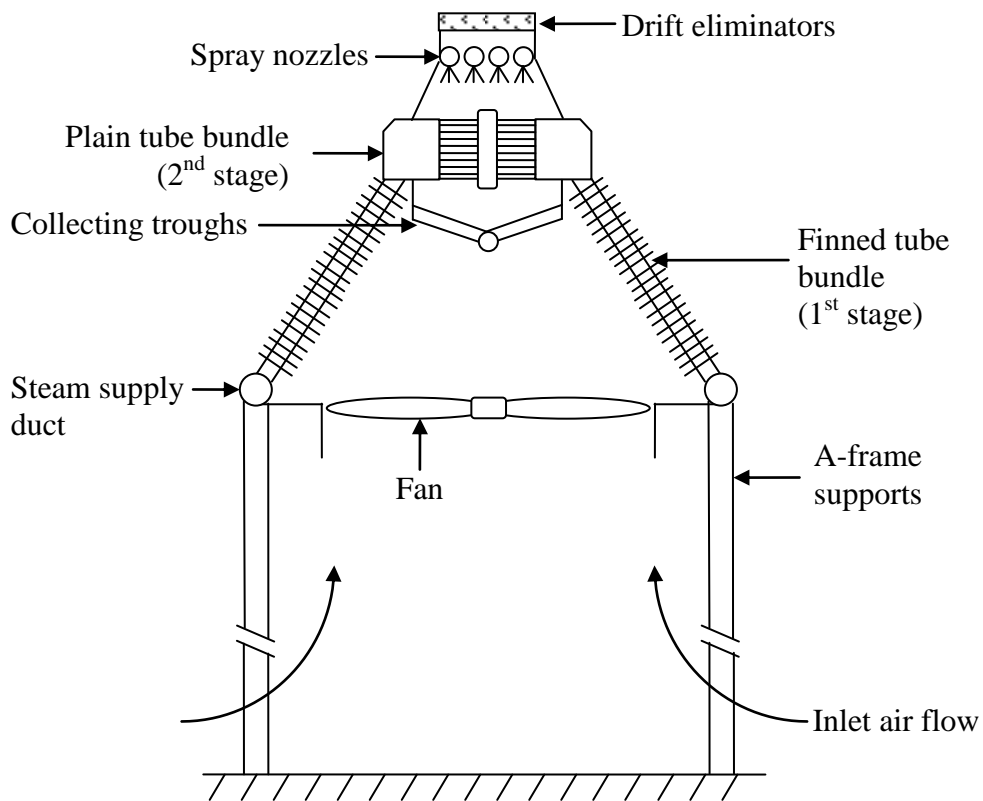


Figure 6.1: Schematic of the forced draft HDWD concept

The first stage of the HDWD is an air-cooled condenser with inclined finned tubes, similar to those used in the conventional A-frame configuration. The tubes in this stage are shorter than in the conventional dephlegmator to create space for the dry/wet second stage.

The second stage consists of a near horizontal, dry/wet heat exchanger. The tubes are plain, or smooth on the outside (no fins), and are made from galvanized steel or a similar corrosion resistant material. This stage can be operated either dry, as an air-cooled condenser, or the air-side surface of the plain-tube bundle can be deluged with water to operate as an evaporative condenser. The use of plain tubes reduces the risk of fouling and corrosion during deluge operation. The deluge water is collected under the tube bundle in droplet collecting troughs. Drift eliminators installed above the second stage reduce water loss due to droplet entrainment in the air flow.

The operating mode of the second stage can be controlled in response to changing ambient conditions and/or demand/price patterns. During periods of low ambient temperature, when air-cooling is sufficient, the second stage is operated dry. During hotter periods, deluge water is sprayed over the plain tubes and the second stage is operated as an evaporative condenser. Similarly, during low demand periods when the price of electricity is low, the HDWD is operated in dry mode. During peak demand periods, the HDWD can be operated wet to provide additional dispatchable clean power (no additional fuel needs to be burnt at fossil fuelled plants) at a high price.

6.3 Performance evaluation

A detailed analytical evaluation of the performance of the HDWD was carried out in this study. The purpose of the evaluation was to identify a second stage configuration that provides the best overall performance. Heat transfer rate, steam-side pressure drop and ejector loading were identified as critical performance measures. Water consumption was also considered. The best configuration would offer a high heat transfer rate, low steam-side pressure drop,

and minimal ejector loading. The air-side pressure drop was found to be similar for all configurations and was therefore not considered as a selection criterion.

Eleven second stage tube bundle configurations were considered. These configurations are described in Table 6.1. The bundle configurations were identified based on geometrical constraints and the availability of suitable experimental data regarding critical performance parameters. In all cases, the configuration of the first stage is the same, with inclined finned tubes shortened from the conventional length of $L_{t1(conv)} = 7.52$ m to $L_{t1(HDWD)} = 4.5$ m.

Table 6.1: HDWD second stage tube bundle configurations

Config.	Tube outside dia. d_o , m	Tube rows n_r	Tubes per row n_{tr}	Vapor passes n_{vp}	Tube rows per pass n_{tp} (1 st /2 nd /3 rd)
A	0.0381	16	156	3	12/3/1
B	0.0381	16	156	2	14/2
C	0.0381	16	156	2	15/1
D	0.0381	16	156	1	16
E	0.019	16	314	3	12/3/1
F	0.019	16	314	2	14/2
G	0.019	16	314	2	15/1
H	0.019	16	314	1	16
I	0.019	25	314	3	20/4/1
J	0.019	25	314	2	20/5
K	0.019	25	314	1	25

6.3.1 Heat transfer rate

Calculation of the heat transfer performance of a HDWD requires simultaneous solution of the energy and draft equations. These equations are described in the following sections for both dry and wet operation of the HDWD second stage.

An iterative solution procedure is used to solve the controlling equations. Initial assumptions are made regarding the solution parameters for the system. The calculations are then executed and the results compared to the initial assumptions. The problem is solved once the calculation results and initial assumptions converge sufficiently. A detailed sample calculation is included in Appendix F.

6.3.1.1 Energy equation

The energy equation expresses the balance between the air- and steam-side heat transfer rates. For the energy equation to be solved the heat transferred from the condensing vapor must equal the heat absorbed by the passing air.

In the first stage of the HDWD, the heat transfer rate (Q) between the condensing steam inside the inclined finned tubes (one or more tube rows) and the passing ambient air is described by Equation (6.1).

$$Q = \sum_{i=1}^{n_r} m_a c_{pa(i)} (T_{ao(i)} - T_{ai(i)}) = \sum_{i=1}^{n_r} m_a c_{pa(i)} e_{(i)} (T_v - T_{ai(i)}) \quad (6.1)$$

Here $T_{ai(i)}$ and $T_{ao(i)}$ are respectively the air inlet and outlet temperatures for tube row i , m_a is the air mass flow rate through the heat exchanger bundle, and c_{pa} is the specific heat of the air stream. T_v is the vapor temperature and $e_{(i)}$, calculated from Equation (6.2), is the heat transfer effectiveness of the finned-tube bundle.

$$e_{(i)} = 1 - \exp(-UA_{(i)}/m_a c_{pa(i)}) \quad (6.2)$$

The overall heat transfer coefficient between the steam and the air, $UA_{(i)}$, is primarily dependant on the air-side heat transfer characteristics of the finned-tube bundles (see Appendix A.1). The air-side heat transfer resistance is usually more than an order of magnitude greater than the steam-side heat transfer resistance for the flattened finned tube (in this case, the effective air-side heat transfer coefficient is less than 10 % of the steam-side heat transfer coefficient). The thermal resistance of the condensate film is therefore much smaller than the air-side resistance and $UA_{(i)}$ is approximated considering only the experimentally

determined characteristic air-side heat transfer parameter, Ny_a , as shown in Equation (6.3).

$$UA_{(i)} = k_{a(i)} Pr_{a(i)}^{0.333} n_b A_{fr(i)} Ny_{a(i)} \quad (6.3)$$

In Equation (6.3), k_a is the thermal conductivity of the air, Pr_a is the Prandtl number, and $A_{fr(i)}$ is the effective frontal area of a lone tube bundle.

As in the first stage, for dry operation of the second stage of the HDWD, the heat transfer rate is dominated by the air-side heat transfer coefficient. For a plain tube, the air-side heat transfer coefficient is even smaller than in the finned tube case and the air-side resistance to heat transfer is thus greater. The energy equation is again described by Equations (6.1) and (6.2).

For plain circular tubes in cross-flow, the local air-side heat transfer coefficient varies around the tube circumference due to variations in the boundary layer thickness and behaviour. Churchill and Bernstein (1977) recommend Equations (6.4) – (6.6) for the average Nusselt number of a horizontal cylinder in cross-flow with $Pr > 0.5$.

$$Nu = 0.3 + \frac{0.62 Re^{1/2} Pr^{1/3}}{\left[1 + (0.4/Pr)^{2/3}\right]^{1/4}}; \quad Re < 10^4 \quad (6.4)$$

$$Nu = 0.3 + \frac{0.62 Re^{1/2} Pr^{1/3}}{\left[1 + (0.4/Pr)^{2/3}\right]^{1/4}} \left[1 + \left(\frac{Re}{282 \times 10^3}\right)^{1/2}\right]; \quad 2 \times 10^4 < Re < 4 \times 10^5 \quad (6.5)$$

$$Nu = 0.3 + \frac{0.62 Re^{1/2} Pr^{1/3}}{\left[1 + (0.4/Pr)^{2/3}\right]^{1/4}} \left[1 + \left(\frac{Re}{282 \times 10^3}\right)^{5/8}\right]^{4/5}; \quad 4 \times 10^5 < Re < 5 \times 10^6 \quad (6.6)$$

The air-side heat transfer coefficient also varies with position in the bundle. Equations (6.4) – (6.6) can be used to calculate the heat transfer coefficient for the first or upstream tube in the bundle. An average Nusselt number for the bundle is then calculated using the arrangement factor given by Mills (1999) which takes into account the bundle configuration. Equation (6.7) describes this arrangement

factor, with d_o the tube outside diameter and P_l the longitudinal tube pitch, while Equation (6.8) illustrates its application.

$$\Phi = 1 + 2d_o/3P_l \quad (6.7)$$

$$Nu_{avg} = \Phi Nu_1 \quad (6.8)$$

Zukauskas and Ulinskas (1988) and Grimison (1937) also give correlations for the average Nusselt number of a plain-tube bundle in cross-flow. For the tube bundle under consideration, these correlations predict similar values for the average Nusselt number. Churchill and Bernstein's correlation, multiplied by Mills' arrangement factor, gives a more conservative value (roughly 10 % smaller than the aforementioned correlations) and Equations (6.4) – (6.8) were therefore used in this analysis.

The average air-side heat transfer coefficient for the plain-tube bundle is subsequently calculated using Equation (6.9) where k_{af} is the thermal conductivity of air evaluated at the mean film temperature through the bundle.

$$h_{avg} = Nu_{avg} k_{af} / d_o \quad (6.9)$$

Since the air-side heat transfer coefficient dominates the heat transfer rate between the condensing steam and the passing air for dry operation of the HDWD, the overall heat transfer coefficient for the second stage tube bundle can be approximated as shown in Equation (6.10) with A_a the total air-side heat transfer surface area.

$$UA_{2nd} = h_{avg} A_a \quad (6.10)$$

When the second stage of the HDWD operates as an evaporative condenser (wet mode), the air-side heat transfer coefficient is significantly enhanced relative to dry operation due to the wetting of the plain tubes. In this case, the second stage heat transfer rate is determined by the air-side coefficients for heat and mass transfer between the deluge water film and the ambient air, as well as the heat

transfer coefficient for condensation inside the round tube. A simplified Merkel-type analysis, described in Kröger (2004), was used in the evaluation of the wet HDWD second stage.

The energy equation for the wet second stage is described in Equation (6.11) where i_{mao} and i_{mai} are enthalpies of the air-water vapor mixture down- and upstream of each tube respectively.

$$Q = \sum_{i=1}^{n_s} m_a (i_{mao} - i_{mai}) = \sum_{i=1}^{n_s} m_a c_{pa(i)} e_{(i)} (T_v - T_{ai(i)}) \quad (6.11)$$

The heat transfer effectiveness, $e_{(i)}$, is again calculated from Equation (6.2) with the overall heat transfer coefficient between the steam and the air described by Equation (6.12).

$$UA_{2nd} = n_b A_a \left[\frac{1}{h_w} + \frac{d_o}{d_i h_c} + \frac{d_o \ln(d_o/d_i)}{2k_{wall}} \right]^{-1} \quad (6.12)$$

In Equation (6.12), d_i is the tube inside diameter, h_w is the heat transfer coefficient between the water film and the tube outer surface, and h_c is the condensation heat transfer coefficient inside the tube. The final term in Equation (6.12) represents the thermal resistance of the tube wall itself, with k_{wall} the thermal conductivity of the tube material (galvanized steel in this case).

Several correlations for the water film heat transfer coefficient are available in the literature. Mizushina et al. (1967), Niitsu et al. (1969) and Leidenfrost and Korenic (1982) express the film heat transfer coefficient as a function of the deluge water mass flow rate, while Parker and Treybal (1961) extended their correlation to include the effect of the deluge water temperature. Heyns (2009) experimentally investigated the performance characteristics of a plain-tube bundle similar to that considered here. He identified the deluge water flow rate as the primary parameter in determining the film heat transfer coefficient. Air mass flow rate and deluge water temperature were found to influence the coefficient to a lesser extent. Heyns compared his experimentally determined film heat transfer

coefficients to the widely cited correlation of Mizushina et al. (1967), shown in Equation (6.13), for air flow and deluge water mass flux ranges of $0.7 \text{ kg/m}^2\text{s} < G_a < 3.6 \text{ kg/m}^2\text{s}$ and $1.8 \text{ kg/m}^2\text{s} < G_w < 4.7 \text{ kg/m}^2\text{s}$ and water temperatures of $35 \text{ }^\circ\text{C} < T_{wm} < 53 \text{ }^\circ\text{C}$; and found there to be a good agreement.

$$h_w = 2102.9(\Gamma_m/d_o)^{1/3} \quad (6.13)$$

In Equation (6.13), Γ_m is the deluge water flow rate over half a tube per unit length.

Chato (1962) recommends Equation (6.14) for h_c when $Re_{vi} < 35000$.

$$h_c = 0.555 \left[\frac{g\rho_l(\rho_l - \rho_v)k_l^3 i'_{fg}}{\mu_l(T_v - T_{wall})d_i} \right]^{0.25} \quad (6.14)$$

In Equation (6.14), ρ_l , μ_l and k_l are respectively the density, dynamic viscosity and thermal conductivity of the liquid condensate in the tube. The vapor density is ρ_v . T_{wall} is the tube inner-wall temperature and the modified latent heat of vaporization, i'_{fg} , is calculated from Equation (6.15).

$$i'_{fg} = i_{fg} + 0.68 c_{pc} (T_v - T_{wall}) \quad (6.15)$$

The enthalpy of air downstream of a tube, i_{mao} in Equation (6.11), can be calculated from Equation (6.16) where i_{maswm} is evaluated at the mean deluge water temperature through the bundle.

$$i_{mao} = i_{maswm} - (i_{maswm} - i_{mai}) \exp(-NTU_a) \quad (6.16)$$

NTU_a is described by Equation (6.17) with h_d the mass transfer coefficient between the deluge water film and the passing air.

$$NTU_a = h_d A_a / m_a \quad (6.17)$$

Heyns (2009) found the air-water mass transfer coefficient in his experiments to be a function of both air and deluge water mass flow rate. This observation is

corroborated by Mizushina et al. (1967). The widely used correlation of Mizushina et al., shown in Equation (6.18), described Heyns' data well.

$$h_d = 5.5439 \times 10^{-8} Re_{avm}^{0.9} Re_{wm}^{0.15} d_o^{-1.6} \quad (6.18)$$

In Equation (6.18), Re_{avm} is the mean air Reynolds number through the bundle and Re_{wm} is the deluge water film Reynolds number.

The correlations for the air-water mass transfer rate presented by Parker and Treybal (1961) and Niitsu et al. (1969) are functions of the air mass flow rate only and were thus not considered in this study.

The equations presented in this section require a constant vapor temperature in each section of the HDWD. For dry operation of the HDWD, a constant vapor temperature is assumed throughout the entire HDWD. This assumption is valid during dry operation because the steam-side pressure changes through the HDWD are small enough that changes in vapor saturation temperature are negligible. It will be shown in Section 6.3.3.4, however, that when the HDWD operates as an evaporative condenser, the steam-side pressure change through the system is relatively large and the corresponding changes in vapor temperature through the system may have a noticeable impact on the HDWD heat transfer rate.

An iterative solution procedure accounts for the effects of such vapor temperature changes during wet operation of the HDWD. First, the pressure drop over each stage or pass in the HDWD is calculated based on a constant vapor temperature through the entire system. These pressure drops are then used to calculate the pressure at the inlet and outlet of each stage/pass and a corresponding mean vapor pressure is determined. The heat transfer rate for each stage/pass is then recalculated based on the respective mean vapor temperatures and the results added to give the total heat transfer rate for the HDWD. The procedure described above is illustrated in the sample calculation of Appendix F.

6.3.1.2 Draft equation

Neglecting the small influence of atmospheric pressure and temperature changes with elevation, the draft equation simply represents the fact that the losses in mechanical energy experienced by the air as it flows through the HDWD must be overcome by the addition of mechanical energy from the fan. These energy losses and additions manifest respectively as decreases and increases in static pressure.

The mechanical energy added by the fan is determined from the fan performance characteristic which relates the fan static pressure rise (Δp_{Fs}) to the volume flow rate of air through the fan (see Appendix A.2). The air-side loss over an HDWD comprises primarily of losses over the heat exchanger bundles. Obstacles up- and downstream of the bundles and fan, such as support structures, collecting troughs, drift eliminators and screens add to the losses through the system.

The draft equation must be solved subject to the constraint of equal air-side pressure drop over the first and second stages of the HDWD as described in Equation (6.19).

$$\Delta p_{Fs} - (\Delta p_{ts} + \Delta p_{up/do}) = \Delta p_{a(1st)} = \Delta p_{a(2nd)} + \Delta p_{ct} + \Delta p_{de} \quad (6.19)$$

In Equation (6.19), $\Delta p_{a(1st)}$ and $\Delta p_{a(2nd)}$ represent the air-side losses over the first and second stage heat exchanger bundles respectively, the losses over the unit tower supports and obstacles up- and downstream of the fan are Δp_{ts} and $\Delta p_{up/do}$, while Δp_{ct} and Δp_{de} respectively represent the losses over the second stage droplet collecting troughs and drift eliminators.

The pressure drop over the first stage finned-tube heat exchanger is calculated as shown in Equation (6.20).

$$\Delta p_{a(1st)} = K_{\theta_t} \rho_{am} v_{am}^2 / 2 \quad (6.20)$$

Here ρ_{am} and v_{am} are the mean air density and velocity through the bundle. The overall loss coefficient for the finned-tube heat exchanger, K_{θ_t} , is described by

Equation (6.21), for a forced draft system, and Equation (6.22) for an induced draft system.

$$K_{\theta} = K_{he} + \frac{2}{\sigma_{min}^2} \frac{(\rho_{ai} - \rho_{ao})}{(\rho_{ai} + \rho_{ao})} + \frac{2\rho_{ao}}{(\rho_{ai} + \rho_{ao})} \left(\frac{1}{\sin\theta_m} - 1 \right) \left(\frac{1}{\sin\theta_m} - 1 + 2K_c^{0.5} \right) \quad (6.21)$$

$$+ \frac{2\rho_{ai}(K_{dj} + K_o)}{(\rho_{ai} + \rho_{ao})}$$

$$K_{\theta} = K_{he} + \frac{2}{\sigma_{min}^2} \frac{(\rho_{ai} - \rho_{ao})}{(\rho_{ai} + \rho_{ao})} + \frac{2\rho_{ai}\alpha_e}{(\rho_{ai} + \rho_{ao})} \quad (6.22)$$

In Equations (6.21) and (6.22), K_{he} is the loss coefficient for normal isothermal flow through the finned-tube bundle, and takes into account the contraction and expansion losses through the bundle under these conditions. The second term in Equations (6.21) and (6.22) accounts for acceleration effects through the bundle as a result of heat transfer to the air. The ratio of minimum to free stream flow area through the bundle is represented by σ_{min} while the air densities up- and downstream of the heat exchanger are respectively ρ_{ai} and ρ_{ao} . Losses due to turning of the flow as it leaves the inclined heat exchanger bundles in the forced draft configuration are represented by the third term in Equation (6.21). The fourth term in Equation (6.21) accounts for losses due to the turbulent decay of the jet after the bundles (K_{dj}) and losses during the final mixing process as the flow leaves the ACC (K_o) (Van Aarde and Kröger, 1993).

The overall loss coefficient for the finned-tube heat exchanger operating in an induced draft format, Equation (6.22), resembles that of its forced draft counterpart. In the induced draft case, however, the flow approaches the heat exchanger normally and the fan ejects the air without any jetting so that the third and fourth terms in Equation (6.21) can be neglected. A kinetic energy loss at the outlet of the ACC remains and is represented by the final term in Equation (6.22). Here, α_e is the kinetic energy correction factor which accounts for non-uniform

flow distributions. In this case it is assumed that the flow is indeed uniform and so $\alpha_e = 1$.

Relatively little published information is available for the prediction of the air-side pressure drop over a deluged tube bundle. Heyns (2009) and Kröger (2004) identify the correlation of Niitsu et al. (1969), shown in Equation (6.23), for the air-side pressure drop over a deluged plain-tube bundle.

$$\Delta p_{a(2nd-wet)} = 4.9 n_r P_l (m_{am}/A_c)^{1.85} (\Gamma_m/d_o)^{0.285} \quad (6.23)$$

In Equation (6.23), m_{am} is the mean air mass flow rate through the bundle, and A_c is the minimum flow air flow area. Equation (6.23) is valid for $2 \text{ kg/m}^2\text{s} \leq m_{am}/A_c \leq 6 \text{ kg/m}^2\text{s}$ and $1.3 \text{ kg/m}^2\text{s} \leq \Gamma_m/d_o \leq 3.5 \text{ kg/m}^2\text{s}$.

Dreyer (1988) conducted a literature survey of available air-side pressure drop correlations for evaporative condensers and identifies the correlations of Diehl and Unruh (1958), shown in Equations (6.24) and (6.25), as useful correlations for design purposes.

$$\frac{\Delta p_{ip}}{\Delta p_a} = 1.370042 + 44591.59 \varphi - \left(\frac{0.0000369198}{0.0001 + \varphi} \right); \quad 0 \leq \varphi \leq 0.007 \quad (6.24)$$

$$- 103378.776 \log_{10}(1 + \varphi)$$

$$\frac{\Delta p_{ip}}{\Delta p_a} = -0.00376946 + 0.0087965111 \varphi + \left(\frac{0.00261965}{0.001 + \varphi} \right); \quad 0.007 < \varphi \leq 1.0 \quad (6.25)$$

$$- 0.0052407713 \varphi^2$$

The parameter φ is defined in Equation (6.26).

$$\varphi = \frac{m_w}{(m_a + m_w \rho_a / \rho_w) Re_a^{0.5}} \quad (6.26)$$

The correlations of Niitsu (1969) – Equation (6.23) – and Diehl and Unruh (1958) – Equations (6.24) and (6.25) – are compared to Heyns' (2009) experimental data in Figure 6.2. Diehl and Unruh's correlation significantly under-predicts the air-

side pressure drop data for a deluged tube bundle of the type considered in this study and is therefore not suitable for use here. Niitsu's correlation over-predicts the air-side pressure drop data by approximately 30 % while giving the same trend in the relationship between this pressure drop and the air and water mass flow rates. The Niitsu correlation is therefore expected to give a conservative estimate of the air-side pressure drop over the deluged bundle in this case and is used in the absence of a more accurate correlation.

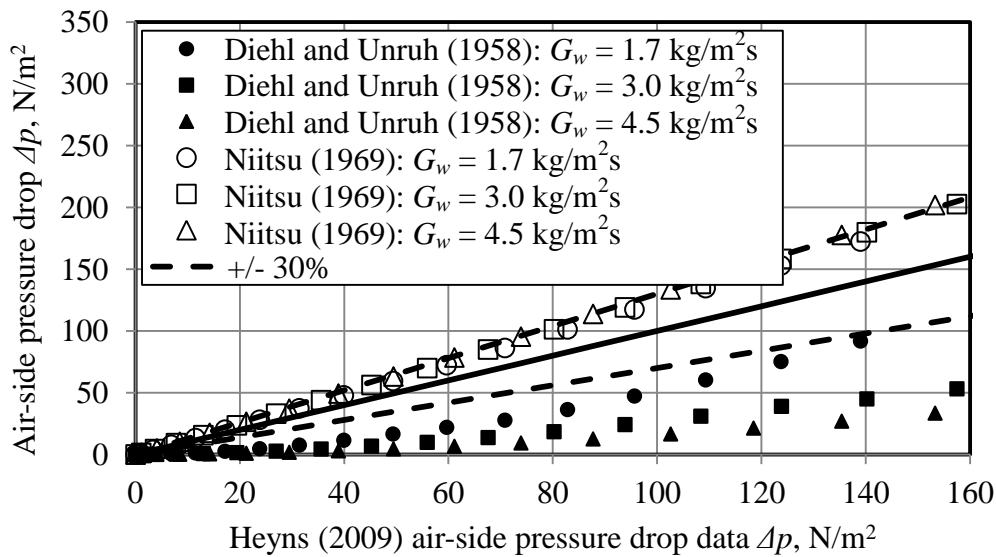


Figure 6.2: Comparison of air-side pressure drop correlations for a deluged tube bundle

Bertrand (2011) measured the pressure loss over droplet collecting troughs operating with water flow. He correlated his data with the expression shown in Equation (6.27).

$$\Delta p_{ct} = 1.563 G_w^{0.184} G_a^{1.693} \quad (6.27)$$

Kröger (2004) describes the loss coefficient for a particular drift eliminator as shown in Equation (6.28) with the characteristic flow parameter Ry described by Equation (6.29).

$$K_{de} = 27.4892 Ry^{-0.14247} \quad (6.28)$$

$$Ry = m_a / \mu_a A_{fr} \quad (6.29)$$

In Equation (6.29), μ_a is the dynamic viscosity of air.

The air-side pressure losses across the rain zone and spray nozzles were not considered here. Kröger (2004) gives a correlation for a cooling tower spray zone loss coefficient based on the data of Lowe and Christie (1961) for $d = 1$ mm drops in down-spray. For purely counter-flow rain zones, De Villiers and Kröger (1999) give a correlation valid for specific operating conditions. The exact conditions in the rain zone of the HDWD and the configuration of the nozzles have not yet been determined. Once these details have been finalized it will be possible to account for their contribution to the losses over the second stage. The obstruction posed by the rain zone and nozzles is, however, expected to be small relative to the heat exchanger bundle, the collecting troughs and the drift eliminators. Ignoring these losses will therefore not significantly affect the accuracy of the evaluation.

Gaddis and Gnielinski (1985) present correlations based on empirical data to calculate the pressure drop over bundles of dry plain tubes in cross-flow. Such a bundle is shown schematically in Figure 6.3.

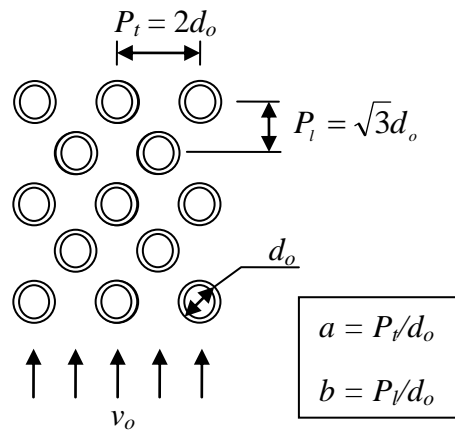


Figure 6.3: Bundle of plain tubes in cross-flow

Equation (6.30) describes the pressure loss across the bundle as a function of the bundle loss coefficient (K_b), the number of tube rows (n_r) the mean air density through the bundle (ρ_{am}), and the air velocity in the narrowest cross-section through the bundle (v_{max}).

$$\Delta p_{a(2nd-dry)} = K_b n_r \rho_{am} v_{max}^2 / 2 \quad (6.30)$$

For a staggered tube arrangement with the narrowest cross-section perpendicular to the flow direction, v_{max} is given by Equation (6.31) where v_o is the average air velocity upstream of the bundle and a is defined in Figure 6.3.

$$v_{max} = v_o a / (a - 1) \quad (6.31)$$

Gaddis and Gnielinski (1985) use Bell's (1963) correlation, shown in Equation (6.32), for the bundle loss coefficient for non-isothermal turbulent cross-flow (i.e. $Re_{max} = \rho_{am} v_{max} d_o / \mu_{aw} > 4000$) through a plain-tube bundle.

$$K_b = \frac{1}{Re_{max}^{0.25}} \left[2.5 + \frac{1.2}{(a - 0.85)^{1.08}} + 0.4 \left(\frac{b}{a} - 1 \right)^3 - 0.01 \left(\frac{a}{b} - 1 \right)^3 \right] \left(\frac{\mu_{aw}}{\mu_{am}} \right)^{0.14} \quad (6.32)$$

In Equation (6.32), μ_{aw} is the dynamic viscosity of air evaluated at the mean film temperature based on the mean air temperature through the bundle: $T_w = (T_{am} + T_v) / 2$.

Bertrand (2011) gives Equation (6.33) for the pressure drop over droplet collecting troughs in the absence of deluge water flow.

$$\Delta p_{ct} = 1.027 G_a^{2.0015} \quad (6.33)$$

6.3.1.3 Heat transfer rate results

The HDWD is essentially a conventional dephlegmator in which a portion of the finned-tube heat exchanger has been removed and replaced with the second stage hybrid (dry/wet) plain-tube bundle. It is therefore instructive to compare the heat

transfer rate of the second stage of the HDWD to the corresponding rate of the section of a conventional dephlegmator it is replacing (section comparison), as well as to compare the heat transfer for the whole dephlegmator (component comparison). Furthermore, the purpose of the HDWD is to enhance ACC performance and so a comparison of the performance of an entire ACC (consisting of four streets with five primary condenser units and one dephlegmator unit as shown in Figure 4.1) equipped with or without a HDWD is the ultimate indicator (system comparison). In the ACC considered here, the conventional air-cooled dephlegmator would provide roughly 15 % of the total heat transfer rate. Any changes in dephlegmator performance are therefore less pronounced on a system scale.

Figure 6.4 compares the heat transfer rate of an HDWD operating as an air-cooled condenser to the heat transfer rate of an ideal conventional dephlegmator (operating 100 % effectively) on a section, component and system level. Details of the conventional dephlegmator specifications are given in Appendix A.

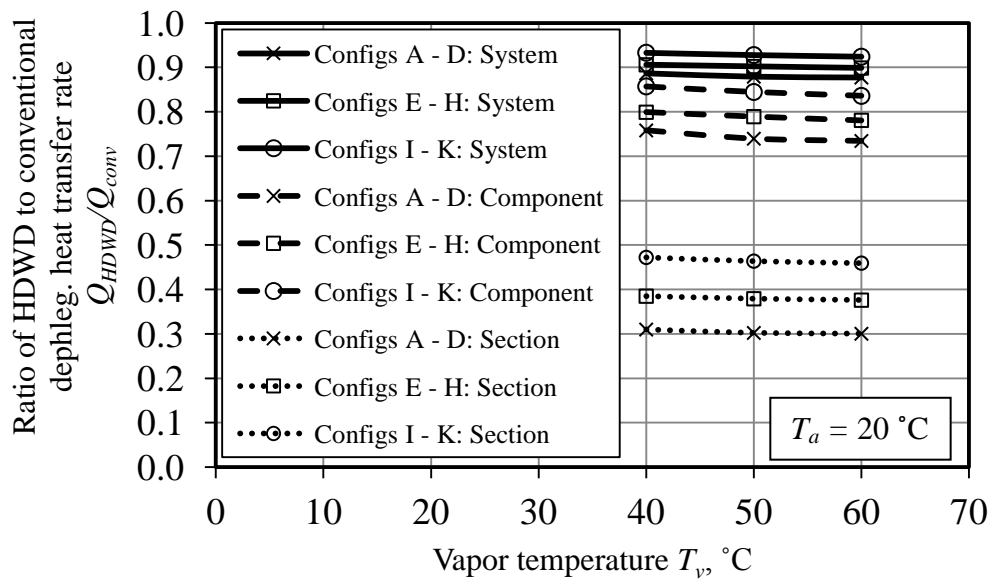


Figure 6.4: Heat transfer rate comparison between a conventional dephlegmator and the HDWD operating as an air-cooled condenser

The plain-tube bundle of the second stage of the HDWD, when operating dry, provides less than half the heat transfer of the section of finned-tube heat exchanger it is replacing. This appears to be severe, but when considered on a component level (whole dephlegmator), the HDWD heat transfer rate is between 73 % and 86 % of its ideal conventional counterpart. On a system level, for the ACC with six cells in each street (five primary condensers and one dephlegmator), the ACC equipped with HDWDs provides 87 % to 95 % of the heat transfer of the ACC with conventional dephlegmators.

The same comparison is shown in Figure 6.5 for a HDWD operating as an evaporative condenser. Note that the performance evaluation for wet operation was only carried out for higher vapor temperatures since it is likely that wet operation of the HDWD will only be initiated during periods of high ambient, and subsequently high vapor, temperatures.

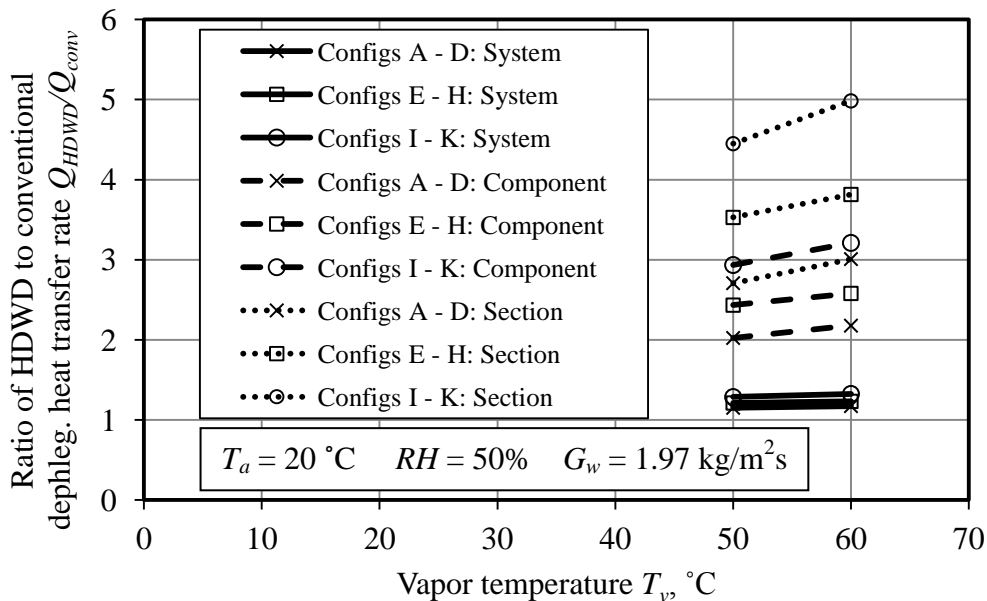


Figure 6.5: Heat transfer rate between a conventional dephlegmator and the HDWD operating as an evaporative cooler

The second stage of the HDWD, operating wet, can provide several times the heat transfer of the portion of finned-tube heat exchanger it is replacing. The

improvement is less pronounced but nonetheless significant on a component level with the HDWD offering two to three times the heat transfer of its conventional counterpart. On a system scale, the heat transfer rate of an ACC with the HDWDs is 15 % to 30 % greater than the rate for an ACC with conventional dephlegmators.

In all cases the smaller diameter tubes used in Configurations E – K provide greater heat transfer rates than the larger tubes of Configurations A – D. Inverse relationships between tube diameter and the various heat and mass transfer coefficients are responsible for the greater heat transfer experienced by the smaller tubes – see Equations (6.13), (6.14) and (6.18).

In summary, the HDWD operating in dry mode results in a slight reduction in ACC cooling performance relative to an ideal conventional dephlegmator (roughly 13 % for Configurations A – D, 9 % for E – H, and 6 % for I – K for the entire ACC). In light of the dephlegmator performance requirements discussed in Chapter 5 (see Figure 5.7), it would appear that Configurations I – K provide just enough suction during dry operation to prevent backflow in the multi-row primary condensers under ideal operating conditions. However, the margin of safety is dangerously small in this case and attention should be directed towards enhancing the HDWD performance during dry operation, or reducing the load on the dephlegmator. The use of a more effective finned-tube in the first stage of the HDWD may provide sufficient heat transfer rate enhancement. Reducing dephlegmator load has been discussed in Chapter 5 with the use of single-row primary condenser bundles identified as the most effective strategy for accomplishing this task. During wet operation the HDWD significantly outperforms the conventional dephlegmator. Should the dry HDWD be able to protect the primary condensers from backflow; the significant advantage provided by wet operation of the HDWD more than outweighs the slight decrease in cooling capacity experienced during dry operation.

The high heat transfer rates associated with wet operation of the HDWD are promising. However, due to the associated high vapor velocities in the counter-flow first stage heat exchanger tubes, it is necessary to carefully consider the possibility of flooding. It is also necessary to examine the implications of these high velocities on the steam-side pressure drop over the HDWD. The following sections address these issues.

6.3.2 Flooding concerns

In the forced draft HDWD, steam flows upwards in the inclined finned tubes of the first stage in counter-flow with the draining condensate. During dry operation the condensate is able to drain freely into the lower header due to relatively low vapor flow rates at the inlets of the first stage tubes. During wet operation, the vapor flow rate at the first stage tube inlets increases measurably due to the high heat transfer rates in the second stage. If the first stage inlet vapor flow rate increases too much, so that the condensate is no longer able to drain freely and instead accumulates in the tubes, then flooding has occurred. Flooding results in a measurable increase in the steam-side pressure drop and a decrease in the thermal performance of the tube (Schoenfeld and Kröger, 2000).

The correlation of Zapke and Kröger (1996), shown in Equation (6.34), was used to investigate the possibility of flooding in the first stage tubes.

$$Fr_{Dv} = a_1 \exp(-a_2 Fr_{Dc}^{0.6} Oh^{0.2}) \quad (6.34)$$

The vapor and condensate Froude numbers, Fr_{Dv} and Fr_{Dc} , are defined by Equations (6.35) and (6.36) respectively. The Ohnesorge number (Oh) (Ohnesorge, 1936) is expressed in Equation (6.37) with σ_l the liquid surface tension.

$$Fr_{Dv} = \frac{\rho_v v_{vs}^2}{(\rho_l - \rho_v)gH_t} \quad (6.35)$$

$$Fr_{Dc} = \frac{\rho_l v_{ls}^2}{(\rho_l - \rho_v) g d_e} \quad (6.36)$$

$$Oh = \mu_l / \sqrt{\rho_l d_e \sigma_l} \quad (6.37)$$

In Equation (6.35), H_t is the flattened tube height. The superficial vapor and condensate velocities, v_{vs} and v_{vl} in Equations (6.35) and (6.36) are respectively defined by Equations (6.38) and (6.39).

$$v_{vs} = m_v / \rho_v A_{ts} \quad (6.38)$$

$$v_{cs} = m_c / \rho_l A_{ts} \quad (6.39)$$

The constants a_1 and a_2 in Equation (6.34) are functions of the tube inclination angle θ as shown in Equations (6.40) and (6.41) where θ is in degrees.

$$a_1 = 7.9143 \times 10^{-2} + 4.9705 \times 10^{-3} \theta + 1.5183 \times 10^{-4} \theta^2 - 1.9852 \times 10^{-4} \theta^3 \quad (6.40)$$

$$a_2 = 18.149 - 1.9471 \theta + 6.0758 \times 10^{-2} \theta^2 - 5.3227 \times 10^{-4} \theta^3 \quad (6.41)$$

Flooding occurs when the vapor Froude number exceeds the limit set by Equation (6.34) at a given condensate Froude number. Figure 6.6 shows the vapor Froude number in the first row of first stage tubes, inclined at 60° to the horizontal, as a function of the corresponding condensate Froude numbers for $T_v = 60^\circ\text{C}$ and $T_a = 20^\circ\text{C}$. The flooding limit in the first stage tubes is exceeded when the second stage of the HDWD is operated as an evaporative cooler in this case. Calculations performed over a range of vapor temperatures and approach temperature differences found flooding to always occur in the first stage during wet operation of the second stage heat exchanger configurations considered in this study.

That flooding in the first stage tubes is predicted to occur when the second stage is operated as an evaporative condenser poses a problem and limits the application of the forced draft HDWD concept to certain tube geometries and operating conditions. Possible solutions to this problem are to modify the geometry of the

finned tubes in the first stage or to change the configuration of the dephlegmator from the forced draft system, shown in Figure 6.1, to an induced draft system as illustrated in Figure 6.7.

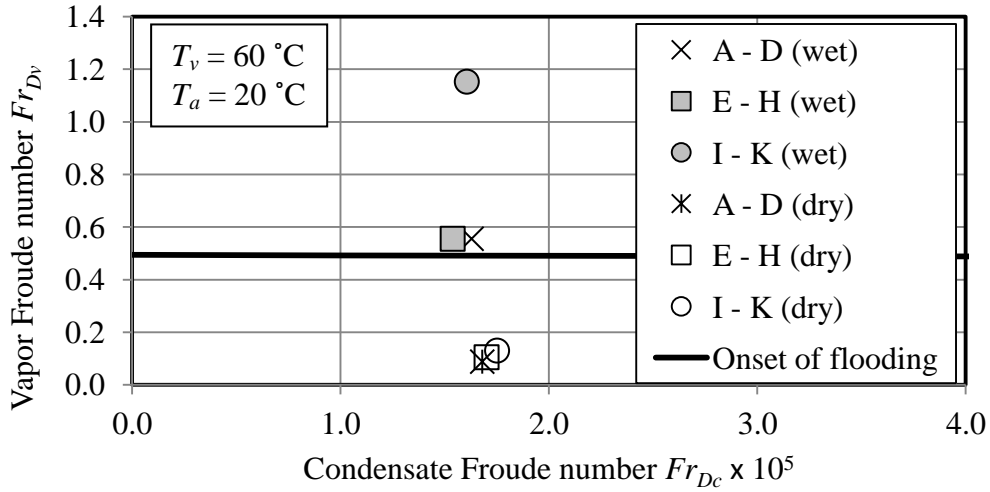


Figure 6.6: Flooding considerations in the first stage of the HDWD

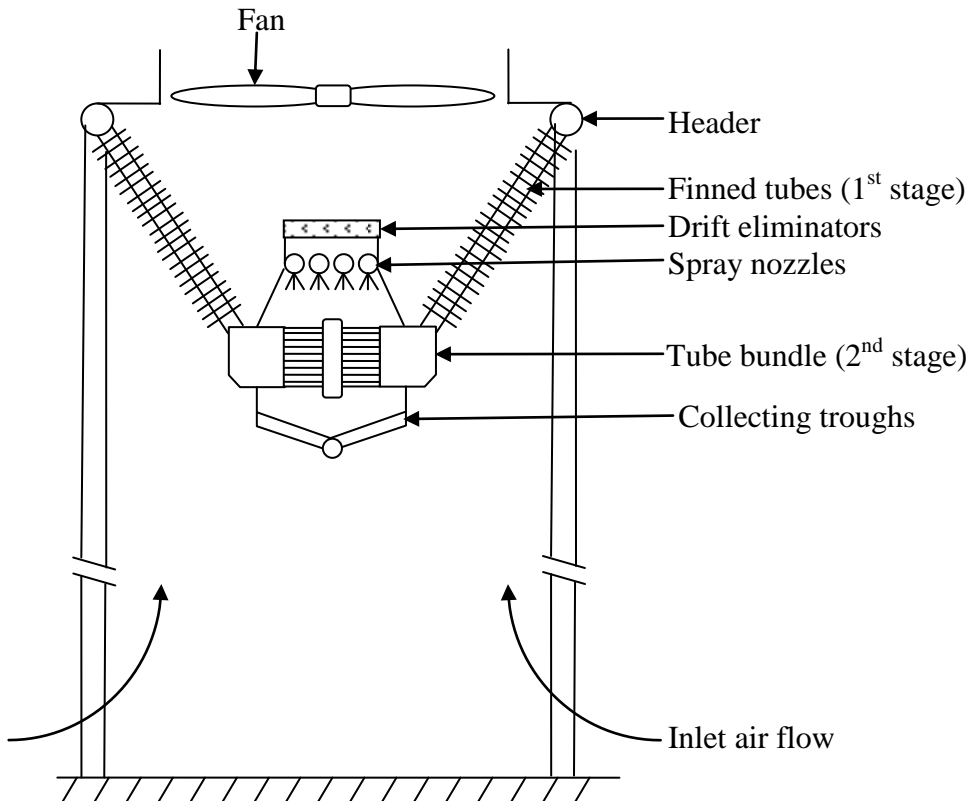


Figure 6.7: Schematic of the induced draft HDWD concept

The induced draft concept has the advantage of a first stage that is operating with co-current vapor/condensate flow and is therefore not susceptible to flooding. For a given fan air mass flow rate, induced draft systems generally require more fan power than forced draft systems because the induced draft fan is operating at a higher air temperature and therefore with less dense air.

At first glance it may therefore seem that the induced draft HDWD would have the disadvantage of increased fan power consumption. In this case, however, the system operating point is shifted to a higher fan mass flow rate for the induced draft HDWD as a result of the difference in the bundle loss coefficients as shown in Equations (6.21) and (6.22). The fan power requirement is thus predicted to be slightly less in the induced draft case for the system considered in this investigation. The heat transfer rates of the induced and forced draft systems differ negligibly and the results of Section 6.3.1.3 are valid for both configurations.

6.3.3 *Steam-side pressure drop*

The steam-side pressure drop over the dephlegmator is influenced by friction, acceleration, inlet/outlet and geodetic effects as shown in Equation (6.42).

$$\Delta p_v = \Delta p_f + \Delta p_m + \Delta p_{i/o} + \Delta p_g \quad (6.42)$$

The geodetic component, Δp_g , is small relative to the other contributors, especially in the second stage where the tubes are near horizontal and Δp_g tends to zero. The friction (Δp_f), acceleration (Δp_m), and inlet/outlet ($\Delta p_{i/o}$) components are discussed in the following sections.

6.3.3.1 Friction pressure loss

No accurate general predictive methods are available for predicting the friction pressure gradient in two-phase liquid-vapor flow (Mauro et al., 2007). Existing methods make use of either the homogeneous or the separated flow model approach (Carey, 1992).

The homogeneous model assumes the liquid and vapor velocities to be equal and that the two-phase fluid behaves as a single-phase fluid with properties analogous to the mean values of the flow. The homogeneous model is recommended for use at high mass flux ($G_v > 2000 \text{ kg/m}^2\text{s}$) and high reduced pressures (Thome, 2006) and gives best results in the bubbly and mist flow regimes where the slip velocity between phases is small (Carey, 1992). Although conveniently simple, the homogeneous model offers reasonable results for limited circumstances only and is therefore seldom used.

In separated flow models, the individual phases in the two-phase flow are considered independently. Typically, the two-phase friction pressure gradient is expressed in terms of the friction pressure gradient of a single-phase fluid, flowing at some mass flux in the tube or duct, multiplied by a two-phase friction multiplier (ϕ), as shown in Equation (6.43). The two-phase multiplier accounts for the effects of interfacial roughness on the friction pressure gradient.

$$\left(\frac{dp}{dx}\right)_{f(tp)} = \phi_i^2 \left(\frac{dp}{dx}\right)_{f(i)} \quad (6.43)$$

The right hand side of Equation (6.43) can be written in terms of the liquid ($i \rightarrow l$), liquid-only ($i \rightarrow lo$), vapor ($i \rightarrow v$) or vapor only ($i \rightarrow vo$) friction pressure gradients. The liquid and vapor single-phase friction gradients are calculated based in the total mass flux of the two-phase mixture while the liquid- and vapor-only gradients are calculated based on the mass flux of the respective phase only.

Empirical correlations are required to determine the two-phase friction multiplier for a given flow situation. The first widely used correlation of this sort was proposed by Lockhart and Martinelli (1949) based on experimental data for adiabatic two-phase, two-component (air-benzene, kerosene-water) flows in a round tube ($1.5 \text{ mm} \leq d_i \leq 26 \text{ mm}$). Lockhart and Martinelli's correlation has been shown to yield reasonably accurate results for a wide variety of two-phase flow circumstances in round tubes (Carey, 1992) and remains one of the most widely

used and best recognised methods today. Many modern correlations, some of which will be discussed here, are based on Lockhart and Martinelli's approach.

Baroczy (1966) claims to offer an improvement on Lockhart and Martinelli's correlation which takes into account the influence of pressure and mass flux as well as the respective fluid flow rates on the two-phase friction multiplier. Baroczy's correlation is based on local pressure gradient data observed during experiments involving steam, air-water, and mercury-nitrogen flows over a range of practical mixture qualities and mass fluxes. The correlations are expressed in the form of two curves: the first expressing the two-phase friction multiplier as a function of fluid properties at a fixed mass flux, and the second scaling the former curve to account for mass flux effects. The scaling curve is very complex and integration to find overall values for a tube is subsequently extremely difficult. This method is thus seldom used in practise (Carey, 1992).

Friedel (1979) developed a correlation for the two-phase liquid-only friction multiplier (ϕ_{lo}) based on an extensive database including 25 000 friction pressure drop results for the adiabatic flow of various single- and two-component two-phase mixtures in both horizontal and vertical tubes over a wide range of flow conditions. Friedel's correlation expresses the friction multiplier as a function of the fluid properties, the quality of the mixture, as well as the Reynolds, Froude and Weber numbers. The correlation therefore accounts for mass flux, surface tension and gravitational effects. Several studies (such as Carey, 1992; Dalkilic et al., 2010; and Shannak, 2008) recommend Friedel's correlation for use when $\mu_l/\mu_v < 1000$.

Due to the extensive database on which Friedel's correlation is based, it is likely to offer a reasonably accurate prediction of the friction pressure gradient in many flow situations (Carey, 1992). Indeed, several studies comparing various friction pressure drop correlations find this to be the case. Mauro et al. (2007) compared five correlations - including Friedel (1979), Grønnerud (1972), Muller-Steinhagen and Heck (1986) and Moreno Quiben and Thome (2007) - to their data for

uniformly heated refrigerant flow in a horizontal tube ($d_i = 0.006$ m). Friedel's correlation gave the most reliable predictions of the two-phase pressure drop over all the flow regimes considered but was not the best in any particular flow regime. Da Silva Lima et al. (2009) present similar findings based on their experiments with Nitrogen flow in smooth horizontal tubes ($d_i = 0.014$ m). Shannak (2008) compared seven two-phase friction pressure drop correlations to data for air-water flow in horizontal and vertical tubes with $d_i = 0.0525$ m. Their data covered mixture qualities of $0 \leq x \leq 1$, mass fluxes of $200 \text{ kg/m}^2\text{s} \leq G \leq 1500 \text{ kg/m}^2\text{s}$ and pressures between $5 \times 10^5 \text{ N/m}^2 \leq p \leq 14 \times 10^5 \text{ N/m}^2$. Friedel's correlation proved most accurate for mixture qualities below $x = 0.8$ but was found to under-predict the data slightly at higher qualities. In light of this under-prediction at high qualities, Shannak recommends an improvement on Friedel's correlation which uses a new definition for the two-phase Reynolds number implemented in a modified version of the Colebrook equation recommended by Chen (1979). Unfortunately the complex form of this correlation makes integration extremely difficult.

Friedel's (1979) correlation was derived from data for adiabatic flows and therefore does not account for condensation effects. Groenewald and Kröger (1995) show that adiabatic two-phase friction pressure drop models yield errors when applied to condensing flow situations since they fail to account for the influence of the condensing mass flux towards the liquid-vapor interface. Condensation alters the vapor velocity profile in the vicinity of the interface resulting in increased interfacial friction. Adiabatic friction factors can be modified to account for condensation through the use of a friction enhancement factor. These factors are typically derived from theoretical analyses for flat plate flows with suction (effectively porous plate flow). Cavallini et al. (2002) recommends that Friedel's correlation be corrected using the friction enhancement factor presented by Mickley et al. (1954) to account for condensation effects when necessary. Dalkilic et al. (2010) showed that this modified Friedel correlation resulted in improved prediction of their data for refrigerant condensation in

horizontal and vertical tubes. A similar comparison to data for condensing steam could not be found.

Owen et al. (1981) applied the annular flow model, used in its no-entrainment limit, to predict the friction pressure gradient during the condensation of two-phase, single component mixtures ($20 \text{ kg/m}^2\text{s} \leq G \leq 1250 \text{ kg/m}^2\text{s}$) in horizontal tubes ($0.007 \text{ m} \leq d_i \leq 0.025 \text{ m}$). Steam, propanol, methanol and a variety of refrigerants were considered. While they show their model to provide good accuracy, it is sensitive to the correlation used to describe the interfacial roughness coefficient.

Groenewald and Kröger (1995) express the two-phase friction pressure gradient for condensing steam in terms of an effective interfacial friction factor (f_{De}) based on the Darcy friction factor (f_D). Their correlations have been presented in Equations (4.8) – (4.12) for high aspect ratio flattened tubes. For round tubes, as used in the second stage of the HDWD, Groenewald and Kröger give Equations (6.44) and (6.45) respectively for the parameters a_1 and a_2 in Equation (4.12).

$$a_1 = 1.0046 + 1.719 \times 10^{-3} Re_{vm} - 9.7746 \times 10^{-6} Re_{vm}^2 \quad (6.44)$$

$$a_2 = 574.3115 + 24.2891 Re_{vm} + 1.8515 Re_{vm}^2 \quad (6.45)$$

The general consensus amongst authors of comparative studies of multi-phase friction pressure drop correlations is that the most accurate prediction will be achieved using the correlation based on experiments that most closely resemble the situation one is trying to predict. Most of the correlations available in the literature, and discussed above, are based on data for refrigerants or on adiabatic flow in short, small diameter tubes. In the HDWD, condensing steam is flowing in long, relatively large diameter tubes. Groenewald and Kröger (1995) tested condensing steam in tubes similar to those considered in this study and their correlations were thus selected for use here.

6.3.3.2 Acceleration effects

The bulk vapor flow experiences a deceleration as it flows through the dephlegmator as a result of mass transfer to the liquid phase during condensation. This loss of momentum manifests as a static pressure recovery in the flow direction. The increase in pressure due to acceleration effects is expressed directly as a function of the momentum of the vapor entering the tube in Equation (6.46) (Kröger, 2004).

$$\Delta p_m = \int G_v^2 [(1-x)/\rho_l + x^2/\alpha\rho_v] dx \quad (6.46)$$

Here α is the local void fraction.

If the flow leaving a tube is stratified and the quality of the vapor is assumed to be unity, then Equation (6.46) reduces to Equation (6.47).

$$\Delta p_m = \rho_v (v_{vi}^2 - v_{vo}^2) \quad (6.47)$$

6.3.3.3 Inlet/outlet effects

Losses of mechanical energy occur at abrupt changes in flow cross-sectional area such as at the inlet and outlet of tubes. Inlet and outlet losses in single-phase flow are typically expressed in terms of the contraction and expansion loss coefficients (K_i and K_o) and inlet and outlet area ratios (σ_i and σ_o) as shown in Equations (6.48) – (6.50) (Kröger, 2004).

$$\Delta p_i = -(1 - \sigma_i^2 + K_i) \rho_v v_{vi}^2 / 2 \quad (6.48)$$

$$(\Delta p_o)_{turb} = -(K_o - 1 + \sigma_o^2) \rho_v v_{vo}^2 / 2 \quad (6.49)$$

$$(\Delta p_o)_{lam} = (K_o + \sigma_o^2 - 1.33) \rho_v v_{vo}^2 / 2 \quad (6.50)$$

The inlet loss coefficient has been described in Equation (4.34) as a function of the contraction ratio (σ_c). The contraction ratio is in turn a function of the inlet area ratio shown in Equation (4.35) for sharp tube inlets (Kays, 1950).

The inlet loss coefficient can be reduced by rounding the inlet edge. Fried and Idelchick (1989) give the information shown in Figure 5.14 for the effect of rounding the inlet edge on the inlet loss coefficient of round tubes.

Equations (6.51) and (6.52) describe the expansion loss coefficient for turbulent and laminar flow respectively.

$$K_o = (1 - \sigma_o)^2 \quad (6.51)$$

$$K_o = 1 - 2.66 \sigma_o + \sigma_o^2 \quad (6.52)$$

Equations (6.48) – (6.52) are valid for the first and second stages of the induced draft HDWD where the vapor and condensate flow co-currently and liquid-vapor interactions at the tube inlets and outlets are negligible due to the high void fraction of the flow.

In the forced draft HDWD the first stage operates under counter-flow vapor-condensate conditions and significant liquid-vapor interactions, notably at the tube inlets, need to be accounted for in the evaluation of the inlet losses (Zapke and Kröger, 1997).

Zapke and Kroger (1997) present the correlations shown in Equations (6.53) and (6.54), derived from their experimental data, for the inlet pressure drop over a sudden contraction in flow area during counter-current vapor-liquid flow.

$$\Delta p_i = -(K_{i(tp)} + \sigma_i^2) \rho_v v_{vi}^2 / 2 \quad (6.53)$$

$$K_{i(tp)} = 1.5636 \exp(2.9526 Fr_{sv}) \quad (6.54)$$

6.3.3.4 Steam-side pressure drop results

The steam-side pressure drop over the HDWD operating as an air-cooled condenser is compared to that over the conventional dephlegmator in Figure 6.8 (component comparison).

It is immediately obvious that the steam-side pressure drop is higher when the smaller tubes are used in the second stage of the HDWD. This higher pressure drop is as an obvious result of the greater vapor velocities associated with using the smaller tubes with higher heat transfer rates. Apart from Configurations E and G the steam-side pressure drop over the HDWD operating dry is generally of a similar magnitude to that of the conventional dephlegmator. The magnitude of this pressure drop is relatively small and the assumption of constant vapor temperature through the HDWD holds in this case.

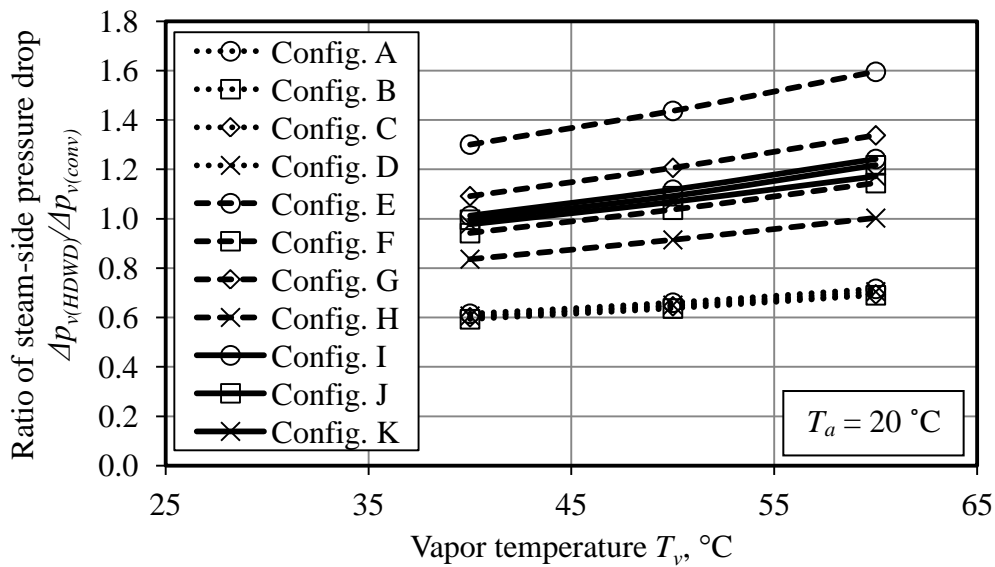


Figure 6.8: Comparison of the steam-side pressure drop over a conventional dephlegmator and the HDWD operating as an air-cooled condenser

In Figure 6.9 the steam-side pressure drop over the HDWD operating as an evaporative condenser is compared to the pressure drop over the conventional dephlegmator. The pressure drop over the HDWD is measurably increased as a result of the very high vapor flow rates.

6.3.3.5 Contributors to steam-side pressure drop in the HDWD

As mentioned previously: friction, acceleration and inlet/outlet effects contribute to the steam-side pressure change over the HDWD.

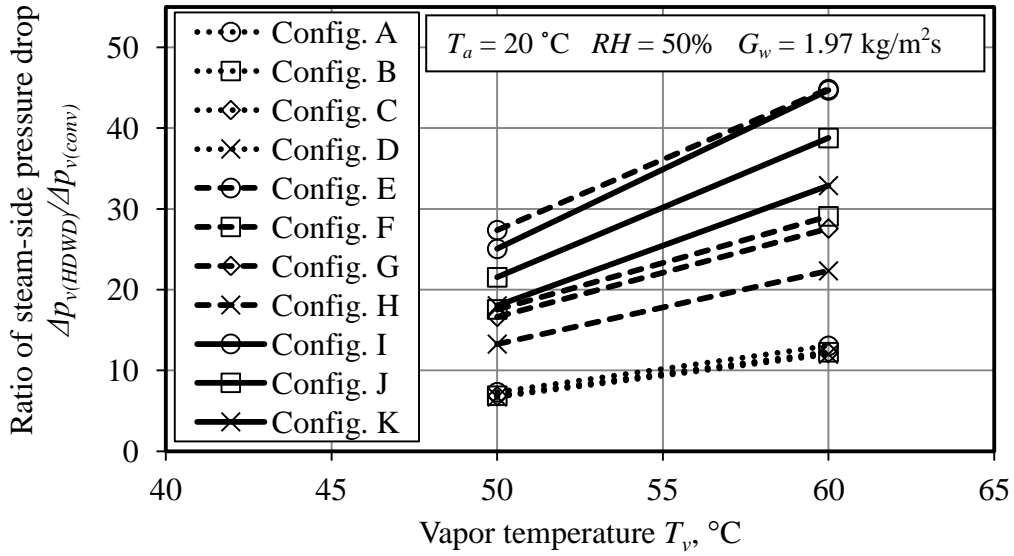


Figure 6.9: Comparison of the steam-side pressure drop over a conventional dephlegmator and the HDWD operating as an evaporative condenser

As the steam flows through the system, friction and inlet/outlet effects result in static pressure losses while deceleration of the flow due to condensation results in a static pressure recovery. Table 6.2 shows the contributions of the friction, inlet/outlet and acceleration pressure changes on the overall steam-side pressure change for the first and second stages of Configuration I ($d_o = 0.019$ m, $n_r = 25$) of the HDWD, operating in wet mode ($T_v = 60$ °C, $T_a = 20$ °C).

Table 6.2: Contributors to steam-side pressure drop in the HDWD (Config. I, wet)

		Δp_f , N/m ²	$\Delta p_{i/o}$, N/m ²	Δp_m , N/m ²	Δp_v , N/m ²
First stage		-1219.77	-922.22	564.59	-1577.40
Second stage	1 st pass	-471.49	-159.18	320.56	-310.11
	2 nd pass	-471.49	-159.18	320.56	-310.11
	3 rd pass	-259.53	-104.02	213.71	-149.84
	Overall	-1202.51	-422.38	854.83	-770.06

From Table 6.2, the net pressure change over the HDWD is,

$$\Delta p_v = -1577.40 - 770.06 = -2347.46 \text{ N/m}^2$$

The first stage accounts for 67 % of the steam-side pressure drop over the HDWD in this case.

When operating as an evaporative condenser, the second stage of the HDWD condenses a large amount of steam. The first stage always operates as an air-cooled condenser and therefore condenses far less steam than the second stage. The first stage experiences measurable inlet/outlet and friction losses as a result of the large amount of vapor drawn through it by the wet second stage. Simultaneously, relatively little steam is condensed in the first stage and the corresponding pressure recovery due to deceleration of the flow under the influence of condensation is small relative to the losses. The net pressure drop over the first stage is therefore substantial.

The friction losses in the second stage are of similar magnitude to those in the first stage due to the relatively long length of small diameter tube used. The inlet losses in the second stage are, however, smaller than in the first stage and there is more pressure recovery due to the higher condensation rates. The net pressure drop over the second stage is therefore significantly less than over the first.

Analysis of Table 6.2 shows that inlet/outlet effects account for nearly 60 % of the net pressure drop over both stages. Figure 5.14 shows that it is possible to measurably reduce the inlet loss coefficient by rounding the tube inlet edges. Rounding the inlet edges of the first and second stage tubes in Configuration I to $r/d = 0.16$, a relatively high rounding ratio, was found to reduce the steam-side pressure drop over the HDWD by approximately 20 % and increase the HDWD heat transfer rate by approximately 1.2 % relative to the sharp-edged case. A detailed economic analysis is necessary to determine if the cost of purposefully rounding the tube inlets during the manufacturing of the HDWD is eventually compensated for by the small increase in cooling performance.

6.3.4 Ejector loading

The performance requirements of the ejector in the dephlegmator cell were described in Chapter 5. An amount of vapor must be ejected along with the non-condensable gases to prevent backflow in the dephlegmator tubes. It is obviously desirable to minimize the required amount of vapor to be ejected to reduce the demands on ejector capacity.

The amount of vapor to be ejected is determined largely by the tube configuration in the dephlegmator. The conventional dephlegmator considered in this study makes use of a two-row heat exchanger and therefore requires additional vapor flow through the second row to prevent vapor backflow in the first. Section 5.3 discussed the ejector requirements to account for row effects in such a dephlegmator. In the second stage of the HDWD, the number of tube rows in the final pass of the plain tube bundle determines the amount of additional vapor flow. For a single-row tube pass, no additional vapor flow is necessary under ideal operating conditions (i.e. each tube operating 100 % effectively with uniform air flow and temperature distribution) and such a configuration is therefore desirable, although not always practical.

Assuming a non-condensable concentration in the vapor of $1:10^4$ as in Chapter 5, the concentration of vapor in the ejection mixture is shown in Figure 6.10 for dry operation of the HDWD second stage.

Configurations A, E and I theoretically require no vapor to be ejected in order to clean out the tubes of non-condensable gases since they have only a single tube row in the final tube pass. For the conventional dephlegmator, over 90 % of the ejection mixture would be vapor and the ejector is being used very ineffectively. Configuration K requires more vapor ejection than the conventional dephlegmator while Configurations D, G and H offer only a small improvement. Configurations B, C, F and J offer measurable improvements in ejector loading relative to the conventional dephlegmator.

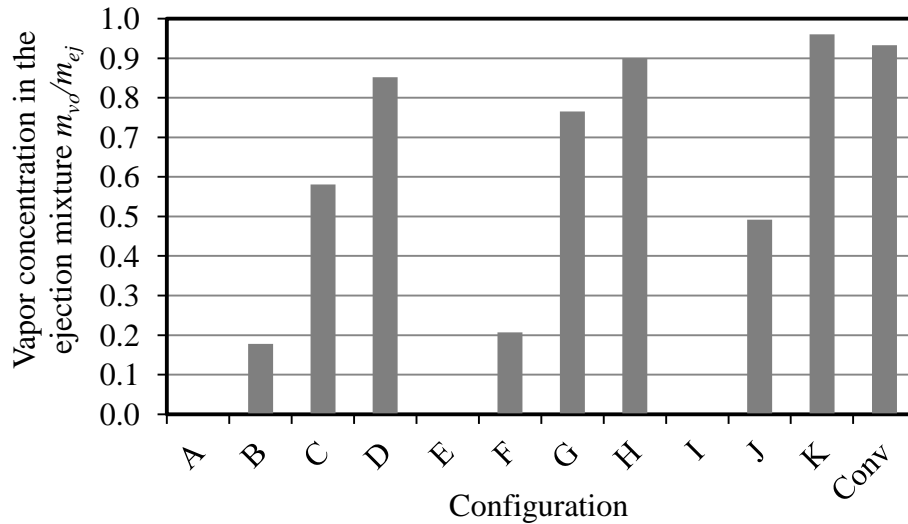


Figure 6.10: Concentration of water vapor in the ejection mixture required to prevent vapor backflow in the dephlegmator

As mentioned in Chapter 5, a small amount of excess vapor will always be ejected (regardless of the bundle configuration) to account for non-ideal operation of the HDWD and to prevent high concentrations of non-condensable gases in the final portion of the heat exchanger.

6.3.5 Water consumption

The enhanced heat transfer rate when operating the HDWD as an evaporative condenser comes at the expense of water consumption. Figure 6.11 shows the predicted water consumption of the HDWD for a deluge water mass flux of $G_w = 1.97 \text{ kg/m}^2\text{s}$, which exceeds the minimum required deluge water mass flux of $G_{w(min)} = 1.7 \text{ kg/m}^2\text{s}$ for uniform wetting of the tubes (Heyns, 2009).

Heyns (2009) showed that an ACC with a HDWD consumes roughly 20 % less water than one at which adiabatic cooling is employed to achieve a similar performance enhancement. An evaporative cooling tower for a 480 MW power plant consumes approximately 14.4 ML of water per day (Gadhamshtetty et al., 2006), or roughly 166 kg/s. The equivalent ACC with a HDWD operating in wet mode full-time would consume at most 56 kg/s (4 ACC streets each with $m_{evap} \approx 14 \text{ kg/s}$) or 4.84 ML of fresh water per day.

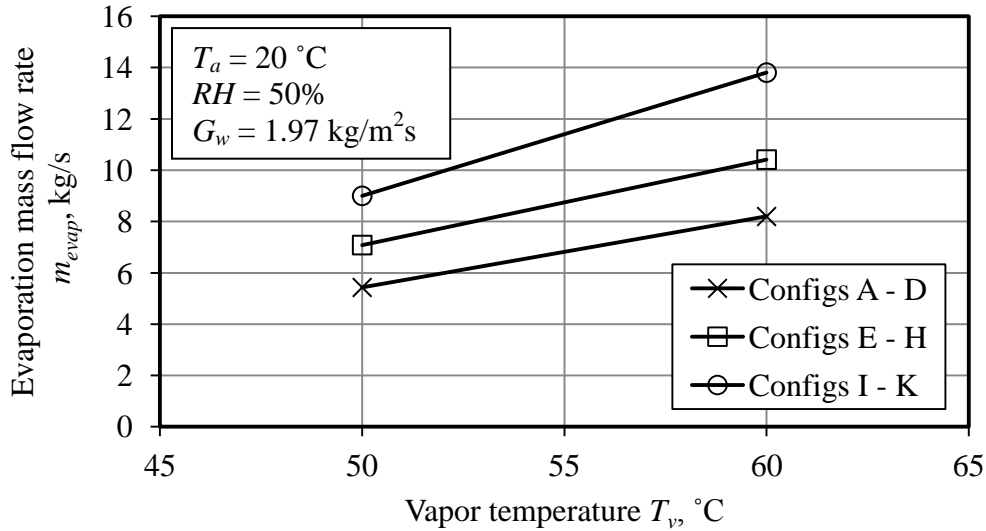


Figure 6.11: Water consumption in the HDWD

While this already offers a considerable water consumption reduction, it is unlikely that the HDWD would be operated wet all the time. The HDWD should operate dry for the majority of the time and only be operated in wet mode for the few hottest hours of the year, or when electricity prices are high enough to justify the consumption of additional water. The water consumption of the ACC with a HDWD will therefore be negligible relative to an evaporative cooling tower.

6.3.6 Recommended HDWD configuration

The results presented thus far in Section 6.3 indicate that the smaller diameter tubes of Configurations E – K ($d_o = 0.019$ m) offer better heat transfer rates than the larger tubes of Configurations A – D ($d_o = 0.0381$ m). Configurations I – K offer the highest heat transfer rates due to the greater number of tube rows ($n_r = 25$) in the second stage bundle. In light of the dephlegmator loading results presented in Chapter 5, only Configurations I – K offer sufficient suction during dry operation to protect the multi-row primary condensers considered here from vapor backflow. The high heat transfer rate in these configurations comes at the expense of higher steam-side pressure drop and increased water consumption. However, the improved heat transfer outweighs the negative effects of increased

steam-side pressure drop while the increase in water consumption is negligible when compared to other methods of cooling. Furthermore, certain HDWD configurations are shown to be capable of measurably reducing the load on the ejector and are therefore more likely to prevent the accumulation of non-condensable gases in the system. Configurations with only a single vapor pass in the final tube row (A, E and I) offer the most desirable configurations in terms of ejector loading. Based on these considerations, Configuration I offers the most attractive configuration for the HDWD.

6.4 The effect of an HDWD on steam turbine output

Section 6.3.1.3 showed that the HDWD is capable of measurably improving the heat transfer rate of an ACC at high ambient temperatures while consuming very little water. Improved ACC performance results in increased steam turbine output, as discussed in Chapter 2. The effect of the HDWD (with second stage Configuration I) on the output of a practical steam turbine is examined here.

The steam turbine performance characteristic and the required ACC heat rejection rate, shown in Figure 2.4, are described by Equations (6.55) and (6.56) respectively (T_v in degrees Celcius).

$$P_{gen} = 225.83 - 0.0043T_v + 0.01332T_v^2 - 0.000163T_v^3, \text{ MW} \quad (6.55)$$

$$Q = 336.4 - 0.18223T_v - 0.01601T_v^2 + 0.00018T_v^3, \text{ MW} \quad (6.56)$$

These characteristics are for a plant cooled by an 18 cell ACC (three streets each with five primary condensers and one dephlegmator) as considered by Heyns and Kröger (2012). The complete operating point specifications of the plant are given in Appendix A.3.

Turbine output decreases at high ambient temperatures due to a reduction in ACC thermal performance. If, however, it is possible to enhance the potential ACC performance at high ambient temperatures, the backpressure can be maintained closer to the optimum and the turbine output can be improved. Figure 6.12 shows

the effect of the dephlegmator configuration in the three-street ACC on the steam turbine backpressure.

The ACC with a conventional dephlegmator and the ACC with a HDWD operating as an air cooled condenser have similar performance capabilities, as was illustrated in Figure 6.4, and they subsequently result in similar backpressures. The ACC with a HDWD operating as an evaporative cooler offers measurably more potential for heat rejection and as such operates at lower backpressures for a given ambient temperature.

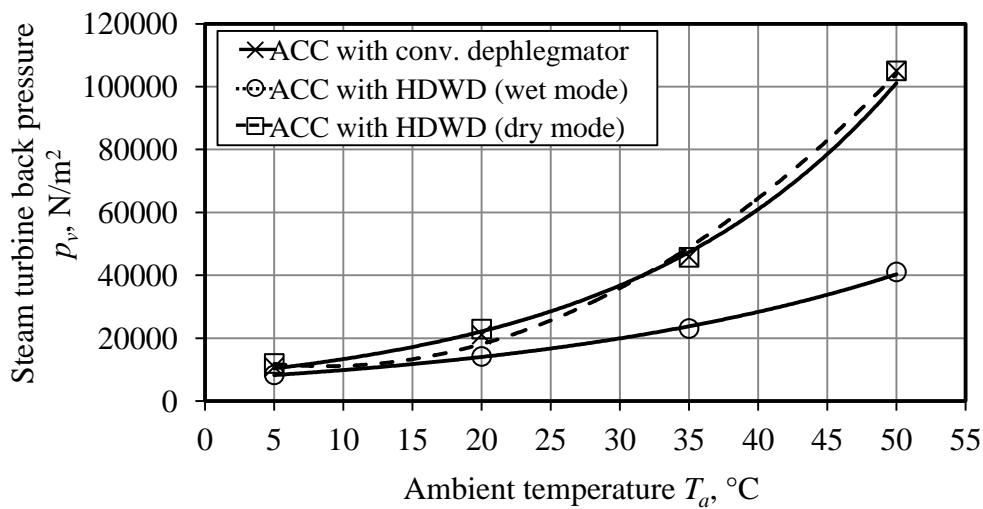


Figure 6.12: The effect of dephlegmator configuration on turbine backpressure

Figure 6.13 illustrates the steam temperatures corresponding to the backpressures shown in Figure 6.12. The steam temperature of $T_v = 54$ °C corresponding to the optimum backpressure in Figure 2.5 is shown as a dashed line.

At higher ambient temperatures the HDWD operating in wet mode results in steam temperatures that are closer to the optimum than for the other configurations. At lower ambient temperatures the wet HDWD results in vapor temperatures further from optimum than the other configurations for this particular turbine. It therefore stands to reason that the HDWD operating in wet mode must offer improved power output at high ambient temperatures while the

HDWD operating in dry mode offers improved turbine performance at lower ambient temperatures.

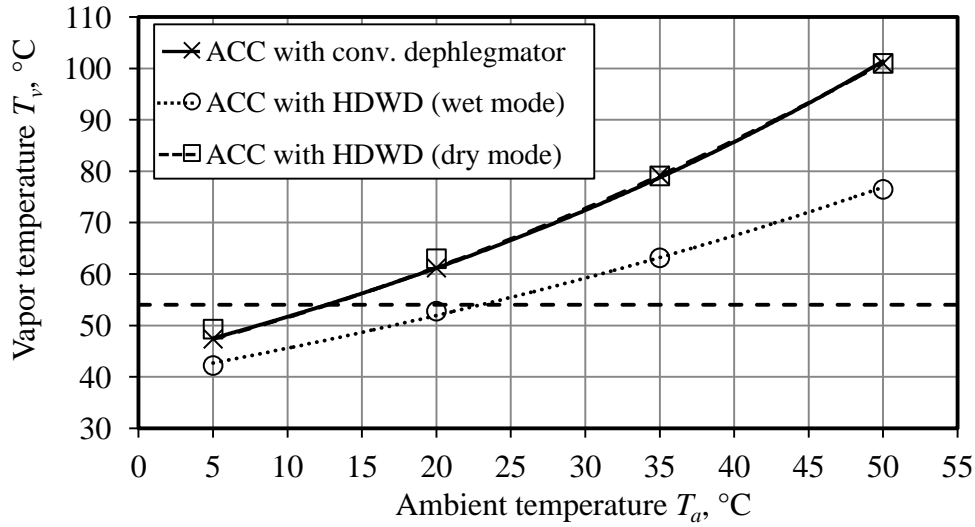


Figure 6.13: The effect of dephlegmator configuration on vapor temperature

This is evident in Figure 6.14 which shows that an ACC with HDWDs can effect a measurable improvement in the power output of the steam turbine considered in this study relative to an ACC with conventional dephlegmators. By operating the HDWDs in dry mode at low ambient temperatures ($T_a < 22$ °C in this case) and in wet mode for higher ambient temperatures, the steam turbine output can be maintained at a measurably higher average.

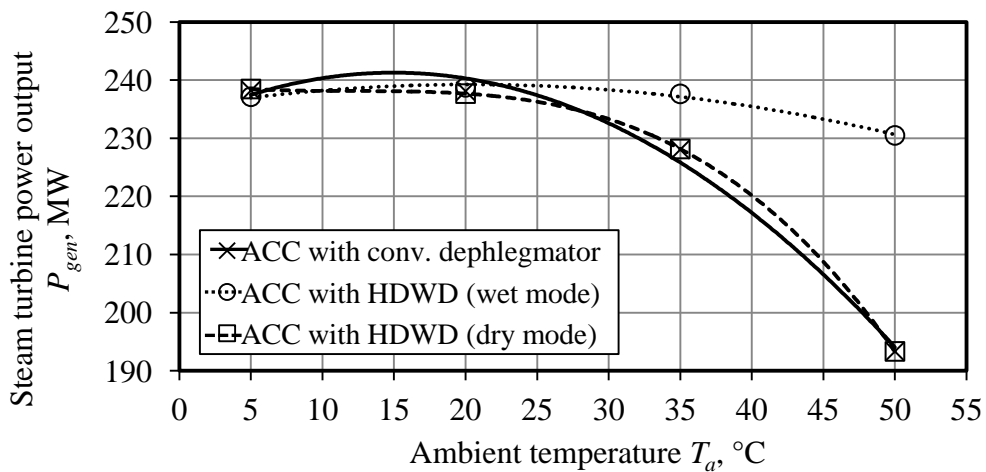


Figure 6.14: The effect of dephlegmator configuration on steam turbine output

7. CONCLUDING REMARKS AND RECOMMENDATIONS

In order to improve the reliability and competitiveness of ACC technology it is necessary to cultivate a greater understanding of the steam-side operation and performance of these systems. The impact of non-uniform vapor flow distributions, vapor backflow and the accumulation of non-condensable gases, and dephlegmator performance are of particular importance.

The objectives of this study were therefore to investigate the steam-side operation of an ACC with particular emphasis on the vapor flow distribution in the primary heat exchanger bundles and dephlegmator performance. A practical hypothetical condenser was considered using a combination of CFD, numerical, analytical and experimental methods.

The vapor flow in the distributing manifold, connecting the steam turbine to the air-cooled heat exchangers, was examined and the importance of careful design of the guide vanes in the junctions and bends was noted. In the ACC considered here, and in many operational ACCs, simple quarter-circle guide vanes are used with a uniform vane thickness and a slightly prolonged trailing edge. Several studies in the field of low-speed wind tunnel design – see Lindgren et al. (1998) for example – have highlighted the benefits, in terms of reduced pressure drop and improved flow distribution, of using more sophisticated guide vane designs. Particular emphasis is placed on varying vane thickness and trailing edge angle in these studies. The results shown in Chapter 3 indicate that considerations seemingly as trivial as the number of guide vanes in a given location can have a measurable impact of the flow through the distributing manifold.

Careful consideration of guide vane configuration in large ACC distributing manifolds would be beneficial to plant performance. Such measures could result in reduced steam-side losses over the manifold as well as improved flow distribution upstream of the heat exchanger bundles. A possible unforeseen benefit of improved guide vane design is that longer ducts can be used in the manifolds and the additional friction losses compensated for by the reduced bend

and junction losses. Longer ducts allow the ACC to be located further away from other power plant structures. This would be beneficial in light of the undesirable air-side flow phenomena associated with ACC proximity to such structures – see studies on wind effects by Goldschagg et al. (1997), Liu et al. (2009) and Gao et al., (2009) for example. Furthermore, it was shown in Section 4.4.2 that the upstream tubes in the first cell of a given ACC street experience very high inlet loss coefficients as a result of highly oblique approaching flow. These high inlet loss coefficients increase the demands on dephlegmator performance and exacerbate the risk of non-condensable accumulation in these tubes. Smart guide vane design in the bends upstream of the heat exchangers may assist in improving the flow conditions at these tube inlets, and thereby contribute towards mitigating the aforementioned concerns.

The investigation of the vapor flow in the primary condensers revealed a definite trend in inlet loss coefficient distribution through the heat exchanger bundles. A very strong relationship between the inlet loss coefficient distributions and the corresponding vapor flow distributions was identified. The inlet losses influence the vapor flow to such an extent that the flow distribution appears to not conform to the expected pattern typical of parallel or reverse flow manifolds (see the trends in Bajura and Jones (1976) for example). The strong influence of the inlet loss coefficients results in an additional demand on the dephlegmator that cannot be overlooked. In the worst case considered here, one third of the dephlegmator capacity was required to prevent vapor backflow due to the non-uniform distribution of inlet loss coefficients alone.

In the case of multi-row primary condenser bundles, row effects may demand as much as two thirds of the dephlegmator capacity under ideal operating conditions. Combined with the demands of inlet loss coefficient distributions, it appears that in some circumstances, the dephlegmator is only capable of catering for ideal primary condenser operation and has no margin of safety to cope with non-ideal operating conditions. A high risk of non-condensable accumulation therefore exists in the upstream regions of the primary condensers.

Based on the findings of this report it is recommended that single-row heat exchanger bundles be considered as the first option when designing an ACC. By using single-row primary condenser bundles, row effects are eliminated and the demand on dephlegmator performance is significantly reduced. The dephlegmator will then have ample cooling capacity to account for heat exchanger tube inlet loss coefficient distributions as well as non-ideal operating conditions. The use of single-row heat exchanger bundles in the dephlegmator will also measurably reduce the demands on the ejector, which was found to be potentially problematic in this case.

A hybrid (dry/wet) dephlegmator concept, originally proposed by Heyns and Kröger (2012), was examined in Chapter 6. The HDWD was shown to be capable of measurably enhancing the performance of an ACC, with subsequent benefits to turbine output, while consuming very little water. A potential pitfall was identified in terms of the HDWD's ability to provide sufficient suction to flush the multi-row primary condenser bundles of non-condensable gases when operating dry. The use of a single-row heat exchanger in the primary condensers would once again lay rest to this concern. If single-row primary condenser bundles are for some reason not feasible at a particular application, then it is recommended that the HDWD performance during dry operation be enhanced to ensure sufficient protection for the primary condensers.

Flooding concerns in the first stage of the original forced draft HDWD concept during wet operation prompted the recommendation to change to an induced draft configuration. In some situations an induced draft configuration may be impractical. A forced draft HDWD can still be used in such cases if careful consideration is given to the selection of an appropriate second stage bundle configuration, in conjunction with an alternative first stage tube (perhaps a tube with a larger steam-side cross-sectional flow area).

A further topic of concern was the relatively high predicted steam-side pressure drop over the HDWD during wet operation. A degree of uncertainty exists

regarding the correlations used to calculate the friction pressure drop in this case. An experimental investigation of friction losses for the specific flow conditions encountered in an HDWD is necessary to accurately specify the performance of the system. Despite the large predicted losses, however, the heat transfer rates during wet operation of the HDWD remain encouragingly high.

The HDWD concept offers a simple, cost effective and sustainable solution to the issue of reduced ACC performance at high ambient temperatures. In addition, it offers a means of providing clean dispatchable power, capable of responding to peaks in electricity demands and capitalizing on fluctuations in electricity prices. Applied in new power plants, or as a retrofit in situations where ACC performance issues are seriously detrimental to the reliable and profitable operation of an existing plant, the HDWD will significantly enhance the cost competitiveness of dry-cooling. Application of the HDWD concept in the next generation of ACCs will no doubt contribute measurably towards establishing dry-cooling as the technology of choice for modern thermoelectric power plants. Taking into account immediate and future global energy and water security concerns, the importance of such an innovation cannot be overstated.

REFERENCES

- Ablanque, N., Oliet, C., Rigola, J., Perez-Segarra, C.D., Oliva, A., *Two-phase flow distribution in multiple parallel tubes*, International Journal of Thermal Sciences, 49, pp. 909 – 921, 2010.
- Acrivos, A., Babcock, B.D., Pigford, R.L., *Flow distribution in manifolds*, Chemical Engineering Science, 10 (1/2), pp. 112 – 124, 1959.
- Al-Shammari, S.B., Webb, D.R., Heggs, P., *Condensation of steam with and without the presence of non-condensable gases in a vertical tube*, Desalination, 169, pp. 151 – 160, 2004.
- Bajura, R.A., *A model for flow distribution in manifolds*, ASME Journal of Engineering for Power, 93, pp. 7 – 12, 1971.
- Bajura, R.A., Jones, E.H., *Flow distribution manifolds*, Journal of Fluids Engineering, pp. 654 – 666, December 1976.
- Barker, B., *Running dry at the power plant*, EPRI Summer Journal, pp. 26 – 35, 2007.
- Baroczy, C.J., *A systematic correlation for two-phase pressure drop*, Chemical Engineering Progress Symposium Series, 62 (64), pp. 232 – 249, 1966.
- Bell, K.J., *Bulletin no. 5: Final Report of the Cooperative Research Program on Shell and Tube Heat Exchangers*, 1963.
- Berg, W.F., Berg, J.L., *Flow patterns for isothermal condensation in one-pass air-cooled heat exchangers*, Heat Transfer Engineering, 1 (4), pp. 21 – 31, 1980.
- Bertrand, T., *Evaluation of a 1.5 x 1.5 m² counter-flow fill performance test facility with a view to contributing to a fill performance standard*, MScEng Dissertation, Department of Mechanical and Mechatronic Engineering, University of Stellenbosch, South Africa, 2011.

Boulay, R.B., Cehra, M.J., Massoudi, M., *Dry and hybrid cooling condenser design to maximize operating income*, ASME Resport, Chicago, IL, 2005.

Breber, G., Palen, J.W., Taborek, J., *Study on non-condensable accumulation in air-cooled condensers*, Proceedings of the International Heat Transfer Conference, Alhambra, CA, Heat Transfer Research Institute Inc., 1982.

Carey, V.P., *Liquid-vapor phase change phenomena*, Hemisphere Publishing Corp., Washington, 1992.

Carney, B., Feeley, T.J., McNemar, A., *NETL Power Plant Water Research Program*, EPRI Workshop on Advanced Thermoelectric Cooling Technologies, Charlotte, NC, 2008.

Cavallini, A., Censi, G., DelCol, D., Doreti, L., Longo, G., Rossetto, L., *Condensation of halogenated refrigerants inside smooth tubes*, HVAR&R Research, 8, pp. 429 – 451, 2002.

Chato, J.C., *Laminar condensation inside horizontal and inclined tubes*, Journal of ASHRAE, pp. 52 – 60, 1962.

Chen, N.H., *An explicit equation for the friction factor in pipes*, Industrial Engineering Fundamentals, 18, pp. 296 – 297, 1979.

Churchill, S.W., Bernstein, M., *A correlation for forced convection from gases and liquids to a circular cylinder in crossflow*, Journal of Heat Transfer, 99, pp. 200 – 306, 1977.

DaSilva Lima, R.J., Moreno Quiben, J., Kuhn, C., Boyman, T., Thome, J.R., *Ammonia two-phase flow in a horizontal smooth tube: Flow pattern observations, diabatic and adiabatic frictional pressure drops and assessment of prediction methods*, International Journal of Heat and Mass Transfer, 52, pp. 2273 – 2288, 2009.

Dalkilic, A.S., Agra, O., Teke, I., Wongwises, S., *Comparison of frictional pressure drop models during annular flow condensation of R600a in a horizontal*

tube at low mass flux and of R134a in a vertical tube at high mass flux, International Journal of Heat and Mass Transfer, 53, pp. 2052 – 2064, 2010.

Datta, A.B., Majumdar, A.K. *Flow distribution in parallel and reverse flow manifolds*, International Journal of Heat and Fluid Flow, 2 (4), pp. 253 – 262, 1980.

De Villiers, E., Kröger, D.G., *Analysis of heat, mass and momentum transfer in the rain zone of counterflow cooling towers*, Journal of Engineering for Gas Turbines and Power, 121 (4), 1999.

Diehl, J.E., Unruh, C.H., *Two-phase pressure drop for horizontal crossflow through tube banks*, ASME Report: 58-HT-20, 1958.

DiFilippo, M., *Reclaiming water for cooling at SCE's Mountainview Power Plant*, EPRI Workshop on Advance Thermoelectric Cooling Technologies, Charlotte, NC, 2008.

Dreyer, A.A., *Analysis of evaporative coolers and condensers*, MScEng Dissertation, Department of Mechanical and Mechatronic Engineering, University of Stellenbosch, South Africa, 1988.

Duvenhage, K., Kröger, D.G., *The influence of wind on the performance of forced draft air-cooled heat exchangers*, Applied Thermal Engineering, 16, pp. 741 – 752, 1996.

Enger, M.L., Levy, M.I., *Pressure in manifold pipes*, Journal of American Water Works Association, pp. 659 – 667, 1929.

Fabbri, G., *Effect of disuniformities in vapor saturation pressure and coolant velocity on vapor backflow phenomena in single pass air-cooled condensers*, International Journal of Heat and Mass Transfer, 43, pp. 147 – 159, 2000.

FLUENT User's Guide, FLUENT, Lebanon, 2006.

Friedel, L., *Improved friction drop correlations for horizontal and vertical two-phase pipe flow*, European Two-phase Flow Group Meeting: Paper E2, Ispra, 1979.

Fried, E., Idelchick, I., *Flow resistance: A design guide for engineers*, Hemisphere, Philadelphia, 1989.

Gaddis, E.S., Gnielinski, V., *Pressure drop in cross flow across tube bundles*, International Journal of Chemical Engineering, 25, pp. 1 – 15, 1985.

Gadhamshetty, V., Nirmalakhandan, N., Myint, M., Ricketts, C., *Improving air-cooled condenser performance in combined cycle power plants*, Journal of Energy Engineering, 132 (2), pp. 81 – 88, 2006.

Gao, X., Zhang, C., Wei, J., Yu, B., *Numerical simulation of heat transfer performance of an air-cooled steam condenser in a thermal power plant*, International Journal of Heat and Mass Transfer, 45, pp. 1423 – 1433, 2009.

Gao, X.F., Zhang, C.W., Wei, J.J., Yu, B., *Performance prediction of an improved air-cooled steam condenser with deflector under strong wind*, Applied Thermal Engineering, 30, pp. 2663 – 2669, 2010.

Goldschagg, H.B., Vogt, F., Du Toit, C.G., Thiart, G.D., Kröger, D.G., *Air-cooled steam condenser performance in the presence of crosswinds*, Proceedings of the 1997 Cooling Tower Technology Conference, pp. 1.61 – 1.77, St Petersburg, 1997.

Grimison, E.D., *Correlation and utilization of new data on flow resistance and heat transfer in crossflow of gases over tube banks*, Transactions of the ASME, 59, pp. 583 – 594, 1937.

Groenewald, W., Kröger, D.G., *Effect of mass transfer on turbulent friction during condensation inside ducts*, International Journal of Heat and Mass Transfer, 38 (18), pp. 3385 – 3392, 1995.

Grønnerud, R., *Investigation of liquid hold-up, flow-resistance and heat transfer in circulation type of evaporators, Part IV: two-phase flow resistance in boiling refrigerant*, Annexe 1972-1 Bull. de l'Inst. du Froid, 1972.

Haaland, S.E., *Simple and explicit formulas for the friction factor in turbulent pipe flow*, Transactions of the ASME Journal of Fluids Engineering, 105 (3), pp. 89 – 90, 1983.

Hassani, V., Dickens, J., Bell, K., *The fin-on-plate heat exchanger: A new configuration for air-cooled power plants*, Transactions of the Geothermal Resources Council, 27, pp. 583 – 586, 2003.

Heat Exchange Institute, *Standards for steam jet vacuum systems*, 4th edition, Cleveland, OH, 1988.

Heyns, J.A., *Performance characteristics of an air-cooled heat exchanger incorporating a hybrid (dry/wet) dephlegmator*, MScEng Dissertation, Department of Mechanical and Mechatronic Engineering, University of Stellenbosch, South Africa, 2009.

Heyns, J.A., Kröger, D.G., *Performance characteristics of an air-cooled steam condenser with a hybrid dephlegmator*, R&D Journal of the SAIMEchE, 28, pp. 31 – 36, 2012.

Ito, H., *Pressure losses in smooth pipe bends*, Journal of Basic Engineering, 82 (1), pp. 131 – 141, 1960.

Ito, H., Imai, K., *Pressure losses in vaned elbows of circular cross section*, Journal of Basic Engineering, 88 (3), pp. 684 – 686, 1966.

Jorgensen, R., *Fan engineering*, Buffalo Forge Co., Buffalo, NY, 1961.

Kays, W.M., *Loss coefficients for abrupt changes in flow cross section with low Reynolds number flow in single and multiple tube systems*, Transactions of the ASME, 72 (8), pp. 1067 – 1074, 1950.

Kröger, D.G., *Air-cooled heat exchangers and cooling towers*, Penwell Corp., Tulsa, OK., 2004.

Leidenfrost, W., Korenic, B., *Evaporative cooling and heat transfer augmentation related to reduced condenser temperatures*, *Heat Transfer Engineering*, 3, pp. 38 – 59, 1982.

Li, J., Saraireh, M., Thorpe, G., *Condensation of vapor in the presence of non-condensable gas in condensers*, *International Journal of Heat and Mass Transfer*, 54, pp. 4078 – 4089, 2011.

Lindgren, B., Johansson, A.V., *Design and evaluation of a low speed wind tunnel with expanding corners*, Technical Report, Royal Institute of Technology Department of Mechanics, Stockholm, 2002.

Lindgren, B., Osterlund, J., Johansson, V., *Measurement and calculation of guide vane performance in expanding bends for wind tunnels*, *Experiments in Fluids*, 24, pp. 265 – 272, 1998.

Liu, P., Duan, H., Zhao, W., *Numerical investigation of hot air recirculation of air-cooled condensers at a large power plant*, *Applied Thermal Engineering*, 29, pp. 1927 – 1934, 2009.

Lockhart, L.W., Martinelli, R.C., *Proposed correlation of data for isothermal two-phase two-component flow in pipes*, *Chemical Engineering Process*, 45, pp. 39 – 48, 1949.

Lowe, H.J., Christie, D.G., *Heat transfer and pressure drop data on cooling tower packings and model studies of the resistance of natural draft towers to air flow*, *Proceedings of the International Heat Transfer Conference*, Boulder, Co., 1961.

Markland, E., *Analysis of flow from pipe manifolds*, *Engineering*, 187, pp. 150 – 151, 1959.

Maulbetsch, J.S., *Comparison of alternative cooling technologies for Californian power plants: economic, environmental and other trade offs*, EPRI: Palo Alto, CA and CEC: Sacramento, CA, 2002.

Maulbetsch, J.S., *Cooling systems: Some things that might work*, EPRI Workshop on Advance Thermoelectric Cooling Technologies, Charlotte, NC, 2008.

Maulbetsch, J.S., DiFilippo, M., *Spray enhancement of air-cooled condensers*, EPRI: Palo Alto, CA; CEC, Sacramento, CA and Crockett Cogeneration, 2003.

Maulbetsch, J.S., DiFilippo, M., *Effects of wind on air-cooled condenser performance*, Paper TP07-04, Cooling Technology Institute, 2007.

Mauro, A.W., Moreno Quiben, J., Mastrullo, R., Thome, J.R., *Comparison of experimental pressure drop data for two-phase flows to prediction methods using a general model*, International Journal of Refrigeration, 30, pp. 1358 – 1367, 2007.

McGowan, C., Zammit, K., Maulbetsch, J.S., *Field testing of wind effects on air-cooled condensers*, EPRI Workshop on Advanced Thermoelectric Cooling Technologies, Charlotte, NC, 2008.

Mehta, R.D., Bradshaw, P., *Design rules for small low speed wind tunnels*, Aeronautical Journal of the Royal Aeronautical Society, pp. 443 – 449, 1979.

Meyer, C.J., *Numerical investigation of the effect of inlet flow distortions on forced draft air-cooled heat exchanger performance*, Applied Thermal Engineering, 25, pp. 1634 – 1649, 2005.

Mickley, H.S., Ross, R.C., Squyers, A.L., Stewart, W.E., *Heat, mass and momentum transfer for flow over a flat plate with blowing or suction*, National Advisory Committee for Aeronautics: Technical Note 3208, 1954.

Mills, A.F., *Heat Transfer*, Prentice Hall, 1999.

Minkowycz, W.J., Sparrow, E.M., *Condensation heat transfer in the presence of noncondensables, interfacial resistance, superheating, variable properties, and diffusion*, International Journal of Heat and Mass Transfer, 9, pp. 1125 – 1144, 1966.

Mizushina, T., Ito, R., Miyasita, H., *Experimental study of an evaporative cooler*, International Chemical Engineering, 7, pp. 727 – 732, 1967.

Modi, P.P., Jayanti, S., *Pressure losses and flow maldistributions in ducts with sharp bends*, Chemical Engineering Research and Design, 82 (3), pp. 321 – 331, 2004.

Moreno Quiben, J., Thome, J.R., *Flow pattern based two-phase frictional pressure drop model for horizontal tubes, Part II: New phenomenological model*, International Journal of Heat and Fluid Flow, 28, pp. 1060 – 1072, 2007.

Muller-Steinhagen, H., Heck, K., *A simple friction pressure correlation for two-phase flow in pipes*, Chemical Engineering Process, 20, pp. 297 – 308, 1986.

Niitsu, Y., Naito, K., Anzai, T., *Studies on the characteristics and design procedure of evaporative coolers*, Journal of SHASE, 43, 1969.

Nikuradse, J., *Law of flow in rough pipes ("Strömungsgesetze in rauhen Rohren")*, VDI-Forschungsheft, pp. 361, 1933.

Ohnesorge, W.V., *Die bildung von Tropfen an Dusen und die auflosung flussiger Strahlen*, Journal of Applied Mathematics and Mechanics, 16 (6), pp. 355 – 358, 1936.

Owen, M.T.F., Kröger, D.G., *The effect of screens on air-cooled steam condenser performance under windy conditions*, Applied Thermal Engineering, 30, pp. 2610 – 2615, 2010.

Owen, R.G., Sardesai, R.S., Butterworth, D., *Two-phase pressure drop for condensation inside a horizontal tube*, Symposium on Advancement in Heat Exchangers, International Centre for Heat and Mass Transfer, 1981.

Palen, J., Yang, Z.H., *Reflux condensation flooding prediction*, Trans IChemE, 79 (A), pp. 463 – 469, 2001.

Parker, R.O., Treybal, R.E., *Heat and mass transfer characteristics of evaporative coolers*, AIChE Chemical Engineering Process Symposium Series, 57, pp. 138 – 149, 1961.

Patankar, S.V., *Numerical heat transfer*, McGraw-Hill, New York, 1980.

Patankar, S.V., Spalding, D.B., *A calculation procedure for heat, mass and momentum transfer in three dimensional duct flows*, International Journal of Heat and Mass Transfer, 15, pp. 1787 – 1806, 1972.

Rouse, H., *Elementary Mechanics of Fluids*, John Wiley and Sons, London, 1946.

Sacramento, J.C., Heggs, P.J., *The role of flooding in the design of vent and reflux condensers*, Applied Thermal Engineering, 29, pp. 1338 – 1345, 2009.

Schoenfeld, P.D., Kröger, D.G., *Flooding during reflux condensation of steam in an inclined elliptical tube*, R&D Journal of the SAIMechE, 16 (1), pp. 1 – 8, 2000.

Shah, M.M., *A general correlation for heat transfer during film condensation inside pipes*, International Journal of Heat and Mass Transfer, 22, pp. 547 – 556, 1979.

Shannak, B.A., *Frictional pressure drop of gas liquid two-phase flow in pipes*, Nuclear Engineering and Design, 238, pp. 3277 – 3284, 2008.

Shi, L., Shi, C., *Optimal design of guide vane in tree-branch shape direct air-cooled exhausted duct system*, International Conference on Energy and Environment Technology, Guilin, 2009.

Shi, L., Wu, X., Shi, C., Cheng, Y., *Numerical investigation on wet steam in manifolds of direct air-cooled exhausted duct in a 600 MW power unit*,

Proceedings of Second International Conference on Modelling and Simulation, Manchester, 2009.

Shih, T., Liu, W., Shabbir, A., Yang, Z., Zu, J., *A new k - ε eddy viscosity model for high Reynolds number turbulent flows*, Computers Fluids, 24 (3), pp. 227 – 238, 1995.

Spalding, B.D., *Basic equations of fluid mechanics and heat and mass transfer, and procedures for their solution*, HTS/76/6, Mechanical Engineering Department, Imperial College, 1976.

Thome, J.R., *Engineering Data Book III*, Wolverine Tube Inc., 2006.

Tritthart, M., Gutknecht, D., *Three-dimensional simulation of free-surface flows using polyhedral finite volumes*, Engineering Applications of Computational Fluid Mechanics, 1 (1), pp. 1 – 14, 2007.

Van Aarde, D.J., Kröger, D.G., *Flow losses through an array of A-frame heat exchangers*, Heat Transfer Engineering, 14 (1), pp. 43 – 51. 1993.

Van der Hegge Zijen, B.G., *Flow through uniformly tapered pipes*, Applied Scientific Research, A (3), pp. 144 – 162, 1952.

Zapke, A., Kröger, D.G., *The influence of fluid properties and inlet geometry on flooding in vertical and inclined tubes*, International Journal of Multiphase Flow, 22 (3), pp. 461 – 472, 1996.

Zapke, A., *Characterisitics of gas-liquid counterflow in inclined ducts with particular reference to reflux condensers*, PhD Dissertation, Department of Mechanical and Mechatronic Engineering, University of Stellenbosch, South Africa, 2007.

Zapke, A., Kröger, D.G., *Pressure drop during gas-liquid countercurrent flow in inclined rectangular ducts*, Proceedings of the 5th International Heat Pipe Symposium, pp. 461 – 472, Melbourne, 1997.

Zapke, A., Kröger, D.G., *Vapor-condensate interactions during counterflow in inclined reflux condensers*, ASME National Heat Transfer Conference, 342, pp. 157 – 162, 1997.

Zipfel, T., Kröger, D.G., *Flow loss coefficients at air-cooled condenser finned tube inlets*, R&D Journal of the SAIMechE, 13 (2), pp. 62 – 67, 1997.

Zipfel, T., Kröger, D.G., *A design method for single-finned-tube-row air-cooled steam condenser to avoid backflow of steam into any finned tube*, R&D Journal of the SAIMechE, 13 (2), pp. 68 – 75, 1997.

Zucrow, M.J., Hoffman, J.D., *Gas dynamics*, Wiley, New York, 1976.

Zukauskas, A., Ulinskas, R., *Heat transfer in tube banks in crossflow*, Hemisphere Publishing Corp., 1988.

APPENDIX A. AIR-COOLED STEAM CONDENSER SPECIFICATIONS

The ACC streets considered in this study consist of five primary condenser cells and one dephlegmator cell. The dephlegmator cell is located third from the inlet of the street (see Figure 2.1). The finned-tube heat exchanger and axial flow fan specifications are given in Appendices A.1 and A.2 (Kröger, 2004). Appendix A.3 describes the design point specification of the power plant considered in the analysis presented in Chapter 6.

A.1 Finned-tube heat exchanger

Table A.1: Finned-tube heat exchanger specifications

Number of heat exchanger bundles per cell	$n_b = 8$
Finned tube length in primary condenser bundles	$L_{t(pri)} = 9.50 \text{ m}$
Finned tube length in dephlegmator bundles	$L_{t(dep)} = 7.52 \text{ m}$
Effective frontal area of a primary condenser bundle	$A_{(fr)pri} = 24.3936 \text{ m}^2$
Effective frontal area of a dephlegmator bundle	$A_{(fr)dep} = 19.3095 \text{ m}^2$
Flattened tube hydraulic diameter	$d_h = 0.02975 \text{ m}$
Tube inside height	$H_t = 0.097 \text{ m}$
Tube inside width	$W_t = 0.017 \text{ m}$
Inside area of tube per unit length	$A_{ti} = 0.2168 \text{ m}$
Inside cross-sectional tube area	$A_{ts} = 0.00159 \text{ m}^2$
Number of tube rows per bundle	$n_r = 2$
Number of tubes per bundle: first row	$n_{tb(1)} = 57$
Number of tubes per bundle: second row	$n_{tb(2)} = 58$
Number of vapor passes	$n_{vp} = 1$
Heat exchanger half-apex angle	$\theta = 30^\circ$
Ratio of minimum to free stream flow area through the bundle	$\sigma = 0.48$
Ratio of minimum to free stream flow area at the inlet of the bundle	$\sigma_{2I} = 0.86$

The finned tube characteristic heat transfer parameters and the bundle air-side loss coefficient for normal isothermal flow are described by Equations (A.1) – (A.3). These equations are based on the characteristic flow parameter Ry , defined in Equation (A.4), which is similar to the Reynolds number but is not a function of

any equivalent or hydraulic diameter (d_e). The use of Ry instead of Re allows for meaningful comparison of the performance characteristics of different finned tube surfaces without the possibility of confusion due to the relatively arbitrary nature of the definition of d_e in such cases (Kröger, 2004).

$$Ny_1 = 366.007945Ry^{0.433256} \quad (\text{A.1})$$

$$Ny_2 = 360.588007Ry^{0.470373} \quad (\text{A.2})$$

$$K_{he} = 4464.831Ry^{-0.43927} \quad (\text{A.3})$$

$$Ry = m/\mu A_{fr} \quad (\text{A.4})$$

A.2 Axial flow fan

Table A.2: Axial flow fan specifications

Fan diameter	$d_F = 9.145 \text{ m}$
Fan casing diameter	$d_c = 9.17 \text{ m}$
Hub/tip ratio	$d_h/d_F = 0.4$
Ratio of hub height to fan diameter	$H_h/d_F = 0.1$
Height of the inlet shroud	$H_b = 1.92 \text{ m}$
Inlet shroud radius	$r_b = 1.16 \text{ m}$
Number of fan blades	$n_{bl} = 8$
Blade angle	$\psi = 34.5^\circ$
Rotational speed	$N = 125 \text{ rpm}$
Inlet screen distance from fan blade (upstream)	$x_{si} = 1.30 \text{ m}$
Support beam distance from fan blade (upstream)	$x_{bi} = 1.34 \text{ m}$
Support beam distance from fan blade (downstream)	$x_{bo} = 0.53 \text{ m}$
Walkway distance from fan blade (downstream)	$x_{so} = 1.0 \text{ m}$
Ratio of inlet screen area to fan casing area	$\sigma_{si} = 0.125$
Ratio of support beam area to fan casing area (upstream)	$\sigma_{bi} = 0.15$
Ratio of support beam area to fan casing area (downstream)	$\sigma_{bo} = 0.05$
Ratio of walkway area to fan casing area	$\sigma_{so} = 0.10$

The fan static pressure characteristic is described by Equation (A.4) with the corresponding fan power consumption described by Equation (A.5).

$$\Delta p_{Fs} = 320.0452 - 0.2975V_a + 6.3515 \times 10^{-4}V_a^2 - 8.14 \times 10^{-7}V_a^3, \quad \text{N/m}^2 \quad (\text{A.4})$$

$$P_F = 186645.2333 - 59.41386339V_a + 0.476168398V_a^2 - 5.08308 \times 10^{-4}V_a^3, \quad \text{W} \quad (\text{A.5})$$

A.3 Plant design point specifications

Table A.3: Design point specifications

Unit output at design point	$P_{gen} = 237.96 \text{ MW}$
Heat load on ACC	$Q_{ACC} = 306.71 \text{ MW}$
Total steam flow rate	$m_v = 133 \text{ kg/s}$
Steam turbine backpressure	$p_v = 19925.16 \text{ N/m}^2$
Condensing temperature	$T_v = 60 \text{ }^\circ\text{C}$

APPENDIX B. FLUID PROPERTIES**B.1 Dry air ($220 \text{ K} \leq T \leq 330 \text{ K}$, $p = 101325 \text{ N/m}^2$)**

$$\rho_a = p_a / 287.08 T_a, \text{ kg/m}^3 \quad (\text{B.1})$$

$$c_{pa} = 1.045356 \times 10^{-3} - 3.161783 \times 10^{-1} T + 7.083814 \times 10^{-4} T^2 - 2.705209 \times 10^{-7} T^3, \text{ J/kgK} \quad (\text{B.2})$$

$$\mu_a = 2.287973 \times 10^{-6} + 6.259793 \times 10^{-8} T - 3.131956 \times 10^{-11} T^2 + 8.15038 \times 10^{-15} T^3, \text{ kg/ms} \quad (\text{B.3})$$

$$k_a = -4.937787 \times 10^{-4} + 1.018087 \times 10^{-4} T - 4.627937 \times 10^{-8} T^2 + 1.250603 \times 10^{-11} T^3, \text{ W/mK} \quad (\text{B.4})$$

B.2 Saturated water vapor ($273.15 \text{ K} \leq T \leq 380 \text{ K}$)

$$p_v = 10^z, \text{ N/m}^2 \quad (\text{B.5})$$

$$z = 10.79586 \left(1 - \frac{273.16}{T} \right) + 5.02808 \log_{10} \left(\frac{273.16}{T} \right) + 1.50474 \times 10^{-4} \left[1 - 10^{-8.29692 \left(\frac{T}{273.16} - 1 \right)} \right] + 4.2873 \times 10^{-4} \left[10^{4.76955 \left(1 - \frac{273.16}{T} \right)} - 1 \right] + 2.786118312 \quad (\text{B.6})$$

$$T_v = 164.630366 + 1.832295 \times 10^{-3} p_v + 4.27215 \times 10^{-10} p_v^2 + 3.738954 \times 10^3 p_v^{-1} - 7.01204 \times 10^5 p_v^{-2} + 16.161488 \ln(p_v) - 1.437169 \times 10^{-4} p_v \ln(p_v), \text{ K} \quad (\text{B.7})$$

$$\rho_v = -4.062329056 + 0.10277044 T - 9.76300388 \times 10^{-4} T^2 + 4.475240795 \times 10^{-6} T^3 - 1.004596894 \times 10^{-8} T^4 + 8.9154895 \times 10^{-12} T^5, \text{ kg/m}^3 \quad (\text{B.8})$$

$$c_{pv} = 1.3605 \times 10^{-3} + 2.31334 T - 2.46784 \times 10^{-10} T^5 + 5.91332 \times 10^{-13} T^6, \text{ J/kg} \quad (\text{B.9})$$

$$\begin{aligned} \mu_v &= 2.562435 \times 10^{-6} + 1.816683 \times 10^{-8} T + 2.579066 \times 10^{-11} T^2 \\ &\quad - 1.067299 \times 10^{-14} T^3, \text{ kg/ms} \end{aligned} \quad (\text{B.10})$$

$$\begin{aligned} k_v &= 1.3046 \times 10^{-2} - 3.756191 \times 10^{-5} T + 2.217964 \times 10^{-7} T^2 \\ &\quad - 1.111562 \times 10^{-10} T^3, \text{ W/mK} \end{aligned} \quad (\text{B.11})$$

B.3 Saturated water liquid (273.15 K ≤ T ≤ 380 K)

$$\rho_l = \left(\begin{array}{l} 1.49343 \times 10^{-3} - 3.7164 \times 10^{-6} T + 7.09782 \times 10^{-9} T^2 \\ -1.90321 \times 10^{-20} T^6 \end{array} \right)^{-1}, \text{ kg/m}^3 \quad (\text{B.12})$$

$$\begin{aligned} c_{pl} &= 8.15599 \times 10^3 - 28.0627 T + 5.11283 \times 10^{-2} T^2 \\ &\quad - 2.17582 \times 10^{-13} T^6, \text{ J/kgK} \end{aligned} \quad (\text{B.13})$$

$$\mu_l = 2.414 \times 10^{-5} \times 10^{247.8/(T-140)}, \text{ kg/ms} \quad (\text{B.14})$$

$$\begin{aligned} k_l &= -0.614255 + 6.9962 \times 10^{-3} T - 1.01075 \times 10^{-5} T^2 \\ &\quad + 4.74737 \times 10^{-12} T^4, \text{ W/mK} \end{aligned} \quad (\text{B.15})$$

$$\begin{aligned} i_{fg} &= 3.4831814 \times 10^6 - 5.8627703 \times 10^3 T + 12.139568 T^2 \\ &\quad - 1.40290431 \times 10^{-2} T^3, \text{ J/kg} \end{aligned} \quad (\text{B.16})$$

$$\begin{aligned} \sigma_l &= 5.148103 \times 10^{-2} + 3.998714 \times 10^{-4} T - 1.4721869 \times 10^{-6} T^2 \\ &\quad + 1.21405335 \times 10^{-9} T^3, \text{ N/m} \end{aligned} \quad (\text{B.17})$$

$$p_{cr} = 22.09 \times 10^6 \text{ N/m}^2 \quad (\text{B.18})$$

B.4 Mixtures of air and water vapor

$$\rho_{av} = (1+w) \left(1 - \frac{w}{w+0.62198} \right) \frac{P_{abs}}{287.08T}, \text{ kg air} \cdot \text{vapour/m}^3 \quad (\text{B.19})$$

$$c_{pav} = (c_{pa} + w c_{pv}) / (1+w), \text{ J/kg air} \cdot \text{vapourK} \quad (\text{B.20})$$

$$c_{pma} = c_{pa} + w c_{pv}, \text{ J/kg dry air} \quad (\text{B.21})$$

$$\mu_{av} = (X_a \mu_a M_a^{0.5} + X_v \mu_v M_v^{0.5}) / (X_a M_a^{0.5} + X_v M_v^{0.5}), \text{ kg air} \cdot \text{vapour/ms} \quad (\text{B.22})$$

$$k_{av} = (X_a k_a M_a^{0.33} + X_v k_v M_v^{0.33}) / (X_a M_a^{0.33} + X_v M_v^{0.33}), \text{ W/mK} \quad (\text{B.23})$$

$$X_a = 1 / (1 + 1.608w) \quad (\text{B.24})$$

$$X_v = w / (w + 0.622) \quad (\text{B.25})$$

$$M_a = 28.97 \text{ kg/mol} \quad (\text{B.26})$$

$$M_v = 18.016 \text{ kg/mol} \quad (\text{B.27})$$

$$w = \left[\frac{2501.6 - 2.3263(T_{wb} - 273.15)}{2501.6 + 1.8577(T - 273.15) - 4.184(T_{wb} - 273.15)} \right] \left(\frac{0.62509 p_{vwb}}{p_{abs} - 1.005 p_{vwb}} \right) - \left[\frac{1.00416(T - T_{wb})}{2501.6 + 1.8577(T - 273.15) - 4.184(T_{wb} - 273.15)} \right], \text{ kg/kg dry air} \quad (\text{B.28})$$

$$i_{av} = \frac{c_{pa}(T - 273.15) + w[i_{fgwo} + c_{pv}(T - 273.15)]}{1 + w}, \text{ J/kg air} \cdot \text{vapour} \quad (\text{B.29})$$

$$i_{ma} = c_{pa}(T - 273.15) + w[i_{fgwo} + c_{pv}(T - 273.15)], \text{ J/kg dry air} \quad (\text{B.30})$$

Note: Equations (B.1) – (B.30) were sourced from Kröger (2004).

APPENDIX C. THE EFFECT OF GUIDE VANES ON MITER BEND LOSS COEFFICIENT

As mentioned in Section 3.4.2, single 90° miter bends are often found in ACC distributing manifolds. These bends typically have cascades of guide vanes to reduce their loss coefficient, as shown in Figure 3.4 and repeated in Figure C.1 for convenience.

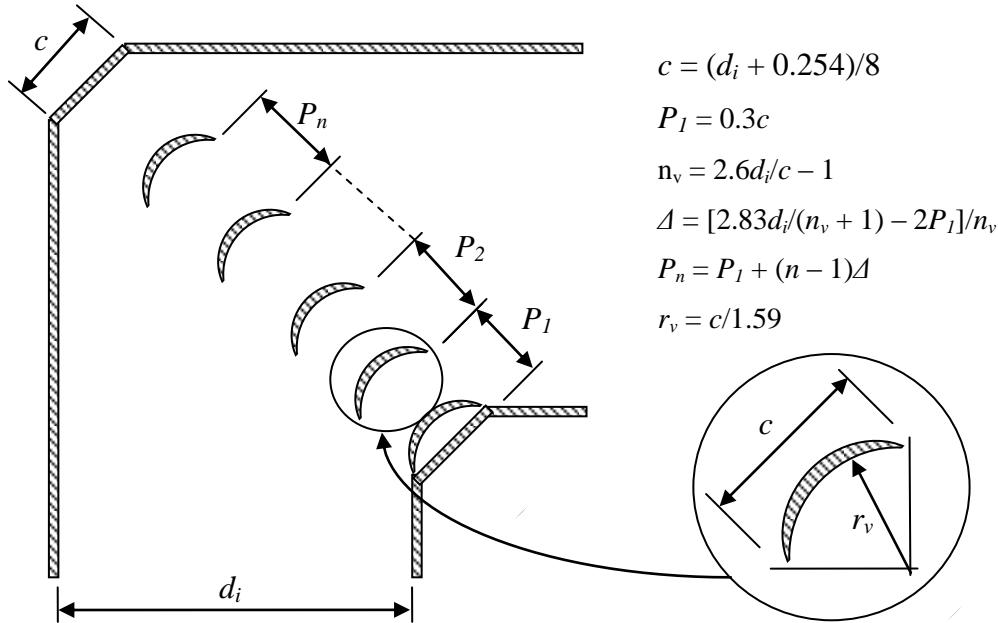


Figure C.1: Single miter bend with a cascade of circular-arc guide vanes (Kröger, 2004)

C.1 Internal flow in a bend

During internal flow through a bend the fluid near the centre is subjected to a larger centrifugal force since it has a higher velocity than the fluid at the walls. A radial pressure gradient is formed in the bend as a result of this force imbalance (Modi and Jayanti, 2004). This pressure gradient causes a secondary flow pattern to establish perpendicular to the primary axial flow direction. The nature of this secondary flow is highly complex and accounts for a large portion of the loss experienced over the bend. The installation of guide vanes in a bend splits the

flow into several narrow channels. As a result, the magnitude of the radial pressure gradient is reduced and the development of the secondary flow patterns is impeded. The installation of vanes should therefore have the desirable effect of reducing the bend loss as well as producing a more uniform flow pattern immediately downstream of the bend.

Ito and Imai (1966) experimentally investigated the effect of guide vanes on the loss coefficient of a 90° bend in a circular duct ($d_i = 0.035$ m). They report a significant decrease in bend loss coefficient when a single vane was added to the bend. Furthermore, they found that the addition of a second guide vane resulted in an additional slight reduction in the bend loss coefficient. Ito and Imai's experiment successfully demonstrated the beneficial effect of guide vanes on bend loss coefficient. However, the small scale of their experiment did not allow for further investigation of the effect of increasing the number of guide vanes on the bend losses. It is expected that for large diameter bends, such as those that might be used in a large scale ACC, the installation of additional guide vanes may have a significant impact on the bend loss. In such bends, the channels created by a single vane are still large enough to result in the development of measurable secondary flow patterns and further division of these channels should aid in mitigating such patterns.

Several studies regarding the use of guide vanes in 90° bends exist in the field of low speed wind tunnel design. Lindgren and Johansson (2002) numerically and experimentally investigated guide vane profile in expanding bends for use in such wind tunnels. They report that carefully designed vane profiles can have a measurable influence on the bend loss coefficient and that these profiles must be optimized for specific bend configurations. Lindgren et al. (1998) report similar results, with airfoil-type blade profiles found to offer up to five times lower bend loss coefficients than the common quarter circle, constant thickness vane profile such as that considered here. Lindgren et al. briefly mention the effect of vane pitch on bend loss coefficient and identify an optimum vane pitch for a specific bend configuration. Mehta and Bradshaw (1979) suggest that guide vane pitch

should not exceed 0.25 times the vane chord length. No comprehensive information on guide vane spacing applicable to miter bends in large circular ducts could be found in the literature.

This appendix presents the findings of a numerical and experimental investigation into the effect of the number of guide vanes on the loss coefficient of a 90° single miter bend in a circular duct ($d_i = 4.99$ m).

C.2 CFD model

The commercially available CFD code FLUENT was used for the numerical investigation. The SIMPLE solution algorithm (Patankar, 1980) was applied with second order upwind differencing and the realizable k- ϵ turbulence model (Shih et al., 1995).

A duct ($d_i = 4.988$ m) similar in size to one employed in the distributing manifold at an existing ACC was considered. Saturated water vapour ($x = 1$) at a temperature of $T_v = 60$ °C flows through the duct at a mass flow rate of $m_v = 200$ kg/s. The corresponding Reynolds number in the duct is $Re_v = 4.6 \times 10^6$. The simulations were later repeated for $Re_v = 8.0 \times 10^6$ for comparison to experimental data.

A polyhedral mesh was used in an attempt to reduce the probability of numerical diffusion in the vicinity of the bend where secondary flow patterns are likely to be present. A grid sensitivity analysis was carried out to determine the appropriate grid resolution. The final mesh consisted of approximately 423 500 polyhedral cells with 68 divisions on the duct circumference. A growth rate of 1.18 was applied away from all surfaces in the radial direction and from the centre of the bend in the axial direction.

A fully developed turbulent velocity profile (Zucrow and Hoffman, 1976) was applied at the model inlet 25 diameters upstream of the bend. A pressure outlet boundary condition was used at the model outlet located 55 diameters downstream of the bend. The duct walls were represented by the “no slip”

boundary condition and standard wall functions were applied to bridge the turbulent boundary layer. The absolute pressure in the duct was recorded on a line surface running along its center.

C.3 Experimental setup

A simple experiment was carried out to verify the numerical results. The experiment consisted of two sections of round duct connected by a vaned miter bend. The duct downstream of the bend was connected to the University of Stellenbosch's atmospheric open-loop induced draft wind tunnel, shown schematically in Figure C.2 (see Kröger (2004) for a detailed description of the wind tunnel). In Figure C.2, items 1 – 4 make up the test setup while items 5 – 11 belong to the wind tunnel.

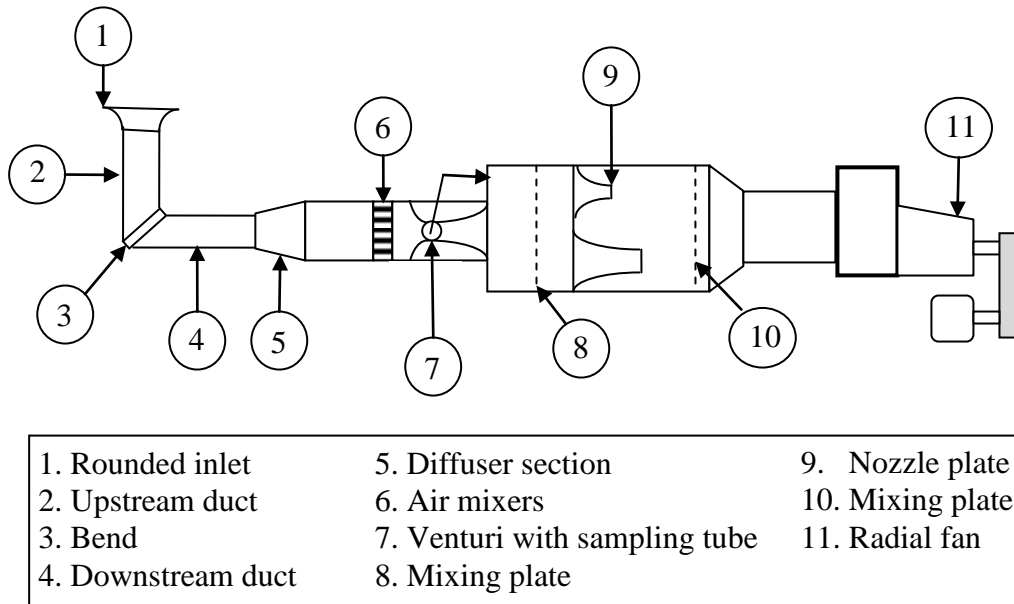


Figure C.2: Experimental setup

Laboratory space restrictions and wind tunnel dimensions limited the experimental bend diameter to $d_i = 0.25$ m with duct lengths of five diameters up- and downstream of the bend (items 2 and 4 in Figure C.2 respectively). A rounded inlet was attached to the upstream duct in an attempt to facilitate fully developed

flow upstream of the bend. The experimental Reynolds number for the flow of air through the test section was $7.65 \times 10^5 \leq Re_a \leq 7.97 \times 10^5$.

The pressure distribution in the ducts was measured at one diameter intervals from the bend in both the up- and downstream sections. Three pressure taps, equally spaced around the duct circumference, were installed in the duct wall at each of the measurement locations in an attempt to measure the average static pressure at each location. The inner surface of the duct was carefully smoothed in the vicinity of the pressure taps. The pressure taps were connected to Endress and Hauser Deltabar S PMD70 pressure transducers (span 0.25 mbar – 3 bar, accuracy 0.075%) for data collection. The pressure transducers were manually calibrated using a Betz manometer before testing was commenced.

C.4 Calculating the bend loss coefficient

The bend loss coefficient was calculated using, as closely as possible, the method described by Ito (1960) in both the numerical and experimental investigations. Figure C.3 shows a schematic of a typical hydraulic gradient for flow through a duct bend. In Figure C.3, A-B-C-D-E represents the actual hydraulic gradient, while A-B1-C1-D1-E1 represents the hydraulic gradient for a corresponding straight duct. A-B1-C2-D2-E2 represents the hydraulic gradient that would exist if the bend section was removed entirely.

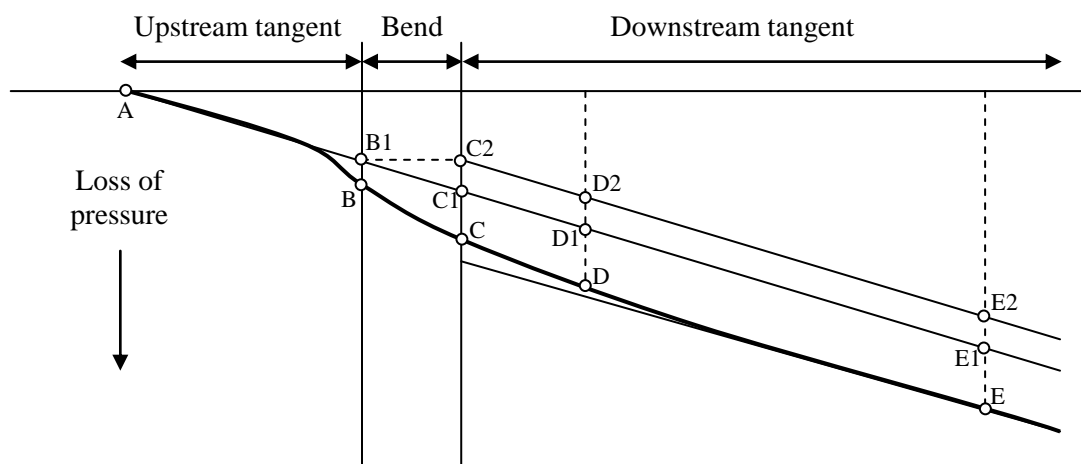


Figure C.3: Typical hydraulic gradient through a bend (Ito, 1960)

The total loss attributable to the bend is given by the difference in pressure between points E and E2 as shown in Equation (C.1).

$$K_{mb} = \frac{P_{E2} - P_E}{(\rho v^2 / 2)} \quad (\text{C.1})$$

The measurement for point E must be made in a region where the flow has become fully developed downstream of the bend. Ito (1960) states that for most of the cases tested by him a distance of 50 diameters was necessary for the flow to develop fully. In this numerical investigation fully developed flow was observed after approximately 10 diameters.

C.5 Results

The CFD prediction of the effect of the number of guide vanes on miter bend loss coefficient was shown in Figure 3.5. The predicted effect is compared to the experimental results in Figure C.4. According to Figure C.1 (Kröger, 2004), 19 guide vanes are recommended for the numerically investigated miter bend.

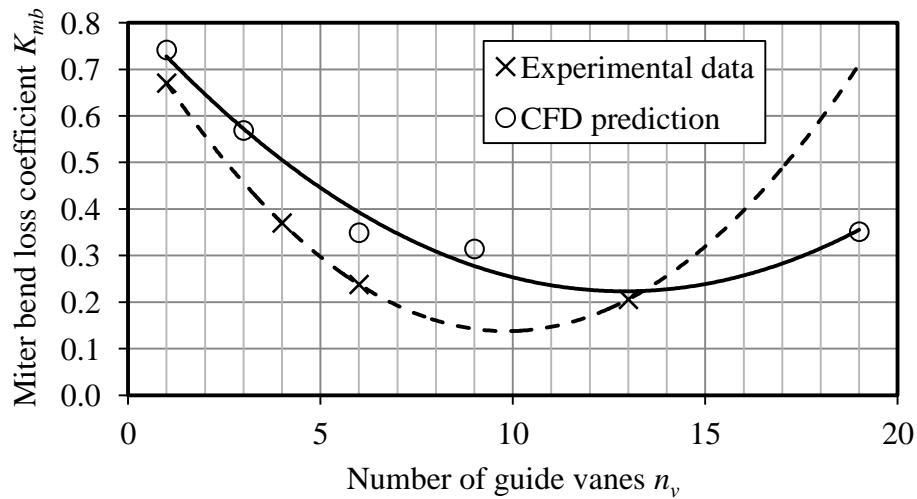


Figure C.4: The effect of the number of guide vanes on miter bend loss coefficient

Jorgensen (1961) suggests the loss coefficient for a single miter bend with guide vanes is $K_{mb} = 0.28$. The CFD data presented in Figure C.4, where the predicted

loss coefficient for $6 \leq n_v \leq 20$ is in the range $0.2 \leq K_{mb} \leq 0.4$ and $K_{mb} = 0.35$ for $n_v = 19$, corresponds relatively well with this suggestion.

Despite discrepancies in the values, the trends in the numerical and experimental data are the same. A vaneless bend has a high loss coefficient. The bend loss coefficient decreases as vanes are added. A minimum loss coefficient is reached in the vicinity of 10 – 15 vanes after which adding more guide vanes is shown to increase the loss coefficient. This behaviour was also identified and briefly reported on by Lindgren et al. (1998) who found that decreasing guide vane pitch initially reduced the bend loss coefficient in their experiments but then sharply increased the losses if decreased beyond an optimum value. Lindgren et al. state that it is likely that the value of the optimum guide vane pitch will be strongly dependant on bend configuration.

The discrepancy between the values of the numerically and experimentally predicted loss coefficients may be caused by several factors. In the experimental setup measurements of the pressure distribution were only carried out to five diameters downstream of the bend due to space constraints. As mentioned previously, fully developed flow is only expected to re-establish after 10 – 50 diameters downstream of the bend. The possibility therefore exists that the flow may not have had sufficient distance to develop fully in the measurement section after the bend. Also, the guide vanes manufactured for the experiment were observed to be not completely smoothly rounded and were instead bent from flat plate into a rounded profile made from several small straight sections. As a result the experimental vanes were not entirely representative of the perfectly rounded and infinitely thin vanes considered in the numerical model. Nonetheless, the experimental data verifies the trend predicted by the numerical results.

C.6 Conclusion

Adding guide vanes to a miter bend can measurably decrease the bend loss coefficient. An optimum number of guide vanes exists after which the bend loss coefficient begins to increase with the addition of more vanes. Traditionally the

number of vanes recommended for a bend is determined as a function of the duct diameter (see Figure C.1). Care should be taken to identify the optimum number of guide vanes for a given installation so as to minimize the pressure loss through the ducting system. This study indicates that for the miter bend considered here, typical of one that may be employed at large ACCs, the lowest bend pressure loss would be achieved with 13 guide vanes, approximately two-thirds the recommended number.

It should be noted that the number of guide vanes that results in the most desirable flow distribution downstream of a bend may be greater than the optimum number of vanes with respect to bend losses. In the case of an ACC distributing manifold it may be useful to optimize flow distributions in the bends immediately upstream of the heat exchangers while focusing on reduced losses in the bends further downstream.

APPENDIX D. VERIFICATION OF THE VAPOR FLOW DISTRIBUTION MODEL

D.1 Verification of the CFD model

The accuracy of the CFD model was verified through a comparison to the experiments of Zipfel (1997). Chapter 4.2.2 describes the comparison in more detail. A comparison of the CFD predictions of the current model to Zipfel's experimental results for various header-to-lateral velocity ratios is shown in Figures D.1 – D.4.

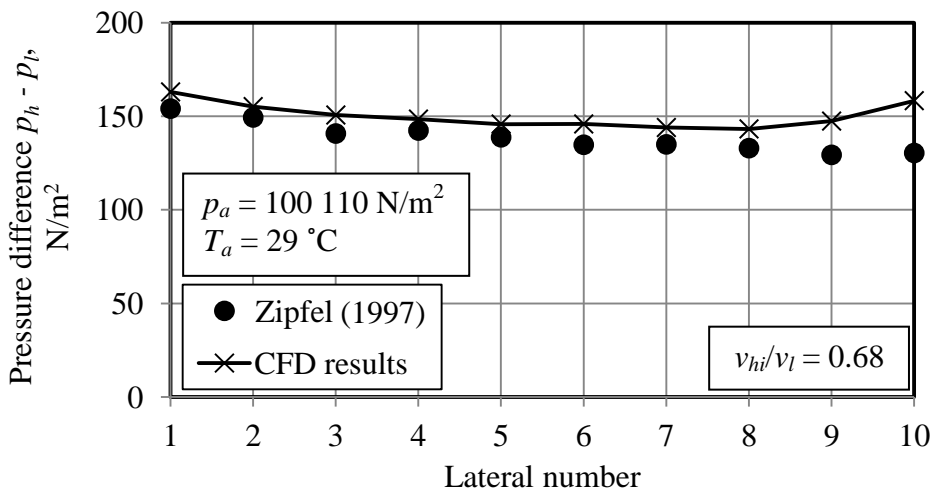


Figure D.1: Comparison of the CFD and experimental results for $v_{hi}/v_l = 0.68$

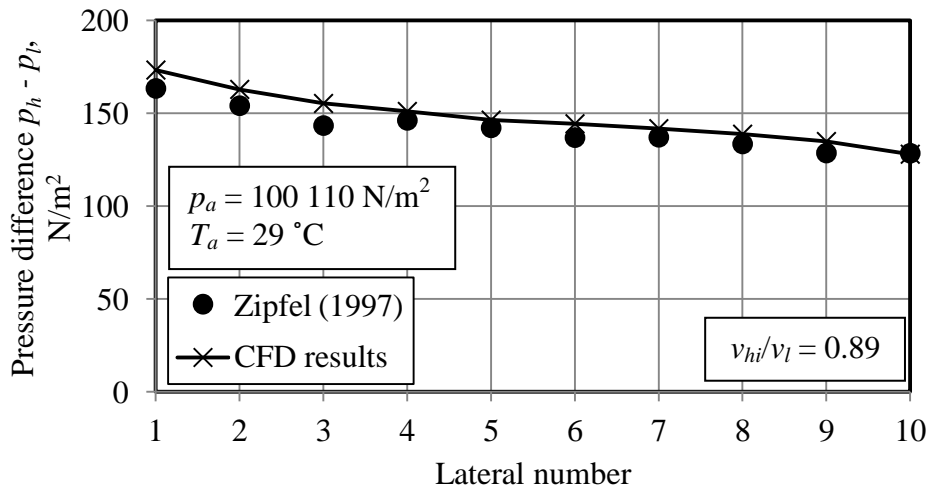


Figure D.2: Comparison of the CFD and experimental results for $v_{hi}/v_l = 0.89$

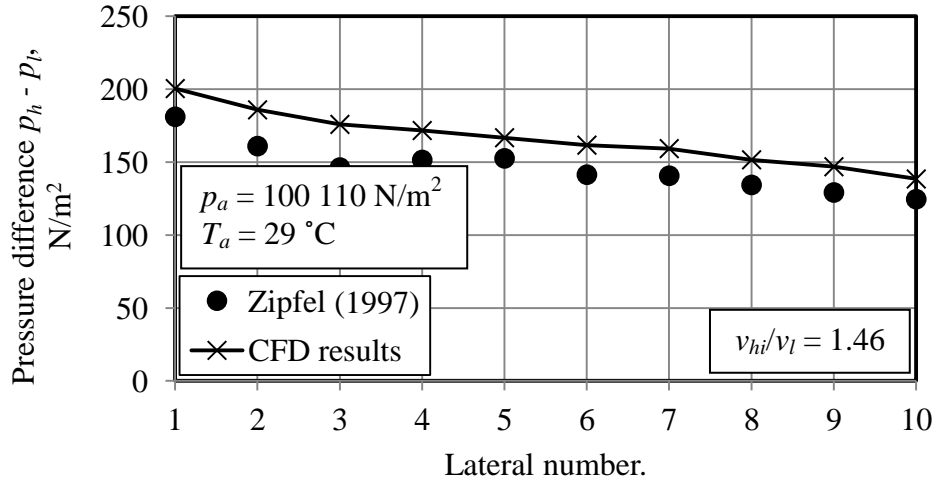


Figure D.3: Comparison of the CFD and experimental results for $v_{hi}/v_l = 1.46$

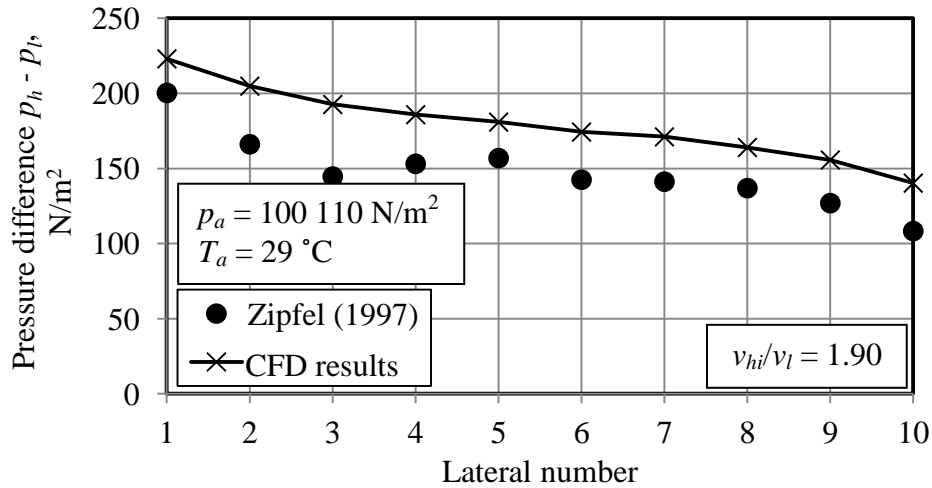


Figure D.4: Comparison of the CFD and experimental results for $v_{hi}/v_l = 1.90$

D.2 Verification of the numerical flow distribution calculation code

The accuracy of the numerical flow distribution calculation code was verified through a comparison to the experiments of Bajura and Jones (1976). Figures D.5 – D.8 show the comparison for various manifold configurations with $C_d = 0.4155$.

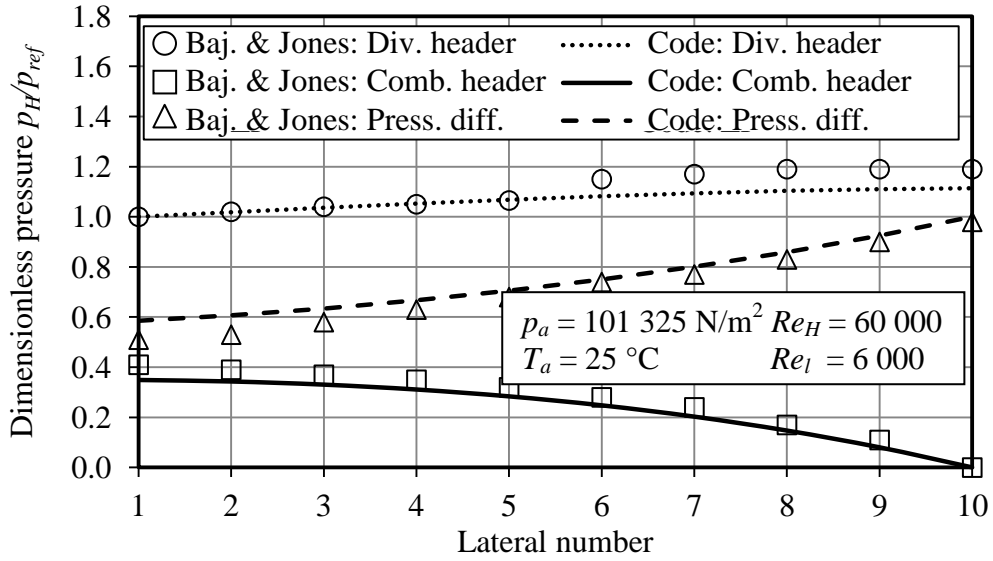


Figure D.5: Comparison of the header pressure distributions for a 10 lateral parallel flow manifold

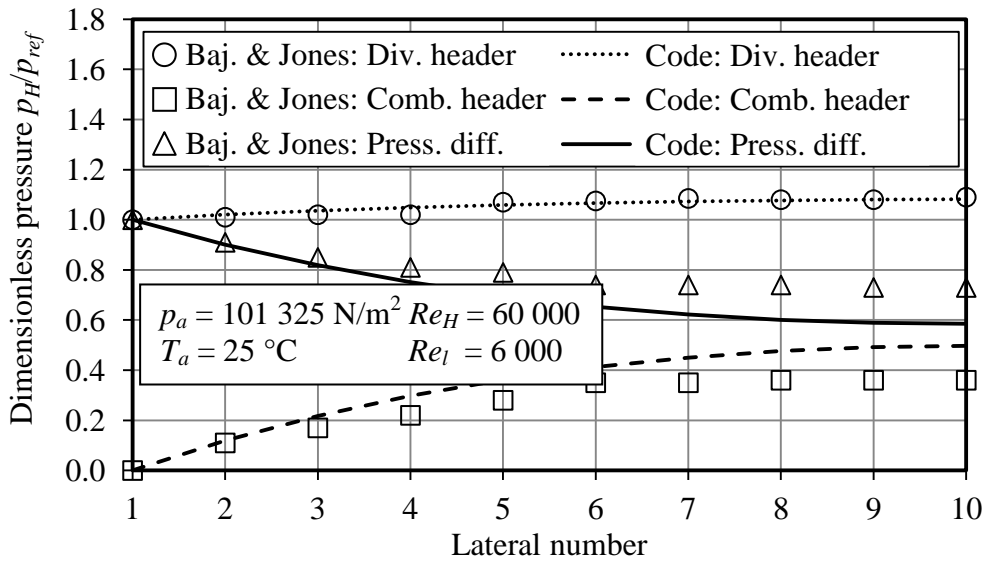


Figure D.6: Comparison of the header pressure distributions for a 10 lateral reverse flow manifold

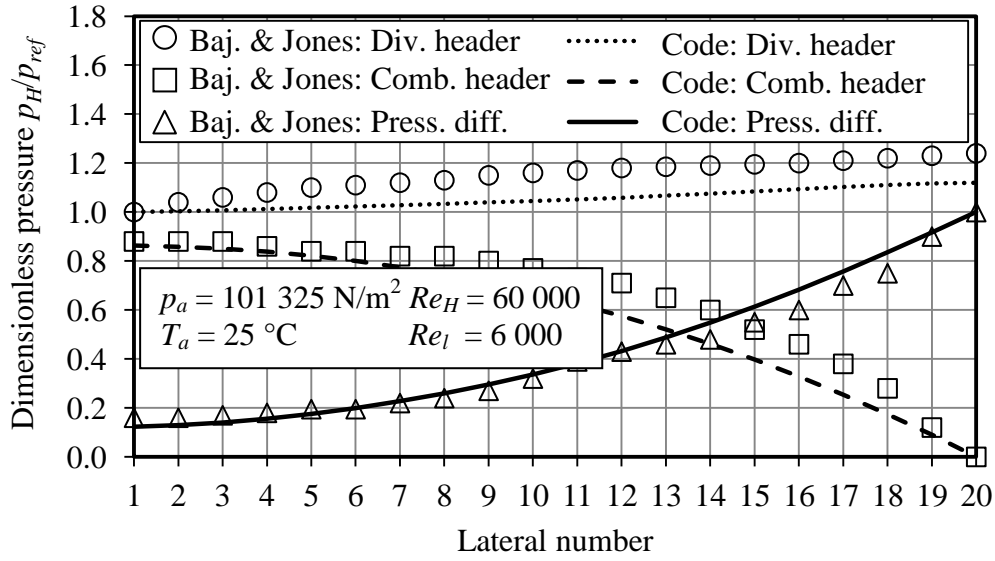


Figure D.7: Comparison of the header pressure distributions for a 20 lateral parallel flow manifold

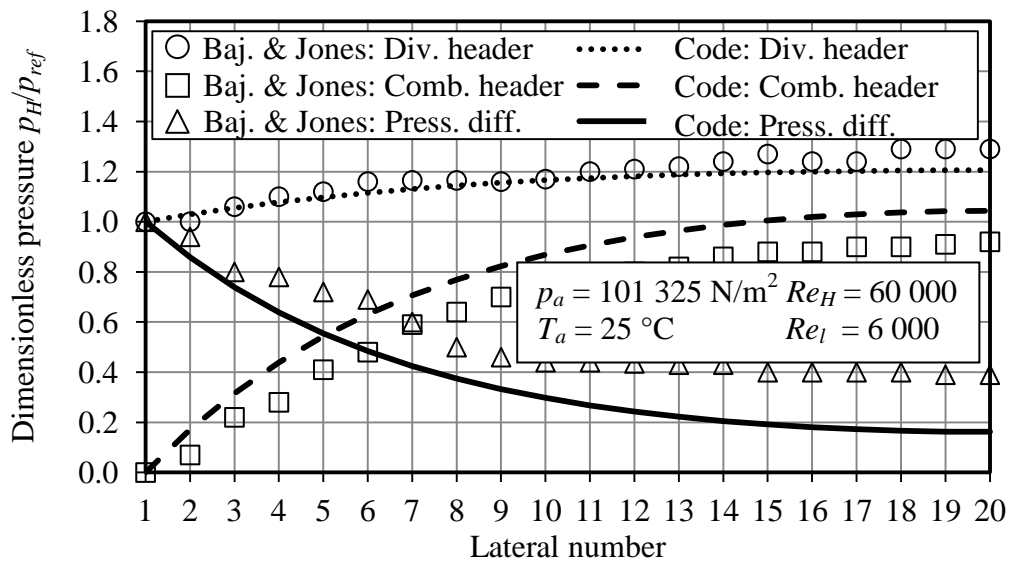


Figure D.8: Comparison of the header pressure distributions for a 20 lateral reverse flow manifold

APPENDIX E. EJECTOR CAPACITY AND VAPOR BACKFLOW IN A CONVENTIONAL DEPHLEGMATOR

E.1 Sample calculation: Required ejector capacity

Consider the two-row dephlegmator shown schematically in Figure E.1.

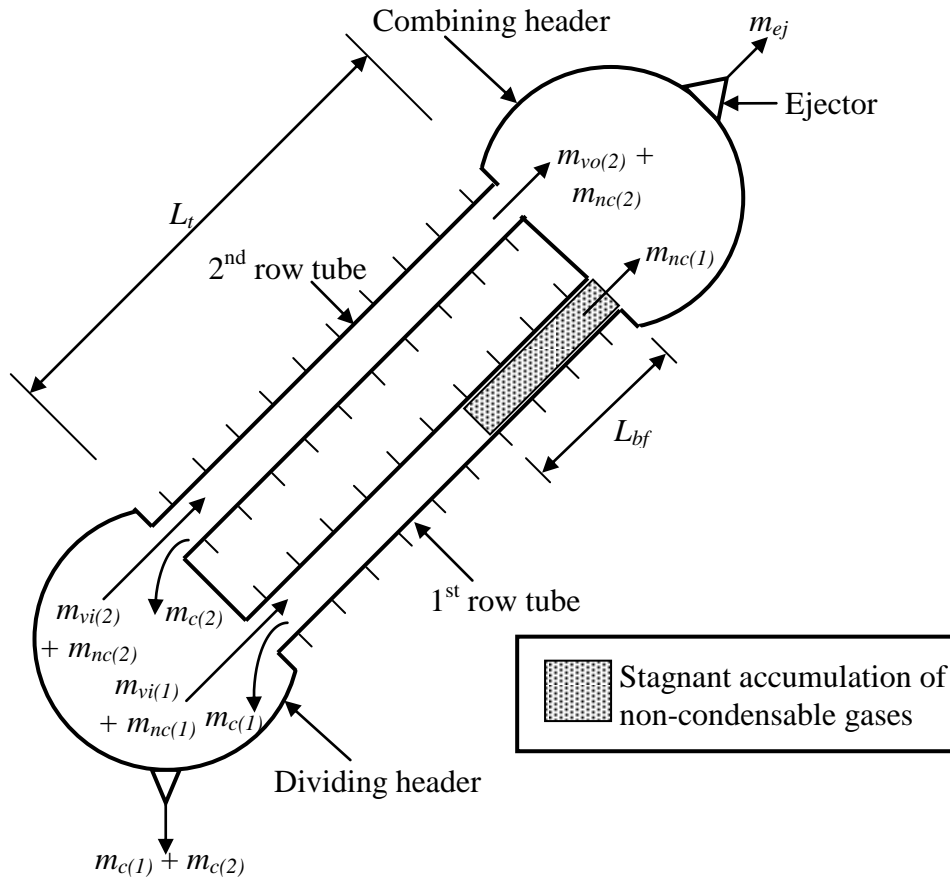


Figure E.1: Dephlegmator tubes with non-condensable gas accumulation

For $T_v = 60\text{ }^\circ\text{C}$ and $T_a = 20\text{ }^\circ\text{C}$, the condensation rates in the primary condenser and dephlegmator tubes for 100 % effective operation are given in Table E.1.

Table E.1: Condensation rates for 100 % effective operation

	Primary condenser, kg/s	Dephlegmator, kg/s
Single tube: First row	9.143×10^{-3}	7.756×10^{-3}
Single tube: Second row	7.286×10^{-3}	6.441×10^{-3}

The total rate of condensation in each primary condenser cell is correspondingly $m_{c(pri)} = 7.55$ kg/s, while in the dephlegmator $m_{c(dep)} = 6.475$ kg/s. The total amount of vapor condensed in the ACC is therefore,

$$m_{c(tot)} = 4 \times (5m_{c(pri)} + m_{c(dep)}) = 4 \times (5 \times 7.55 + 6.475) = 179.6 \text{ kg/s}$$

With a $1:10^4$ concentration of non-condensable gases based on the turbine outlet condition, the amount of non-condensables in the system is,

$$m_{nc(tot)} = 179.6/10^4 = 0.01769 \text{ kg/s}$$

The mass flow rate of non-condensable gases entering each dephlegmator is therefore,

$$m_{nc(1)} + m_{nc(2)} = m_{nc(tot)}/4 = 4.423 \times 10^{-3} \text{ kg/s}$$

The vapor density and dynamic viscosity can be calculated from Equations (B.8) and (B.10) respectively.

$$\begin{aligned} \rho_v &= -4.062329056 + 0.10277044(333.15) - 9.76300388 \times 10^{-4}(333.15)^2 \\ &\quad + 4.475240795 \times 10^{-6}(333.15)^3 - 1.004596894 \times 10^{-8}(333.15)^4 \\ &\quad + 8.9154895 \times 10^{-12}(333.15)^5 \\ &= 0.1302 \text{ kg/m}^3 \end{aligned}$$

$$\begin{aligned} \mu_v &= 2.562435 \times 10^{-6} + 1.816683 \times 10^{-8}(333.15) + 2.579066 \times 10^{-11}(333.15)^2 \\ &\quad - 1.067299 \times 10^{-14}(333.15)^3 \\ &= 1.1083 \times 10^{-5} \text{ kg/ms} \end{aligned}$$

The condensate density can be calculated from Equation (B.12).

$$\begin{aligned} \rho_c &= \left(\begin{array}{l} 1.49343 \times 10^{-3} - 3.7164 \times 10^{-6}(333.15) + 7.09782 \times 10^{-9}(333.15)^2 \\ -1.90321 \times 10^{-20}(333.15)^6 \end{array} \right)^{-1} \\ &= 983.2168 \text{ kg/m}^3 \end{aligned}$$

With the dephlegmator geometry described in Appendix A, find the vapor velocities at the inlets of a tube in the first and second tube rows assuming complete condensation in both rows.

$$v_{vi(1)} = m_{vi(1)} / \rho_v A_{ts} = 7.756 \times 10^{-3} / (0.1302 \times 0.00159) = 37.46 \text{ m/s}$$

$$v_{vi(2)} = m_{vi(2)} / \rho_v A_{ts} = 6.441 \times 10^{-3} / (0.1302 \times 0.00159) = 31.11 \text{ m/s}$$

The corresponding tube inlet and condensation Reynolds numbers are,

$$Re_{vi(1)} = \rho_v v_{vi(1)} d_e / \mu_v = 0.1302 \times 37.46 \times 0.02975 / 1.1083 \times 10^{-5} = 13094.71$$

$$Re_{vi(2)} = \rho_v v_{vi(2)} d_e / \mu_v = 0.1302 \times 31.11 \times 0.02975 / 1.1083 \times 10^{-5} = 10874.69$$

$$Re_{vn(1)} = Re_{vi(1)} W_t / 2L_t = 13094.71 \times 0.017 / (2 \times 7.52) = 14.8$$

$$Re_{vn(2)} = Re_{vi(2)} W_t / 2L_t = 10874.69 \times 0.017 / (2 \times 7.52) = 12.29$$

while the vapor Froude numbers at the tube inlets are,

$$\begin{aligned} Fr_{Dv(1)} &= \rho_v v_{vi(1)}^2 / [gH_t (\rho_c - \rho_v)] \\ &= 0.1302 \times 37.46^2 / [9.81 \times 0.097 \times (983.2168 - 0.1302)] \\ &= 0.1953 \end{aligned}$$

$$\begin{aligned} Fr_{Dv(2)} &= \rho_v v_{vi(2)}^2 / [gH_t (\rho_c - \rho_v)] \\ &= 0.1302 \times 31.11^2 / [9.81 \times 0.097 \times (983.2168 - 0.1302)] \\ &= 0.1347 \end{aligned}$$

The frictional pressure drop over the tubes can now be calculated by integrating the correlations of Groenewald and Kröger (1995), described in Section 4.3, for condensing steam in inclined flattened tubes.

$$\Delta p_{f(1)} = -303.55 \text{ N/m}^2$$

$$\Delta p_{f(2)} = -219.49 \text{ N/m}^2$$

The inlet losses to the tubes are calculated from Equation (6.53) based on inlet loss coefficients determined from Equation (6.54).

$$K_{i(1)} = 1.5636 \exp(2.9526 \times 0.1953) = 2.7835$$

$$K_{i(2)} = 1.5636 \exp(2.9526 \times 0.1347) = 2.3273$$

$$\Delta p_{i(1)} = -(2.7835 + 0.5^2) \times 0.1302 \times 37.46^2 / 2 = -231.46 \text{ N/m}^2$$

$$\Delta p_{i(2)} = -(2.3273 + 0.5^2) \times 0.1302 \times 31.11^2 / 2 = -130.89 \text{ N/m}^2$$

Since the vapor is flowing upwards, the flow experiences a decrease in pressure due to geodetic effects. The magnitude of the geodetic loss is,

$$\begin{aligned} \Delta p_{g(1)} = \Delta p_{g(2)} &= -\rho_v gh = -\rho_v g L_t \cos \theta = -0.1302 \times 9.81 \times 7.52 \times \cos 30^\circ \\ &= -8.32 \text{ N/m}^2 \end{aligned}$$

A pressure recovery is experienced due to the deceleration of the vapor flow as it condenses. From Equation (6.47) find,

$$\Delta p_{m(1)} = 0.1302 \times (37.46^2 - 0) = 182.72 \text{ N/m}^2$$

$$\Delta p_{m(2)} = 0.1302 \times (31.11^2 - 0) = 126.02 \text{ N/m}^2$$

The total steam-side pressure changes over tubes in the first and second tube rows, for complete condensation and 100 % effective operation, are therefore:

$$\begin{aligned} \Delta p_{v(1)} &= \Delta p_{f(1)} + \Delta p_{i(1)} + \Delta p_{g(1)} + \Delta p_{m(1)} \\ &= -303.55 - 231.46 - 8.32 + 182.72 \\ &= -360.61 \text{ N/m}^2 \end{aligned}$$

$$\begin{aligned}
\Delta p_{v(2)} &= \Delta p_{f(2)} + \Delta p_{i(2)} + \Delta p_{g(2)} + \Delta p_{m(2)} \\
&= -219.49 - 130.89 - 8.32 + 126.02 \\
&= -232.69 \text{ N/m}^2
\end{aligned}$$

Since the tubes are connected between common headers they must have the same steam-side pressure drop. Additional vapor flow must therefore be drawn through the second row tubes to increase the losses over these tubes sufficiently to prevent backflow into the first row.

Assume the required additional vapor flow to be $m_{vo(2)} = 0.942 \times 10^{-3}$ kg/s per tube. With this additional vapor flow the total mass flow rate at the inlet of the second row tube is,

$$m_{vi(2)} = 6.441 \times 10^{-3} + 0.942 \times 10^{-3} = 7.383 \times 10^{-3} \text{ kg/s}$$

Now find,

$$v_{vi(2)} = m_{vi(2)} / \rho_v A_{ts} = 7.383 \times 10^{-3} / (0.1302 \times 0.00159) = 35.66 \text{ m/s}$$

$$Re_{vi(2)} = \rho_v v_{vi(2)} d_e / \mu_v = 0.1302 \times 35.66 \times 0.02975 / 1.1083 \times 10^{-5} = 12465.53$$

$$Re_{vi(2)} = Re_{vi(2)} W_t / 2L_t = 12465.53 \times 0.017 / (2 \times 7.52) = 14.09$$

$$\begin{aligned}
Fr_{Dv(2)} &= \rho_v v_{vi(2)}^2 / [gH_t(\rho_c - \rho_v)] \\
&= 0.1302 \times 35.66^2 / [9.81 \times 0.097 \times (983.2168 - 0.1302)] \\
&= 0.177
\end{aligned}$$

$$\Delta p_{f(2)} = -317.55 \text{ N/m}^2$$

$$K_{i(2)} = 1.5636 \exp(2.9526 \times 0.177) = 2.6369$$

$$\Delta p_{i(1)} = -(2.6369 + 0.5^2) \times 0.1302 \times 35.66^2 / 2 = -197.62 \text{ N/m}^2$$

The change in pressure due to the geodetic effect remains unchanged.

The velocity at the tube outlet is,

$$v_{vi(2)} = 0.942 \times 10^{-3} / (0.1302 \times 0.00159) = 4.55 \text{ m/s}$$

The corresponding tube outlet loss is negligible compared to the inlet loss and can be ignored.

The pressure recovery due to deceleration of the flow is,

$$\Delta p_{m(2)} = 0.1302 \times (35.66^2 - 4.55^2) = 162.89 \text{ N/m}^2$$

Giving a net steam-side pressure change over the second tube row of,

$$\begin{aligned} \Delta p_{v(2)} &= -317.55 - 197.62 - 8.32 + 162.89 \\ &= -360.61 \text{ N/m}^2 \end{aligned}$$

This value is suitably similar to the steam-side pressure change over the first row tubes and the assumed additional vapor flow requirement is correct.

The total required rate of vapor ejection is thus,

$$m_{vo(tot)} = m_{vo(2)} n_{ib(2)} n_b = 0.942 \times 10^{-3} \times 58 \times 8 = 0.437 \text{ kg/s}$$

The method described by the Heat Exchange Institute (1988) is now used to convert the required vapor mass flow rate to be ejected to the dry air equivalent (DAE) rate. The required vapor ejection rate, in kilograms of vapor per second, must be divided by a molar weight entrainment ratio (R_M), which accounts for the difference in the molar mass of water vapor relative to air, and a temperature entrainment ratio (R_T) which accounts for variations in vapor temperature from that on which the Heat Exchange Institute (HEI) data is based. From HEI (1988), for water vapor at $T_v = 60 \text{ }^\circ\text{C}$ find $R_M = 0.8$ and $R_T = 0.9784$. The DAE flow rate of vapor to be ejected is therefore,

$$m_{vo(tot)} = 0.437 / (0.8 \times 0.9784) = 0.559 \text{ kg/s (DAE)}$$

The required ejection rate of non-condensable gases must also be corrected. Since the non-condensable gas is dry air, $R_M = 1$. For air at $T_v = 60$ °C find $R_T = 0.9844$ (HEI, 1988). The DAE rate of non-condensable gases to be ejected is then,

$$m_{nc(tot)} = 4.423 \times 10^{-3} / (1 \times 0.9844) = 4.493 \times 10^{-3} \text{ kg/s (DAE)}$$

The total required ejection mass flow rate (DAE) per hour in each ACC street is therefore,

$$m_{ej(req)} = (0.559 + 4.493 \times 10^{-3}) \times 3600 = 2027.07 \text{ kg/h (DAE)}$$

E.2 Sample calculation: Backflow length in the dephlegmator

Consider the dephlegmator operating as described above. The required ejection rate was determined to be $m_{ej(req)} = 2027.07$ kg/h (DAE). The backpressure corresponding to $T_v = 60$ °C can be calculated from Equations (B.5) and (B.6) to be $p_v = 19\,925.12$ N/m².

Based on the performance characteristic shown in Figure 5.11, the capacity of a single holding ejector at this backpressure is approximately $m_{ej(hold)} = 230$ kg/h (DAE). Two holding ejectors are specified per ACC street such that the total possible ejection rate is $m_{ej} = 460$ kg/h (DAE). Since this ejection rate is less than that required, backflow will occur in the first tube row of the dephlegmator heat exchanger bundles. For the purpose of this investigation it is assumed that non-condensable gases occupy the entire backflow region and that the temperature of the gases in this region is equal to the ambient temperature.

First, the possible ejection rate is manipulated to determine the possible additional vapor flow in a second row tube. The possible ejection rate per second is,

$$m_{ej} = 460/3600 = 0.1278 \text{ kg/s (DAE)}$$

Subtract the non-condensable gases to be ejected from this value and divide by the number of tubes in the second row of the dephlegmator to determine the DAE additional vapor flow per tube.

$$m_{vo(2)} = (0.1278 - 4.493 \times 10^{-3}) / (58 \times 8) = 2.658 \times 10^{-4} \text{ kg/s (DAE)}$$

This value is now multiplied by the molar weight and temperature entrainment ratios discussed in the previous section to give the additional vapor flow rate in kilograms of water vapor per second.

$$m_{vo(2)} = 2.658 \times 10^{-4} \times 0.8 \times 0.9784 = 2.080 \times 10^{-4} \text{ kg/s}$$

Now assume backflow to have occurred to a distance of $L_{bf} = 0.515$ m (see Figure E.1). As a result, the effective length of the tube in the first tube row is reduced and the condensation rate for this tube, shown in Table E.1 for 100% effective operation, decreases proportionally.

$$m_{c(1)} = 7.756 \times 10^{-3} \times \frac{L_t - L_{bf}}{L_t} = 7.756 \times 10^{-3} \times \frac{7.52 - 0.515}{7.52} = 7.225 \times 10^{-3} \text{ kg/s}$$

For a second row tube exposed to the heated air downstream of the first row, the condensation rate per unit length is,

$$m_{c(2)} / L_t = 6.441 \times 10^{-3} / 7.52 = 0.857 \times 10^{-3} \text{ kg/sm}$$

In the backflow region a portion of the second row tube is exposed to ambient air. With $T_v = 60$ °C and $T_a = 20$ °C, the condensation rate per unit length in the second row tube is calculated to be $m_{c(2)} / L_t = 1.392 \times 10^{-3}$ kg/sm. The condensation rate in the second row tube is now,

$$\begin{aligned} m_{c(2)} &= 0.857 \times 10^{-3} \times (L_t - L_{bf}) + 1.392 \times 10^{-3} \times L_{bf} \\ &= 0.857 \times 10^{-3} \times (7.52 - 0.515) + 1.392 \times 10^{-3} \times 0.515 \\ &= 6.717 \times 10^{-3} \text{ kg/s} \end{aligned}$$

The vapor flow rate entering a second row tube is then,

$$m_{vi(2)} = m_{c(2)} + m_{vo(2)} = 6.717 \times 10^{-3} + 2.080 \times 10^{-4} = 6.925 \times 10^{-3} \text{ kg/s}$$

Following the same procedure as in Section E.1, calculate the steam-side pressure change over the first and second row tubes.

$$v_{vi(1)} = m_{vi(1)} / \rho_v A_{ts} = 7.225 \times 10^{-3} / (0.1302 \times 0.00159) = 34.89 \text{ m/s}$$

$$v_{vi(2)} = m_{vi(2)} / \rho_v A_{ts} = 6.925 \times 10^{-3} / (0.1302 \times 0.00159) = 33.44 \text{ m/s}$$

$$v_{vo(2)} = m_{vo(2)} / \rho_v A_{ts} = 2.080 \times 10^{-4} / (0.1302 \times 0.00159) = 1.01 \text{ m/s}$$

$$Re_{vi(1)} = \rho_v v_{vi(1)} d_e / \mu_v = 0.1302 \times 34.89 \times 0.02975 / 1.1083 \times 10^{-5} = 12197.23$$

$$Re_{vi(2)} = \rho_v v_{vi(2)} d_e / \mu_v = 0.1302 \times 33.44 \times 0.02975 / 1.1083 \times 10^{-5} = 11692.03$$

$$Re_{vn(1)} = Re_{vi(1)} W_t / 2L_t = 12197.23 \times 0.017 / [2 \times (7.52 - 0.302)] = 14.80$$

$$Re_{vn(2)} = Re_{vi(2)} W_t / 2L_t = 11692.03 \times 0.017 / (2 \times 7.52) = 13.22$$

$$\begin{aligned} Fr_{Dv(1)} &= \rho_v v_{vi(1)}^2 / [gH_t (\rho_c - \rho_v)] \\ &= 0.1302 \times 34.89^2 / [9.81 \times 0.097 \times (983.2168 - 0.1302)] \\ &= 0.1694 \end{aligned}$$

$$\begin{aligned} Fr_{Dv(2)} &= \rho_v v_{vi(2)}^2 / [gH_t (\rho_c - \rho_v)] \\ &= 0.1302 \times 33.44^2 / [9.81 \times 0.097 \times (983.2168 - 0.1302)] \\ &= 0.1557 \end{aligned}$$

The corresponding frictional pressure drops are $\Delta p_{f(1)} = -247.79 \text{ N/m}^2$ and $\Delta p_{f(2)} = -256.67 \text{ N/m}^2$ while the inlet losses become $\Delta p_{i(1)} = -184.6 \text{ N/m}^2$ and $\Delta p_{i(2)} = -162.15 \text{ N/m}^2$.

Finally, the geodetic and deceleration related pressure changes are,

$$\begin{aligned} \Delta p_{g(1)} &= -\rho_v gh = -\rho_v gL_t \cos \theta = -0.1302 \times 9.81 \times (7.52 - 0.302) \times \cos 30^\circ \\ &= -7.99 \text{ N/m}^2 \end{aligned}$$

$$\begin{aligned}\Delta p_{g(1)} &= -0.1302 \times 9.81 \times 7.52 \times \cos 30^\circ \\ &= -8.32 \text{ N/m}^2\end{aligned}$$

$$\Delta p_{m(1)} = 0.1302 \times (34.89^2 - 0) = 158.53 \text{ N/m}^2$$

$$\Delta p_{m(2)} = 0.1302 \times (33.44^2 - 1.01^2) = 145.54 \text{ N/m}^2$$

The total steam-side pressure change over tubes in the first and second tube rows, taking into account backflow in the first tube row, are therefore,

$$\Delta p_{v(1)} = -247.79 - 184.6 - 7.99 + 158.53 = -281.61 \text{ N/m}^2$$

$$\Delta p_{v(2)} = -256.67 - 162.15 - 8.32 + 145.54 = -281.61 \text{ N/m}^2$$

These values match and the assumption of $L_{bf} = 0.515$ m was correct.

In practise, this predicted backflow length is somewhat conservative as it is unlikely that the entire backflow region in the first tube row will be at ambient temperature. The air passing through this region will therefore be heated slightly and the condensation rate in this portion of the second row will be less than that assumed here. Backflow will therefore be somewhat more severe.

Zapke and Kröger (1997) present a similar analysis to determine the extent of vapor backflow in a two-row dephlegmator. This analysis differs from theirs in that it takes into account the accumulation of non-condensables and the subsequent formation of a stagnant dead zone in the first tube row. The results presented here are therefore indicative of an eventual stable operating point for the ACC whereas Zapke and Kröger's method is representative of point of first establishment of a backflow region in the dephlegmator.

APPENDIX F. INDUCED DRAFT HDWD PERFORMANCE EVALUATION

A sample calculation of the performance of an induced draft HDWD operating as both an evaporative cooler and an air-cooled condenser is illustrated here. The following assumptions are made:

- Saturated water vapor ($x = 1$) enters the HDWD at $T_v = 60$ °C.
- Complete condensation takes place so that all the entering vapor leaves as saturated liquid condensate.
- For dry operation of the second stage, the steam-side pressure drop over the HDWD is low enough that the steam temperature remains essentially constant throughout the HDWD.
- For wet operation of the second stage the steam-side pressure drop results in a measurable change in vapor temperature through the HDWD that must be accounted for.
- The vapor is distributed uniformly amongst all the tubes in any given tube row.

The relevant system geometrical and performance parameters are described in Appendix A and Chapter 6. The second stage plain-tube bundle Configuration I from Chapter 6, described again in Table F.1 for convenience, is considered.

Table F.1: Second stage plain-tube bundle Configuration I

Tube outside dia.	Tube rows	Tubes per row	Vapor passes	Tubes per pass n_p
d_o , m	n_r	n_{tr}	n_{vp}	(1 st /2 nd /3 rd)
0.019	25	314	3	20/4/1

F.1 Solution parameters and performance evaluation results

Table F.2: Operating conditions

Ambient air drybulb temperature at ground level	$T_a = 20 \text{ }^\circ\text{C}$ (293.15 K)
Ambient air wetbulb temperature at ground level	$T_{wb} = 13.3 \text{ }^\circ\text{C}$ (286.45 K)
Relative humidity of ambient air	$RH = 50 \%$
Ambient pressure at ground level	$p_a = 84600 \text{ N/m}^2$
Vapor temperature at the HDWD inlet	$T_v = 60 \text{ }^\circ\text{C}$ (333.15 K)
Vapor quality at HDWD inlet	$x = 1$
Deluge water mass flow rate in wet mode	$m_w = 118 \text{ kg/s}$

Table F.3: Solution parameters for wet operation of the HDWD

<u>First stage</u>	
Air mass flow rate	$m_{a(1)} = 321.0117 \text{ kg/s}$
Air temperature after the first tube row	$T_{ao(1)} = 35.8567 \text{ }^\circ\text{C}$ (309.0067 K)
Air temperature after the second tube row	$T_{ao(2)} = 49.1858 \text{ }^\circ\text{C}$ (322.3358 K)
<u>Second stage</u>	
Air-vapor mass flow rate at the bundle inlet	$m_{avi} = 154.747 \text{ kg/s}$
Air temperature after the tube bundle	$T_{ao} = 47.8806 \text{ }^\circ\text{C}$ (321.0306 K)
Mean deluge water temperature	$T_{wm} = 49.7305 \text{ }^\circ\text{C}$ (322.8805 K)
Vapor condensation rate	$m_s = 16.3092 \text{ kg/s}$

Table F.4: Solution parameters for dry operation of the HDWD

<u>First stage</u>	
Air mass flow rate	$m_{a(1)} = 332.1048 \text{ kg/s}$
Air temperature after the first tube row	$T_{ao(1)} = 35.612 \text{ }^\circ\text{C}$ (308.762 K)
Air temperature after the second tube row	$T_{ao(2)} = 48.9124 \text{ }^\circ\text{C}$ (322.0624 K)
<u>Second stage</u>	
Air mass flow rate	$m_{a(2)} = 124.7771 \text{ kg/s}$
Air temperature after the tube bundle	$T_{ao} = 47.8865 \text{ }^\circ\text{C}$ (321.0365 K)

Table F.5: Converged performance evaluation results

	<i>Wet mode</i>	<i>Dry mode</i>
First stage heat transfer rate, MW	9.2684	9.6718
Second stage heat transfer rate, MW	35.8205	3.5048
Total heat transfer rate, MW	45.0889	13.1766
Fan power consumption, kW	162.5121	162.1001
Water consumption, kg/s	13.1528	0

F.2 Sample calculation: HDWD operating as an evaporative cooler

In this calculation, the draft equation is first evaluated based on initial assumptions of the solution parameters (Table F.3). Once the draft equation has been balanced the energy equation is considered. The calculation is complete once both the draft and energy equations are suitably balanced.

F.2.1 Draft equation

F.2.1.1 First stage heat exchanger bundle air-side pressure drop

The mean air temperature through the first stage heat exchanger is,

$$T_{am} = (T_{ai} + T_{ao})/2 = (293.15 + 322.3358)/2 = 307.7429 \text{ K}$$

The density and dynamic viscosity of dry air at this mean temperature are calculated from Equations (B.1) and (B.3).

$$\rho_{am} = 84600/(287.08 \times 307.7429) = 0.9576 \text{ kg/m}^3$$

$$\begin{aligned} \mu_{am} &= 2.287973 \times 10^{-6} + 6.259793 \times 10^{-8} (307.7429) - 3.131956 \times 10^{-11} (307.7429)^2 \\ &\quad + 8.15038 \times 10^{-15} (307.7429)^3 \\ &= 1.8823 \times 10^{-5} \text{ kg/ms} \end{aligned}$$

The density of air at the heat exchanger inlet and outlet are calculated similarly.

$$\rho_{ai} = 84600 / (287.08 \times 293.15) = 1.0053 \text{ kg/m}^3$$

$$\rho_{ao} = 84600 / (287.08 \times 322.3358) = 0.9142 \text{ kg/m}^3$$

The characteristic flow parameter through the heat exchanger is calculated from Equation (6.29).

$$\begin{aligned} Ry_{(1)} &= m_{a(1)} / (\mu_{am} n_b A_{fr} n_{tb1} / n_{tb2}) = 321.0117 / (1.8823 \times 10^{-5} \times 8 \times 13.189 \times 57 / 58) \\ &= 164464.8228 \text{ m}^{-1} \end{aligned}$$

The heat exchanger loss coefficient for normal isothermal flow is calculated from Equation (A.3).

$$K_{he} = 4464.831 \times (164464.8228)^{-0.43927} = 21.3607$$

With K_{he} known, the overall loss coefficient for the finned-tube heat exchanger is calculated from Equation (6.22).

$$K_{\alpha} = 21.3607 + \frac{2}{0.875^2} \frac{(1.0053 - 0.9142)}{(1.0053 + 0.9142)} + \frac{2 \times 1.0053 \times 1}{(1.0053 + 0.9142)} = 22.8198$$

The air-side pressure drop over the first stage heat exchanger is now calculated from Equation (6.20) with,

$$v_{am} = m_{a(1)} / \rho_{am} n_b A_{fr} = 321.0117 / (0.9576 \times 8 \times 13.189) = 3.1771 \text{ m/s}$$

$$\Delta p_{a(1st)} = 22.8198 \times \frac{0.9576 \times 3.1771^2}{2} = 110.291 \text{ N/m}^2$$

F.2.1.2 Second stage heat exchanger bundle air-side pressure drop

The water flow rate over half a tube per unit length is,

$$\Gamma_m = m_w d_o / 2 n_b n_{tr} L_t P = (118 \times 0.019) / (2 \times 2 \times 314 \times 2.5 \times 0.038) = 0.0188 \text{ kg/ms}$$

The air-side pressure drop over the second stage bundle can now be calculated from Equation (6.23).

$$\begin{aligned}\Delta p_{a(2nd-wet)} &= 4.9 \times 25 \times 0.0329 \times [154.747 / (2 \times 14.9388)]^{1.85} \times (0.0188 / 0.019)^{0.285} \\ &= 84.2341 \text{ N/m}^2\end{aligned}$$

F.2.1.3 Solution of the draft equation

The mean air temperature leaving the first and second stage heat exchangers is approximated by,

$$\begin{aligned}T_{ao} &= (T_{ao(1)}m_{a(1)} + T_{ao(2)}m_{a(2)}) / (m_{a(1)} + m_{a(2)}) \\ &= (322.3358 \times 321.0117 + 321.0306 \times 154.747) / (321.0117 + 154.747) \\ &= 321.9113 \text{ K}\end{aligned}$$

The corresponding density of air flowing through the fan is thus,

$$\rho_{aF} = 84600 / (287.08 \times 321.9113) = 0.9154 \text{ kg/m}^3$$

and the fan volumetric flow rate is,

$$V_F = (m_{a(1)} + m_{a(2)}) / \rho_{aF} = (321.0117 + 154.747) / 0.9154 = 519.7277 \text{ m}^3/\text{s}$$

The corresponding fan static pressure rise and fan power consumption are calculated from Equations (A.4) and (A.5).

$$\begin{aligned}\Delta p_{Fs} &= \left[320.0451719 - 0.297521548 \times (519.7277) \right. \\ &\quad \left. + 6.35149 \times 10^{-4} \times (519.7277)^2 - 8.14 \times 10^{-7} \times (519.7277)^3 \right] \left(\frac{0.9154}{1.2} \right) \\ &= 169.9006 \text{ N/m}^2\end{aligned}$$

$$\begin{aligned}P_F &= \left[186645.2333 - 59.41386339 \times (519.7277) \right. \\ &\quad \left. + 0.476168398 \times (519.7277)^2 - 5.08308 \times 10^{-4} \times (519.7277)^3 \right] \left(\frac{0.9154}{1.2} \right) \\ &= 162.5121 \times 10^3 \text{ W}\end{aligned}$$

The total loss coefficient for obstacles up- and downstream of the fan considered here is $K_{up/do} = 0.6877$ while the heat exchanger support tower loss coefficient is $K_{ts} = 1.5$ (Kröger, 2004). The losses due to these obstacles are subsequently,

$$\begin{aligned}\Delta p_{up/do} &= \frac{K_{up/do}}{2\rho_{aF}} \left(\frac{m_{a(1)} + m_{a(2)}}{A_e} \right)^2 = \frac{0.6877}{2 \times 0.9154} \left(\frac{321.0117 + 154.747}{64.5039} \right)^2 \\ &= 20.4343 \text{ N/m}^2\end{aligned}$$

$$\Delta p_{ts} = \frac{K_{ts}}{2\rho_{ai}} \left(\frac{m_{a(1)} + m_{a(2)}}{A_c} \right)^2 = \frac{1.5}{2 \times 1.0053} \left(\frac{321.0117 + 154.747}{66.0433} \right)^2 = 38.7152 \text{ N/m}^2$$

The average free stream velocity upstream of the plain tube bundle is,

$$v_o = m_{a(2)} / n_b A_{fr} \rho_{ai} = 154.747 / (2 \times 29.925 \times 1.0053) = 2.5719 \text{ m/s}$$

The density and dynamic viscosity of the air at the bundle outlet are,

$$\rho_{ao} = 84600 / (287.08 \times 321.0306) = 0.918 \text{ kg/m}^3$$

$$\begin{aligned}\mu_{am} &= 2.287973 \times 10^{-6} + 6.259793 \times 10^{-8} (321.0306) - 3.131956 \times 10^{-11} (321.0306)^2 \\ &\quad + 8.15038 \times 10^{-15} (321.0306)^3 \\ &= 1.9426 \times 10^{-5} \text{ kg/ms}\end{aligned}$$

The pressure drop over the droplet collecting troughs is calculated from Equation (6.27).

$$\Delta p_{ct} = 1.563 \times [118 / (2 \times 29.925)]^{0.184} \times [154.747 / (2 \times 29.925)]^{1.693} = 8.8444 \text{ N/m}^2$$

The loss coefficient over the drift eliminators is calculated from Equation (6.28).

$$K_{de} = 27.4892 \times (2.5719 \times 0.918 / 1.9426 \times 10^{-5})^{-0.14247} = 5.1507$$

The corresponding loss over the drift eliminators is,

$$\Delta p_{de} = K_{de} \rho_{ao} v_0^2 / 2 = 5.1507 \times 0.918 \times 2.5719^2 / 2 = 17.1621 \text{ N/m}^2$$

The left side of Equation (6.19) equates to,

$$\Delta p_{Fs} - (\Delta p_{ts} + \Delta p_{up/do}) = 169.9006 - (38.7152 + 20.4343) = 110.7511 \text{ N/m}^2$$

The right hand side of Equation (4.19) equals,

$$\Delta p_{a(2nd)} + \Delta p_{ct} + \Delta p_{de} = 84.2341 + 8.8444 + 17.1621 = 110.2406 \text{ N/m}^2$$

These values correspond well with one another and with $\Delta p_{a(1st)} = 110.291 \text{ N/m}^2$.

The draft equation is therefore balanced.

F.2.2 First stage energy equation

F.2.2.1 Air-side energy balance

The mean air temperature through the respective bundles is,

$$T_{am(1)} = (T_{ai} + T_{ao(1)}) / 2 = (293.15 + 309.0066) / 2 = 301.0783 \text{ K}$$

$$T_{am(2)} = (T_{ao(1)} + T_{ao(2)}) / 2 = (309.0066 + 322.3358) / 2 = 315.6712 \text{ K}$$

The corresponding properties of air are calculated from Equations (B.1) – (B.4).

$$\rho_{am(1)} = 84600 / (287.08 \times 301.0783) = 0.9788 \text{ kg/m}^3$$

$$\begin{aligned} c_{pam(1)} &= 1.045356 \times 10^{-3} - 3.161783 \times 10^{-1} (301.0783) + 7.083814 \times 10^{-4} (301.0783)^2 \\ &\quad - 2.705209 \times 10^{-7} (301.0783)^3 \\ &= 1006.9919 \text{ J/kgK} \end{aligned}$$

$$\begin{aligned} \mu_{am(1)} &= 2.287973 \times 10^{-6} + 6.259793 \times 10^{-8} (301.0783) - 3.131956 \times 10^{-11} (301.0783)^2 \\ &\quad + 8.15038 \times 10^{-15} (301.0783)^3 \\ &= 1.8518 \times 10^{-5} \text{ kg/ms} \end{aligned}$$

$$\begin{aligned}
 k_{am(1)} &= -4.937787 \times 10^{-4} + 1.018087 \times 10^{-4} (301.0783) - 4.627937 \times 10^{-8} (301.0783)^2 \\
 &\quad + 1.250603 \times 10^{-11} (301.0783)^3 \\
 &= 0.0263 \text{ W/mK}
 \end{aligned}$$

$$\rho_{am(2)} = 84600 / (287.08 \times 315.6712) = 0.9335 \text{ kg/m}^3$$

$$\begin{aligned}
 c_{pa(2)} &= 1.045356 \times 10^{-3} - 3.161783 \times 10^{-1} (315.6712) + 7.083814 \times 10^{-4} (315.6712)^2 \\
 &\quad - 2.705209 \times 10^{-7} (315.6712)^3 \\
 &= 1007.6271 \text{ J/kgK}
 \end{aligned}$$

$$\begin{aligned}
 \mu_{am(2)} &= 2.287973 \times 10^{-6} + 6.259793 \times 10^{-8} (315.6712) - 3.131956 \times 10^{-11} (315.6712)^2 \\
 &\quad + 8.15038 \times 10^{-15} (315.6712)^3 \\
 &= 1.9184 \times 10^{-5} \text{ kg/ms}
 \end{aligned}$$

$$\begin{aligned}
 k_{am(2)} &= -4.937787 \times 10^{-4} + 1.018087 \times 10^{-4} (315.6712) - 4.627937 \times 10^{-8} (315.6712)^2 \\
 &\quad + 1.250603 \times 10^{-11} (315.6712)^3 \\
 &= 0.0274 \text{ W/mK}
 \end{aligned}$$

The Prandtl numbers for air at the mean temperatures through the first and second bundles are respectively $Pr_{am(1)} = 0.709$ and $Pr_{am(2)} = 0.7049$ (Kröger, 2004).

The rate of heat transfer to the air is now calculated from Equation (6.1).

$$\begin{aligned}
 Q_{(1)} &= m_a c_{pa(1)} (T_{ao(1)} - T_{ai}) = 321.0117 \times 1006.9919 \times (309.0066 - 293.15) \\
 &= 5.1257 \times 10^6 \text{ W}
 \end{aligned}$$

$$\begin{aligned}
 Q_{(2)} &= m_a c_{pa(2)} (T_{ao(2)} - T_{ao(1)}) = 321.0117 \times 1007.6271 \times (322.3358 - 308.7463) \\
 &= 4.3115 \times 10^6 \text{ W}
 \end{aligned}$$

$$Q = \sum_{i=1}^n m_a c_{pa(i)} (T_{ao(i)} - T_{ai(i)}) = 5.1257 \times 10^6 + 4.3115 \times 10^6 = 9.4372 \times 10^6 \text{ W}$$

F.2.2.2 Steam-side energy balance

The characteristic heat transfer parameter is calculated according to Equation (A.1).

$$Ny_{(1)} = 366.007945 \times \left(\frac{321.0117}{1.8518 \times 10^{-5} \times 13.189 \times 57/58} \right)^{0.433256} = 67059.6634 \text{ m}^{-1}$$

The effective air-side heat transfer coefficient is now calculated from Equation (6.3).

$$UA_{(1)} = 0.0263 \times 0.709^{0.333} \times 8 \times 13.189 \times 67059.6634 = 163203.8657 \text{ W/K}$$

The effectiveness of the first tube row is calculated from Equation (6.2).

$$e_{(1)} = 1 - \exp[-163203.8657 / (321.0117 \times 1006.9919)] = 0.3964$$

The heat transferred from the first tube row can now be calculated according to Equation (6.1).

$$\begin{aligned} Q_{(1)} &= m_a c_{pa(1)} e_{(1)} (T_v - T_{ai(1)}) = 321.0117 \times 1006.9919 \times 0.3964 \times (333.15 - 293.15) \\ &= 5.1258 \times 10^6 \text{ W} \end{aligned}$$

This value compares well with the value of $Q_{(1)} = 5.1257 \text{ MW}$ determined using the air-side energy balance.

A similar procedure is followed for the second tube row with the characteristic heat transfer parameter calculated according to Equation (A.2).

$$Ny_{(2)} = 360.588007 \times \left(\frac{321.0117}{1.9184 \times 10^{-5} \times 8 \times 13.189} \right)^{0.470373} = 100712.8517 \text{ m}^{-1}$$

$$UA_{(2)} = 0.0274 \times 0.7049^{0.333} \times 8 \times 13.189 \times 100712.8517 = 259462.1155 \text{ W/K}$$

$$e_{(2)} = 1 - \exp[-259462.1155 / (321.0117 \times 1007.6271)] = 0.5516$$

$$\begin{aligned}
 Q_{(2)} &= m_a c_{pa(2)} e_{(2)} (T_v - T_{ai(2)}) \\
 &= 321.0117 \times 1007.6271 \times 0.5516 \times (333.15 - 309.0066) \\
 &= 4.3115 \times 10^6 \text{ W}
 \end{aligned}$$

This value matches the value of $Q_{(2)} = 4.3115$ MW calculated using the air-side energy balance. The energy equation is therefore balanced and the initial assumptions were correct. The total heat transfer rate for the first stage of the HDWD is $Q = 9.4372$ MW assuming a constant vapor temperature of $T_v = 60$ °C throughout the system.

F.2.3 Second stage energy equation

F.2.3.1 Air-side energy balance

At $T = (T_{ai} + 273.15)/2 = (293.15 + 273.15)/2 = 283.15$ K find the specific heats of air and water vapor according to Equations (B.2) and (B.9) respectively.

$$\begin{aligned}
 c_{pai} &= 1.045356 \times 10^{-3} - 3.161783 \times 10^{-1} (283.15) + 7.083814 \times 10^{-4} (283.15)^2 \\
 &\quad - 2.705209 \times 10^{-7} (283.15)^3 \\
 &= 1006.4827 \text{ J/kgK}
 \end{aligned}$$

$$\begin{aligned}
 c_{pvi} &= 1.3605 \times 10^{-3} + 2.31334 (283.15) - 2.46784 \times 10^{-10} (283.15)^5 \\
 &\quad + 5.91332 \times 10^{-13} (283.15)^6 \\
 &= 1871.1044 \text{ J/kgK}
 \end{aligned}$$

The partial vapor pressure in the ambient air is calculated by evaluating Equations (B.5) and (B.6) at $T_{wb} = 286.45$ K.

$$\begin{aligned}
 z &= 10.79586 \times \left(1 - \frac{273.16}{286.45} \right) + 5.02808 \log_{10} \left(\frac{273.16}{286.45} \right) \\
 &\quad + 1.50474 \times 10^{-4} \times \left[1 - 10^{-8.29692 \left(\frac{286.45}{273.16} - 1 \right)} \right] + 4.2873 \times 10^{-4} \times \left[10^{4.76955 \left(1 - \frac{273.16}{286.45} \right)} - 1 \right] \\
 &\quad + 2.786118312 \\
 &= 3.1837
 \end{aligned}$$

$$p_{vwb} = 10^{3.1837} = 1526.2862 \text{ N/m}^2$$

The humidity ratio of the inlet air is now calculated from Equation (B.28).

$$w_i = \left[\frac{2501.6 - 2.3263 \times (286.45 - 273.15)}{2501.6 + 1.8577 \times (293.15 - 273.15) - 4.184 \times (286.45 - 273.15)} \right] \\ \times \left(\frac{0.62509 \times 1526.2862}{84600 - 1.005 \times 1526.2862} \right) \\ - \left[\frac{1.00416 \times (293.15 - 286.45)}{2501.6 + 1.8577 \times (293.15 - 273.15) - 4.184 \times (286.45 - 273.15)} \right] \\ = 0.0087 \text{ kg/kg dry air}$$

With the latent heat of water at $T_0 = 273.15 \text{ K}$ calculated from Equation (B.16), the enthalpy of the inlet air-vapor mixture per kilogram dry air is determined from Equation (B.30).

$$i_{fgwo} = 3.4831814 \times 10^6 - 5.8627703 \times 10^3 (273.15) + 12.139568 (273.15)^2 \\ - 1.40290431 \times 10^{-2} (273.15)^3 \\ = 2.5016 \times 10^6 \text{ J/kg} \\ i_{mai} = 1006.4827 \times (293.15 - 273.15) \\ + 0.008719 \times [2.5016 \times 10^6 + 1871.1044 \times (293.15 - 273.15)] \\ = 42.2664 \times 10^3 \text{ J/kg}$$

The enthalpy of the saturated air-vapor mixture is calculated at the mean deluge water film temperature following the same procedure as above. The specific heats are evaluated at $T = (T_{wm} + 273.15)/2 = (322.8804 + 273.15)/2 = 298.0152 \text{ K}$

$$c_{pawm} = 1.045356 \times 10^{-3} - 3.161783 \times 10^{-1} (298.0152) + 7.083814 \times 10^{-4} (298.0152)^2 \\ - 2.705209 \times 10^{-7} (298.0152)^3 \\ = 1006.8835 \text{ J/kgK}$$

$$\begin{aligned}
 c_{pvwm} &= 1.3605 \times 10^{-3} + 2.31334(298.0152) - 2.46784 \times 10^{-10} (298.0152)^5 \\
 &\quad + 5.91332 \times 10^{-13} (298.0152)^6 \\
 &= 1884.0516 \text{ J/kgK}
 \end{aligned}$$

$$\begin{aligned}
 z &= 10.79586 \times \left(1 - \frac{273.16}{322.8804}\right) + 5.02808 \log_{10} \left(\frac{273.16}{322.8804}\right) \\
 &\quad + 1.50474 \times 10^{-4} \left[1 - 10^{-8.29692 \left(\frac{322.8804}{273.16}\right)^{-1}}\right] + 4.2873 \times 10^{-4} \left[10^{4.76955 \left(1 - \frac{273.16}{322.8804}\right)} - 1\right] \\
 &\quad + 2.786118312 \\
 &= 4.0855
 \end{aligned}$$

$$p_{vwm} = 10^{4.0855} = 12174.6725 \text{ N/m}^2$$

$$\begin{aligned}
 w_{wm} &= \left[\frac{2501.6 - 2.3263 \times (322.8804 - 273.15)}{2501.6 + 1.8577 \times (322.8804 - 273.15) - 4.184 \times (322.8804 - 273.15)} \right] \\
 &\quad \times \left(\frac{0.62509 \times 12174.6725}{84600 - 1.005 \times 12174.6725} \right) \\
 &\quad - \left[\frac{1.00416 \times (322.8804 - 322.8804)}{2501.6 + 1.8577 \times (322.8804 - 273.15) - 4.184 \times (322.8804 - 273.15)} \right] \\
 &= 0.1052 \text{ kg/kg dry air}
 \end{aligned}$$

$$\begin{aligned}
 i_{mavm} &= 1006.8835 \times (322.8804 - 273.15) \\
 &\quad + 0.1052 \times [2.5016 \times 10^6 + 1884.0516 \times (322.8804 - 273.15)] \\
 &= 323.0089 \times 10^3 \text{ J/kg}
 \end{aligned}$$

The mean air temperature through the bundle is,

$$T_{am} = (T_{ai} + T_{ao})/2 = (293.15 + 321.0306)/2 = 307.0903 \text{ K}$$

The dynamic viscosity of dry air and saturated water vapor at the mean air temperature are calculated according to Equations (B.3) and (B.10) respectively.

$$\begin{aligned}\mu_{am} &= 2.287973 \times 10^{-6} + 6.259793 \times 10^{-8} (307.0903) - 3.131956 \times 10^{-11} (307.0903)^2 \\ &\quad + 8.15038 \times 10^{-15} (307.0903)^3 \\ &= 1.8794 \times 10^{-5} \text{ kg/ms}\end{aligned}$$

$$\begin{aligned}\mu_{vm} &= 2.562435 \times 10^{-6} + 1.816683 \times 10^{-8} (307.0903) + 2.579066 \times 10^{-11} (307.0903)^2 \\ &\quad - 1.067299 \times 10^{-14} (307.0903)^3 \\ &= 1.0264 \times 10^{-5} \text{ kg/ms}\end{aligned}$$

The vapor pressure and humidity ratio are calculated from Equations (B.5), (B.6) and (B.28).

$$\begin{aligned}z &= 10.79586 \times \left(1 - \frac{273.16}{307.0903}\right) + 5.02808 \log_{10} \left(\frac{273.16}{307.0903}\right) \\ &\quad + 1.50474 \times 10^{-4} \left[1 - 10^{-8.29692 \left(\frac{307.0903}{273.16} - 1\right)}\right] + 4.2873 \times 10^{-4} \left[10^{4.76955 \left(1 - \frac{273.16}{307.0903}\right)} - 1\right] \\ &\quad + 2.786118312 \\ &= 3.7344\end{aligned}$$

$$p_{vam} = 10^{3.725} = 5301.8471 \text{ N/m}^2$$

$$\begin{aligned}w_{am} &= \left[\frac{2501.6 - 2.3263(307.0903 - 273.15)}{2501.6 + 1.8577 \times (307.0903 - 273.15) - 4.184 \times (307.0903 - 273.15)} \right] \\ &\quad \times \left(\frac{0.62509 \times 5301.8471}{84600 - 1.005 \times 5301.8471} \right) \\ &\quad - \left[\frac{1.00416 \times (307.0903 - 307.0903)}{2501.6 + 1.8577 \times (307.0903 - 273.15) - 4.184 \times (307.0903 - 273.15)} \right] \\ &= 0.0418 \text{ kg/kg dry air}\end{aligned}$$

From Equations (B.24) and (B.25) find,

$$X_a = 1/(1 + 1.608 \times 0.0418) = 0.937$$

$$X_v = 0.0418/(0.0418 + 0.622) = 0.063$$

The dynamic viscosity of the air-vapor mixture is now calculated from Equation (B.22).

$$\begin{aligned}\mu_{avm} &= \left(0.937 \times 1.8794 \times 10^{-5} \times 28.97^{0.5} + 0.063 \times 1.0264 \times 10^{-5} \times 18.016^{0.5}\right) / \\ &\quad \left(0.937 \times 28.97^{0.5} + 0.063 \times 18.016^{0.5}\right) \\ &= 1.8364 \times 10^{-5} \text{ kg/ms}\end{aligned}$$

The air-side Reynolds number evaluated at the mean air temperature through the bundle is,

$$\begin{aligned}Re_{avm} &= m_a d_o / n_b A_c \mu_{avm} = (154.747 \times 0.019) / (2 \times 14.9388 \times 1.8364 \times 10^{-5}) \\ &= 5236.2511\end{aligned}$$

The dynamic viscosity of the deluge water temperature at T_{wm} is calculated from Equation (B.14).

$$\mu_{wm} = 2.414 \times 10^{-5} \times 10^{247.8 / (322.8804 - 140)} = 5.4666 \times 10^{-4} \text{ kg/ms}$$

With $\Gamma_m = 0.0188 \text{ kg/ms}$, as calculated during the solution of the draft equation, find the corresponding deluge water Reynolds number.

$$Re_{wm} = 4\Gamma_m / \mu_{wm} = 4 \times 0.0188 / 5.4666 \times 10^{-4} = 137.4871$$

The mass transfer coefficient between the deluge water film and the passing air can now be calculated from Equation (6.18).

$$h_d = 5.5439 \times 10^{-8} \times (5236.2511)^{0.9} \times (137.4871)^{0.15} \times (0.019)^{-1.6} = 0.1464 \text{ kg/m}^2\text{s}$$

The mass flow rate of dry air only at the bundle inlet is,

$$m_{ai} = m_a / (1 + w_i) = 154.747 / (1 + 0.0087) = 153.4095 \text{ kg/s}$$

Now find, from Equation (6.17),

$$NTU_a = 0.1464 \times 2 \times 1171.421 / 153.4095 = 2.2364$$

The enthalpy of the air at the heat exchanger outlet can now be calculated according to Equation (6.15).

$$\begin{aligned} i_{mao} &= 323.0089 \times 10^3 - (323.0089 \times 10^3 - 42.2664 \times 10^3) \times \exp(-2.2364) \\ &= 293.105 \times 10^3 \text{ J/kg dry air} \end{aligned}$$

Now calculate the specific heats of air and water vapor at,

$$T = (T_{ao} + 273.15)/2 = (321.0306 + 273.15)/2 = 297.0903 \text{ K}$$

according to Equations (B.2) and (B.9).

$$\begin{aligned} c_{pao} &= 1.045356 \times 10^{-3} - 3.161783 \times 10^{-1} (297.0903) + 7.083814 \times 10^{-4} (297.0903)^2 \\ &\quad - 2.705209 \times 10^{-7} (297.0903)^3 \\ &= 1006.8525 \text{ J/kgK} \end{aligned}$$

$$\begin{aligned} c_{pvo} &= 1.3605 \times 10^{-3} + 2.31334 (297.0903) - 2.46784 \times 10^{-10} (297.0903)^5 \\ &\quad + 5.91332 \times 10^{-13} (297.0903)^6 \\ &= 1883.204 \text{ J/kgK} \end{aligned}$$

The vapor pressure and humidity ratio at the bundle out let are calculated as before assuming the air-vapor mixture at the heat exchanger outlet to be 100 % saturated.

$$\begin{aligned} z &= 10.79586 \times \left(1 - \frac{273.16}{321.0306} \right) + 5.02808 \times \log_{10} \left(\frac{273.16}{321.0306} \right) \\ &\quad + 1.50474 \times 10^{-4} \left[1 - 10^{-8.29692 \left(\left(\frac{321.0306}{273.16} \right)^{-1} \right)} \right] + 4.2873 \times 10^{-4} \left[10^{4.76955 \left(1 - \frac{273.16}{321.0306} \right)} - 1 \right] \\ &\quad + 2.786118312 \\ &= 4.0453 \end{aligned}$$

$$p_{vo} = 10^{4.0453} = 11098.2246 \text{ N/m}^2$$

$$\begin{aligned}
 w_o &= \left[\frac{2501.6 - 2.3263 \times (321.0306 - 273.15)}{2501.6 + 1.8577 \times (321.0306 - 273.15) - 4.184 \times (321.0306 - 273.15)} \right] \\
 &\quad \times \left(\frac{0.62509 \times 11098.2246}{84600 - 1.005 \times 11098.2246} \right) \\
 &\quad - \left[\frac{1.00416 \times (321.0306 - 321.0306)}{2501.6 + 1.8577 \times (321.0306 - 273.15) - 4.184 \times (321.0306 - 273.15)} \right] \\
 &= 0.0945 \text{ kg/kg dry air}
 \end{aligned}$$

The temperature at the outlet of the plain-tube bundle is now calculated by manipulating Equation (B.30) as shown below.

$$\begin{aligned}
 T_{ao} &= 273.15 + \frac{i_{mao} - w_o i_{fgwo}}{c_{pao} + w_o c_{pvo}} \\
 &= 273.15 + \frac{293.015 \times 10^3 - 0.0945 \times 2.50196 \times 10^6}{1006.8525 + 0.0945 \times 1883.204} \\
 &= 321.0308 \text{ K}
 \end{aligned}$$

This value matches the initial guess of $T_{ao} = 321.0306 \text{ K}$.

The heat transferred to the air can now be calculated according to Equation (6.11).

$$Q = m_a (i_{mao} - i_{mai}) = 154.747 \times (293.015 \times 10^3 - 42.2664 \times 10^3) = 38.4672 \times 10^6 \text{ W}$$

F.2.3.2 Steam-side energy balance

The heat transfer coefficient between the deluge water film and the tube surface can be calculated according to Equation (6.13).

$$h_w = 2102.9 \times (0.01878/0.019)^{1/3} = 2095.1244 \text{ W/m}^2 \text{ K}$$

The density and dynamic viscosity of saturated water vapor at $T_v = 333.15 \text{ K}$ are calculated from Equations (B.8) and (B.10).

$$\begin{aligned}
 \rho_v &= -4.062329056 + 0.10277044(333.15) - 9.76300388 \times 10^{-4}(333.15)^2 \\
 &\quad + 4.475240795 \times 10^{-6}(333.15)^3 - 1.004596894 \times 10^{-8}(333.15)^4 \\
 &\quad + 8.9154895 \times 10^{-12}(333.15)^5 \\
 &= 0.1302 \text{ kg/m}^3
 \end{aligned}$$

$$\begin{aligned}
 \mu_v &= 2.562435 \times 10^{-6} + 1.816683 \times 10^{-8}(333.15) + 2.579066 \times 10^{-11}(333.15)^2 \\
 &\quad - 1.067299 \times 10^{-14}(333.15)^3 \\
 &= 1.1083 \times 10^{-5} \text{ kg/ms}
 \end{aligned}$$

The properties of condensate at $T_v = 333.15 \text{ K}$ are calculated from Equations (B.12) – (B.16).

$$\begin{aligned}
 \rho_c &= \left[\frac{1.49343 \times 10^{-3} - 3.7164 \times 10^{-6}(333.15) + 7.09782 \times 10^{-9}(333.15)^2}{-1.90321 \times 10^{-20}(333.15)^6} \right]^{-1} \\
 &= 983.2168 \text{ kg/m}^3
 \end{aligned}$$

$$\mu_c = 2.414 \times 10^{-5} \times 10^{247.8/(333.15-140)} = 4.6310 \times 10^{-4} \text{ kg/ms}$$

$$\begin{aligned}
 c_{pc} &= 8.15599 \times 10^3 - 28.0627(333.15) + 5.11283 \times 10^{-2}(333.15)^2 \\
 &\quad - 2.17582 \times 10^{-13}(333.15)^6 \\
 &= 4184.0936 \text{ J/kgK}
 \end{aligned}$$

$$\begin{aligned}
 k_c &= -0.614255 + 6.9962 \times 10^{-3}(333.15) - 1.01075 \times 10^{-5}(333.15)^2 \\
 &\quad + 4.74737 \times 10^{-12}(333.15)^4 \\
 &= 0.6532 \text{ W/mK}
 \end{aligned}$$

$$\begin{aligned}
 i_{fg} &= 3.4831814 \times 10^6 - 5.8627703 \times 10^3(333.15) + 12.139568(333.15)^2 \\
 &\quad - 1.40290431 \times 10^{-2}(333.15)^3 \\
 &= 2.3586 \times 10^6 \text{ J/kgK}
 \end{aligned}$$

The condensate Prandtl number at $T_v = 333.15 \text{ K}$ is $Pr_c = 2.9665$ (Kröger, 2004) while the vapor pressure in the tube can be calculated according to Equations (B.5) and (B.6).

$$\begin{aligned}
 z &= 10.79586 \times \left(1 - \frac{273.16}{333.15}\right) + 5.02808 \log_{10} \left(\frac{273.16}{333.15}\right) \\
 &\quad + 1.50474 \times 10^{-4} \left[1 - 10^{-8.29692 \left(\left(\frac{333.15}{273.16}\right)^{-1} - 1\right)}\right] + 4.2873 \times 10^{-4} \left[10^{4.76955 \left(1 - \frac{273.16}{333.15}\right)} - 1\right] \\
 &\quad + 2.786118312 \\
 &= 4.2994
 \end{aligned}$$

$$p_v = 10^{4.2994} = 19925.1161 \text{ N/m}^2$$

The vapor Reynolds number at the inlet to a tube in the first vapor pass is,

$$Re_{vi} = \frac{m_s d_i}{n_b n_{tp1} n_{tr} A_{ts} \mu_v} = \frac{16.3092 \times 0.0158}{2 \times 20 \times 314 \times 1.96 \times 10^{-4} \times 1.1083 \times 10^{-5}} = 17166.9871$$

Since $Re_{vi} < 35\,000$, Equation (6.14) can be used to calculate the condensation heat transfer coefficient inside the tube. This correlation requires knowledge of the tube wall temperature. As a first approximation estimate,

$$T_{wall} = (T_v + T_{wm})/2 = (333.15 + 322.8804)/2 = 328.0152 \text{ K}$$

The modified latent heat of vaporization is calculated from Equation (6.15).

$$i'_{fg} = 2.3586 \times 10^6 + 0.68 \times 4184.0936 \times (333.15 - 328.0152) = 2.3732 \times 10^6 \text{ J/kg}$$

Now find,

$$\begin{aligned}
 h_c &= 0.555 \times \left[\frac{9.8 \times 983.2168 \times (983.2168 - 0.1302) \times 0.6532^3 \times 2.3732 \times 10^6}{4.6310 \times 10^{-4} \times (333.15 - 328.0152) \times 0.0158} \right]^{0.25} \\
 &= 11215.2809 \text{ W/m}^2\text{K}
 \end{aligned}$$

The overall heat transfer coefficient between the deluge film and the condensing steam is now calculated from Equation (6.12).

$$\begin{aligned}
 UA_{2nd} &= 2 \times 1171.421 \left[\frac{1}{2095.1244} + \frac{0.019}{0.0158 \times 11215.2809} + \frac{0.019 \ln(0.019/0.0158)}{2 \times 43} \right]^{-1} \\
 &= 3.7469 \times 10^6 \text{ W/K}
 \end{aligned}$$

The mean deluge water temperature is subsequently,

$$T_{wm} = T_v - Q/UA_{2nd} = 333.15 - 38.4672/3.7469 = 322.8837 \text{ K}$$

This value corresponds well with the original assumption of $T_{wm} = 322.8804 \text{ K}$.

The condensation rate is calculated below and matches the initial assumption of $m_s = 16.3092 \text{ kg/s}$.

$$m_s = Q/i_{fg} = 38.4672/2.3586 = 16.3092 \text{ kg/s}$$

The energy equation for the second stage is balanced.

The water consumed in the HDWD is,

$$m_{evap} = m_a(w_o - w_i) = 153.4095 \times (0.0945 - 0.0087) = 13.1528 \text{ kg/s}$$

F.2.4 The effect of pressure drop related vapor temperature changes

Based on a constant vapor temperature, the heat transfer rate in the HDWD is determined in the sections above to be,

$$Q_{HDWD} = Q_{1st} + Q_{2nd} = 9.4372 + 38.4672 = 47.9044 \text{ MW}$$

Assume vapor enters the first pass of the HDWD at $T_v = 60 \text{ }^\circ\text{C}$ (333.15 K). The corresponding vapor pressure is calculated below.

$$\begin{aligned}
 z &= 10.79586 \left(1 - \frac{273.16}{333.15} \right) + 5.02808 \log_{10} \left(\frac{273.16}{333.15} \right) \\
 &\quad + 1.50474 \times 10^{-4} \left[1 - 10^{-8.29692 \left(\frac{333.15}{273.16} - 1 \right)} \right] + 4.2873 \times 10^{-4} \left[10^{4.76955 \left(1 - \frac{273.16}{333.15} \right)} - 1 \right] \\
 &\quad + 2.786118312 \\
 &= 4.2994
 \end{aligned}$$

$$p_{vi(1st)} = 10^{4.2994} = 19925.1161 \text{ N/m}^2$$

The steam-side pressure drop over the first stage, based on a constant vapor temperature of $T_v = 60 \text{ }^\circ\text{C}$ is calculated to be $\Delta p_{v(1st)} = 1618.6271 \text{ N/m}^2$ using Groenewald and Kröger's (1995) correlations for the frictional pressure drop. The vapor pressure at the first stage outlet is therefore,

$$p_{vo(1st)} = p_{vi(1st)} - \Delta p_{v(1st)} = 19925.1161 - 1618.6371 = 18306.479 \text{ N/m}^2$$

The corresponding vapor temperature is calculated from Equation (B.7).

$$\begin{aligned} T_{vo(1st)} &= 164.630366 + 1.832295 \times 10^{-3} (18306.479) + 4.27215 \times 10^{-10} (18306.479)^2 \\ &\quad + 3.738954 \times 10^3 (18306.479)^{-1} - 7.01204 \times 10^5 (18306.479)^{-2} \\ &\quad + 16.161488 \ln(18306.479) - 1.437169 \times 10^{-4} (18306.479) \ln(18306.479) \\ &= 331.5174 \text{ K} \end{aligned}$$

The mean vapor temperature through the first stage is then,

$$T_{vm(1st)} = (T_{vi(1st)} + T_{vo(1st)})/2 = (333.15 + 331.5174)/2 = 332.3338 \text{ K}$$

The steam-side pressure drop over the first, second and third passes of the HDWD are respectively $\Delta p_{v(2nd-1)} = 312.3645 \text{ N/m}^2$, $\Delta p_{v(2nd-2)} = 312.3645 \text{ N/m}^2$ and $\Delta p_{v(2nd-3)} = 150.854 \text{ N/m}^2$. The corresponding mean vapor temperature through each pass is shown in Table F.6.

Table F.6: Mean vapor temperatures through the HDWD second stage

Pass	1	2	3
$T_v, \text{ }^\circ\text{C (K)}$	58.3296 (331.4796)	58.1696 (331.3196)	58.0496 (331.1996)

The calculations described in Sections F.2.2 and F.2.3 are repeated taking into account the different vapor temperatures in each stage/pass of the HDWD. The draft equation was found to change very little as a result of the vapor temperature changes under consideration. The new predicted heat transfer rate in the first stage

of the HDWD is $Q_{1st} = 9.2684$ MW, representing a decrease of 1.8 % relative to the constant vapor temperature case. In the second stage, $Q_{2nd} = 35.8205$ MW, represents an approximately 7 % reduction in heat transfer rate. The new total heat transfer rate is thus $Q = 45.0889$ MW, which is approximately 6 % less than the value of $Q = 47.9044$ MW predicted based on the constant vapor temperature.

F.3 Sample calculation: HDWD operating as an air-cooled condenser

F.3.1 Draft equation

F.3.1.1 First stage heat exchanger bundle air-side pressure drop

The mean air temperature through the first stage heat exchanger is,

$$T_{am} = (T_{ai} + T_{ao})/2 = (293.15 + 322.0624)/2 = 307.6062 \text{ K}$$

The corresponding density and dynamic viscosity of dry air at this mean temperature are,

$$\rho_{am} = 84600/(287.08 \times 307.6062) = 0.958 \text{ kg/m}^3$$

$$\begin{aligned} \mu_{am} &= 2.287973 \times 10^{-6} + 6.259793 \times 10^{-8} (307.6062) - 3.131956 \times 10^{-11} (307.6062)^2 \\ &\quad + 8.15038 \times 10^{-15} (307.6062)^3 \\ &= 1.8817 \times 10^{-5} \text{ kg/ms} \end{aligned}$$

The density of air at the heat exchanger inlet has been previously calculated to be $\rho_{ai} = 1.0053 \text{ kg/m}^3$. The density at the outlet is in this case,

$$\rho_{ao} = 84600/(287.08 \times 322.0624) = 0.915 \text{ kg/m}^3$$

The characteristic flow parameter through the heat exchanger is,

$$\begin{aligned} Ry_{(1)} &= m_{a(1)} / (\mu_{am} n_b A_{fr} n_{tb1} / n_{tb2}) = 332.1048 / (1.8817 \times 10^{-5} \times 8 \times 13.189 \times 57/58) \\ &= 170204.6305 \text{ m}^{-1} \end{aligned}$$

The heat exchanger loss coefficient for normal isothermal flow is calculated from Equation (A.3) and the overall air-side loss coefficient from Equation (6.22).

$$K_{he} = 4464.831 \times (170204.6305)^{-0.43927} = 21.0413$$

$$K_{\theta} = 21.0413 + \frac{2}{0.875^2} \frac{(1.0053 - 0.915)}{(1.0053 + 0.915)} + \frac{2 \times 1.0053 \times 1}{(1.0053 + 0.915)} = 22.4962$$

The air-side pressure drop over the first stage heat exchanger is calculated using Equation (6.20) with,

$$v_{am} = m_{a(1)} / \rho_{am} n_b A_{fr} = 332.1048 / (0.958 \times 8 \times 13.189) = 3.2855 \text{ m/s}$$

$$\Delta p_{a(1st)} = 22.4962 \times \frac{0.958 \times 3.2855^2}{2} = 116.3198 \text{ N/m}^2$$

F.3.1.2 Second stage heat exchanger bundle air-side pressure drop

The mean air temperature through the second stage heat exchanger is,

$$T_{am} = (T_{ai} + T_{ao}) / 2 = (293.15 + 321.0365) / 2 = 307.0933 \text{ K}$$

The mean density and dynamic viscosity of dry air are then,

$$\rho_{am} = 84600 / (287.08 \times 307.0933) = 0.9596 \text{ kg/m}^3$$

$$\begin{aligned} \mu_{am} &= 2.287973 \times 10^{-6} + 6.259793 \times 10^{-8} (307.0933) - 3.131956 \times 10^{-11} (307.0933)^2 \\ &\quad + 8.15038 \times 10^{-15} (307.0933)^3 \\ &= 1.8794 \times 10^{-5} \text{ kg/ms} \end{aligned}$$

The average free stream velocity upstream of the bundle is,

$$v_o = m_{a(2)} / \rho_{am} n_b A_{fr} = 124.7771 / (0.9596 \times 2 \times 29.925) = 2.1726 \text{ m/s}$$

From Figure 6.3 find,

$$P_t = 2 \times 0.019 = 0.038 \text{ m}$$

$$P_i = \sqrt{3} \times 0.019 = 0.0329 \text{ m}$$

$$a = 0.038/0.019 = 2$$

$$b = 0.0329/0.019 = 1.7321$$

The air velocity in the narrowest cross-section through the bundle is calculated from Equation (6.31).

$$v_{max} = 2.1726 \times 2 / (2 - 1) = 4.3451 \text{ m/s}$$

The corresponding Reynolds number is,

$$Re_{am} = \rho_{am} v_{max} d_o / \mu_{am} = 0.9596 \times 4.3451 \times 0.019 / 1.8794 \times 10^{-5} = 4215.4107$$

The mean film temperature, based on the mean air temperature through the bundle is,

$$T_{aw} = (T_{am} + T_v) / 2 = (307.0933 + 333.15) / 2 = 320.1216 \text{ K}$$

The corresponding air density and dynamic viscosity are,

$$\rho_{aw} = 84600 / (287.08 \times 320.1216) = 0.9177 \text{ kg/m}^3$$

$$\begin{aligned} \mu_{aw} &= 2.287973 \times 10^{-6} + 6.259793 \times 10^{-8} (320.1216) - 3.131956 \times 10^{-11} (320.1216)^2 \\ &\quad + 8.15038 \times 10^{-15} (320.1216)^3 \\ &= 1.9385 \times 10^{-5} \text{ kg/ms} \end{aligned}$$

Now find from Equation (6.32),

$$\begin{aligned} K_b &= \frac{1}{4215.4107^{0.25}} \left[\begin{aligned} &2.5 + \frac{1.2}{(2 - 0.85)^{1.08}} + 0.4 \times \left(\frac{1.7321}{2} - 1 \right)^3 \\ &- 0.01 \times \left(\frac{2}{1.7321} - 1 \right)^3 \end{aligned} \right] \left(\frac{1.9385}{1.8794} \right)^{0.14} \\ &= 0.4429 \end{aligned}$$

The air-side pressure drop over the second stage tube bundle, operating as an air-cooled condenser, is now found using Equation (6.30).

$$\Delta p_{a(2nd-dry)} = 0.4429 \times 25 \times 0.9596 \times 4.3451^2 / 2 = 100.2558 \text{ N/m}^2$$

F.3.1.3 Solution of the draft equation

The mean air temperature leaving the first and second stage heat exchangers is approximated by,

$$\begin{aligned} T_{ao} &= (T_{ao(1)} m_{a(1)} + T_{ao(2)} m_{a(2)}) / (m_{a(1)} + m_{a(2)}) \\ &= (322.0624 \times 332.1048 + 321.0365 \times 124.7771) / (332.1048 + 124.7771) \\ &= 321.7822 \text{ K} \end{aligned}$$

The density of air flowing through the fan is then,

$$\rho_{aF} = 84600 / (287.08 \times 321.7822) = 0.9158 \text{ kg/m}^3$$

The volumetric flow rate through the fan is,

$$V_F = (m_{a(1)} + m_{a(2)}) / \rho_{aF} = (332.1048 + 124.7771) / 0.9158 = 498.8883 \text{ m}^3/\text{s}$$

The corresponding fan static pressure rise and fan power consumption are calculated from Equations (A.4) and (A.5).

$$\begin{aligned} \Delta p_{Fs} &= \left[320.0451719 - 0.297521548 \times (498.8883) \right. \\ &\quad \left. + 6.35149 \times 10^{-4} \times (498.8883)^2 - 8.14 \times 10^{-7} \times (498.8883)^3 \right] \left(\frac{0.9158}{1.2} \right) \\ &= 174.4819 \text{ N/m}^2 \end{aligned}$$

$$\begin{aligned} P_F &= \left[186645.2333 - 59.41386339 \times (498.8883) \right. \\ &\quad \left. + 0.476168398 \times (498.8883)^2 - 5.08308 \times 10^{-4} \times (498.8883)^3 \right] \left(\frac{0.9158}{1.2} \right) \\ &= 162.1001 \times 10^3 \text{ W} \end{aligned}$$

The total loss coefficient for obstacles up- and downstream of the fan considered here is $K_{up/do} = 0.6877$ while the heat exchanger support tower loss coefficient is $K_{ts} = 1.5$ (Kröger, 2004). The losses due to these obstacles are subsequently,

$$\begin{aligned}\Delta p_{up/do} &= \frac{K_{up/do}}{2\rho_{aF}} \left(\frac{m_{a(1)} + m_{a(2)}}{A_e} \right)^2 = \frac{0.6877}{2 \times 0.9158} \left(\frac{332.1048 + 124.7771}{64.5039} \right)^2 \\ &= 18.8367 \text{ N/m}^2\end{aligned}$$

$$\Delta p_{ts} = \frac{K_{ts}}{2\rho_{ai}} \left(\frac{m_{a(1)} + m_{a(2)}}{A_c} \right)^2 = \frac{1.5}{2 \times 1.0053} \left(\frac{332.1048 + 124.7771}{66.0433} \right)^2 = 35.7039 \text{ N/m}^2$$

The density and dynamic viscosity of the air at the second stage plain tube bundle outlet are,

$$\rho_{ao} = 84600 / (287.08 \times 321.0365) = 0.9179 \text{ kg/m}^3$$

$$\begin{aligned}\mu_{ao} &= 2.287973 \times 10^{-6} + 6.259793 \times 10^{-8} (321.0365) - 3.131956 \times 10^{-11} (321.0365)^2 \\ &\quad + 8.15038 \times 10^{-15} (321.0365)^3 \\ &= 1.9426 \times 10^{-5} \text{ kg/ms}\end{aligned}$$

The loss coefficient over the drift eliminators is now calculated using Equation (6.28).

$$K_{de} = 27.4892 \times (2.1726 \times 0.9179 / 1.9426 \times 10^{-5})^{-0.14247} = 5.3111$$

The corresponding loss over the drift eliminators is,

$$\Delta p_{de} = K_{de} \rho_{ao} v_0^2 / 2 = 5.3111 \times 0.9179 \times 2.1726^2 / 2 = 11.5056 \text{ N/m}^2$$

The loss over the collecting troughs is calculated from Equation (6.33).

$$\Delta p_{ct} = 1.027 \times [124.7771 / (2 \times 29.925)] = 4.4688 \text{ N/m}^2$$

The left side of Equation (6.19) equates to,

$$\Delta p_{Fs} - (\Delta p_{is} + \Delta p_{up/do}) = 174.4819 - (35.7039 + 18.8367) = 119.9413 \text{ N/m}^2$$

The right side of Equation (6.19) equals,

$$\Delta p_{a(2nd)} + \Delta p_{ct} + \Delta p_{de} = 100.2558 + 4.4688 + 11.5056 = 116.23 \text{ N/m}^2$$

These values are suitably similar to one another and $\Delta p_{a(1st)} = 116.3198 \text{ N/m}^2$. The draft equation is therefore balanced.

F.3.2 First stage energy equation

F.3.2.1 Air-side energy balance

The mean air temperature through the respective bundles is,

$$T_{am(1)} = (T_{ai} + T_{ao(1)})/2 = (293.15 + 308.762)/2 = 300.956 \text{ K}$$

$$T_{am(2)} = (T_{ao(1)} + T_{ao(2)})/2 = (308.762 + 322.0624)/2 = 315.4122 \text{ K}$$

The corresponding properties of air are,

$$\rho_{am(1)} = 84600/(287.08 \times 300.956) = 0.9792 \text{ kg/m}^3$$

$$\begin{aligned} c_{pam(1)} &= 1.045356 \times 10^{-3} - 3.161783 \times 10^{-1} (300.956) + 7.083814 \times 10^{-4} (300.956)^2 \\ &\quad - 2.705209 \times 10^{-7} (300.956)^3 \\ &= 1006.9874 \text{ J/kgK} \end{aligned}$$

$$\begin{aligned} \mu_{am(1)} &= 2.287973 \times 10^{-6} + 6.259793 \times 10^{-8} (300.956) - 3.131956 \times 10^{-11} (300.956)^2 \\ &\quad + 8.15038 \times 10^{-15} (300.956)^3 \\ &= 1.8513 \times 10^{-5} \text{ kg/ms} \end{aligned}$$

$$\begin{aligned} k_{am(1)} &= -4.937787 \times 10^{-4} + 1.018087 \times 10^{-4} (300.956) - 4.627937 \times 10^{-8} (300.956)^2 \\ &\quad + 1.250603 \times 10^{-11} (300.956)^3 \\ &= 0.0263 \text{ W/mK} \end{aligned}$$

$$\rho_{am(2)} = 84600 / (287.08 \times 315.4122) = 0.9343 \text{ kg/m}^3$$

$$\begin{aligned} c_{pam(2)} &= 1.045356 \times 10^{-3} - 3.161783 \times 10^{-1} (315.4122) + 7.083814 \times 10^{-4} (315.4122)^2 \\ &\quad - 2.705209 \times 10^{-7} (315.4122)^3 \\ &= 1007.6141 \text{ J/kgK} \end{aligned}$$

$$\begin{aligned} \mu_{am(2)} &= 2.287973 \times 10^{-6} + 6.259793 \times 10^{-8} (315.4122) - 3.131956 \times 10^{-11} (315.4122)^2 \\ &\quad + 8.15038 \times 10^{-15} (315.4122)^3 \\ &= 1.9172 \times 10^{-5} \text{ kg/ms} \end{aligned}$$

$$\begin{aligned} k_{am(2)} &= -4.937787 \times 10^{-4} + 1.018087 \times 10^{-4} (315.4122) - 4.627937 \times 10^{-8} (315.4122)^2 \\ &\quad + 1.250603 \times 10^{-11} (315.4122)^3 \\ &= 0.02741 \text{ W/mK} \end{aligned}$$

The Prandtl numbers for air at the mean temperatures through the first and second bundles are respectively $Pr_{am(1)} = 0.709$ and $Pr_{am(2)} = 0.7049$ (Kröger, 2004).

The heat transfer rate to the air is now calculated from Equation (4.1).

$$\begin{aligned} Q_{(1)} &= m_a c_{pa(1)} (T_{ao(1)} - T_{ai}) = 332.1048 \times 1006.9874 \times (308.762 - 293.15) \\ &= 5.2211 \times 10^6 \text{ W} \end{aligned}$$

$$\begin{aligned} Q_{(2)} &= m_a c_{pa(2)} (T_{ao(2)} - T_{ao(1)}) = 332.1048 \times 1007.6141 \times (322.0624 - 308.6976) \\ &= 4.4507 \times 10^6 \text{ W} \end{aligned}$$

$$Q = \sum_{i=1}^{n_r} m_a c_{pa(i)} (T_{ao(i)} - T_{ai(i)}) = 5.2211 \times 10^6 + 4.4507 \times 10^6 = 9.6718 \times 10^6 \text{ W}$$

F.3.2.2 Steam-side energy balance

The characteristic heat transfer parameter for the first row is,

$$\begin{aligned}
 Ry_{(1)} &= m_a / (\mu_{am(1)} n_b A_{fr} n_{tb1} / n_{tb2}) = 332.1048 / (1.8513 \times 10^{-5} \times 8 \times 13.189 \times 57 / 58) \\
 &= 173005.0387 \text{ m}^{-1}
 \end{aligned}$$

The corresponding characteristic heat transfer parameter is calculated according to Equation (A.1)

$$Ny_{(1)} = 366.007945 \times (173005.0387)^{0.433256} = 68062.9699 \text{ m}^{-1}$$

The effective air-side heat transfer coefficient is then calculated from Equation (6.3).

$$UA_{(1)} = 0.0263 \times 0.709^{0.333} \times 8 \times 13.189 \times 68062.9699 = 165586.0766 \text{ W/K}$$

The effectiveness of the first tube row is calculated from Equation (6.2).

$$e_{(1)} = 1 - \exp[-165586.0766 / (332.1048 \times 1006.9874)] = 0.3905$$

The heat transferred from the first tube row is now calculated according to Equation (6.1).

$$\begin{aligned}
 Q_{(1)} &= m_a c_{pa(1)} e_{(1)} (T_v - T_{ai(1)}) = 332.1048 \times 1006.9874 \times 0.3905 \times (333.15 - 293.15) \\
 &= 5.2256 \times 10^6 \text{ W}
 \end{aligned}$$

This value compares well with the value of $Q_{(1)} = 5.2211 \text{ MW}$ determined using the air-side energy balance.

A similar procedure is followed for the second tube row with the characteristic heat transfer parameter calculated according to Equation (A.2).

$$Ry_{(2)} = m_a / (\mu_{am(2)} n_b A_{fr}) = 332.1048 / (1.9172 \times 10^{-5} \times 8 \times 13.189) = 164174.1419 \text{ m}^{-1}$$

$$Ny_{(2)} = 360.588007 \times (164174.1419)^{0.470373} = 102364.6066 \text{ m}^{-1}$$

$$UA_{(2)} = 0.02741 \times 0.7049^{0.333} \times 8 \times 13.189 \times 102364.6066 = 263527.3795 \text{ W/K}$$

$$e_{(2)} = 1 - \exp\left[-263527.3795 / (332.1048 \times 1007.6141)\right] = 0.545$$

$$\begin{aligned} Q_{(2)} &= m_a c_{pa(2)} e_{(2)} (T_v - T_{ai(2)}) = 332.1048 \times 1007.6141 \times 0.545 \times (333.15 - 308.6976) \\ &= 4.4508 \times 10^6 \text{ W} \end{aligned}$$

This value corresponds well with the value of $Q_{(2)} = 4.4507$ MW calculated using the air-side energy balance. The energy equation is therefore balanced and the initial assumptions were correct. The total heat transfer rate for the first stage of the HDWD is $Q = 9.6718$ MW.

F.3.3 Second stage energy equation

F.3.3.1 Air-side energy balance

The specific heat of air at the mean temperature through the second stage bundle, $T_{am} = 307.0933$ K, is calculated from Equation (B.2).

$$\begin{aligned} c_{pa} &= 1.045356 \times 10^{-3} - 3.161783 \times 10^{-1} (307.0933) + 7.083814 \times 10^{-4} (307.0933)^2 \\ &\quad - 2.705209 \times 10^{-7} (307.0933)^3 \\ &= 1007.2301 \text{ J/kgK} \end{aligned}$$

The heat transferred to the air is simply calculated directly from Equation (6.1).

$$\begin{aligned} Q &= m_a c_{pam} (T_{ao} - T_{ai}) = 124.7771 \times 1007.2301 \times (321.0365 - 293.15) \\ &= 3.5048 \times 10^6 \text{ W} \end{aligned}$$

F.3.3.2 Steam-side energy balance

The mean air velocity through the second stage heat exchanger has been previously calculated to be $v_{am} = 2.1726$ m/s, while the air velocity in the narrowest cross-section of the heat exchanger is $v_{max} = 4.3451$ m/s. The density and dynamic viscosity of air at the mean film temperature through the bundle, $T_{aw} = 320.1216$ K, have also been found previously as $\rho_{aw} = 0.9206$ kg/m³ and

$\mu_{aw} = 1.9385 \times 10^{-5}$ kg/ms. The thermal conductivity of air at the mean film temperature is calculated from Equation (B.4).

$$\begin{aligned} k_{aw} &= -4.937787 \times 10^{-4} + 1.018087 \times 10^{-4} (320.1216) - 4.627937 \times 10^{-8} (320.1216)^2 \\ &\quad + 1.250603 \times 10^{-11} (320.1216)^3 \\ &= 0.0278 \text{ W/mK} \end{aligned}$$

The Prandtl number at the mean film temperature is $Pr_{aw} = 0.7037$ (Kröger, 2004).

The Reynolds number corresponding to the maximum velocity and mean film temperature properties is,

$$Re_{am} = \rho_{aw} v_{max} d_o / \mu_{aw} = 0.9206 \times 4.3451 \times 0.019 / 1.9385 \times 10^{-5} = 3920.5725$$

The air-side Nusselt number for a tube in the first tube row is calculated from Equation (6.4).

$$Nu = 0.3 + \frac{0.62 \times 3920.5725^{1/2} \times 0.7037^{1/3}}{\left[1 + (0.4/0.7037)^{2/3}\right]^{1/4}} = 31.663$$

The arrangement factor is calculated from Equation (6.7) and the average Nusselt number for the bundle subsequently from Equation (6.8).

$$\Phi = 1 + 2 \times 0.019 / (3 \times 0.0329) = 1.385$$

$$Nu_{avg} = 1.385 \times 31.663 = 43.8501$$

The corresponding air-side heat transfer coefficient is calculated from Equation (6.9).

$$h_{avg} = Nu_{avg} k_{aw} / d_o = 43.8501 \times 0.0278 / 0.019 = 64.0813 \text{ W/m}^2\text{K}$$

The overall heat transfer coefficient between the steam and the air is now approximated using Equation (6.10).

$$\begin{aligned}
 UA_{2nd} &= h_{avg} A_a = h_{avg} \pi d_o L_t n_r n_{ir} n_b = 64.0813 \times \pi \times 0.019 \times 2.5 \times 25 \times 314 \times 2 \\
 &= 150132.3749 \text{ W/K}
 \end{aligned}$$

The heat transfer effectiveness is now calculated from Equation (6.2).

$$e = 1 - \exp[-150132.3749 / (124.7771 \times 1007.2301)] = 0.6972$$

The heat transfer rate is determined using Equation (6.1).

$$Q = 124.7771 \times 1007.2301 \times 0.6972 \times (333.15 - 293.15) = 3.5048 \times 10^6 \text{ W}$$

This value matches the previously predicted value of $Q = 3.5048 \text{ MW}$ and the energy equation is balanced.

The total heat transfer rate in the HDWD when operating in dry mode is therefore,

$$Q_{HDWD} = Q_{1st} + Q_{2nd} = 9.6718 + 3.5048 = 13.1766 \text{ MW}$$